Fall 1994

Simulation of Active Control of Asymmetric Flows Around Slender Pointed Forebodies

Hazem Sharaf El-Din
Old Dominion University

SIMULATION OF ACTIVE CONTROL OF ASYMMETRIC FLOWS AROUND SLENDER POINTED FOREBODIES

by

Hazem Sharaf El-Din Hafez Sharaf El-Din
B.Sc. July 1985, Cairo University, Egypt
M.Sc. November 1988, Cairo University, Egypt

A Dissertation Submitted to the Faculty of Old Dominion University in Partial Fulfillment of the Requirements for the Degree of

DOCTOR OF PHILOSOPHY
Engineering Mechanics

Old Dominion University

December 1994

Approved by:

Osama A. Kandil (Director)

Robert L. Ash

Oktay Baysal

Colin P. Britcher

Chen-Huei Liu (NASA LaRC)

ABSTRACT

SIMULATION OF ACTIVE CONTROL OF ASYMMETRIC FLOWS AROUND SLENDER POINTED FOREBODIES

Hazem Sharaf El-Din Hafez Sharaf El-Din

Old Dominion University, December 1994

Dirctor: Dr. Osama A. Kandil

At high angles of attack, the flowfield over slender forebodies becomes asymmetric with substantial side force, which may exceed the available control capability. The unsteady compressible Navier-Stokes equations are used to investigate the effectiveness of different active control methods to alleviate and possibly eliminate the flow asymmetry and the subsequent side force. Although the research work focuses on active control methods, a passive control method has been investigated. The implicit, Roe flux-difference splitting, finite volume scheme is used for the numerical computations. Both locally-conical and three-dimensional solutions of the Navier-Stokes equations are obtained.

The asymmetric flow over five-degree semi-apex angle cone is used as a reference case to which the different control methods are applied and compared. For the passive control method, the side-strakes control is investigated. The parametric study includes the control effectiveness of the strake span length.

For the active control methods, flow injection in the normal and tangential directions to the body surface has been investigated. Both uniform and pressure-sensitive mass flow injection are applied, and the effects of mass flow rate, injection angle and injection length have also been studied. Injection, with a parabolic profile, is applied from the cone sides tangent to its surface. Surface-heating, where temperature of the

cone surface is increased, is also investigated. The effectiveness of a hybrid method of flow control which combines injection with surface heating has been studied. The cone spinning and rotary oscillation around its axis are applied as an active control method. The computational applications include the effects of uniform spinning rates and periodic rotary oscillations at different amplitudes and frequencies on the flow asymmetry.

DEDICATION

To My Father, My Mother

My Wife, My Daughter And My Son

With All My Love

ACKNOWLEDGMENTS

All my thanks are due to Allah (Great and Glorious is He);
His grace alone brings succor.

My most heartfelt and sincere thanks go to my to my advisor Prof. Osama A. Kandil without his guidance, patience and support, in good and bad times, none of this would have been realized.

Also, I would like to express my appreciation to Prof. Robert L. Ash, Prof. Oktay Baysal, Dr. Colin C. Britcher and Dr. Chen-Huei Liu for serving on my committee and reviewing the dissertation.

This research work has been supported by the Aerodynamics and Acoustics Methods Branch and the former Theoretical Flow Physics Branch of NASA Langley Research Center under NASA Grant No. NAG-1-994, monitored by Dr. Chen-Huei Liu. My sincere thanks are also extended to Dr. James Thomas, head of the Aerodynamics and Acoustics Methods Branch and Dr. Ajay Kumar, head of the former Theoretical Flow Physics Branch, for their support of this research. I would like to acknowledge the substantial computational resources provided by the NASA Langley Research Center and the Numerical Aerodynamics Simulation (NAS) Program at NASA Ames Research Center.

I would like to extend my thanks to my colleagues and friends, especially, Dr. Tin-Chee Wong and Dr. Hamdy A. Kandil.

Most of all, It is an honor and a privilege to show my deepest gratitude to my parents for their never-ending support during my whole academic career. I would like also to thank my lovely wife, daughter and son for their patience, understanding and continuous encouragement.

TABLE OF CONTENTS

LIST OF FIGURES

LIST OF SYMBOLS

a	Local speed of sound
A	Inviscid Jacobian matrix
c	Sutherland constant
C_p	Specific heat at constant pressure
CFL	Courant-Friedrichs-Lewy number
e	Total energy per unit mass
E	Inviscid flux
E_v	Viscous flux
$\tilde{F}$	Inviscid flux in conical coordinates
$\tilde{F}_v$	Viscos flux in conical coordinates
h	Side-strake span length
I	Identity matrix
J	Jacobian of coordinate transformation
J^{-1}	Inverse Jacobian of coordinate transformation
k	Coefficient of thermal conductivity
l_i	Effective injection length
L	Characterstic length
M	Mach number
p	Static pressure
P_r	Prandtl number
q	Heat-flux component
$\bar{q}$	Flowfield vectors
$\bar{Q}$	Conservavtive variables vector in body fitted coordinates
R_e	Reynolds number
R^+, R^-	Riemann invariants
t	Nondimensional time
T	Static temperature
T_s	Surface temperature
TPL	Total pressure loss
u_1, u_2, u_3	Cartesian components of velocity

$\acute{u}_1$, $\acute{u}_2$, $\acute{u}_3$	Velocity component in conical coordinates
U_1, U_2, U_3	Contravariant velocities
V_s	Surface velocity
x_1, x_2, x_3	Cartesian coordinates
α	Angle of attack
β	Side-slip angle
γ	Ratio of specific heats
δ_{ij}	Kronecker delta function
λ_1, λ_2, λ_3	Eigenvalues
μ	Molecular viscosity
ξ_1, ξ_2, ξ_3	Computational coordinates
η_1, η_2, η_3	Conical coordinates
ρ	Density
τ	Shear stress tensor and period of rotary oscillation
θ	Azimuthal angle
θ_i	Effective injection angle
θ_h	Effective heating angle
θ_a	Rotary oscillation angle
∂	Partial derivative

CHAPTER 1

INTRODUCTION

1.1 Motivation

In the last two decades, there has been an increasing interest in high angle-of-attack (AOA) aerodynamics due to its importance in the design of modern fighter aircraft, missiles, and the aerospace vehicles such as aerospace plane. For modern fighter aircraft, flight at high AOA is an inherent part of both offensive and defensive maneuvering. Maximum lift in modern aircraft is obtained at 25° to 35° AOA while during maneuvering AOA may reach 60° or more. On the other hand, there is a tendency toward high AOA in missile design because of the need for high maneuverability, and specific requirements on flight behavior.

The flow structure over a slender body changes with increases in AOA. Four main flow patterns can be observed as the AOA increases from 0° to 90°, as shown in Fig. 1.1. At low AOA, the axial flow component dominates, and the flow is attached. Meanwhile a thick viscous layer will be generated on the leeside. At intermediate AOA, the crossflow separates and rolls up into a symmetric vortex pair. With further increases in the AOA, the vortex pair becomes asymmetric. Shedding and unsteady vortices will result at higher AOA. At AOA near 90°, the axial-flow component has less and less influence and the leeside flow resembles the wake of a two dimensional cylinder normal to the flow [2].

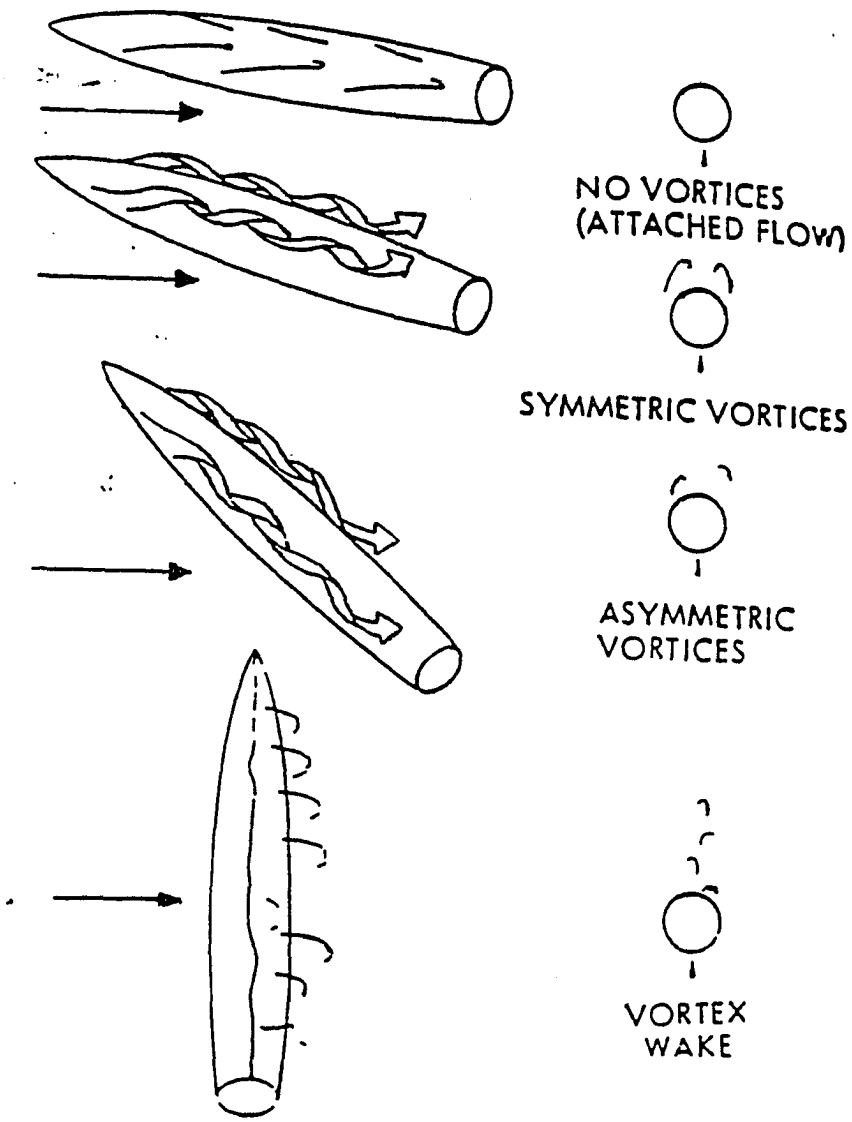

Figure 1.1: Flow structures at different angles of attack, Ref. [1].

It was shown [3] that the side forces, which arise due to the flow asymmetry at zero side-slip, can exceed the control capacity available at high AOA of attack. This problem can be overcome by introducing new control methodology to control, suppress, alleviate or eliminate the flow asymmetry and consequently the side forces.

In the past, most of the effort was concerned with developing passive control methods. Passive control methods deal mainly with geometric perturbation, such as nose bluntness, strakes, and boundary layer trips. These methods have proven to be effective within certain AOA ranges. Such control methods introduce changes in the geometry of the missile or aircraft which may be unfavorable from other design aspects, i.e. reduction in storage space. Another disadvantage of the passive control methods is their effect on the directional stability of missiles [4].

Recently, research has started to focus on new approaches to the flow-asymmetry control problem. Active control methods include injection or blowing in different directions, nose spinning or rotation, and surface heating. These methods have the advantage that they can be adaptive compared to the passive methods. On the other hand, their main disadvantage is that they require some sort of energy to make them effective.

1.2 The Scope of the Study

In the present study, the unsteady compressible Navier-Stokes equations are used to investigate the effectiveness of different control methods to alleviate and possibly eliminate the side forces and the flow asymmetry that arise at high AOA. Pointed slender bodies are commonly used to represent aerodynamic components of both missiles and aircraft. The cone, which is used extensively in the present research, has a simple geometry which simplifies some of the computational effort, however, it has a very complicated three-dimensional separated flowfield. Also, the cone is

used widely as a basic shape for ballistic re-entry vehicles. Flow around isolated aerodynamic components has been used to study the vortex dynamics and the flow asymmetry.

Several methods of flow asymmetry control are presented. These methods can be divided into two categories: passive and active. Passive control methods that are presented here, are concerned mainly with the use of strakes to prevent interactions between the forebody vortices. In the study of the effect of active control methods, blowing—both normal and tangential—surface heating, spinning and rotary oscillations are presented.

To avoid the large computational resources required for the solution of the three-dimensional problems, the locally-conical-flow assumption has been used in most of the cases studied in the present dissertation. With such an assumption, the problem solution reduces to that of a two-dimensional flow problem which represents a saving in the computational time and storage by an order of magnitude. Thus, the dynamic behavior of the flow asymmetry and the effectiveness of different control methods can be studied efficiently. This methodology allows us to investigate more control methods and cases than would be feasible with three-dimensional approach.

In Chap. 2, a literature survey which covers the onset of asymmetric flow and the different control techniques is presented. This chapter covers both experimental and computational research and focuses on the most recent publications.

Chapter 3 presents the mathematical formulation of the unsteady compressible three-dimensional Navier-Stokes equations. The conical form of the Navier-Stokes equations are derived and the various approximation levels are discussed. In Chap. 4, the computational scheme which is used to solve the Navier-Stokes equations, is discussed. The implicit, upwind, finite-volume, flux difference-splitting scheme is described. At the end of this chapter, the boundary and initial conditions for the different problems are discussed.

The computational results are presented and discussed in Chapters 5, 6, 7 and 8. In Chap. 5, the results of the passive control methods are presented. The effect of strake span is addressed in this chapter. Chapter 6 discusses the effect of both normal and tangential injection as an active method to control flow asymmetry. Surface heating as a flow disturbance-damping factor is addressed in this chapter. Spinning and rotary oscillations are presented as means to suppress flow asymmetry in chapter 7. In Chap. 5, 6 and 7, the locally-conical flow assumption is used while in Chap. 8, three-dimensional effects are studied with applications to flow-injection control over a three-dimensional configuration. Concluding remarks for the present study and suggestions for future work are presented in Chap. 9.

CHAPTER 2

LITERATURE SURVEY

2.1 Introduction

Conventional control methods have limited the effective AOA range which limits aircraft maneuverability. Exceeding this range without providing the aircraft with an additional control technique may result in unrecoverable flight modes such as spin. Flying at high AOA usually leads to asymmetric flow on the forebody and hence unfavorable side forces and yawing moments.

The interest in the study of asymmetric flow, and the side force and yawing moment has increased in the last decade due to the need to increase the flight envelope of fighter aircraft and the rockets. The non-conventional control methods include forebody fixed and movable strakes, trips, and normal and tangential blowing. In this chapter, a literature survey of the topics related to the subject of our study is presented. First, origins of flow asymmetry are discussed and the effect of the different parameters (Mach number and Reynolds number) on the flow asymmetry is presented. Computational and experimental work on asymmetric flow over cones is presented. The literature is surveyed concerning passive and active control methods and covers both computational and experimental work with emphasis on the most recent publications. A discussion of the advantages and disadvantages of the different methods is included.

2.2 Flow Asymmetry

2.2.1 Experimental

Pictures of the flowfield over a tangent-ogive forebody produced by Fiechter [5] showed clearly the different patterns of the flowfield with increasing AOA. At low AOA, an attached flow dominated by the axial flow component is observed. At medium ranges of AOA, a symmetrical pair of vortices on the leeward side of the body is observed. With the increase of the AOA, the vortices become asymmetric and vortex shedding and unsteadiness show up at higher AOA. As the AOA approaches 90°, the flow resembles that of the wake over a circular cylinder. While Fiechter's experiment was conducted with very low Mach number and Reynolds number, similar observations were made at a Mach number of 0.6 and a Reynolds number of 4.3×10^5 [6].

Letko in 1953 [7] made the first measurement of the side force at zero side slip for an aircraft configuration, while Dunn in 1954 [8] reported the existence of side forces on a missile configuration. There was not much interest in the 1950's and 1960's in the side force phenomena. Starting in 1970, there has been an increasing interest in that phenomena due to the need of higher maneuverability and flight at high AOA for both aircraft and missiles. The study of the side force on ogive-cylinder bodies at high AOA and subsonic to transonic Mach number was investigated by Pick in 1971 [9]. The direction of the side force which started to appear at an AOA of 20°, was unpredictable and the peak in the side force was between 35° and 40°.

Keener and Chapman [10] investigated the side force at zero sideslip on several symmetric forebodies in the AOA range of 0° to 90° and the Mach number range of 0.1 to 0.7. In their conclusion, they pointed out that sharp noses are more likely to introduce side forces when compared to blunt noses and the direction of vortex asymmetry was found to depend on small imperfections in the body surface.

The effects of Reynolds number on the magnitude of the side force was studied for the flow over a tangent-ogive forebody [1,11]. These experiments were conducted in the AOA range of 36° to 88°, Mach number of 0.2 and Reynolds numbers based on the diameter range of 0.4×10^6 to 3.7×10^6. The maximum side force was as large as the normal force and the side force showed up only at Reynolds number above 2×10^6. Mach number effects were studied by Wardlaw and Morrison [12] for the flow over cones, tangent-ogives and paraboloids. The side force was found to decrease with increasing subsonic cross-flow Mach number (above 0.4) and became insignificant at supersonic cross-flow Mach numbers.

Two types of asymmetric flow were recognized, depending on the origin of the asymmetry. The first was concerned with aft body asymmetric vortices and usually occurred at low AOA if the body was long enough. The induced side force due to this type of asymmetry was insignificant compared to the second type, nose-induced asymmetry, in which the magnitude of the side force can exceed that of the normal force [13]. The aft body asymmetry is associated with loss of lift while the nose-induced asymmetry is often associated with increases in lift. The nose-induced asymmetry dominates the flowfield when the relative incidence—the ratio between the AOA and the nose angle—exceeds a certain value, which depends mainly on the forebody shape.

2.2.2 Computational

Degani et al. [14–18] determined that in the absence of spatial disturbances, numerical solutions for flowfields around bodies did not become asymmetric, in contrast with experimental observations. The introduction of some sort of spatial disturbance, e.g. a small asymmetry in the body shape, changed the symmetric flowfield into an asymmetric one, but the flow regained its symmetry as soon as the geometric disturbance was removed. They also concluded that the level of asymmetry was a

function of the spatial disturbance location. Convective stability theory, where all the disturbances are carried away unless the disturbance is maintained for all times, is used to explain that situation compared to the absolute instability where any disturbance will grow in time. On the other hand, Kandil et al. [19–21] and Wong [22] numerically applied a 2° side slip transient disturbance on a cone and the resultant asymmetric solution was found to be persistent, upon removing the source of the disturbance. Also, they found at the physical conditions considered, the asymmetric solution thus obtained was unique irrespective of the disturbance source. For three-dimensional solutions [23], the disturbance required for the asymmetry was larger but the asymmetry was persistent upon removing the source of disturbance. Siclari et al. [24,25] obtained naturally occurring asymmetric, conical, steady solutions for cones at supersonic Mach numbers. The conical-flow solution was used as the initial conditions for the three-dimensional problem in which the asymmetry remained.

2.2.3 Asymmetric flow over cones

While the cones represent the simplest body form, the flowfield over them is complex with three-dimensional separation. Such features have made the cone the choice of many researchers as a representation for forebodies of aircraft, and missiles. The three-dimensional separation of the flow over cones, into a symmetric or asymmetric pair of vortices, was reviewed by Rainbird et al. [26]. The effect of the ratio between the AOA and the nose semi-angle was determined to be $\frac{3}{4}$ for the symmetric vortices. The differences in the flowfield structures between the sharp and blunt cones with semi-apex angles of 5.6° were studied in 1972 by Stetson [27]. Those experiments were conducted at a very high Mach number of 14.2 and a Reynolds number of 0.62×10^6. The sharp cone separation started at the nose and for the blunt nose, the separation started relatively downstream and moved in the upstream direction with increases in the AOA. The difference can be viewed as the difference in the origin of asymmetry which has been described in the previous section.

The steady Navier-Stokes equations, while neglecting the streamwise derivative terms for the flow over the downstream part of the cone, were solved by Lubard and Helliwell [28]. The AOA considered was 8° and hence while separation appeared, the flow retained its symmetry. On the other hand, McRae and Hussaini [29] solved the conical form of the Navier-Stokes equations utilizing Cross's conclusion [30] that the viscous layer growth on the lee side is essentially conical. The solution covers only half of the cone, assuming symmetric boundary conditions. This case was for flow with a Mach number of 1.8, a Reynolds number of 29.4×10^6, and AOA of 12.5° and 24°, and 5° semi-apex angle cone.

Kandil et al. solved the conical form of the Navier-Stokes equations [19, 20, 31] and the three-dimensional Navier-Stokes equations [32] for the supersonic flow over a cone. The onset of asymmetry was found to be unique irrespective of the source of the disturbance—numerical or physical. The results of this research were presented in more detail in Ref. 22. Siclari et al. [24,25] solved the flow over cones with different cross sections at AOA of 20° using the conical form of the Navier-Stokes equations. The asymmetric flow appeared at $\alpha/\theta_c = 4.0$, where α is the AOA and θ_c is the semi-apex angle of the cone. Thomas [33], using the CFL3D code solved the conical form of Navier-Stokes equations and found out that a fine grid was needed for the numerical disturbance to grow into an asymmetric solution. Recently, Dusing and Orkwis, using the conical Navier-Stokes equations [34], verified the results obtained previously by [24,32] for the flow over a 5° semi-apex angle cone.

For more information regarding the flow asymmetry and its origin, the reader is advised to consult Chap. 2 in Ref. 22, the book by Rom [35], conference proceedings [36–43] as well as numerous review articles [2,4,44–50]

2.3 Passive Control Methods

2.3.1 Strakes and fins

2.3.1.1 Fins or single strakes

Using a fin or a single strake placed on the lee-side of the plane of geometric symmetry reduces the interaction between the flows on the two sides of the body, and the perturbation imposed at the apex, which causes the asymmetry, is not allowed to be amplified.

The effect of the fin on the flow asymmetry has been discussed by Stahl [51]. The study covered the AOA range from 15° to 50° for flow over an 8° semi-apex angle cone with a Reynolds number, based on the diameter, of 7800 and freestream velocity of 0.14 m/s. Different fins were used with the ratio of fin height to the cone radius equal to 1.25, 1.0, 0.75 and 0.5. While the onset of asymmetry of the lee-side flows was observed at an AOA of 35° for the no-fin configuration, no asymmetry was observed for the AOA range considered with the fin height of $1.25r$, where r was the local radius of the cone.

Ng [52] studied the effect of a single strake on the forebody vortex asymmetry over a 4.0 caliber tangent-ogive forebody, with the length of strake as 8% of the body and strake base height as $\frac{1}{3}$ of the local forebody diameter. The experiment was conducted at a Reynolds number of 2.8×10^4 per unit length and freestream velocity of 4 in/sec. While the asymmetry showed up at an AOA of 30° with no-strake configuration, the level of the asymmetry is reduced significantly but not eliminated by the strake configuration.

Numerical solutions for the case of asymmetric flow control using fins over circular, elliptic and diamond cross section forbodies were investigated by Kandil et al. [53]

in 1990. Using conical solutions, they found that at an AOA of 25°, a fin of length equal to 1.5 thus the length of the minor axis was required to render the flow to be symmetric for the diamond shape while that length was found to be 2.0 of the length of the minor axis for the elliptic shape.

Computationally and experimentally, Degani [17] studied the effect of splitter plates, i.e. fins, for the flow over ogive cylinders with a Mach number of 0.2, Reynolds number based on the diameter of 26,000 and an AOA of 40°. In the experiments, the ratio of the total body length to the diameter of the body was 15.0 with 3.5 (the ratio of body length to its diameter) tangent-ogive as forebody, while in the computations, the afterbody length was decreased to 7.0 diameters. The computational results were compared qualitatively with experimental surface pressure and smoke visualization. Both experimental and numerical results show that the fin presence in the leeward plane of symmetry suppressed the disturbances and left the two primary vortices symmetric. In the experimental configuration, the splitter plate extended to the wind tunnel wall preventing any type of interactions between the primary vortices.

2.3.1.2 Double strakes

In 1972, Coe et al. [54] investigated the effect of strakes for flows over a cone, a tangent ogive and a paraboloid of revolution where Reynolds number based on the diameter ranged from 0.15×10^6 to 0.35×10^6 and an AOA range of 0° to 75°. The two strakes, placed in the horizontal plane at zero AOA, were effective in extending the symmetric flow to higher AOA.

Modi et al. [55,56] investigated the effect of delta double strakes when added to a circular cylinder with conical-shaped forebodies. Their experiments were conducted for the AOA range from 0° to 50° with different values for the roll angle and strake length. They found out that the side force was minimum for the case with a rolling

angle of 90°—double strake action was similar to that of the fin or single strake placed in the lee-side.

Rao and Sharma [57] studied the effect of a deployable strake on one of the lower facets of a diamond cross section forebody in a low-speed wind tunnel. This method of control was found to be effective up to an AOA of 70°. This experiment was conducted at low Mach number with Reynolds number based on the length of 0.5×10^6 and an AOA range of 0° to 70°. A similar principle was applied by Murri et al. [58] on an F-18 High Alpha Research Vehicle (HARV). These experiments included wind tunnel as well as flight tests.

Kandil et al. [20] investigated numerically the effect of double symmetric strakes using the thin-layer and full Navier-Stokes equations. They considered both sharp and rounded strakes and both thin and thick strakes. The flow parameters were taken as a Mach number of 1.8, Reynolds number of 10^5 and AOA of 20°, and 30°. Without strakes, steady asymmetry showed up at AOA of 20° while with strakes, symmetric solutions were obtained for AOA up to 30°.

While the nose strakes and fins are found to be quite effective in alleviating the side force, they have some disadvantages which can be summarized as [59]

1. Their optimum size, shape and location appear to be critically dependent on the forebody geometry.

2. If the strakes are relatively large, they may contribute pitching instability.

3. Adverse interference of the strake vortices with downstream components, such as air intakes and tail controls, is possible.

4. Nose strakes may become a source of disturbance to radar operation.

2.3.2 Trips

Trips were employed in the 1960's as a means of vortex-wake suppression on cylinders with two-dimensional flows [60]. The cylinder boundary layers are forced to separate at varying peripheral locations along the cylinder length, and the vortex formation is disrupted. In 1971, Pick [9] found that the side forces decreased by up to 80% of the initial value when a boundary layer trip was installed on the windward side of the ogive cylinder body, over a Mach number range from 0.5 to 1.1 and an AOA range from 15° to 42°.

Applying the same principle, Rao [59] in 1979 investigated the effect of the helical trips in alleviating the side force compared to the straight trips that had been employed by Brown [61] in 1965. In this experiment with a Mach number of 0.3, Reynolds number based on the length of 6.2×10^6 and AOA range of 0° to 55°, he found out that the helical trips are highly effective in alleviating the side force. On the other hand, straight trips were not as effective.

The main advantage of trips over the strakes is that while the strakes generate their own vortices, the trips affect the existing boundary layer without introducing vortices into the flowfield. Moreover, with trips the body weight is not increased.

2.3.3 Nose Geometry

The bluntness ratio is the ratio between the nose radius and the maximum body radius—base radius. The effect of the nose bluntness was first investigated by Pick in 1971 [9] who found that the bluntness of ogive-cylinder bodies reduced the side force. On the other hand, Keener and Chapman [10] found that while small bluntness reduced the side force, large bluntness did not eliminate the side force. In the same paper, nose booms were found to be effective in reducing the side force.

Kruse et al. in an extensive report [62], investigated the effect of the nose geometry on flow asymmetry for AOA up to 58°, Mach number up to 2 and Reynolds number of 0.32×10^6. The fineness ratios of the tangent-ogive forebodies varied from 0.5 to 3.5 and bluntness ratios varied from 8 to 50 percent. They found out that bluntness produced mixed effects on the side forces, depending on the forebody fineness ratio, AOA and the degree of bluntness. For a forebody with fineness ratio of 3.5, bluntness reduced the side force while a forebody with fineness ratio of 2.5, behaves such that bluntness increased the side forces. The results obtained by Baysal et al. [63] for the flow over a blunt-nose-cylinder at high angles of attack were compared fairly to the experiments and the asymmetric flow was not captured due to the body bluntness.

Moskovitz et al. [64–66] discussed the effects of surface perturbations, bluntness and roughness on the flow around slender bodies at high AOA. The experiments were conducted on a cone cylinder configuration with a 10° semi-apex angle cone and a 3.0 caliber tangent ogive model, with Reynolds numbers of 24,000 and 84,000, AOA ranged from 30° to 60°, at very low Mach numbers. Their conclusions can be summarized as:

1. The flow asymmetry may be reversed due to local surface perturbations if they are large enough.

2. Nose bluntness reduced the side forces by decreasing the asymmetry of the flowfield.

3. The maximum level of asymmetry with respect to AOA was independent of tip bluntness.

4. Elliptical tips resulted in large side force even at moderate AOA.

Kandil, Wong and Liu [53] investigated the effect of the cross section shape of the forebody on flow asymmetry. It was found out that for the same flow conditions, circular and elliptic cross sections are more likely to produce strong asymmetric flow compared to a diamond shapes.

2.4 Active Control Methods

2.4.1 Blowing and suction

2.4.1.1 Experimental

Blowing and suction were applied as a method for vortex control for the first time in 1978 by Sharir et al. [67]. In this paper, they applied the injection at two stations, one close to the nose while the other was further downstream. Three pairs of ports at each location were used at $\pm 30°$, $\pm 60°$ and $\pm 120°$, measured from the leeward plane of geometric symmetry. The experiments were conducted in a subsonic wind tunnel with a flow speed of 20 m/sec for a Reynolds number of 1.08×10^5, based on the diameter and utilized three types of forebodies—a pointed cone, a blunt cone and a blunt ogive.

In their conclusions, they pointed out some important observations for vortex control using injection which can be summarized as follows:

1. It is possible to reduce the side forces or even change their direction by using symmetric blowing.

2. Injection is ineffective for AOA higher that 52°.

3. The mass flow rate required for jets needed to affect the side force was very small.

4. The effect of increasing the mass flow rate above the minimum required to affect the side force was insignificant.

5. Blowing had no effect on the angle of onset of asymmetry.

Peake, in two papers [68,69], discussed the effect of normal injection on the flow asymmetry and side force over a 5° semi-angle cone and 16° semi-angle tangent ogive. They correlated the onset of asymmetric flow with the ratio α/θ_c, where θ_c was the semi-angle of the body at the nose. They found that:

1. blowing on one side of the leeward meridian, from a single jet placed between the primary and secondary vortices, reduced or reversed the side force,

2. normal blowing was more effective than upstream or downstream tangential blowing,

3. asymmetric blowing was more effective than symmetric blowing and

4. the mass flow rate required for effective control was relatively small considering its amplified effect on the flowfield.

Almosnino and Rom [70,71] extended the Sharir et al. [67] study. Their experiments were conducted in both subsonic and transonic wind tunnels covering the Mach number ranged from 0.1 to 1.1, AOA from $-10°$ to 90° and the Reynolds number range from 0.6×10^5 to 0.5×10^6. The experiments were performed on a cone-cylinder configuration. Their conclusions were in agreement with those of Sharir et al. [67]. In addition, they concluded that with increased Mach number, the mass flow rate required to control the flowfield increased.

In the above mentioned five papers, injection was applied normal to the body surface. Wood and Roberts [72,73] applied tangential blowing on the leading edge

of a 60° delta wing. The experiment was conducted at low Mach number (about 0.2) and AOA up to 60°. The tangential leading-edge mass injection was capable of extending the regime of stable, controlled vortical flow over the upper surface of the delta wing by approximately 30° AOA.

Starting from 1989, many papers have been published discussing the different aspects of controlling the forebody vortical flow using injection. Most of these papers have been experimental and concentrated on the subsonic flow regime. Williams, El-Khabiry and Papazian [74] conducted an experiment, in a low speed wind tunnel on a 20° angle-cone and a cylindrical afterbody. The experiment was performed at a Reynolds number of 2100 and a very low Mach number of 0.01. The results indicated that the unsteady base bleed was effective in controlling the asymmetric system of vortices.

Ng and Malcolm [75] investigated the effect of blowing type. They applied blowing from localized jets and from a slot. In addition, they investigated surface suction. The blowing they used was forward and aft. The experiment was performed with a Mach number of 0.025 and AOA of 45°, 50° and 60°. All the methods applied were found to be effective. In their experiments, the main purpose was to show the effectiveness of the various methods as means of control to produce yaw moment and therefore not eliminate or alleviate the side force.

Tangential [76] and oplique blowing [77] was investigated on a 1/8 scale X-29 forebody model. The optimum angle for blowing was found to be 60°. In the two papers the effect of the blowing was to increase the level of asymmetry and to produce a yawing moment. The ability of tangential blowing to create side forces, yawing and rolling moments in a controllable manner was investigated on a model which is a combination of a delta wing and a forebody with a cylindrical pointed ogive-nose which blends smoothly with the delta wing. Tangential blowing was found to be more effective when applied on the forebody rather than when applied on the delta wing [78].

Lanser and Meyn [79] conducted an experiment for the flow over full-scale F/A-18 aircraft at a Mach number of 0.15, and Reynolds numbers of 4.5×10^6 to 12×10^6, in the AOA range of 25° to 50° and $\beta = 0°$ to $\pm 15°$, where β is the side slip angle in degrees. They used two methods for the aft injection—a circular jet and a tangential slot. The significance of injection was influenced by the jet or slot location and size. The slot lengths of 16 and 32 inches were found to be more effective than those of 8 and 48 inches and blowing slightly downstream was more effective than blowing too close to the nose. In most cases, the injection produced the desired yawing moments. In another paper [80], Lanser and James verified the experimental results using computational fluid dynamics (CFD).

Cornelius and Lucius [81] investigated the ability of injection to produce side forces over an elliptic forebody with and without strake. The strakes effect was found to damp the instability that grows due to injection. The experiment was conducted at low Mach number. The effect of injection on a 1/8-scale X-29 forebody model was investigated by Cornelius et al. [82] at a Mach number of 0.3, Reynolds number based on the length of 1.25×10^6 and the AOA ranged from 31° to 50°. Their main interest was to produce controllable side forces rather than eliminating the side forces that arise at high AOA.

Several recent papers [83–86] have investigated experimentally the effects of slot size, location and injection rate. Crowther [83] found out that increasing the slot angle, increases the yawing moment and side force. Kramer et al. [87], who investigated the blowing over an F/A-18 using jet and slot techniques, concluded that both techniques were effective in producing large yaw control power at high AOA. He also pointed out the importance of jet and slot location. An experimental investigation of forebody vortex control of the flow over an F/A-18 and an F-16 was conducted by Kramer and Smith [87]. They applied both jet and slot blowing close to the aircraft nose. The two methods were found to be effective for AOA over 30°. Ross [88] studied the effect of nose jets on the flow over 3.5 tangent-ogive with AOA ranged

from 0° to 60°. Ross found out that normal injection was less effective compared to forward blowing.

2.4.1.2 Computational

Tavella, Schiff and Cummings [89] investigated computationally the control of forebody vortices over F-18 aircraft. They solved the problem using thin-layer Navier-Stokes equations on a multi-block grid. Tangential injection was applied through a thin slot located on each side of the fuselage forebody. Blowing was applied either symmetrically or antisymmetrically. The flow conditions were, Reynolds number of 11.52×10^6, Mach number of 0.2 and AOA of 30°. With no blowing, the solution obtained was a symmetric solution while with blowing the solution became asymmetric only in the case of antisymmetric blowing. They concluded that the effect of symmetric blowing was negligible. This contradicts the conclusions of Sharir et al. [67] in which symmetric and antisymmetric blowing had a significant effect on the flowfield structure. The main difference between the two cases is that in Ref. 67, the initial solution was asymmetric while in Ref. 89 the initial solution was symmetric. This problem was expanded in 1992 [90] to study the effect of varying the jet width and jet exit velocity for a fixed slot location. They found that the effective control factor was the mass flow rate rather than the jet width.

The solution of the above problem for an X-29 aircraft was done by Rosen and Davis [91] at AOA of 40°, Mach number of 0.3 and Reynolds number per unit length of 1.6×10^6. The initial solution, with no blowing, was asymmetric. Asymmetric forward and aft blowing increased the level of asymmetry while symmetric aft blowing reduced the vortical flow asymmetry.

Expanding Tavella and Schiff results [89], Font and Tavella solved the problem over a tangent ogive cylinder at AOA of 10°, 30° and 45°, at a Reynolds number of 52,000 and a Mach number of 0.2, using thin-layer Navier-Stokes equations keeping

only the viscous terms in the direction normal to the body surface. They used a 7-zone grid with 324,000 points, with tangential blowing applied from a slot near the nose of the body. They found that large side forces may be produced due to the injection and the side forces do not always increase with increases in the jet momentum coefficient.

Using a similar approach, Celik and Roberts [92] investigated the same problem over a cylindrical body with a pointed ogive nose with and without wings, covering the AOA range from 20° to 55° at the very low Mach number of 0.025. Their main interest again was to explore the concept of tangential blowing to create lateral control on a missile-like body with a tangent ogive head at high AOA. They found that tangential blowing resulted in large side forces and yawing moments. Also, they studied the effect of the blowing slot location.

The effect of tangential injection through a slot on the tangent-ogive cylinder configuration at a Mach number of 0.2, a Reynolds number of 52,000 and an AOA of 30° was investigated by Font [93]. It was found that such blowing was capable of producing significant side forces. In his conclusions, he described the mechanisms that produced side force to be

1. a centrifugal force component created at the wall due to the curvature of the surface,

2. vorticity added to the flowfield nearby the slot region, and

3. a change in the nose vortices position due to a change in the separation location as a result of the injection.

Kandil et al. [21,94] investigated the effect of both normal and tangential injection, on the flow over a cone at a Mach number of 1.8, and a Reynolds number of 10^5, over the AOA range of 20° to 30°. Both uniform injection and pressure-dependent

injection were applied and found to be effective. The effect of the mass-flow rate and effective injection angle were investigated. The pressure-dependent injection was found to be independent of the initial shape of the vortex asymmetry and capable of eliminating the side force at certain AOA. Details of this research are presented in Chap. 6. The three-dimensional problem with Reynolds number of 6×10^6, Mach number of 1.4 and AOA of 40° for a flow over 5° semi-apex angle cone was solved using the thin-layer Navier-Stokes equations [95, 96]. Both normal and injection control were found to be effective and the influence of the injection effective length and mass flow rate were investigated.

Gee et al. [97–99] studied the concept of forebody flow control using tangential slot blowing on an F-18 aircraft. The Reynolds-averaged, thin-layer Navier-Stokes equations were solved numerically using the F3D code which uses an implicit, finite difference algorithm with flux splitting and the Baldwin-Lomax turbulence model. The physical conditions at which the problem was solved were a Mach number of 0.243, AOA of 30.3°, $\beta = -4.5°$ and Reynolds number of 11×10^6. The initial solution was asymmetric due to side slip with no blowing. The effect of the blowing and side slip were discussed as a means to generate side forces and yawing moments.

2.4.2 Spinning and rotary oscillations

Many ballistic missiles are given some spin for stabilization purposes. Also, some satellites spin continuously due to mission requirements. Such applications have created an early interest in the study of spinning bodies. Swanson [100] presented an overview of the research up to 1961. Since then, several papers [101–103] studied, analytically, experimentally and numerically, the Magnus force for the flow over spinning cones. The asymmetric viscous displacement, as a result of spinning, was found to be a major contribution to Magnus force [104]. Four significant sources were identified [105] as being due to the spin-boundary-layer interaction. They are

displacement thickness, centrifugal pressure differences, cross-flow wall-shear stresses and primary-flow wall-shear flow stresses. In the last decade, there has been an interest in the experimental [106–108] and numerical [109, 110] study of the spinning bodies without focusing on their effect upon the side force.

Kruse [111] was the first to consider experimentally the influence of spin rate on side force for the flow over a 10° semi-apex angle cone with a Reynolds number based on the diameter of 10^6 and a Mach number of 0.6. The shape of the side force curve was not a strong function of spin rate, but the peak to peak value of the side force decreased significantly with increases in the spin rate. Fidler [112] investigated the effect of rotating the nose, the nose tip, and a surface band just aft of the nose. The vortex structures and associated side forces and moments were cyclically altered in a repeatable fashion. As the spin increased, the peak-to-peak variations in the side force decreased. Small rotatable tip-strakes were employed on an F/A-18 aircraft model to investigate the capability of this technique in producing controllable yawing moments and side forces [113]. The rotatable strakes were effective in controlling the separation points and hence the yawing moments.

Kandil et al. [114] studied numerically the effect of spinning and rotary oscillations as a method to alleviate the asymmetry of the flowfield over a cone at a Mach number of 1.8, Reynolds number of 10^5 and AOA of 20°. They found out that rotary oscillations were more effective than uniform spinning and rotary oscillation does not require any particular initial shape for the vortex asymmetry. The details of this research are presented in Chap. 7.

The reader can refer to several review papers covering different aspects of the passive and active control methods for side force alleviation and vortex asymmetry control [2, 115–121].

CHAPTER 3

MATHEMATICAL FORMULATION

3.1 Introduction

With the introduction of computers four decades ago, a new scientific era began which depends heavily on numerical techniques and their computer implementations. Aerodynamics and fluid dynamics were no exception. Computational aerodynamics and computational fluid dynamics (CFD) started to develop at that time.

Historical progress in CFD was related to the advancement of computers, in terms of memory and speed. With the continuous increases in both, computational fluid dynamics passed through different stages, each representing a successively refined approximation to the full Navier-Stokes equations. Those stages can be summarized as [122], linearized inviscid equations, nonlinear inviscid equations, parabolized Navier-Stokes equations, thin-layer Navier-Stokes equations, Reynolds averaged Navier-Stokes equations and full Navier-Stokes equations.

Only recently, has investigating problems such as asymmetric flow control become feasible. That is due to the advancement in the computational resources. Highly vortical flows cannot be solved accurately without the use of Navier-Stokes equations. While Euler equations tend to give the same solutions as Navier-Stokes equations in the region of the primary vortices, the location of secondary and tertiary vortices

and the boundary-layer flow can only be predicted correctly using Navier-Stokes equations.

In this chapter, the three-dimensional full Navier-Stokes equations are presented in a fixed frame of reference followed by presentation of the different approximations that are used for the different applications. It should be noted here that applying the different control methods is a disturbance which may result in turbulent flow. Meanwhile, no turbulence models were considered in the present study because of the lack in the models that can simulate the highly vortical turbulent flow accurately.

3.2 Three-Dimensional Navier-Stokes Equations

Using tensor or indicial notation, the conservative form of non-dimensional unsteady compressible Navier-Stokes equations in Cartesian coordinates (x_1, x_2, x_3) is given by

$$\frac{\partial \bar{q}}{\partial t} + \frac{\partial\left(\bar{E}_j - \bar{E}_{vj}\right)}{\partial x_j} = 0 \quad , j = 1,2,3 \tag{3.1}$$

where the flowfield vector $\bar{q}$ is given by

$$\bar{q} = [\rho, \rho u_1, \rho u_2, \rho u_3, \rho e]^t \tag{3.2}$$

and the inviscid flux vectors can be expressed as

$$\bar{E}_j = \left[\rho u_j, \rho u_1 u_j + \delta_{j1} p, \rho u_2 u_j + \delta_{j2} p, \rho u_3 u_j + \delta_{j3} p, \rho u_j \left(e + \frac{p}{\rho}\right)\right]^t \quad , j = 1,2,3 \tag{3.3}$$

where δ_{ij} is the Kronecker delta function, and the viscous fluxes can be written in the form

$$\left(\bar{E}_v\right)_j = [0, \tau_{j1}, \tau_{j2}, \tau_{j3}, u_m \tau_{jm} - q_j]^t \quad , j = 1,2,3, \;\; m = 1,2,3 \tag{3.4}$$

The flow variables in the above equations are in their non-dimensional forms where freestream parameters are used as reference values. The reference parameters used

are L, a_∞, L/a_∞, ρ_∞ and μ_∞ for the length, velocity, time, density and molecular viscosity, respectively. The pressure is non-dimensionalized by $\rho_\infty a_\infty^2$, and is related to the total energy for an ideal gas by the equation

$$p = (\gamma - 1)\rho\left[e - \frac{1}{2}\left(u_1^2 + u_2^2 + u_3^2\right)\right] \tag{3.5}$$

where γ is the ratio of specific heats and is assumed to be constant (1.4). The Cartesian coordinates are non-dimensionalized using characteristic length, L, while time is non-dimensionalized using L/a_∞.

In Eq. 3.4, the τ's represent the Cartesian components of shear stress tensor for a Newtonian fluid satisfying Stokes hypothesis. Also, in Eq. 3.4, the term $u_m\tau_{jm}$ represents the shear dissipation power components and q_j represents the heat flux components. The Cartesian components of shear stress tensor are given by

$$\tau_{ij} = \frac{\mu M_\infty}{R_e}\left(\frac{\partial u_i}{\partial x_j} + \frac{\partial u_j}{\partial x_i} - \frac{2}{3}\delta_{ij}\frac{\partial u_k}{\partial x_k}\right) \quad ,i,j,k = 1,2,3 \tag{3.6}$$

and the shear dissipation power and the heat flux components are given by

$$u_m\tau_{jm} = \frac{\mu M_\infty}{R_e}u_m\left(\frac{\partial u_j}{\partial x_m} + \frac{\partial u_m}{\partial x_j} - \frac{2}{3}\delta_{jm}\frac{\partial u_k}{\partial x_k}\right) \quad ,j,k,m = 1,2,3 \tag{3.7}$$

$$q_j = \frac{-\mu M_\infty}{(\gamma - 1)P_r R_e}\frac{\partial T}{\partial x_j} \quad ,j = 1,2,3 \tag{3.8}$$

Sutherland's law is used to calculate the viscosity—μ

$$\mu = T^{\frac{3}{2}}\left(\frac{1+c}{T+c}\right) \tag{3.9}$$

where T is the non-dimensional temperature and c is the Sutherland's constant, $c \approx 0.4317$. The Prandtl number, P_r is chosen to be 0.72 throughout the present work.

The freestream Reynolds number, R_e, is defined using the equation

$$R_e = \frac{\rho_\infty U_\infty L}{\mu_\infty} \tag{3.10}$$

and the characteristic length, L, is chosen as the length or diameter of the body for the particular three-dimensional applications. The values of all the freestream flow quantities, which are used as the initial conditions for all applications, are given as follows

$$\begin{aligned} u_{1\infty} &= M_\infty \cos\alpha \cos\beta \\ u_{2\infty} &= M_\infty \sin\beta \\ u_{3\infty} &= M_\infty \sin\alpha \cos\beta \\ e_\infty &= \frac{1}{\gamma(\gamma-1)} + \frac{M_\infty^2}{2} \\ p_\infty &= \frac{1}{\gamma} \\ U_\infty &= \sqrt{u_{1\infty}^2 + u_{2\infty}^2 + u_{3\infty}^2} \\ M_\infty &= \frac{U_\infty}{a_\infty} \end{aligned} \tag{3.11}$$

To complete the mathematical model for any flow problem using the Navier-Stokes equations, initial and boundary conditions for the corresponding application should be provided. The complete discussion of initial and boundary conditions will be presented in Chap. 4.

3.3 Conical Flow Assumptions

3.3.1 Global conical flow assumption

The assumptions necessary for such global conical equations to be valid can be summarized as following [123]

- The fluid is a homogeneous, nonconducting ideal gas. This assumption is necessary for the Navier-Stokes equations as well.

- The Reynolds number is infinite.
- The Peclet number, $\rho U_\infty C_p L/k$, is infinite.
- The flowfield is conically self-similar.

Strict applications of these assumptions will limit their applicability to supersonic, inviscid flow over a conically self-similar geometry. In practical situations the Reynolds number and Peclet number will not be infinite.

Following the same notation as in Sec. 3.2, the conservative form of the Euler equations can be written as

$$\frac{\partial \bar{q}}{\partial t} + \frac{\partial \bar{E}_j}{\partial x_j} = 0 \quad ,j = 1,2,3 \tag{3.12}$$

where $\bar{q}$ and $\bar{E}_j$ are defined in Eqs 3.2 and 3.3, respectively.

A flow is considered to be conically self-similar if no length scale exists in the radial direction. Transforming Eq. 3.12 to a conical coordinate system using the relations

$$\begin{aligned} \eta_1 &= \sqrt{x_1^2 + x_2^2 + x_3^2} \\ \eta_2 &= \frac{x_2}{x_1} \\ \eta_3 &= \frac{x_3}{x_1} \end{aligned} \tag{3.13}$$

and using the conical assumption

$$\frac{\partial q}{\partial \eta_1} = 0 \tag{3.14}$$

we can write Eq. 3.12 as

$$\frac{r}{\kappa}\frac{\partial \bar{q}}{\partial t} + \frac{\partial \acute{G}_j}{\partial \acute{\eta}_j} + 2\acute{F} \quad ,j = 2,3 \tag{3.15}$$

where

$$\kappa = \sqrt{1 + \eta_2^2 + \eta_3^2} \tag{3.16}$$

$$\acute{G}_j = \left[\rho\acute{u}_j, \rho u_1\acute{u}_j - \eta_j p, \rho u_2\acute{u}_j + \delta_{2j}p, \rho u_3\acute{u}_j + \delta_{3j}p, \rho\left(e+\frac{p}{\rho}\right)\acute{u}_j\right]^t \quad , j = 2,3 \tag{3.17}$$

$$\acute{F} = \left[\rho u_1, \rho u_1^2 + p, \rho u_1 u_2, \rho u_1 u_3, \rho u\left(e+\frac{p}{\rho}\right)\right]^t \tag{3.18}$$

$$\begin{aligned} \acute{u}_1 &= u_1 + \eta_2 u_2 + \eta_3 u_3 \\ \acute{u}_j &= u_j - \eta_j u_1 \quad , j = 2,3 \end{aligned} \tag{3.19}$$

where $\acute{u}_j$ is the velocity component in the conical coordinate η_j.

Examining the above equations, we can see that while we have velocity components in the three directions, the derivative with respect to η_1 is absent from the equations. This result is quite similar to that for the axisymmetric approximation.

3.3.2 Locally conical flow assumption

As mentioned in the previous section, physical flow problems have finite values for both Reynolds number and Peclet number. Many experimental flows at supersonic speeds demonstrate approximate self-similarity. The existence of a length scale in the conical Navier-Stokes equations prevents the self similarity. Meanwhile, the equations can be thought of as locally conical, where the local Reynolds number is calculated at the location corresponding to the conical solution. Several computations using locally conical flow assumptions show only small differences with experimental work [29,124]. In this subsection, the locally conical Navier-Stokes equations are presented, with a brief discussion of their limitations.

For supersonic flows, the three-dimensional equations in Cartesian coordinates, that were presented in Sec. 3.2, are transformed into the conical flow equations using

$$\begin{aligned} \eta_1 &= x_1 \\ \eta_2 &= \frac{x_2}{x_1} \end{aligned}$$

$$\eta_3 = \frac{x_3}{x_1} \tag{3.20}$$

Then, the conical form of Navier -Stokes equation is written as

$$\eta_1 \frac{\partial \bar{q}}{\partial t} + \frac{\partial \left(\tilde{F}_j - \tilde{F}_{vj}\right)}{\partial \eta_j} + 2\left(E_1 - E_{v1}\right) = 0 \quad , j = 2,3 \tag{3.21}$$

where the inviscid fluxes are

$$\begin{aligned}
\tilde{F}_j &= E_j - \eta_j E_1 \\
&= \left[\rho u_j, \rho u_1 u_j, \rho u_2 u_j + \delta_{2j}, \rho u_3 u_j + \delta_{3j}, \rho u_j \left(e + \frac{p}{\rho}\right)\right]^t \\
&\quad -\eta_j \left[\rho u_1, \rho u_1^2 + p, \rho u_1 u_2, \rho u_1 u_3, \rho u_1 \left(e + \frac{p}{\rho}\right)\right]^t \quad , j = 2,3
\end{aligned} \tag{3.22}$$

and the viscous fluxes are

$$\begin{aligned}
\tilde{F}_{vj} &= E_{vj} - \eta_j E_{v1} \\
&= \left[0, \tau_{j1}, \tau_{j2}, \tau_{j3}, u_m \tau_{jm} - q_j\right]^t \\
&\quad -\eta_j \left[0, \tau_{11}, \tau 12, \tau_{13}, u_m \tau_{1m} - q_1\right]^t
\end{aligned} \tag{3.23}$$

The equations of the shear stress and the thermal dissipation terms are obtained by enforcing the conical flow condition, i.e. $\partial/\partial\eta_1$ is zero.

Similar to Eq. 3.15, Eq. 3.21 is a two-dimensional equation with source terms. The computational resources required to solve Eq. 3.21 are one order of magnitude less than the resources required for three-dimensional Navier-Stokes equations solution.

CHAPTER 4

COMPUTATIONAL METHODS

4.1 *Introduction*

Navier-Stokes equations are of mixed type depending on flow features. If the flow is supersonic, the equations are of hyperbolic type, while if the flow is subsonic, the equations are parabolic or elliptic. According to the theory of characteristics, physical disturbances propagate along the characteristics. This is a typical feature of hyperbolic equations where perturbations propagate in certain directions.

Central difference schemes do not distinguish between upstream and downstream influences. In addition to that, central difference schemes generate oscillations in the vicinity of discontinuities such as shocks. Artificial dissipation must be used to damp these oscillations. On the other hand, upwind schemes, which have been used since 1952 [125], are sensitive to the direction of propagation of disturbances and they prevent the creation of unwanted oscillations at shock locations. The above statements are true only for those upwind schemes that take into account the physical nature of the equations.

In most schemes, the inviscid fluxes are treated independently in each direction and summed for multidimensional applications. It has also been proved [126] that the upwind schemes are equivalent to central difference schemes with artificial viscosities that are direction dependent.

In this chapter, the transformations of the governing equations from the physical domain into the computational domain are presented for the different approximation levels, starting with the full Navier-Stokes equations. A discussion of the implicit upwind schemes is presented with emphasis on the flux-difference splitting scheme of Roe. Finally, the initial and boundary conditions for conical and three-dimensional Navier-Stokes equations are presented for both static and dynamic grids.

4.2 Governing Equations in Computational Domain

4.2.1 Three-Dimensional Navier-Stokes equations

The three dimensional Navier-Stokes equations are transformed from the physical Cartesian domain (x, y, z) into computational domain (ξ^1, ξ^2, ξ^3) using the relations

$$\begin{aligned} \xi^m &= \xi^m(x, y, z, t) \quad , m = 1, 2, 3 \\ \tau &= t \end{aligned} \tag{4.1}$$

It should be noted that the computational domain is time dependent which permits the implementation of dynamic grids and allows us to simulate different unsteady motions such as plunging and pitching. The details of the derivation of metrics can be found in several references including [127].

Using the chain rule, one can write

$$\xi^m_{x_n} = J \ \ cofactorial \left[J^{-1}_{nm} \right] \tag{4.2}$$

$$\xi^m_t = -\left(x_i\right)_\tau \xi^m_{x_i} \tag{4.3}$$

where

$$J = \frac{\partial(\xi^1, \xi^2, \xi^3)}{\partial(x_1, x_2, x_3)} \tag{4.4}$$

Then, the three-dimensional Navier-Stokes equations in the Cartesian coordinate system given by, Eq. 3.1 are transformed to the form

$$\frac{\partial \hat{q}}{\partial t} + \frac{\partial \left(\hat{E}_m - \hat{E}_{vm}\right)}{\partial \xi^m} = 0 \quad , m = 1,2,3 \tag{4.5}$$

where the flowfield vector $\hat{q}$ is given by

$$\hat{q} = J^{-1}\bar{q} = J^{-1}\left[\rho, \rho u_1, \rho u_2, \rho u_3, \rho e\right]^t \tag{4.6}$$

and the inviscid flux vectors can be expressed as

$$\begin{aligned}\hat{E}_m &= J^{-1}\left(\bar{q}\xi_t^m + \xi_{x_n}^m \bar{E}_n\right) \\ &= J^{-1}\left[\rho U_m, \rho u_1 U_m + \xi_{x_1}^m p, \rho u_2 U_m + \xi_{x_2}^m p, \rho u_3 U_m + \xi_{x_3}^m p, U_m\left(\rho e + p\right) - \xi_t^m p\right]^t\end{aligned} \tag{4.7}$$

and the viscous fluxes can be written in the form

$$\begin{aligned}\hat{E}_{vm} &= J^{-1}\left(\xi_{x_n}^m \bar{E}_{vn}\right) \\ &= J^{-1}\left[0, \xi_{x_j}^m \tau_{j1}, \xi_{x_j}^m \tau_{j2}, \xi_{x_j}^m \tau_{j3}, \xi_{x_j}^m\left(u_n \tau_{jn} - q_j\right)\right]^t \quad , j = 1,2,3\end{aligned} \tag{4.8}$$

The contravariant velocity in the curvilinear coordinate system is given by

$$U_m = \xi_{x_j}^m u_j + \xi_t^m \quad , j = 1,2,3 \tag{4.9}$$

and the shear stress tensor and heat transfer vector are transformed to

$$\tau_{jl} = \frac{\mu M_\infty}{R_e}\left(\frac{\partial \xi_m}{\partial x_l}\frac{\partial u_j}{\partial \xi^m} + \frac{\partial \xi_m}{\partial x_j}\frac{\partial u_l}{\partial \xi^m} - \frac{2}{3}\delta_{jl}\frac{\partial \xi_m}{\partial x_k}\frac{\partial u_k}{\partial \xi^m}\right) \tag{4.10}$$

$$q_j = \frac{\mu M_\infty}{(\gamma - 1)P_r R_e}\frac{\partial \xi_m}{\partial x_j}\frac{\partial T}{\partial \xi^m} \tag{4.11}$$

4.2.2 Thin-Layer Navier-Stokes Equations

Solving the full Navier-Stokes equations for three-dimensional configurations at high Reynolds number requires substantial computational resources in terms of memory

and speed. A possible simplification to the full Navier-Stokes equations is the thin-layer Navier-Stokes equations. In the generalized curvilinear coordinate system, the body coordinate is given as a surface of constant generalized coordinate lines. The thin-layer approximation retains only the derivative in the direction normal to the wall for the viscous terms. In such a case, the cross-derivatives are dropped and the computational resources required for the viscous part of the equations are reduced to one third. In fact, the reduction is more than this, since no fine grid resolution is required in the other two directions.

The thin-layer Navier-Stokes equations can be considered as an intermediate step between full Navier-Stokes equations and the boundary layer equations. In these equations, the approximations are justified by order of magnitude analysis similar to the boundary layer. On the other hand, the pressure in thin-layer equations can vary in the normal direction unlike the boundary layer approximation. The thin-layer equations in their most general form include all three viscous flux terms but drops all cross-derivative terms.

The thin-layer equations can be written as

$$\frac{\partial \hat{q}}{\partial t} + \frac{\partial \hat{E}_m}{\partial x_m} - \frac{\partial \left(\hat{E}_{vt}\right)_n}{\partial \xi^n} = 0 \quad , m = 1,2,3 \tag{4.12}$$

where n is a summation index. If we consider the case of only one viscous direction then n takes the value of this direction. If the viscous terms are to be considered in more than one direction, then n takes the values of all the directions to be considered. As expected the inviscid fluxes remain unchanged as given by Eq. 4.7. The viscous fluxes are expressed as

$$\left(\hat{E}_{vt}\right)_n = J^{-}1 \quad \left[0,\ \xi^n_{x_j}\tau_{j1},\ \xi^n_{x_j}\tau_{j2},\ \xi^n_{x_j}\tau_{j3},\ \xi^n_{x_j}\left(u_n\tau_{jn} - q_j\right)\right]^t \quad , j = 1,2,3 \tag{4.13}$$

The thin-layer equations have fewer terms than the full Navier-Stokes equations, which means a reduction in required memory and time. Comparisons between the full

Navier-Stokes equations and the thin-layer equations have indicated little difference in results at high Reynolds number [128]. All of the three-dimensional applications in the present work use the thin-layer Navier-Stokes equations considering the viscous terms in the three directions and neglecting the cross-derivatives.

4.2.3 Locally-Conical Navier-Stokes Equations

Similar to full and thin-layer Navier-Stokes equations, the conical flow equations can be transformed into the computational domain. Unsteady conical Navier-Stokes equations are not self-similar but the equations can be solved at a fixed location and the solution is said to be a locally-conical solution. Instead of using the conical Navier-Stokes equations, the three-dimensional Navier-Stokes equations are used to produce locally-conical flow solutions. This can be achieved by setting the conserved components of the flowfield, $\hat{q}$, equal at two planes in close proximity to each other, where one of the two planes is located at the required axial station. All of the locally-conical solutions in the present work were obtained following this method.

4.3 Implicit Upwind Schemes

The unsteady Navier-Stokes equations are of mixed type. They are hyperbolic-parabolic in time, and hyperbolic-elliptic in space. To take advantage of this fact, time-accurate marching is used for unsteady or time-dependent applications and pseudo-time is used for steady-state cases. Upwind schemes can be classified as explicit and implicit schemes. The explicit schemes are easier to implement, require less memory and computational time than are required by the implicit schemes. On the other hand, implicit methods are frequently unconditionally stable. Choosing large time steps can more than compensate for the extra work per time step. Even though there are no stability restrictions on the time step, the time step is usually

chosen to be a small value in order to satisfy the accuracy requirements since the error grows with increases in the size of the time step. It should be mentioned here that although the explicit schemes are more suitable for parallel computers, there has been continuous progress in parallel computer implementation of implicit schemes as well. Throughout this research work, the implicit upwind scheme has been used.

4.3.1 Finite-Volume Formulation

The governing equations in curvilinear coordinates are integrated over the computational domain (ξ^1, ξ^2, ξ^3)

$$\iiint_V \frac{\partial \hat{q}}{\partial t}\, dV + \iiint_V \frac{\partial \left(\hat{E}_m - \hat{E}_{vm}\right)}{\partial \xi^m}\, dV = 0 \tag{4.14}$$

where

$$dV = d\xi^1\, d\xi^2\, d\xi^3 \tag{4.15}$$

Using the divergence theorem, Eq. 4.14 can be written in the form

$$\iiint \frac{\partial \hat{q}}{\partial t} dV + \iint_S \left(\hat{E}_m - \hat{E}_{vm}\right) \cdot \hat{n}\, dS = 0 \tag{4.16}$$

where $\hat{n}$ is the outward unit vector normal to the surface S, bounding volume V. Equation 4.16 is the integral form of the Navier-Stokes equations. The integral form is valid everywhere in the computational domain, while the differential form of the equations is valid only in smooth regions.

Equation 4.16 is applied at each cell assuming the flow quantities are cell averaged values. The hexahedral cells in the physical domain are mapped into unit cubes in the computational domain. The integral form, given by Eq. 4.16, is determined as

$$\begin{aligned}\left(\frac{1}{J}\frac{\partial \hat{q}}{\partial t}\right)_{i,j,k} = &- \left(\hat{E}_1 - \hat{E}_{v1}\right)_{i+\frac{1}{2},j,k} + \left(\hat{E}_1 - \hat{E}_{v1}\right)_{i-\frac{1}{2},j,k} \\ &- \left(\hat{E}_2 - \hat{E}_{v2}\right)_{i,j+\frac{1}{2},k} + \left(\hat{E}_2 - \hat{E}_{v2}\right)_{i,j-\frac{1}{2},k} \\ &- \left(\hat{E}_3 - \hat{E}_{v3}\right)_{i,j,k+\frac{1}{2}} + \left(\hat{E}_3 - \hat{E}_{v3}\right)_{i,j,k-\frac{1}{2}} = R\left(\hat{q}_{i,j,k}\right)\end{aligned} \tag{4.17}$$

Where i, j, k denote the value at the cell centroid, while $i+\frac{1}{2}$, $i-\frac{1}{2}$, $j+\frac{1}{2}$, $j-\frac{1}{2}$, $k+\frac{1}{2}$ and $k-\frac{1}{2}$ denote the values at the cell interface. The term $\frac{1}{J}$ represents the cell volume.

Using Euler implicit time integration [129], Eq. 4.17 can be written as

$$\frac{\hat{q}^{n+1}-\hat{q}^{n}}{J\Delta t}=R\left(\hat{q}^{n+1}\right) \tag{4.18}$$

where

$$R\left(\hat{q}^{n+1}\right)=-\left[\delta_{\xi^1}\left(\hat{E}_1^{n+1}-\hat{E}_{v1}^{n+1}\right)+\delta_{\xi^2}\left(\hat{E}_2^{n+1}-\hat{E}_{v2}^{n+1}\right)+\delta_{\xi^3}\left(\hat{E}_3^{n+1}-\hat{E}_{v3}^{n+1}\right)\right] \tag{4.19}$$

A Taylor series expansion was used to linearize the inviscid and viscous fluxes at time level $n+1$ in Eq. 4.18

$$\frac{1}{J\Delta t}\Delta\hat{q}+\left[\delta_{\xi^m}\left(\frac{\partial\left(\hat{E}_m-\hat{E}_{mv}\right)}{\partial\hat{q}}\right)^{n}\right]\Delta\hat{q}+\delta_{\xi^m}\left(\hat{E}_m-\hat{E}_{mv}\right)^{n}=0 \tag{4.20}$$

$$\left[\frac{1}{J\Delta t}+\left(\delta_{\xi^m}\left(\frac{\partial\left(\hat{E}_m-\hat{E}_{mv}\right)}{\partial\hat{q}}\right)^{n}\right)\right]\Delta\hat{q}=-\delta_{\xi^m}\left(\hat{E}_m-\hat{E}_{mv}\right)^{n}\quad,m=1,2,3 \tag{4.21}$$

where I is the identity matrix and δ_{ξ^m} is the spatial difference operator in the ξ^m direction.

To avoid the penalty of solving Eq. 4.21 directly, which requires the solution of a 5×5 banded block matrix equation, the approximate factorization method was used. Then, the left hand side of Eq. 4.21 is written in the form

$$\left[I+J\Delta t\delta_{\xi^1}\left(\frac{\partial\hat{E}_1}{\partial\hat{q}}-\frac{\partial\hat{E}_{v1}}{\partial\hat{q}}\right)\right]\left[I+J\Delta t\delta_{\xi^2}\left(\frac{\partial\hat{E}_2}{\partial\hat{q}}-\frac{\partial\hat{E}_{v2}}{\partial\hat{q}}\right)\right]\left[I+J\Delta t\delta_{\xi^3}\left(\frac{\partial\hat{E}_3}{\partial\hat{q}}-\frac{\partial\hat{E}_{v3}}{\partial\hat{q}}\right)\right]\Delta\hat{q}=-J\Delta t\left(R^n-R_v^n\right) \tag{4.22}$$

and the solution is obtained by solving three one-dimensional problems

$$\left[I+J\Delta t\delta_{\xi^1}\left(\frac{\partial\hat{E}_1}{\partial\hat{q}}-\frac{\partial\hat{E}_{v1}}{\partial\hat{q}}\right)\right]\Delta\hat{q}'=-J\Delta t\left(R^n-R_v^n\right)$$

$$\left[I + J\Delta t \delta_{\xi^2}\left(\frac{\partial \hat{E}_2}{\partial \hat{q}} - \frac{\partial \hat{E}_{v2}}{\partial \hat{q}}\right)\right]\Delta\hat{q}'' = \Delta\hat{q}'$$
$$\left[I + J\Delta t \delta_{\xi^3}\left(\frac{\partial \hat{E}_3}{\partial \hat{q}} - \frac{\partial \hat{E}_{v3}}{\partial \hat{q}}\right)\right]\Delta\hat{q}^n = \Delta\hat{q}'' \qquad (4.23)$$

Solution of a block tri- or penta-diagonal set of equations depending on the spatial accuracy of the left hand side operator is required to solve Eq. 4.23.

The Monotone Upstream-centered Scheme for Conservative Laws (MUSCL) [129] was used to difference the inviscid fluxes. A mid-mode Flux limiter was used to eliminate oscillations in the shock regions. The viscous fluxes were evaluated at the cell faces with the first derivative terms centrally differenced. For the thin-layer, only the the normal derivatives were retained, while in the full Navier-Stokes, all viscous terms were retained [130].

4.3.2 Flux-Difference Splitting Scheme

The idea of flux vector splitting according to the signs of the eigenvalues has been introduced by Steger and Warming [131]. The Jacobian of the split fluxes obtained using Steger and Warming flux vector splitting are not continuously differentiable. At sonic velocities and stagnation points, the Jacobian of the split fluxes have discontinuous slope. By expressing the split fluxes as a polynomial function of Mach number with the lowest possible order, van Leer devised a better flux splitting to alleviate this problem. In both cases however, the stagnation enthalpy of steady flow problems is not necessarily constant. Hanel et al. [132] have ensured constancy of stagnation enthalpy for such flows in van Leer splitting by introducing higher order polynomial.

On the other hand, in Godunov-type schemes [133], the solution is considered to be piecewise constant over each cell, at certain time levels and the solution at the next time level is obtained from the wave interactions originating at the boundaries. The

new piecewise constant solution at the new time level is obtained by averaging the fluid states over each cell. In this way, Godunov-type schemes require solving non-linear algebraic equations, and are is time consuming. Several approximate Riemann solvers have been employed including Roe [134], Osher [135] and others.

A complete review of the flux splitting methods can be found in Ref. 129. In the rest of this subsection, we will present, in some detail, the flux-difference splitting scheme of Roe, which is used in the present work.

Roe flux-difference splitting is based on a characteristics decomposition of the flux differences, taking into consideration the conservation properties of the scheme. Consider the one-dimensional equation where $\hat{E}$ is the linear function of $\hat{q}$:

$$\frac{\partial \hat{q}}{\partial t} + \frac{\partial \hat{E}}{\partial x_1} = 0 \tag{4.24}$$

Using the chain rule, this equation can be written as

$$\frac{\partial \hat{q}}{\partial t} + A\frac{\partial \hat{q}}{\partial x_1} = 0 \tag{4.25}$$

where $A = \frac{\partial \hat{E}}{\partial \hat{q}}$. The exact solution of the Riemann problem can be written in terms of the flux differences as

$$\hat{E}_R - \hat{E}_L = \sum_{k=1}^{3} \alpha_k \lambda_k e_k \tag{4.26}$$

where α_k represents the strength of the wave, and λ_k and e_k are the eigenvalues and eigenvectors of the Jacobian matrix A, respectively. As shown in Ref. 134, the interface flux can be determined using

$$\hat{E}_{i+\frac{1}{2}}(q_L, q_R) = \frac{1}{2}\left(\hat{E}_L + \hat{E}_R - \sum_{k=1}^{3} \alpha_k \lambda_k e_k\right] \tag{4.27}$$

Now, consider the case of Euler equations, where $\hat{E}$ is not a linear function of $\hat{q}$, Roe [134] suggested the following form

$$\frac{\partial \hat{q}}{\partial t} + \tilde{A}\frac{\partial \hat{q}}{\partial x_1} = 0 \tag{4.28}$$

where $\tilde{A}$ is the Roe-average matrix and is constructed such that it satisfies the following conditions:

1. It constitutes a linear mapping from the vector space $\hat{q}$ to the vector space $\hat{E}$.
2. As $\hat{q}_l \rightarrow \hat{q}_R \rightarrow \hat{q}$, $\tilde{A}(\hat{q}_l, \hat{q}_R) \rightarrow A(\hat{q})$
3. For any $\hat{q}_L$, $\hat{q}_R$; $\tilde{A}(\hat{q}_l, \hat{q}_R) \times (\hat{q}_L - \hat{q}_R) = \hat{E}_L - \hat{E}_R$
4. The eigenvectors of $\tilde{A}$ are linearly independent.

Then, the flux difference between the left and right states and the interface fluxes can be written as

$$\hat{E}_R - \hat{E}_L = \tilde{A}(\hat{q}_R - \hat{q}_L) \tag{4.29}$$

$$\hat{E}_{i+\frac{1}{2}}(\hat{q}_R - \hat{q}_L) = \frac{1}{2}\left[\left(\hat{E}_L + \hat{E}_R\right) - |\tilde{A}|(\hat{q}_R - \hat{q}_L)\right]_{i+\frac{1}{2}} \tag{4.30}$$

For three-dimensional flows, the above equation can be written as

$$\left(\hat{E}_m(\hat{q}_R, \hat{q}_L)\right)_{i+\frac{1}{2}} = \frac{1}{2}\left[\left(\hat{E}_{mR} - \hat{E}_{mL}\right) - |\tilde{A}|(\hat{q}_R - \hat{q}_L)\right]_{i+\frac{1}{2}} \quad , m = 1,2,3 \tag{4.31}$$

where j,k (spatial counters) and n (time level counter) are kept constant. The last term of the above equation can be expressed as

$$\begin{aligned} |\tilde{A}|(\hat{q}_R - \hat{q}_L) &= |\tilde{A}|\Delta\hat{q} \\ &= \begin{bmatrix} \alpha_4 \\ \tilde{u}_1\alpha_4 + \xi^m_{x_1}\alpha_5 + \alpha_6 \\ \tilde{u}_2\alpha_4 + \xi^m_{x_2}\alpha_5 + \alpha_7 \\ \tilde{u}_3\alpha_4 + \xi^m_{x_3}\alpha_5 + \alpha_8 \\ \tilde{H}\alpha_4 + \tilde{\bar{u}}_m\alpha_5 + \tilde{u}_1\alpha_6 + \tilde{u}_2\alpha_7 + \tilde{u}_3\alpha_8 - \left(\frac{\tilde{a}^2}{\gamma-1}\right)\alpha_1 \end{bmatrix} \end{aligned} \tag{4.32}$$

where

$$\alpha_1 = \left|\frac{\nabla\xi^m}{J}\right| |\tilde{\bar{u}}_m| \left(\Delta\rho - \frac{\Delta p}{\tilde{a}^2}\right) \tag{4.33}$$

$$\alpha_2 = \frac{1}{2\tilde{a}^2}\left|\frac{\nabla\xi^m}{J}\right|\left|\tilde{\tilde{u}}_m + \tilde{c}\right|\left(\Delta p + \tilde{\rho}\tilde{a}\Delta\tilde{u}_m\right) \tag{4.34}$$

$$\alpha_2 = \frac{1}{2\tilde{a}^2}\left|\frac{\nabla\xi^m}{J}\right|\left|\tilde{\tilde{u}}_m - \tilde{c}\right|\left(\Delta p - \tilde{\rho}\tilde{a}\Delta\tilde{u}_m\right) \tag{4.35}$$

$$\alpha_4 = \alpha_1 + \alpha_2 + \alpha_3 \tag{4.36}$$

$$\alpha_5 = \tilde{a}\left(\alpha_2 - \alpha_3\right) \tag{4.37}$$

$$\alpha_{5+j} = \left|\frac{\nabla\xi^m}{J}\right|\left|\tilde{\tilde{u}}_m\right|\left(\tilde{\rho}\Delta u_j - \xi^m_{x_1}\tilde{\rho}\Delta\tilde{u}_m\right) \quad , j = 1,2,3 \tag{4.38}$$

The $\sim$ superscripts denote Roe-averaged values where

$$\begin{aligned}
\tilde{\rho} &= \sqrt{\rho_L\rho_R} \\
\tilde{u}_j &= \frac{u_{jL} + u_{jR}\sqrt{\rho_L\rho_R}}{1+\sqrt{\rho_L\rho_R}} \\
\tilde{H} &= \frac{H_L + H_R\sqrt{\rho_L\rho_R}}{1+\sqrt{\rho_L\rho_R}} \\
\tilde{a}^2 &= (\gamma-1)\left[\tilde{H} - \frac{\tilde{u}_1^2 + \tilde{u}_2^2 + \tilde{u}_3^2}{2}\right]
\end{aligned} \tag{4.39}$$

4.4 Boundary and Initial Conditions

4.4.1 Initial Conditions

All the numerical solutions of steady flow problems are obtained by impulsively started initial conditions, i.e. the body under consideration is suddenly placed in the freestream at the specified conditions of the problem. For unsteady flow problems, the solutions obtained from the pseudo time-stepping calculations corresponding to the same flow conditions are used as initial conditions in order to save the computational cost of the transient state.

4.4.2 Surface Boundary Conditions

The surface boundary conditions are determined explicitly. Viscous wall boundary conditions are used, i.e. no slip and no penetration conditions are enforced

$$\bar{u} = \bar{u}_s \tag{4.40}$$

where $\bar{u}$ is the Cartesian velocity vector and $\bar{u}_s$ is the body surface velocity vector. For stationary bodies $\bar{u}_s = 0$, while for moving bodies $\bar{u}_s$ is the relative velocity of the fluid with respect to the body, which is set to zero. The relative velocity is determined from the physical motion of the body. The normal pressure gradient is set equal to zero for stationary bodies. For moving bodies in rotational motions, the normal pressure gradient is given by

$$\frac{\partial p}{\partial n} = -\rho \bar{a}_s . \hat{n} \tag{4.41}$$

where $\bar{a}_s$ is the acceleration of the body surface defined as

$$\bar{a}_s = \bar{\omega} \times (\bar{\omega} \times \bar{r}) + \dot{\bar{\omega}} \times \bar{r} \tag{4.42}$$

where $\bar{\omega} \times (\bar{\omega} \times \bar{r})$ is the centripetal acceleration, $\dot{\bar{\omega}} \times \bar{r}$ is the tangential acceleration and $\dot{\bar{\omega}}$ is the time derivative of the angular velocity vector $\bar{\omega}$ and $\bar{r}$ is the position vector of the point under consideration.

For temperature, adiabatic and isothermal boundary conditions are used, depending on the physical circumstances of the problem.

4.4.3 Far-Field Boundary Conditions

For locally-conical flow problems, freestream boundary conditions were used. This choice is justified by the fact that the bow shock was found to be included entirely in the computational domain and its location was far from the far-field boundary. The

flow outside the bow shock was entirely supersonic and, as a result disturbances will not reach the far-field boundary.

For three-dimensional problems, a non-reflecting boundary condition based on the theory of characteristics, as well as freestream boundary condition was applied. They were found to be equivalent for the cases considered. That was due to the size of the computational domain, which was taken to be $21r$, where r was the local radius of the cone. In the characteristics boundary condition [127,136], the eigenvalues of the Jacobian matrix of the Euler equations were determined and found to be u_n, $u_n + a$ and $u_n - a$ for one-dimensional flow. For the three-dimensional Euler equations, the characteristic variables are u_n, u_n, u_n, $u_n + a$ and $u_n - a$. These equations, along with the Riemann invariants, were used to impose the boundary condition.

4.4.4 Zonal Boundary Conditions

For multi-block cases, a zonal boundary condition was used at the block interfaces. Since for all the multi-block cases presented, the lines of the blocks at the interface are one to one, there was no need for interpolations and simple continuation boundary conditions were used. In such case, the "ghost cells" needed to calculate boundary conditions at the interface of a certain block were taken from the neighboring block on the interface.

The computer code which has been described in this chapter is FTNS3D [20,130] which is a modified version of CFL3D [137–140]. This code has been validated and its results were compared to the experimental results for both steady [22,137–141] and unsteady problems [142–145].

CHAPTER 5

PASSIVE CONTROL USING SIDE-STRAKES

5.1 *Introduction*

Side forces arise when slender bodies are placed at high relative incidence. The side force magnitude and direction at zero side slip for certain configurations and flow conditions may exceed the normal force [1,146]. Also, the vortex-induced asymmetric force and yawing moment may switch suddenly from one side to the other, as a result of vehicle roll. These factors should be considered carefully during the design process. This is not a simple task since the asymmetric loads cannot be predicted accurately and many parameters affect the side-force magnitude. These relatively large forces represent a hazard to aircraft safety and a problem for missile control and accuracy.

Both passive and active control methods have been employed to alleviate and possibly eliminate the side-force. Passive control methods are those methods that do not require energy for operation. They include nose bluntness, fins, side strakes and straight or helical trips. In this chapter, which is an extension of Ref. 22, passive control using side strakes will be presented in terms of effect of the side-strake span length, at different AOA, on control. A reference case for the asymmetric flow is presented in the next section. This case is used in this chapter and the following chapters to evaluate the effectiveness of the different control methods.

To avoid the relatively expensive three-dimensional Navier-Stokes equations solution, the locally-conical flow assumption is used in this chapter. The sharp cone is the simplest aerodynamic component and apart from the base and viscous effects, the flow will be globally conical for steady cases. At high Reynolds number, the locally-conical flow assumption is valid for supersonic flows—both steady and unsteady [29,147]. The three-dimensional Navier-Stokes equations are not self-similar. The solution is obtained by enforcing the solution to be equal at two planes located at $x = 1.0$ and $x = 0.95$. The locally-conical flow assumption reduces both the memory and time required for the solution, by almost an order of magnitude compared to the solution of the three-dimensional Navier-Stokes equations. Most of the asymmetric flow characteristics can be obtained from the locally-conical flow solutions [20,22,32,53,128].

The implicit, upwind, Roe flux-difference splitting, finite-volume scheme is used to solve the unsteady, compressible, full Navier-Stokes equations. The smooth flux limiters are used to eliminate the oscillations which show up at large flow gradient locations. The computational scheme is coded in the computer program "FTNS3D" which is a modified version of "CFL3D" where the cross derivatives and the implicit terms are added. For the locally-conical flow solutions, an axial station of $x_1 = 1.0$ is selected and the variables of the flowfield are forced to be equal between this axial station and another axial station in close proximity to $x_1 = 1.0$. This ensures that the flow variables are locally independent of the axial direction at $x_1 = 1.0$ [128]. The computations were carried out on the Cray YMP at NASA Langley Research Center and the Cray C-90 at NASA Ames Research Center.

5.2 *Asymmetric Flow, Reference Case*

The locally-conical flow over a cone of 5° semi apex angle at a freestream Mach number of 1.8 and a Reynolds number of 10^5 is considered to be the test case (in

which many of the control methods are to be applied in this chapter and the next chapters). The grid has been generated using the modified Joukowski transformation with a geometric series for grid clustering in the normal direction. The computational grid (shown in Fig. 5.1) was 241 $\times$ 81 in the wrap-around and normal directions, respectively. The minimum spacing between grid lines in the normal direction was 10^{-4} and the grid was distributed uniformly in the circumferential direction. The effect of minimum spacing, grid density and computational domain size for the shown configuration were investigated by Wong [22].

In this case, the boundary conditions used are the no-slip and no-penetration boundary condition at the wall, and the freestream boundary condition at the far-field boundary. This is justified since the computational domain is extended to $21r$, where r is the local radius of the cone. Hence, the domain is large enough to capture the bow shock as part of the solution.

The residual, lift coefficient, and side force coefficient are shown in Fig. 5.2. Examining these figures closely, one can see that the residual drops four orders of magnitude after 1200 time steps. Thereafter, it starts to increase, then it drops again to the machine zero (ten orders of magnitude) after 7500 time steps. If we examine the history of side-force in a similar manner, we see that up to 1200 time steps, the side force is almost zero and the flowfield is symmetric. After 1200 time steps, the side force starts to grow and reaches its steady state value which is about -6.5×10^{-4} at about 2500 time steps. A slight increase in the lift coefficient is observed when the asymmetry appears, as shown in Fig. 5.2.

The onset of asymmetry in wind tunnel tests and real flights is due to the disturbances that grow both spatially and temporally. Such a disturbance can be due to imperfections in the wind tunnel models, wind tunnel wall effects or sudden (even slight) changes in freestream direction. Computationally, these disturbances can be simulated either

- by using a physical disturbance, such as imposing a side-slip for a short period of time, or

- (in the present solution), by having the machine round-off error act as a random source of disturbances to the flowfield.

Kandil and his co-authors [20, 32, 53, 128] showed that the steady asymmetric flow that arises from the physical conditions mentioned above is unique, irrespective of the disturbance source level or type.

The asymmetry level can be realized by examining Fig. 5.3, which shows the surface pressure coefficient versus θ, which is the azimuthal angle measured from the plane of geometric symmetry at the wind ward side. The suction pressure on the left side (vortex closer to the body) is higher (more negative) than the suction pressure on the right side.

Figure 5.4 shows the total pressure loss contours, the crossflow velocity vectors and the crossflow streamlines around the circular cone section. The difference in the level of the separation point between the left and right sides can be identified from the total pressure loss contours and the crossflow velocity vectors. The side with the lower separation point is the one with higher vortex structure. The total pressure loss is determined using the equation

$$TPL = 1 - \gamma p \left(\frac{1 + \frac{\gamma-1}{2} M^2}{1 + \frac{\gamma-1}{2} M_\infty^2} \right)^{\frac{\gamma}{\gamma-1}} \tag{5.1}$$

5.3 *Side-Strakes*

One of the main factors that allows disturbances to grow, resulting in asymmetric flow, is the interaction between the vortices from the left and right sides on the lee ward side of the forebody. That might result in an asymmetry of the separation

points on the right and left sides of the forebody, and consequently, the asymmetry extends to the whole flowfield. Considering these facts, side-strakes have two primary effects 5.5

1. The horizontal distance between the vortices on the lee-ward side of the forebody increases by the span length of the side-strakes span and so is the horizontal distance between the primary vortices. This means that the interaction between vortices is reduced.

2. The separation points, in this case, are usually located at the side-strake tips which means that the locations of the separation points on the right and left sides are enforced to be symmetric.

In this section, we investigate the effect of side-strakes and their span lengths in alleviating or eliminating the side-forces. The grid used in all the computational applications is 161×81 in the wrap-around and normal directions, respectively. The grid is generated using a hyperbolic grid generator with a transfinite grid interpolation to cluster the grid in the strake regions. Similar to the previous case, the minimum spacing in the normal direction is 10^{-4} and the grid extends far enough ($21r$) for the freestream boundary condition to be applicable. The boundary conditions are the same as the previous case.

5.3.1 Side-strakes of span length $h = 0.35r$

Figure 5.6 shows the grid used with the sharp-edged strakes, of span length $0.35r$. Figure 5.7 shows the surface pressure coefficient of the flow over a circular cone at AOA of 30°. The figure shows a jump in the surface pressure at $\theta = \pm 90°$ due to the existence of side strakes. The symmetry in the surface pressure coefficient over the body is an indication of zero side force and the symmetry of the flowfield. The total

pressure loss contours, velocity vectors and streamlines shown in Fig. 5.8 indicate the symmetry of the flowfield at the specified AOA, $\alpha = 30°$.

Figures 5.9 and 5.10 are corresponding to Figs. 5.7 and 5.8 for $\alpha = 40°$. With the increase in the AOA, the lee ward side vortices are closer to each other, and simultaneously the surface pressure coefficient and the flowfield are both symmetric. We can see in Fig. 5.11 that the flowfield begins to exhibit asymmetry when α increases to 50°.

5.3.2 Side-strakes of span length $h = 0.4r$

The cases presented here are similar to those of the previous subsection with the exception that the strake span length h has been increased to $0.4r$ and the AOA considered are $\alpha = 40°$ and 50°. The grid used was the same density as that of the previous case. Figure 5.13 shows the convergence history of the residual, lift coefficient and the side-force coefficient for the flow at $\alpha = 40°$. From the side-force coefficient history, we can see that the side force is not zero. However, the side-force is about 0.16% of that of Fig. 5.2 where the AOA, $\alpha = 20°$ with no side-strakes. The difference in the lift coefficients in Fig. 5.13 and Fig. 5.2 is due to two factors: the first is the difference in the AOA and the second is the effect of the side-strakes (acting as small wings) in increasing the lift. Figures 5.14 and 5.15 show the surface pressure coefficient, total pressure loss contours, crossflow velocity vectors and crossflow streamlines for the present case.

When the AOA is increased to 50°, the side-force, Fig. 5.16, oscillates between $\pm 0.23 \times 10^{-4}$, which corresponds to about 3.5% of the side-force shown in Fig. 5.2. This high frequency oscillation does not produce significant asymmetry since the average is zero (see Figs. 5.17 and 5.18). The surface pressure coefficient is almost symmetric. There is a slight asymmetry that can be observed in total pressure loss contours.

5.3.3 *Side-strakes of span length* $h = 0.5r$

Now, extending the side-strake span length to $0.5r$, with $\alpha = 50°$, Fig. 5.19 shows that the side-force coefficient oscillates between $\pm 0.35 \times 10^{-4}$, which is a larger amplitude than the corresponding case with $h = 0.4r$. The degree of asymmetry in the present case is greater and the frequency is lower, as shown in Fig. 5.20, compared to previous case. This gives an indication of the limitations of the side-strakes as a method to eliminate the side forces. The level of the asymmetry is also shown clearly in Fig. 5.21.

5.4 *Summary*

In this chapter, several computational cases were presented to investigate the effects of the side-strakes and their span lengths in reducing the side-forces that arise at high AOA due to flow asymmetry. These cases covered an AOA range from 30° to 50° and the side-strake span length range from $0.35r$ to $0.5r$. The side-strakes were found to be effective in eliminating or reducing the side force and the flow asymmetry, up to a high AOA. Also, the side strakes acted as small wings to the body and hence, an increase in the lift coefficient was observed. The effect of increasing the span length of the side-strake was to enhance the flow stability and hence, damped the unwanted oscillations that result in flowfield asymmetries and side forces. While a minimum side-strake span length was found to be effective in certain AOA range, increasing the span length was not of much effect on the flow asymmetry at higher AOA.

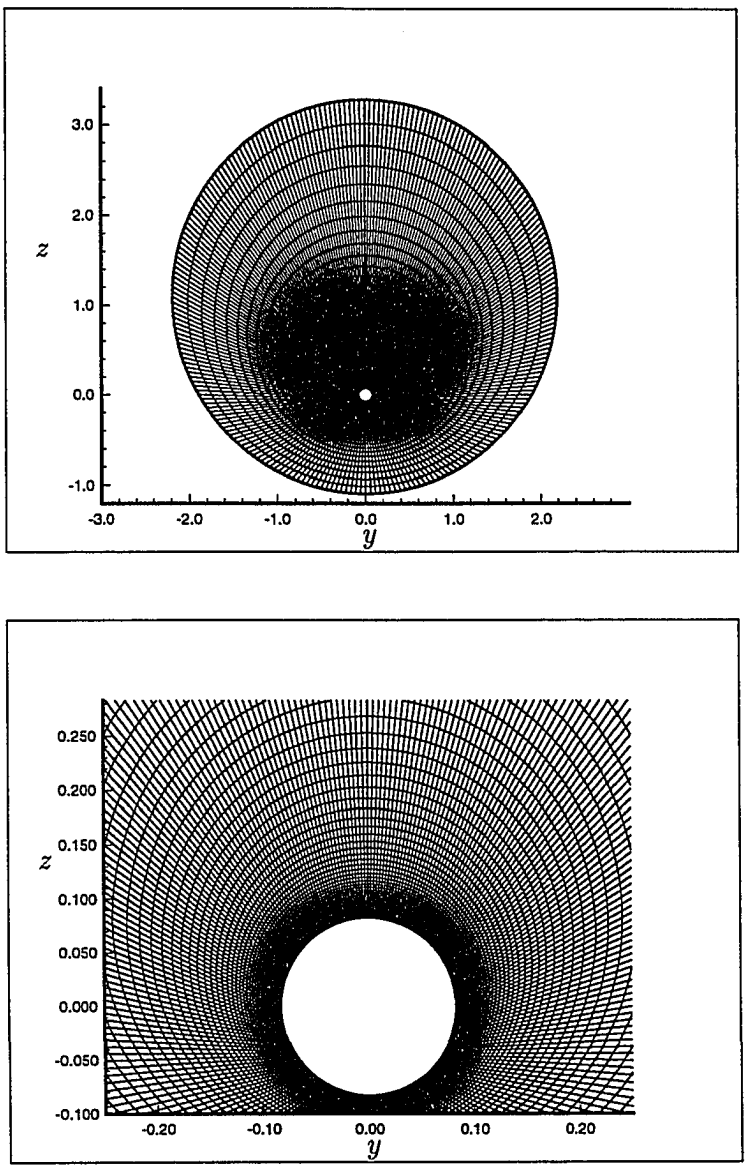

Figure 5.1: Grid over circular cross section of the cone, 241 × 81 points

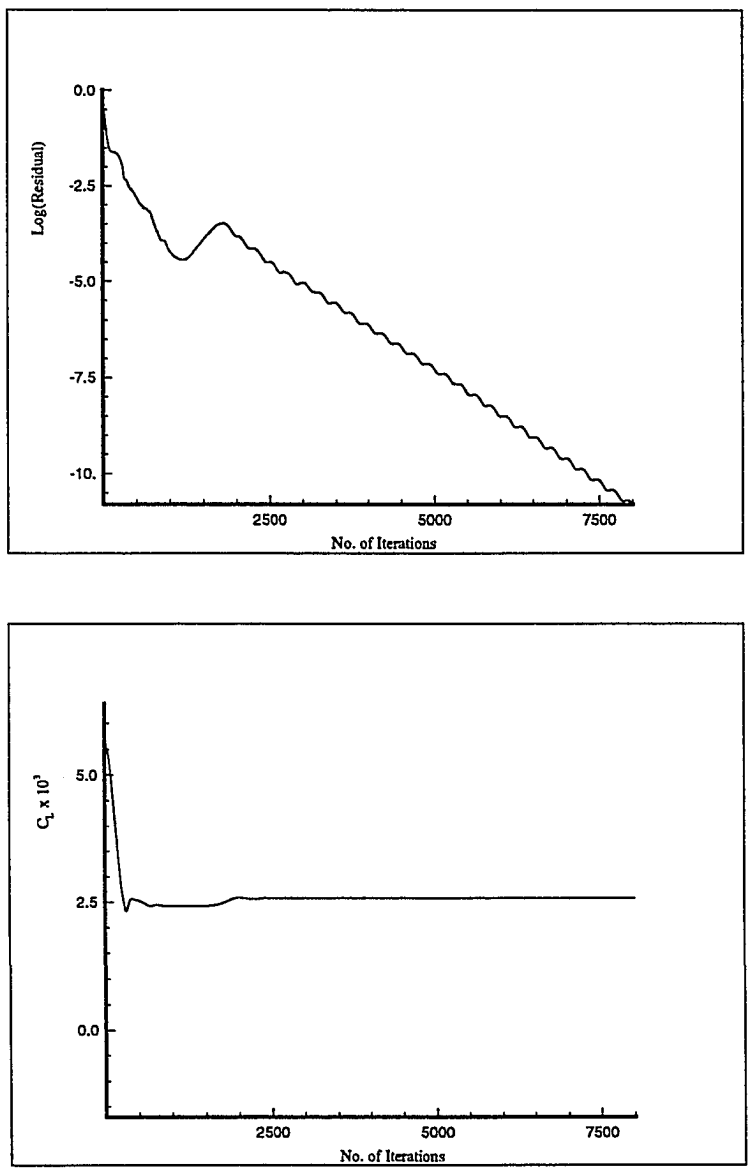

Figure 5.2: Residual, lift coefficient and side-force coefficient history of steady asymmetric flow for a circular cone at $\alpha = 20°$, $M_\infty = 1.8$, $R_e = 10^5$.

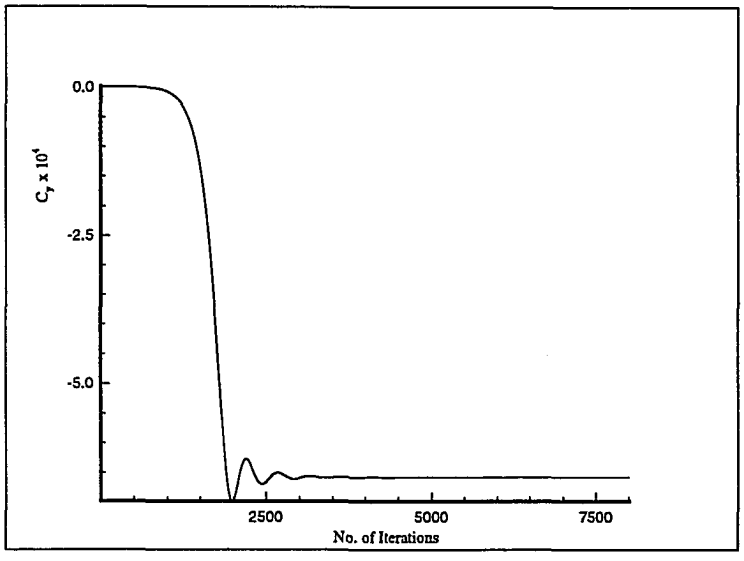

Figure 5.2: Continued

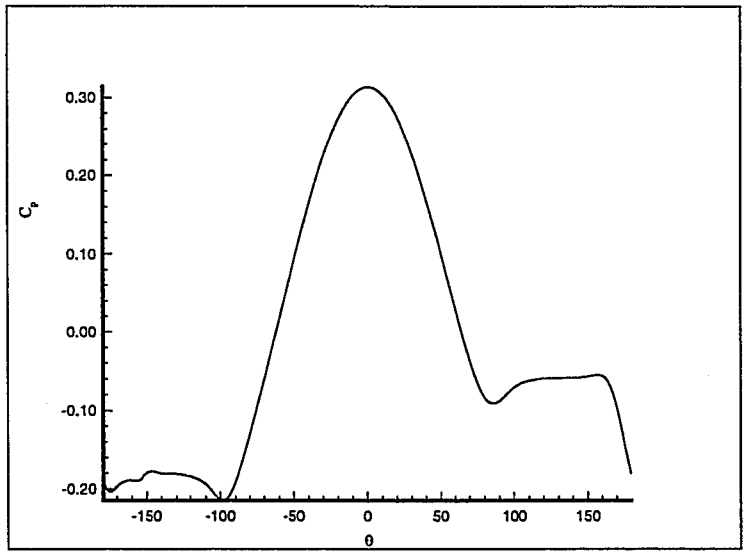

Figure 5.3: Surface pressure coefficient for steady asymmetric flow around a circular cone at $\alpha = 20°$, $M_\infty = 1.8$, $R_e = 10^5$.

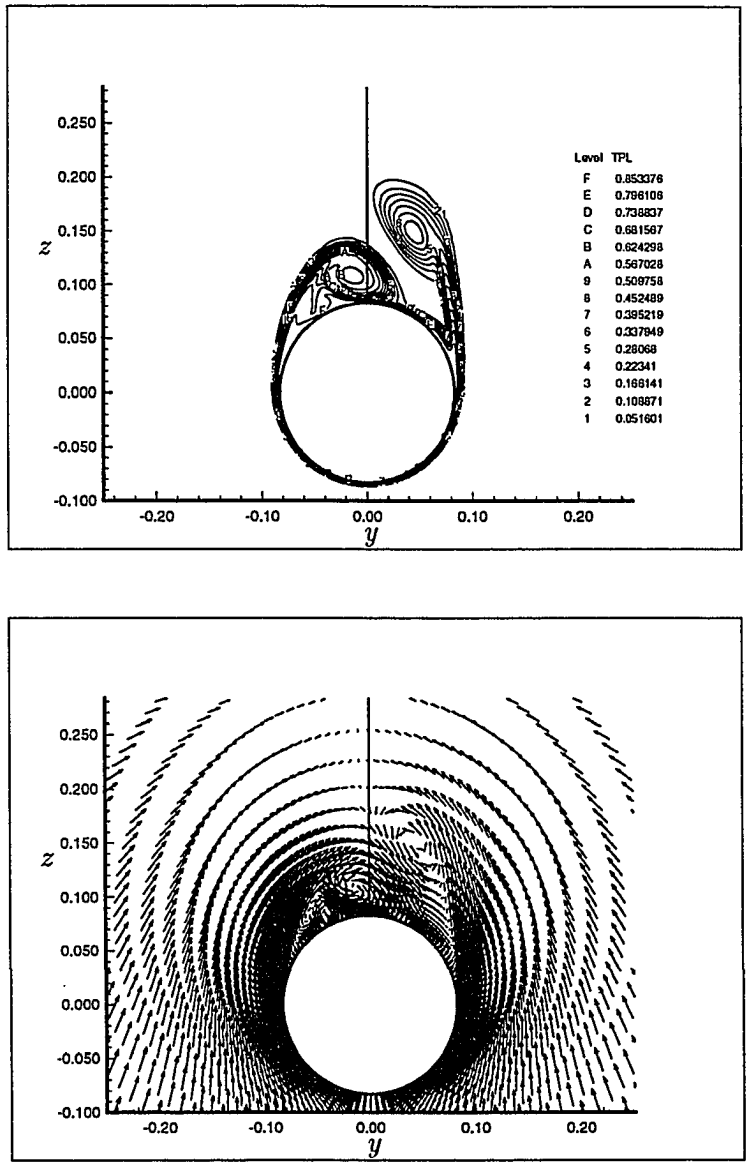

Figure 5.4: Total pressure loss contours, cross-flow velocity vectors and cross-flow streamlines for flow around a circular cone at $\alpha = 20°$, $M_\infty = 1.8$, $R_e = 10^5$.

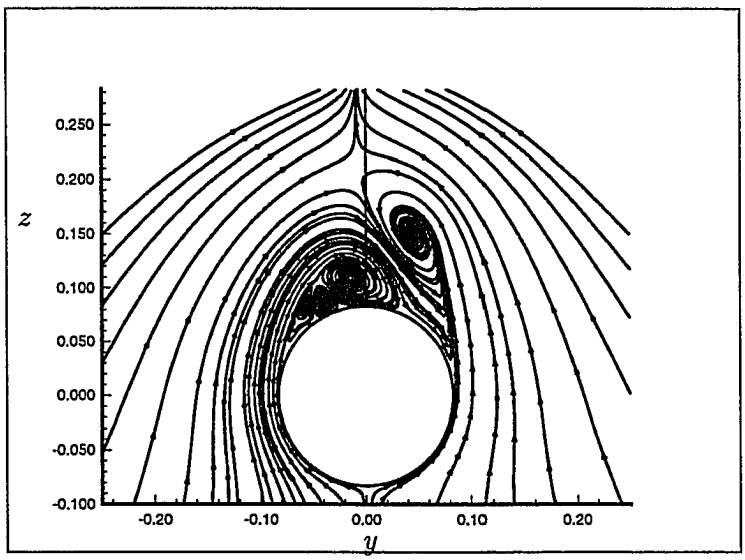

Figure 5.4: Continued

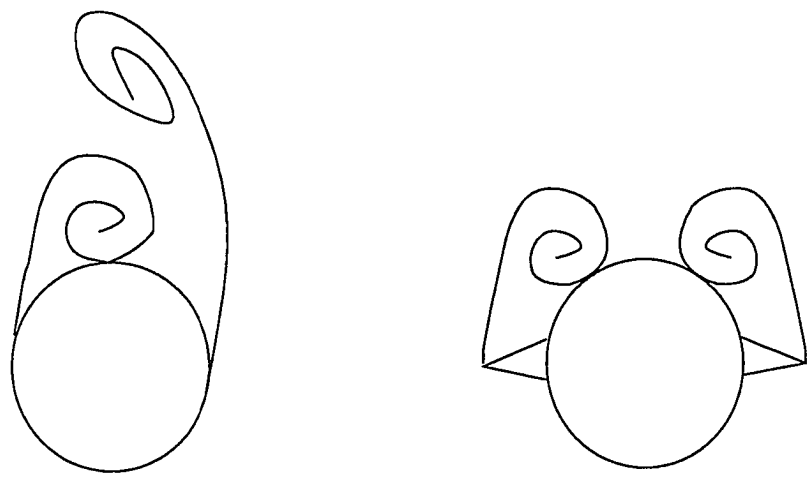

Figure 5.5: Side-strake effect on flow asymmetry

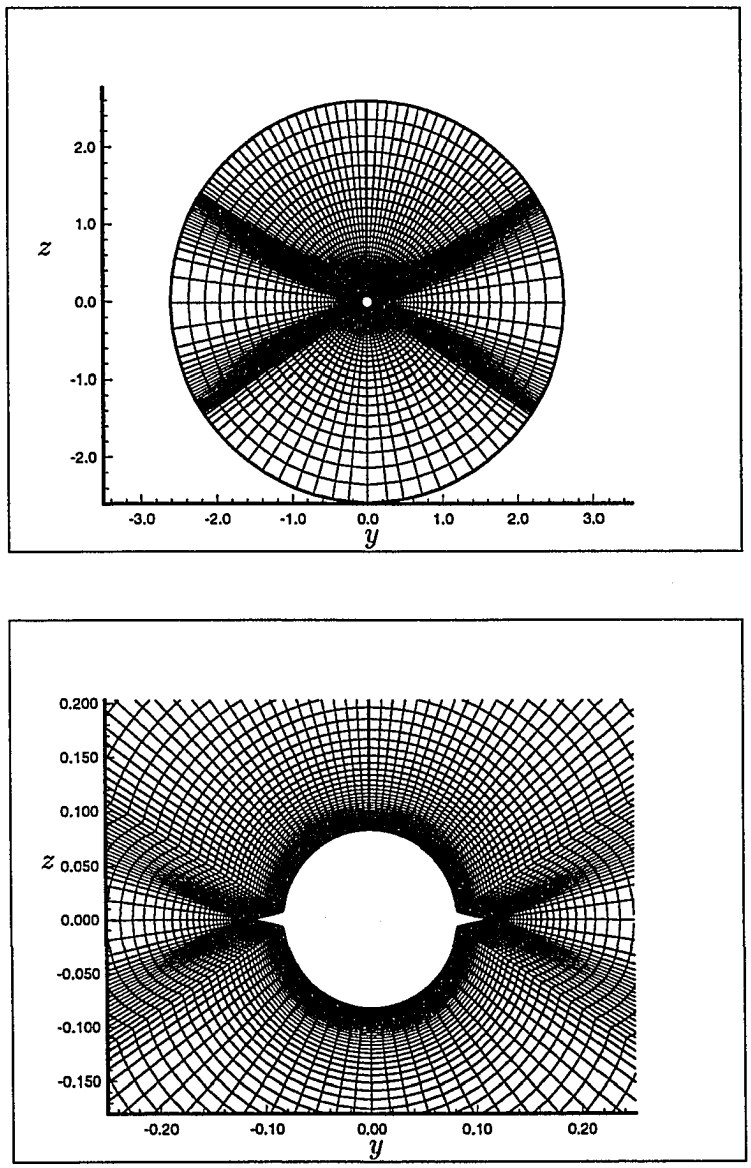

Figure 5.6: Grid over circular cross section of the cone, 161×81 points, $h = 0.35r$.

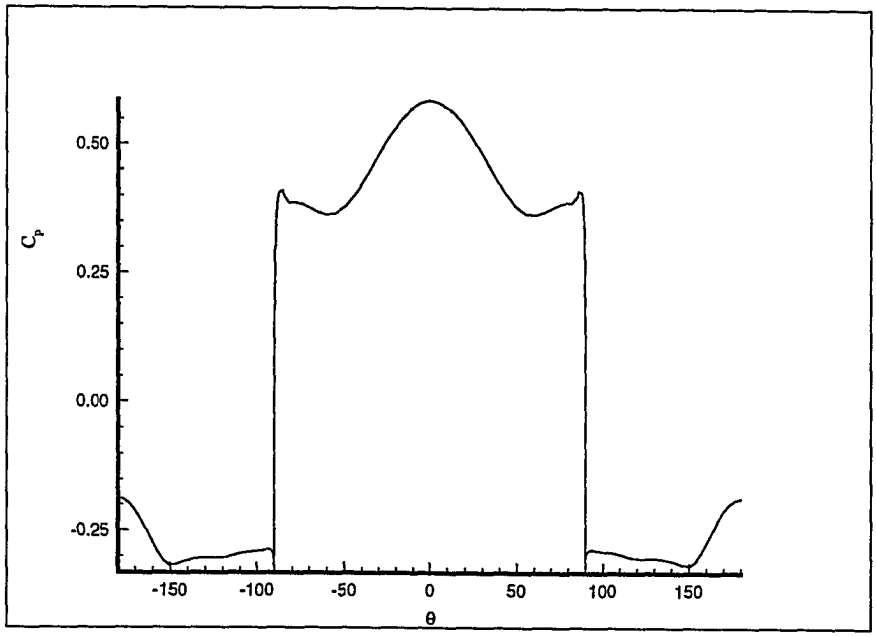

Figure 5.7: Surface pressure coefficient for flow around a circular cone at $\alpha = 30°$, $M_\infty = 1.8$, $R_e = 10^5$, $h = 0.35r$.

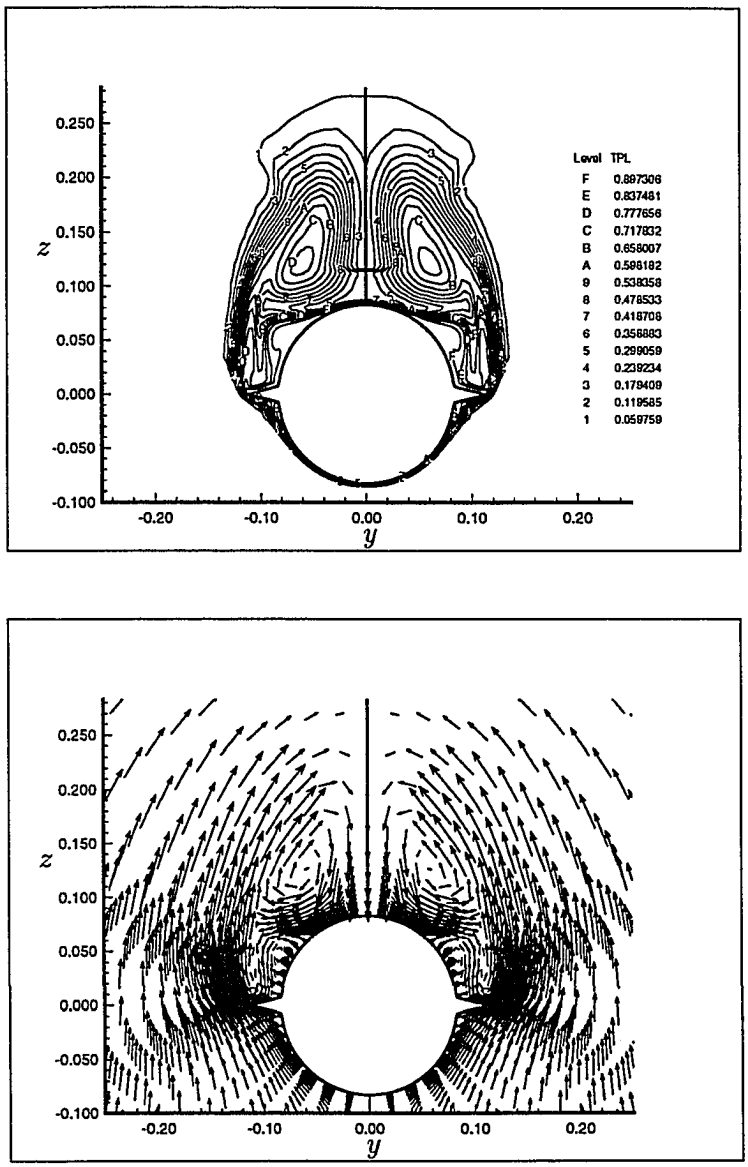

Figure 5.8: Total pressure loss contours, cross-flow velocity vectors and cross-flow streamlines for flow around a circular cone at $\alpha = 30°$, $M_\infty = 1.8$, $R_e = 10^5$, $h = 0.35r$.

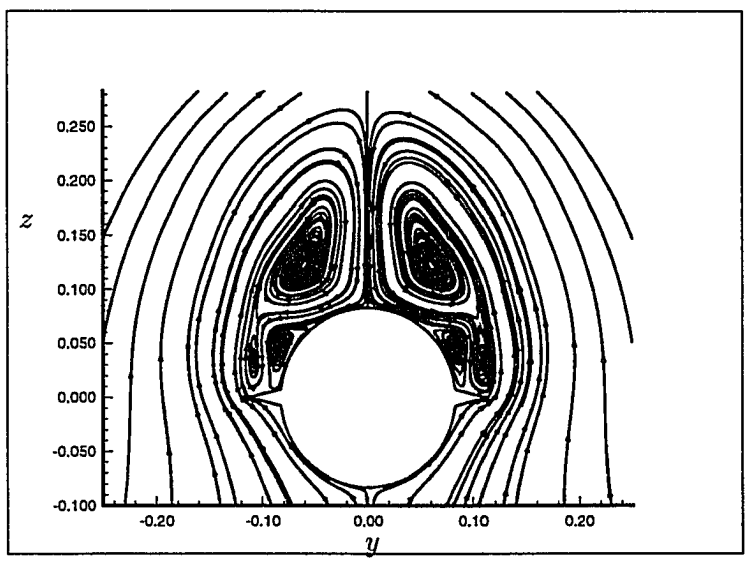

Figure 5.8: Continued

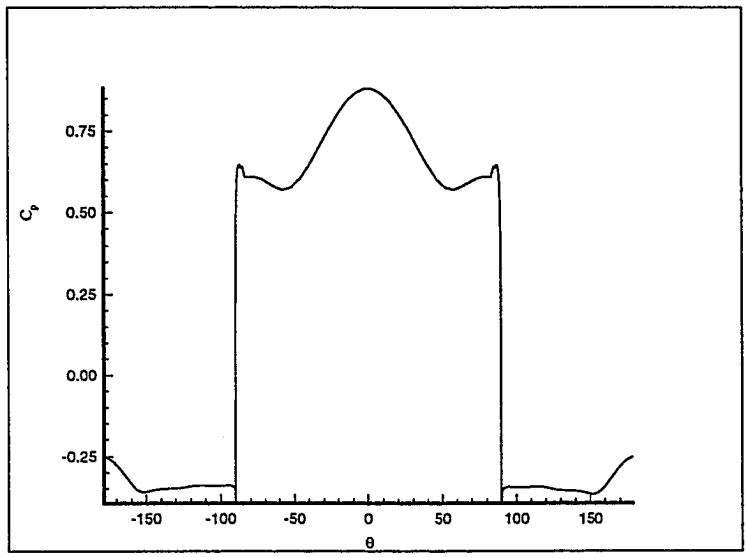

Figure 5.9: Surface pressure coefficient for flow around a circular cone at $\alpha = 40°$, $M_\infty = 1.8$, $R_e = 10^5$, $h = 0.35r$.

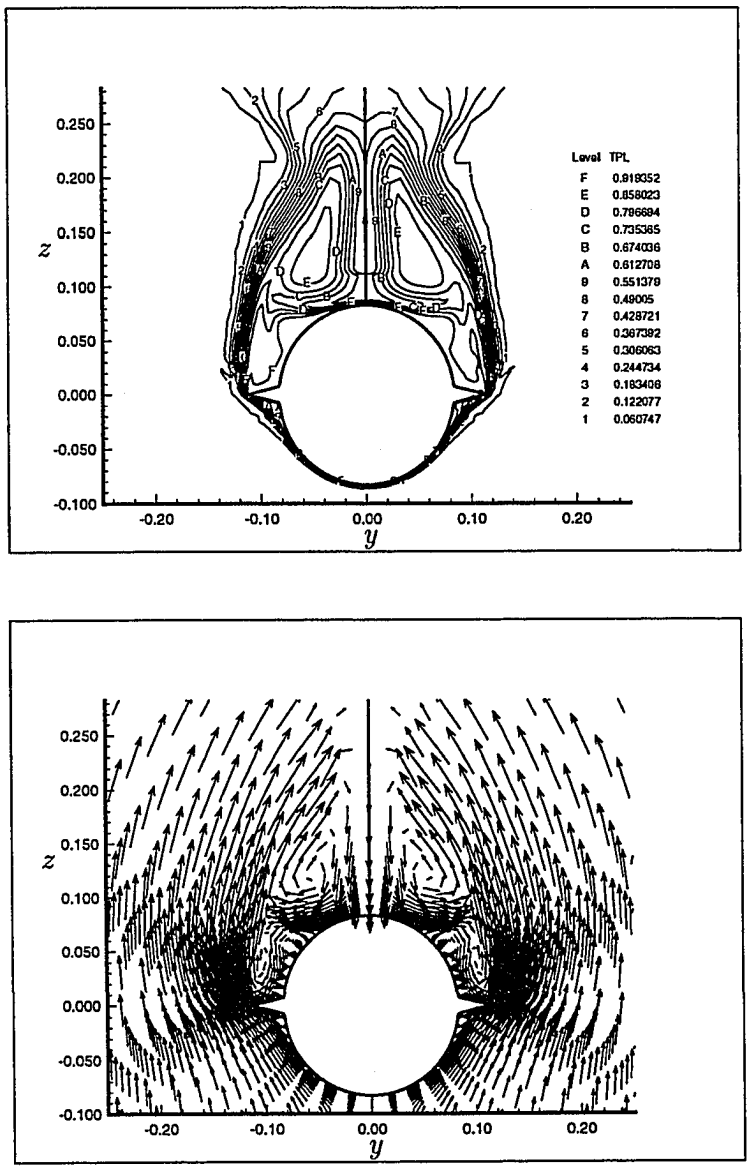

Figure 5.10: Total pressure loss contours, cross-flow velocity vectors and cross-flow streamlines for flow around a circular cone at $\alpha = 40°$, $M_\infty = 1.8$, $R_e = 10^5$, $h = 0.35r$.

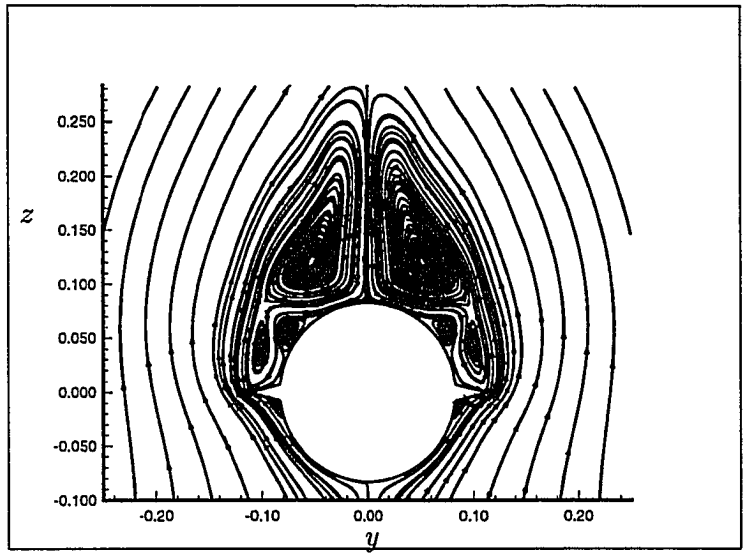

Figure 5.10: Continued

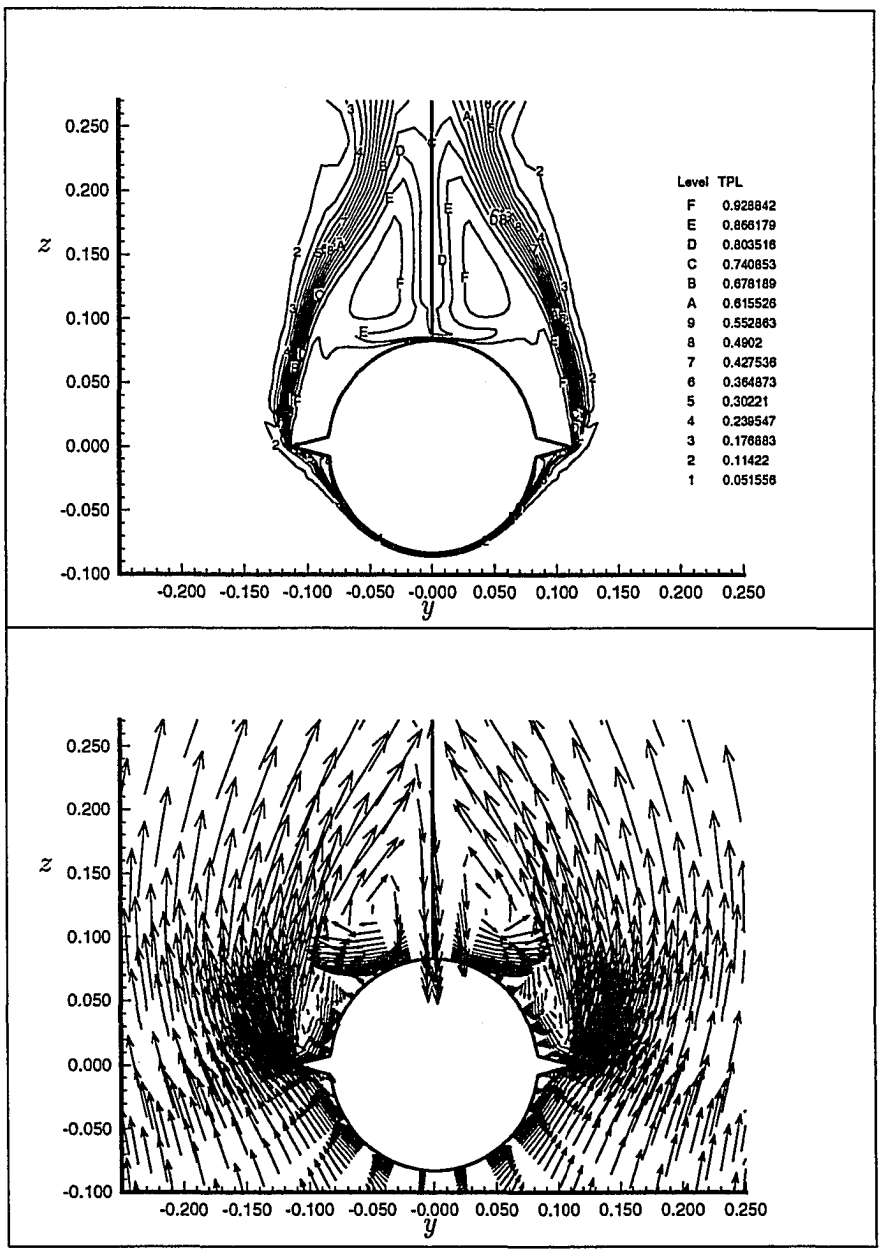

Figure 5.11: Total pressure loss contours, cross-flow velocity vectors and cross-flow streamlines for flow around a circular cone at $\alpha = 50°$, $M_\infty = 1.8$, $R_e = 10^5$, $h = 0.35r$.

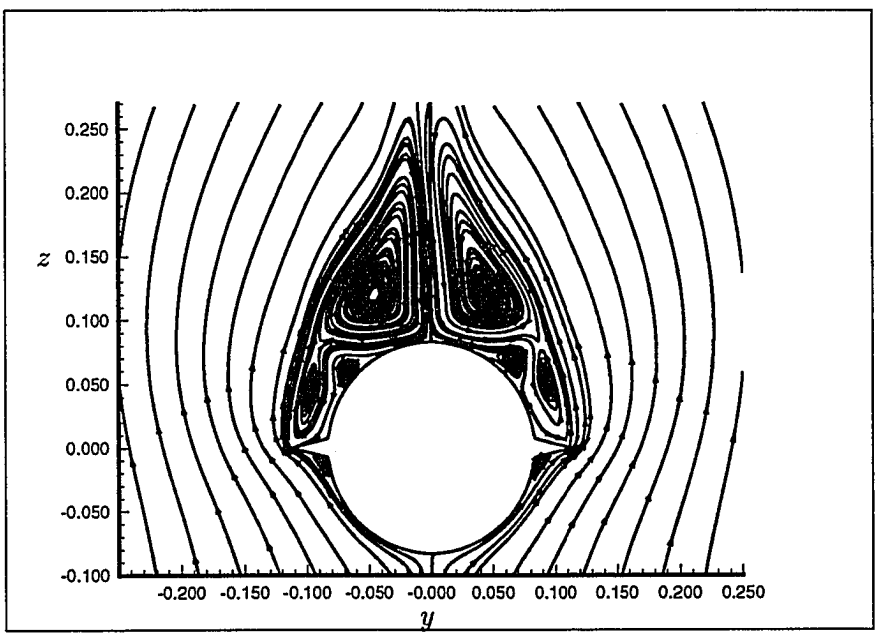

Figure 5.11: Continued

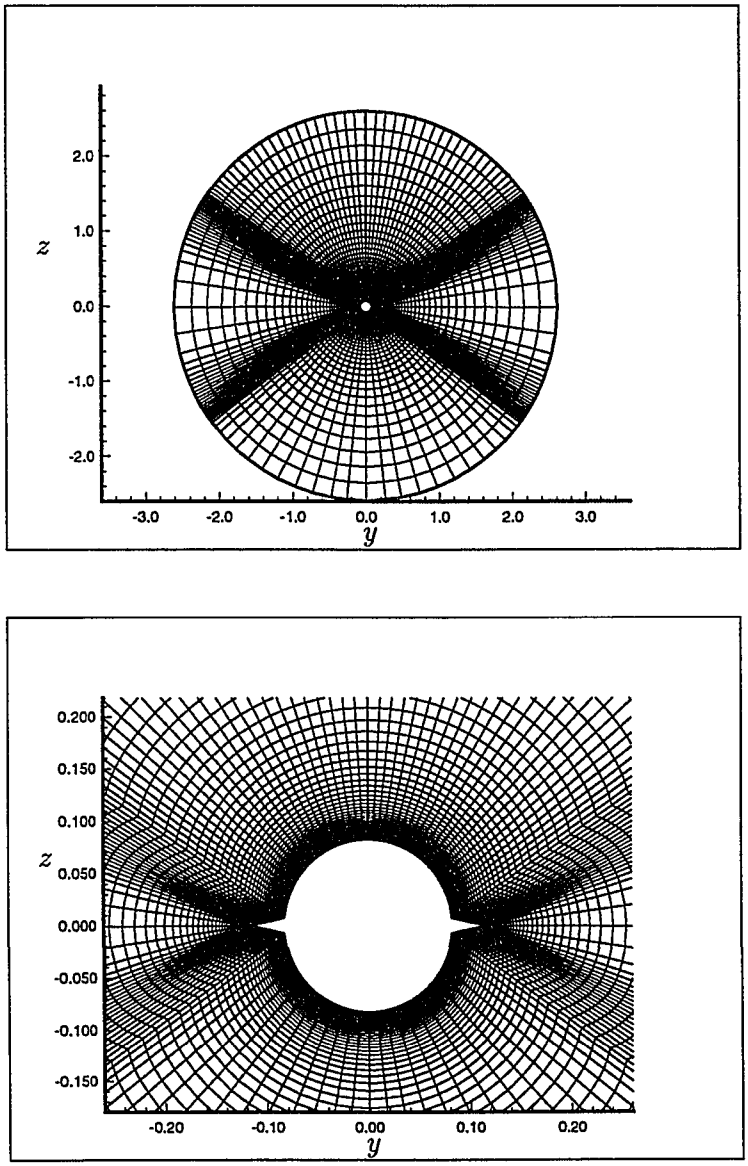

Figure 5.12: Grid over circular cross section of the cone, 161×81 points, $h = 0.4r$.

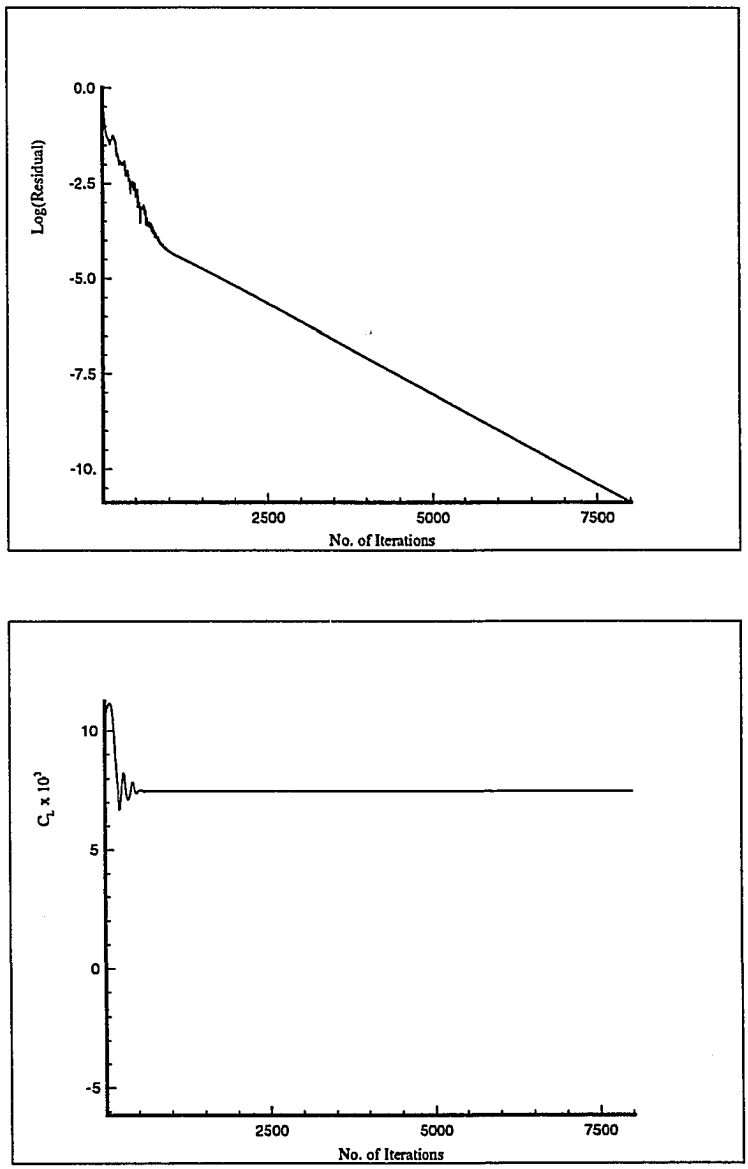

Figure 5.13: Residual, lift coefficient and side-force coefficient history of flow around circular cone at $\alpha = 40°$, $M_\infty = 1.8$, $R_e = 10^5$, $h = 0.4r$.

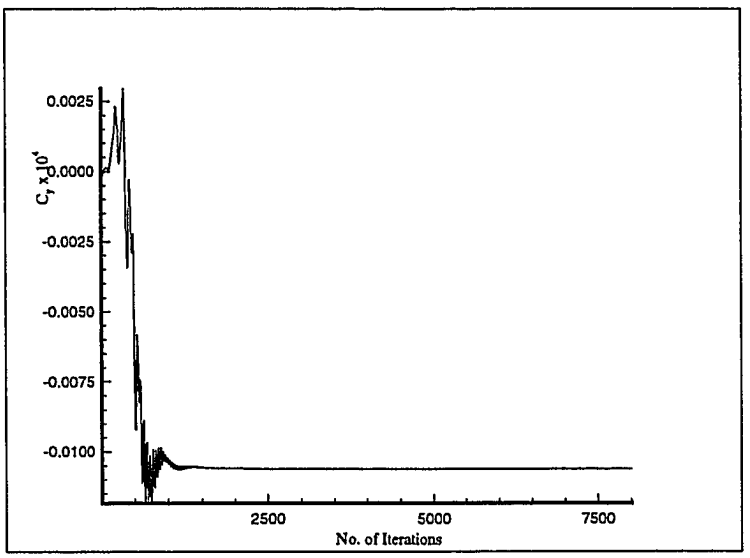

Figure 5.13: Continued

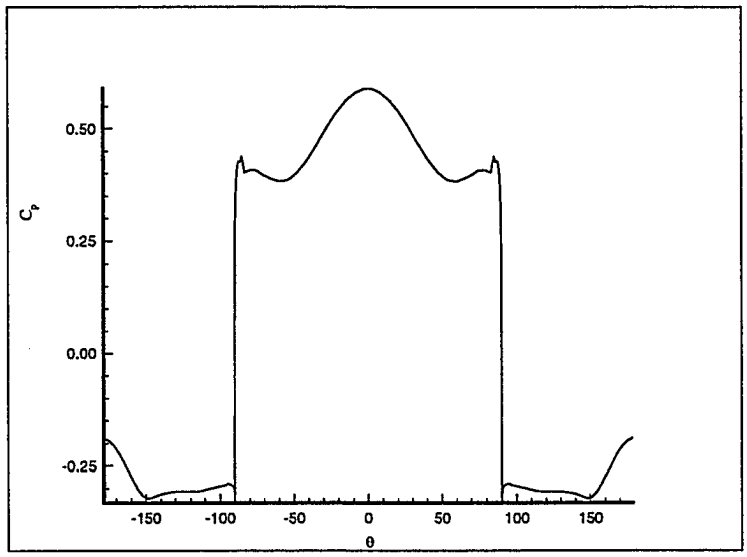

Figure 5.14: Surface pressure coefficient for flow around a circular cone at $\alpha = 40°$, $M_\infty = 1.8$, $R_e = 10^5$, $h = 0.4r$.

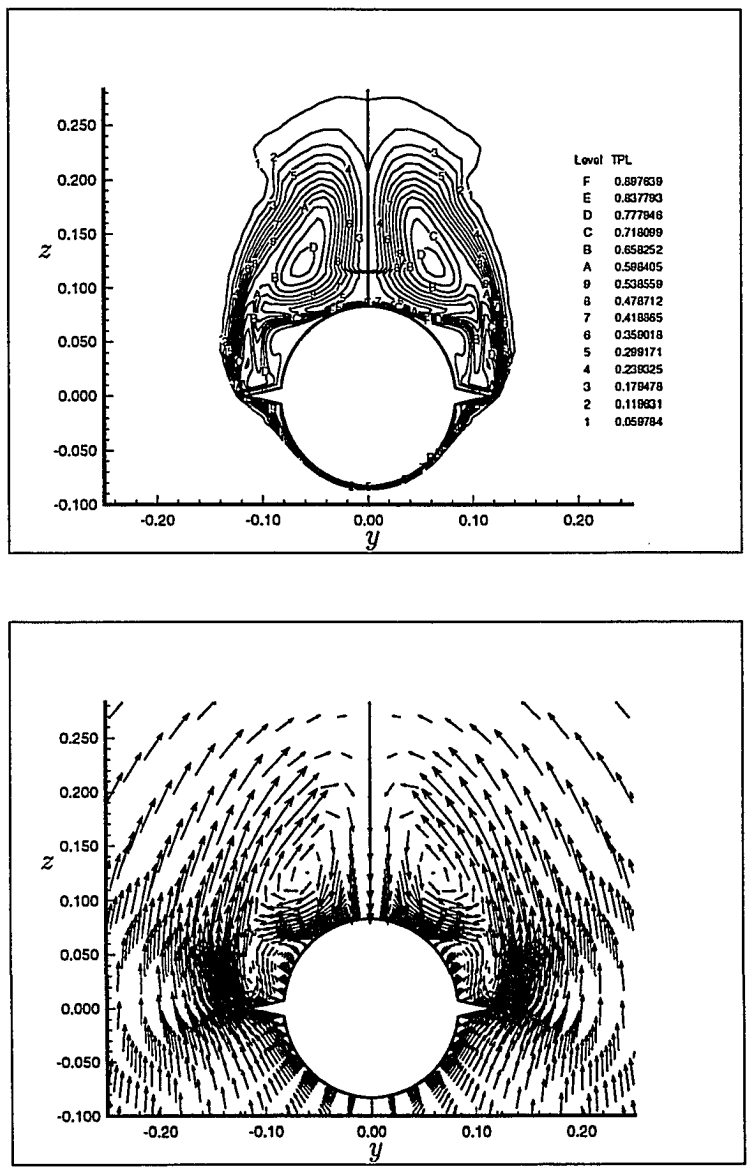

Figure 5.15: Total pressure loss contours, cross-flow velocity vectors and cross-flow streamlines for flow around a circular cone at $\alpha = 40°$, $M_\infty = 1.8$, $R_e = 10^5$, $h = 0.4r$.

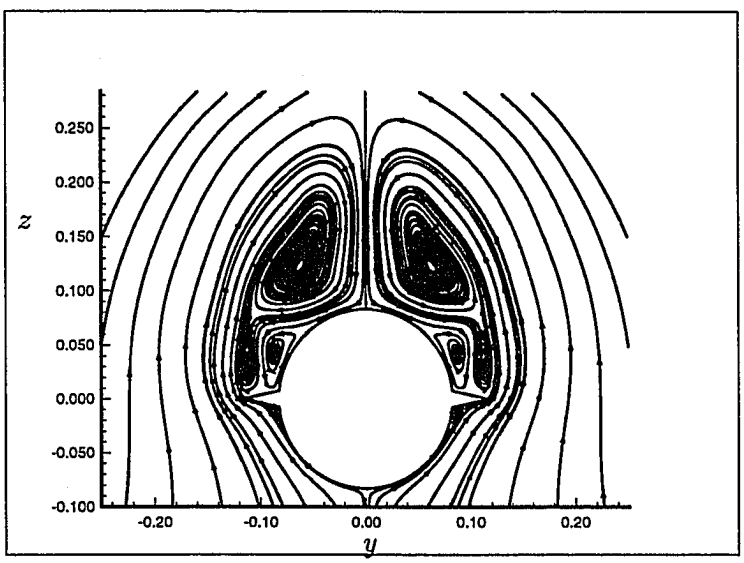

Figure 5.15: Continued

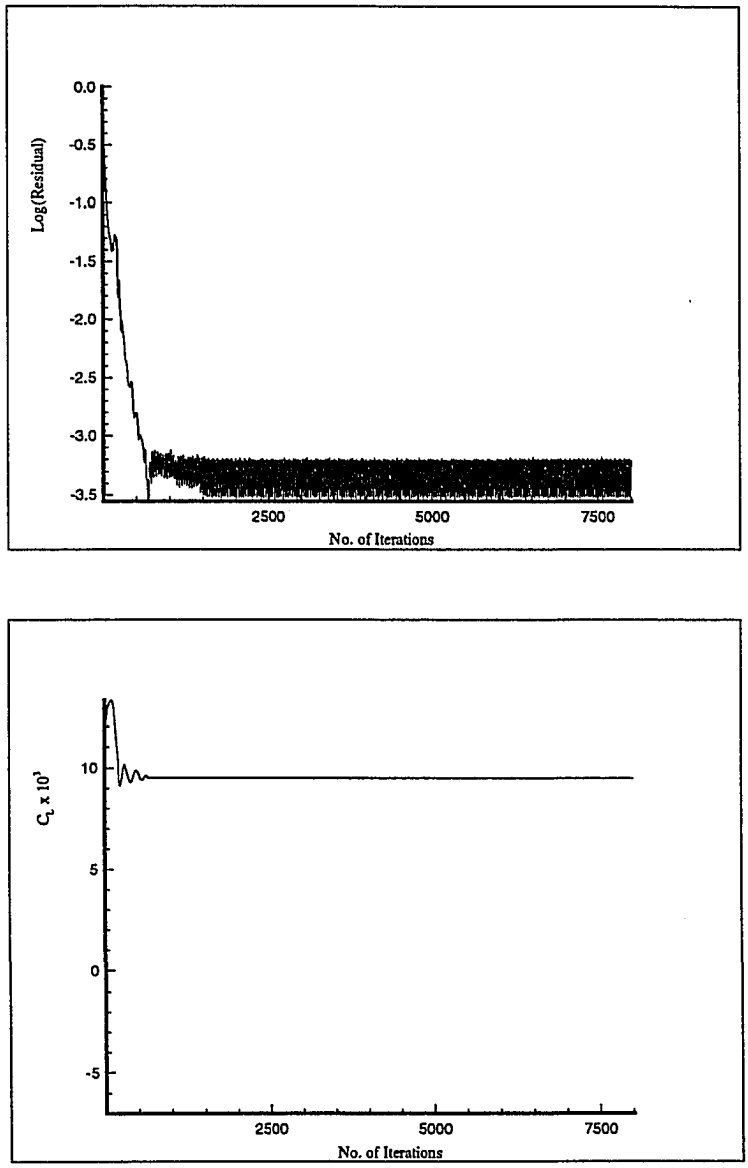

Figure 5.16: Residual, lift coefficient and side-force coefficient history of flow around circular cone at $\alpha = 50°$, $M_\infty = 1.8$, $R_e = 10^5$, $h = 0.4r$.

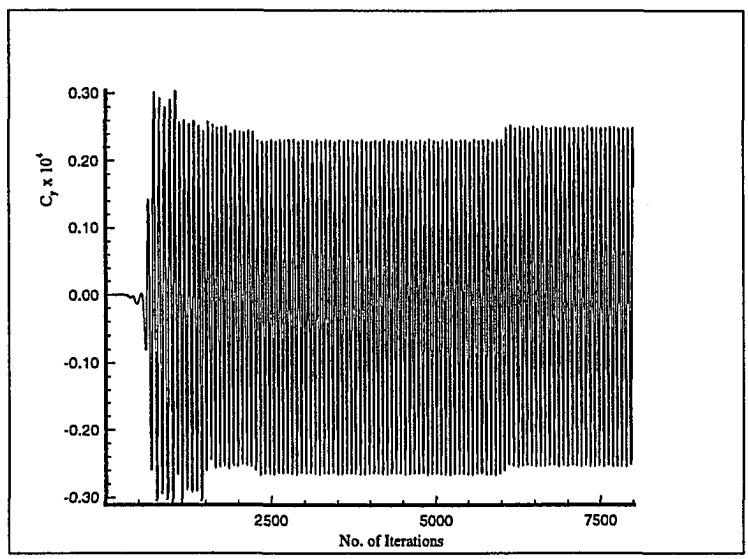

Figure 5.16: Continued

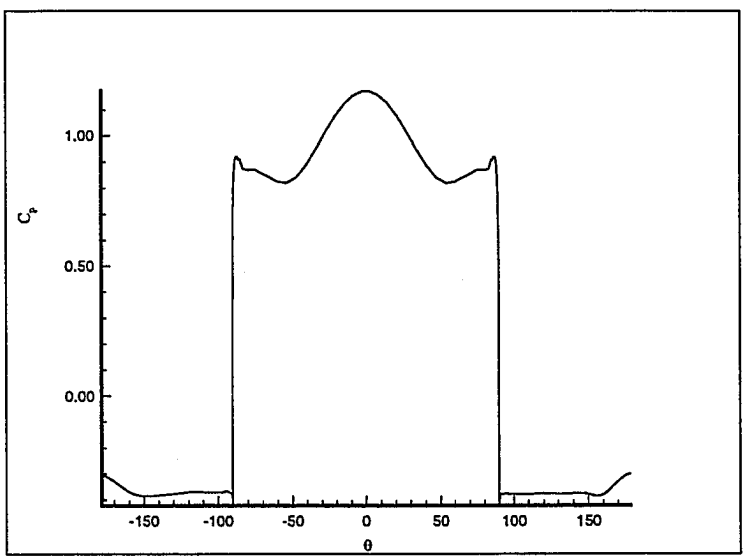

Figure 5.17: Surface pressure coefficient for flow around a circular cone at $\alpha = 50°$, $M_\infty = 1.8$, $R_e = 10^5$, $h = 0.4r$.

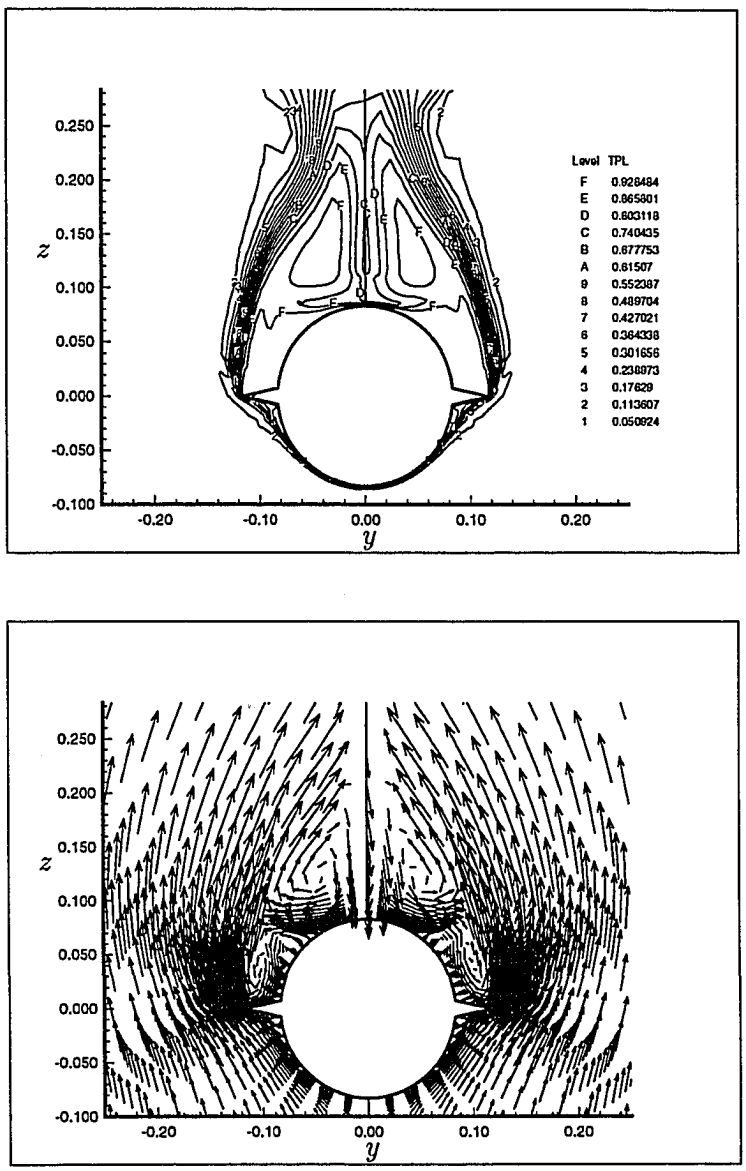

Figure 5.18: Total pressure loss contours, cross-flow velocity vectors and cross-flow streamlines for flow around a circular cone at $\alpha = 50°$, $M_\infty = 1.8$, $R_e = 10^5$, $h = 0.4r$.

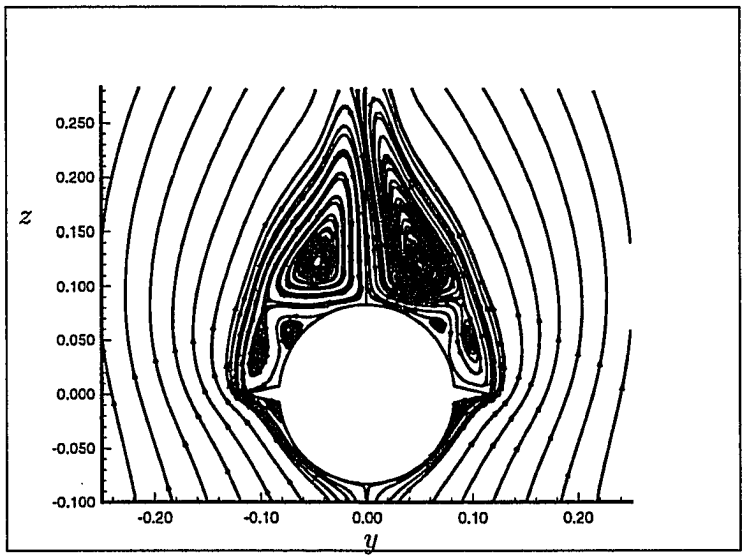

Figure 5.18: Continued

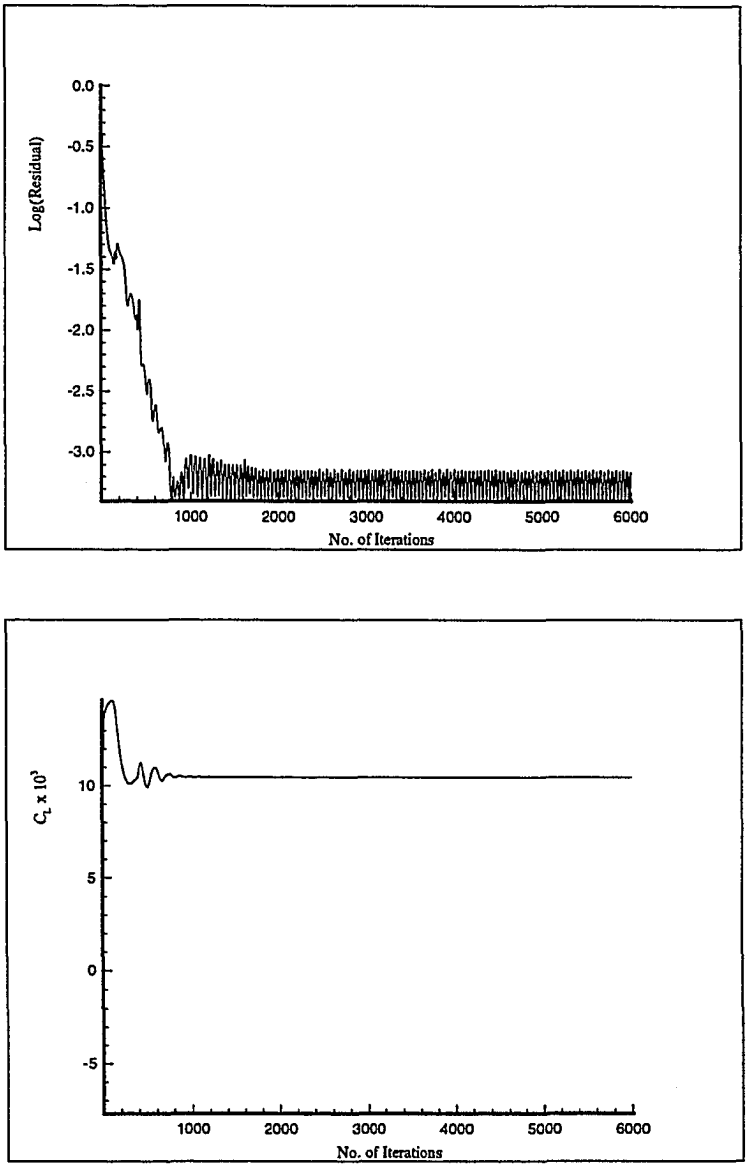

Figure 5.19: Residual, lift coefficient and side-force coefficient history of flow around circular cone at $\alpha = 50°$, $M_\infty = 1.8$, $R_e = 10^5$, $h = 0.5r$.

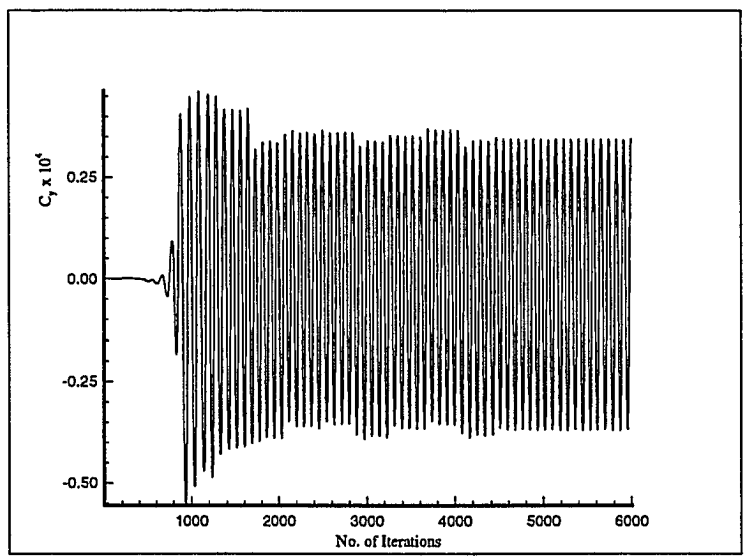

Figure 5.19: Continued

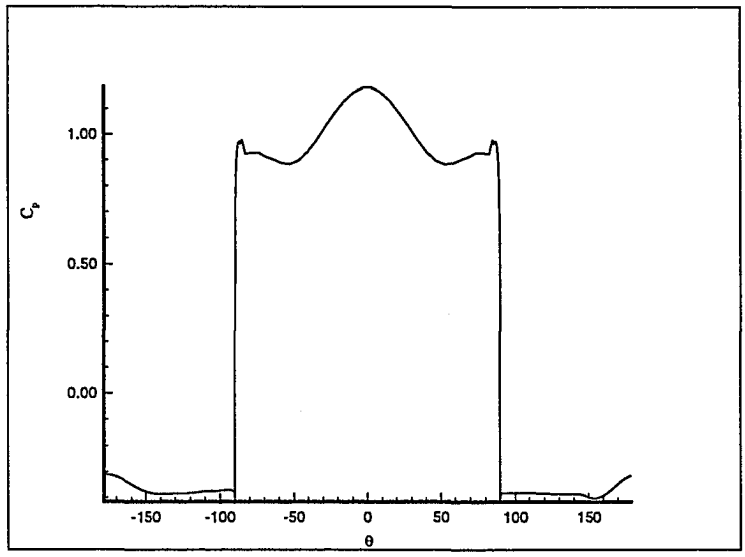

Figure 5.20: Surface pressure coefficient for flow around a circular cone at $\alpha = 50°$, $M_\infty = 1.8$, $R_e = 10^5$, $h = 0.5r$.

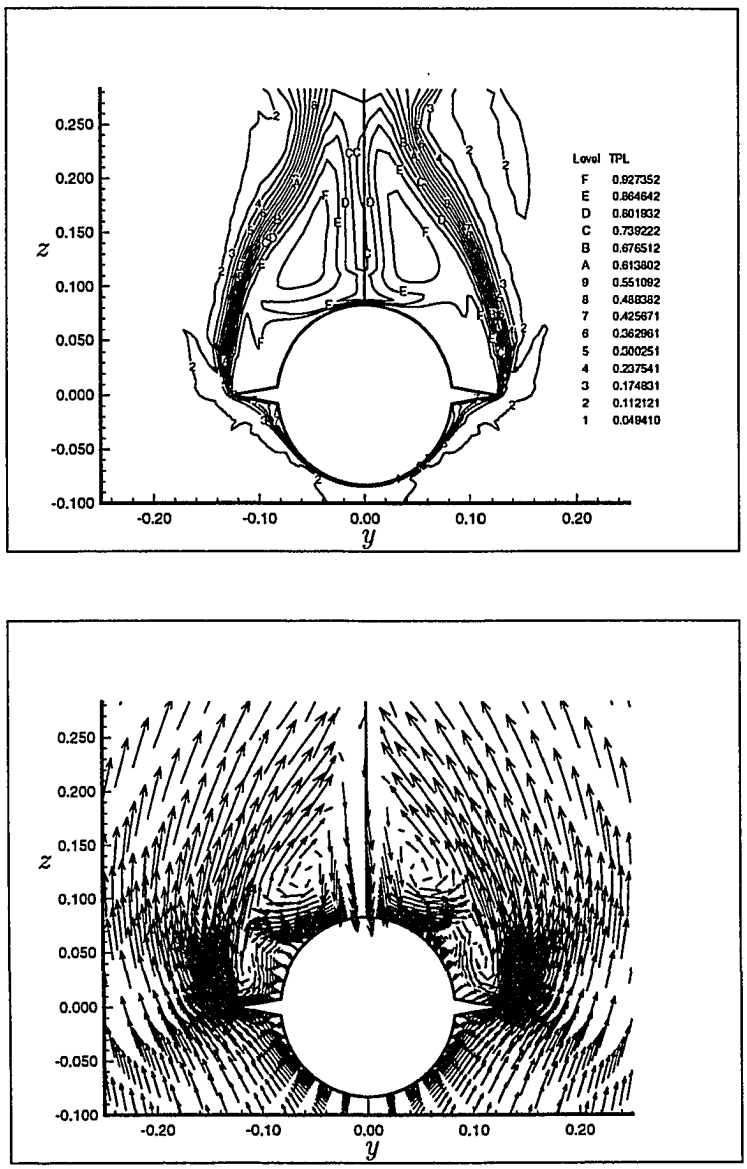

Figure 5.21: Total pressure loss contours, cross-flow velocity vectors and cross-flow streamlines for flow around a circular cone at $\alpha = 50°$, $M_\infty = 1.8$, $R_e = 10^5$, $h = 0.5r$.

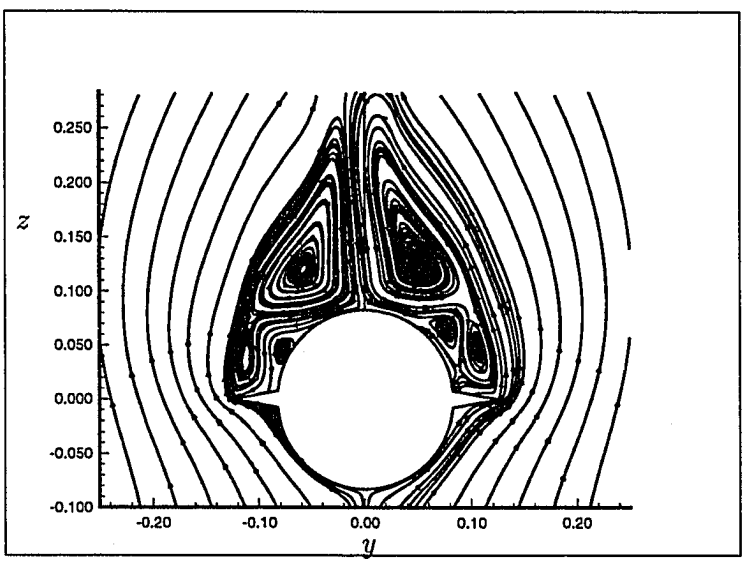

Figure 5.21: Continued

CHAPTER 6

ACTIVE CONTROL USING INJECTION AND HEATING

6.1 Introduction

When the asymmetry becomes detectable with increases in the AOA, the pressure distribution over the body surface becomes asymmetric and the suction pressure on one side of the body is larger than the other side. Passive control methods, in most cases, are applied equally on both sides and while these methods are effective in delaying the onset of asymmetry, they are not as effective in alleviating or eliminating the asymmetry, once it starts to appear. Meanwhile, active control methods can be applied whenever the asymmetry starts to appear.

The effect of asymmetric injection from the body surface is to add, in an uneven way, momentum to the flowfield. Also, the velocity at the body surface is no longer zero, which has a direct effect on the surface pressure and hence, on the side force 6.1. On the other hand, heating is a stabilizing factor, since the viscosity increases with temperature and hence, the disturbances that lead to the asymmetry die out.

In this chapter, the effect of two active control methods—injection and surface heating— is investigated. Injection control is applied in both the normal and tangential directions to the 5° semi-apex angle cone surface. Next, the surface heating control method is presented and followed by the use of hybrid injection-heating control. This part of the dissertation has been published in Refs. 21, 94.

The asymmetric flow reference case, which was presented in Sec. 5.2, is used to evaluate and investigate the effects of the various active control methods presented in this chapter. In all the cases, the grid used is the same one used in the reference case which is shown in Fig. 5.1. The initial solution used in this chapter is the solution obtained and described in Sec. 5.2.

6.2 Normal Injection Control

Injection is applied on the cone surface in the radial direction of the cone axis, i.e. normal to the circumference of the circular section of the cone. The mass flow rate per unit area, $\dot{m}$, (the nondimensional mass flow rate per unit area) is taken to be constant, and the injection is applied to the side of the cone with lower surface pressure. The choice of injection location is motivated by the vortex structure indicated in Fig. 5.3. The injection location is chosen to be on the side with the lower vortex location relative to the cone surface. The injection is expected to raise the vortex on that side and equalize the surface pressure to that on the other side, and hence alleviate or eliminate the side force.

6.2.1 Constant injection rate

In this section, the mass injection rate, $\dot{m}$, is chosen to be constant. $\dot{m}$ is the nondimensional mass flow rate per unit area. Three values of $\dot{m}$ ($\dot{m} = 0.01$, 0.02 and

0.03) are applied to investigate the effect of the mass injected. Also for $\dot{m} = 0.02$, the effect of the injection effective angle (the angle measured from the plane of geometric symmetry on the leeward side in the clockwise direction) is investigated.

The mass flow rate per unit area is taken to be constant ($\dot{m} = 0.01$) over the effective injection angle which extends from 0° to −67.5°. Figure 6.2 shows the effect of injection, for $\dot{m} = 0.01$, on the side force and lift coefficient when applied after 12,000 iterations. The level of the side force is decreased from -6.5×10^{-4} to about -3.8×10^{-4}. Simultaneously, the lift coefficient has experienced a relatively small drop of about 8%. Figure 6.3 shows the surface pressure coefficient for the same case. Comparing Fig. 6.3 with Fig. 5.3, we can see that the difference in the surface pressure on the two sides of the cone has decreased due to the constant injection on the left side of the cone. In Fig. 6.4, the total pressure loss contours, cross-flow velocity vectors and cross-flow streamlines are presented. Since the velocity is no longer zero at all the points on the body surface on the left side, some of the streamlines originate from the injection port locations, since this part of the surface is not a stream surface. The height of the vortex on the right side of the cone (where no injection occurs) is decreased and the vortex on the other side has diffused, due to the injection.

6.2.1.1 Effect of injection rate

The mass flow rate per unit area, $\dot{m}$, is increased to 0.02, i.e. double the previous case. In Figs 6.5, 6.6 and 6.7, the results are shown for this case. The higher injection is, as expected, more effective compared to the case with $\dot{m} = 0.01$. The distance between the primary vortex on the right side and the body surface has decreased while the vortex on the left side is diffused more than the diffusion in the previous case. The side force coefficient history shows that the side force in this case is smaller

(almost zero) compared to that of the previous case and the reference case with no control. Also, the lift coefficient has decreased more than for the previous case.

The last three figures in this subsection, Figs. 6.8, 6.9 and 6.10 show the results of the case with $\dot{m} = 0.03$. The effect of the injection is more pronounced and the observations of the last two cases are still valid. However, since the injection level is relatively high, the primary vortex on the right side is also raised above the body surface and the left-side vortex is entirely diffused. The lift coefficient drops to a level lower than that of the cases of $\dot{m} = 0.01$ and $\dot{m} = 0.02$, and the side force coefficient drops to almost a zero level.

6.2.1.2 Effect of effective injection angle

The effect of the effective injection angle, θ_i, is investigated in this subsection. Three values of θ_i are chosen to study such an effect. The injection is applied from the cone surface at all the points within θ_i range. In these three cases, while fixing the mass flow rate $\dot{m} = 0.02$, the effective injection angle has been chosen to be $\theta_i = 0°$ to $-45°$, $-67.5°$, $-90°$. The results of the cases of $\theta_i = 0°$ to $-45°$ and $90°$ are shown in Figs. 6.11-6.16.

While increasing the magnitude of the effective angle of injection, θ_i, from 67.5° to 90°, little effect is observed on the final level of the side force. The results with $\theta_i = -45°$, are surprising with the side force changing its sign and a new vortex structure appearing. This indicates that the mass flow rate is not the only factor but also the effective angle of the injection is an important parameter.

6.2.2 *Variable injection rate*

The results obtained in the last subsection in which a zero side force has been obtained while the flowfield is still asymmetric around the body, prompted an investigation searching for an optimum solution. The "optimum solution" was to devise some way to allow the flowfield to become symmetric or to eliminate the surface pressure difference between corresponding points on the two-sides of the body surface. Therefore, the idea of using a variable, $\dot{m}$, was considered and is applied in this section to examine such a possibility.

In this case, the circumferential range of injection ports is extended to cover a symmetric range of $\theta_i = -67.5°$ to $67.5°$. Moreover, the injected mass-flow rate per unit area, $\dot{m}$, is made proportional to the difference in the surface pressure between corresponding points on the right and left sides of the body (within $\theta_i = -67.5°$ to $67.5°$). The maximum injected mass-flow rate per unit area, $\dot{m}_{max}$, which corresponds to the maximum pressure difference is restricted to $\dot{m}_{max} = 0.03$. Practically, this control method can be achieved by sensing the pressure difference between the right and left ports, and using it as a feedback control in order to inject a mass-flow rate proportional to that pressure difference. This case has been run in a time accurate form with $\Delta t = 0.001$. To examine the time step effect, this case was run with smaller Δt and similar results were obtained.

Figure 6.17 shows the lift coefficient and the side-force coefficient versus the number of iterations. The iteration and time-accurate stepping history of Fig. 6.17 can be described as follows:

1. No control is applied until the 12,000 iteration step. Up to that point, pseudo time marching was used. Steady asymmetry evolves at the 2000th iteration step, and the residual reached machine zero at the 10,000th iteration step.

2. Time accurate solutions were used for 3,000 time steps with $\Delta t = 0.001$. No change in the solution was observed.

3. While keeping the AOA, α, fixed at 20°, the injection control method was applied for 6,000 time steps through which the asymmetric solution has been changed into a symmetric one.

4. The AOA was increased 2° after each 6000 time steps, until $\alpha = 30°$.

The corresponding history of the side force shows that the side force becomes zero at the end of 21,000 time steps. Snapshots of the evolution of the symmetric controlled flow solution at $\alpha = 20°$, in terms of the total pressure loss contours and velocity vectors are given in Figures 6.18 and 6.19. The vortical flow is rendered symmetric using the present method.

Snapshots of the total pressure loss contours and velocity vectors at different AOA ($\alpha = 22°$, 24°, 26° and 28°) are given in Figs. 6.20 and 6.21. When the AOA reaches 30°, normal injection control was incapable of achieving flow asymmetry. It is interesting to study the snapshots of the total pressure loss contours at different AOA. Moreover, it is noticed that the primary vortices grow in size in the normal direction and their inner boundaries approach each other. At $\alpha = 28°$, the inner boundaries of the primary vortices touch each other, and thereafter at $\alpha = 30°$, the primary vortices from the right and left sides become asymmetric. The asymmetric response of the primary vortices at $\alpha = 30°$ is believed to be due to a strong instability arising as a result of the strong interaction between the inner shear layers of the primary vortices.

At $\alpha = 30°$, the injected mass-flow rate in the normal direction to the body surface $\dot{m}$ is increased to 0.05, 0.06 and 0.07, in order to recover the flow symmetry. Figure 6.22 shows the results of these tests. Both the total pressure loss contours and the surface pressure coefficient curves show that the flow is asymmetric and

the side force does not vanish. It is also observed that the flow asymmetry changes from the right side to the left, as does the side force. Therefore, it is apparent that normal-injection control loses its effectiveness when the AOA approaches 30° for the conditions considered.

6.3 *Tangential Injection Control*

In this case, the circular section of the lower portion of the cone has a radius larger than that of the upper portion. The lower local radius is 1.05 that of the upper one. Flow is injected from the lip of the lower portion in the direction tangent to the surface of the upper portion. The maximum mass flow rate, $\dot{m}_{max}$ is taken to be 0.2 and the velocity profile at the lip exit is assumed to be parabolic. Figure 6.23 shows the grid used for the thin layer computations. Three grid blocks are used for the present computation. The first block is $121 \times 19 \times 2$, the second is $121 \times 63 \times 2$ and the third is $121 \times 63 \times 2$ all in the circumferential, normal and axial directions, respectively. Injection is applied asymmetrically, i.e. the injection is applied on one of the two sides at each time step, depending on the surface pressure difference between corresponding points on the left and right sides of the cone—similar to the normal injection case.

Since the geometric configuration has changed from that of the reference case, the solution for the present case is summarized as follows:

1. No control is applied until the 12,000th iteration step. Up to this point, pseudo time marching is used. Steady asymmetric flow is observed at the 2000th iteration step and the residual reaches machine zero at the 10,000th iteration step. The level of asymmetry is higher than the reference case and the side force coefficient has a value of 14.0×10^{-4} at steady state.

2. Time accurate solutions were used for 3,000 time steps with $\Delta t = 0.001$. No changes in the solution were observed.

3. While keeping the AOA, α, fixed at 20°, the injection control method was applied for 5,000 time steps with $\dot{m}_{max} = 0.05$, which reduced the level of asymmetry by about 7%.

4. Increasing the injection level $\dot{m}_{max}$ to 0.1 for 4000 time steps reduced the side force by almost another 7%. Again, the increase in $\dot{m}_{max}$ to 0.15 proved to be insufficient to reduce the side force substantially.

5. Then, $\dot{m}_{max}$ was increased to 0.2 which was found to be the optimum value for the injection to reduce the side force to about 7% of its original value. Up to this point the AOA was maintained at 20°.

6. The AOA was increased by 1° each 2000 time steps, until $\alpha = 31°$.

Figures 6.24 and 6.25 show the total pressure loss contours and velocity vectors at different AOA. With the increase in the AOA, the sizes of the primary vortices increased and when the two vortices began to overlay, an instability started to grow and the flow lost its symmetry.

6.4 Surface Heating Control

By heating the surface of the body, the temperature of the flowfield near the body was increased and hence, viscosity was increased according to Sutherland's law. The increase in the viscosity acted as a damping factor to disturbances in the flowfield. To utilize such an idea for flow control, isothermal boundary conditions were used on the body surface, replacing the adiabatic boundary condition that had been used in all the cases mentioned earlier.

Figure 6.26 shows the lift and side force coefficients versus the number of iterations for the case where the left side of the body ($-180° < \theta_h < 0°$) surface was heated to 5 times the freestream temperature, T_∞, starting at the 12001 iteration step for 6000 iteration steps. Then, the left-side temperature was raised to $7T_\infty$. Again, the initial solution for the present case is the reference case obtained in section 5.2. The new boundary condition was applied while keeping the AOA constant at 20°. The side-force curve shows that the side force decreases as the temperature increases until it vanishes. Although the side force is zero, the vortical flow is still asymmetric. Lower values of heating were ineffective in alleviating the side forces.

6.5 *Hybrid Heating-Injection Control*

In the hybrid control method, two or more control methods are applied simultaneously to extend their range of effectiveness. Since both surface heating control and normal injection control are found to be effective within certain AOA ranges, hybrid heating-injection control was applied to extend the symmetric-flow AOA range.

In this case, surface heating control was followed by normal-injection control. Figures 6.28, and 6.29 show the results of this study. The control process is applied as follows. First, the whole surface is heated to $T_s = 5T_\infty$ and the heating starts at $\alpha = 20°$, where the number of iterations was 12,000. Next, the AOA was increased 4° and the symmetric flow was recovered after 18,000 iterations. Then, the AOA was increased 2° after each 1,000 iterations, until an AOA of 38° is achieved. Flow symmetry has been recovered continuously until the AOA reached 36°, where a slight flow asymmetry appeared in the solution. At $\alpha = 38°$, the flow asymmetry became stronger and heating control was ineffective for $T_s = 5T_\infty$.

At $\alpha = 38°$, normal-injection control was applied with $\dot{m}_{max} = 0.05$ and $\theta_i = -67.5°$ to 67.5°. The AOA was then increased in 2° increments after each 3,000

iterations. The history of the residual and the side force coefficient is shown in Fig. 6.28. Figure 6.29 shows snapshots of the total pressure loss contours and surface pressure coefficient curves at $\alpha = 38°$, $40°$ and $42°$. Although the total pressure loss contours show asymmetric flows, the surface pressure coefficient curves show symmetry resulting in zero side forces. Thus it is concluded that a hybrid control of heating and normal injection is very effective in eliminating the side force at very high AOA.

6.6 Summary

In this chapter, the effectiveness of the different active control methods on the flow asymmetry was investigated. Uniform injection was effective in eliminating the side force at the angle of attack considered ($\alpha = 20°$), but the flowfield was found to be sensitive to the effective injection angle and the mass flow rate. Normal injection was found to be effective in eliminating the side force when a constant mass flow rate (per unit area) was used. When the pressure difference between the right and left sides of the cone was used as a means to determine the injection location, not only the side force vanished but the flowfield became symmetric. Tangential injection was found to have a similar effect to that of normal injection, but with lower mass flow rates. Injection control lost its effectiveness when the AOA exceeded 30°. Surface heating control was found to be effective in an AOA range larger than that of the injection. Surface heating followed by normal injection was found to be the most effective control method for AOA up to 42°.

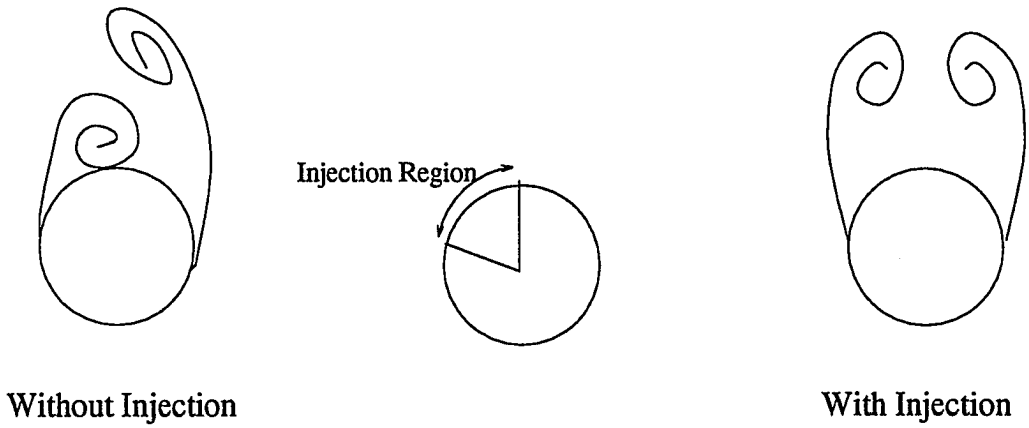

Figure 6.1: Injection effect on flow asymmetry

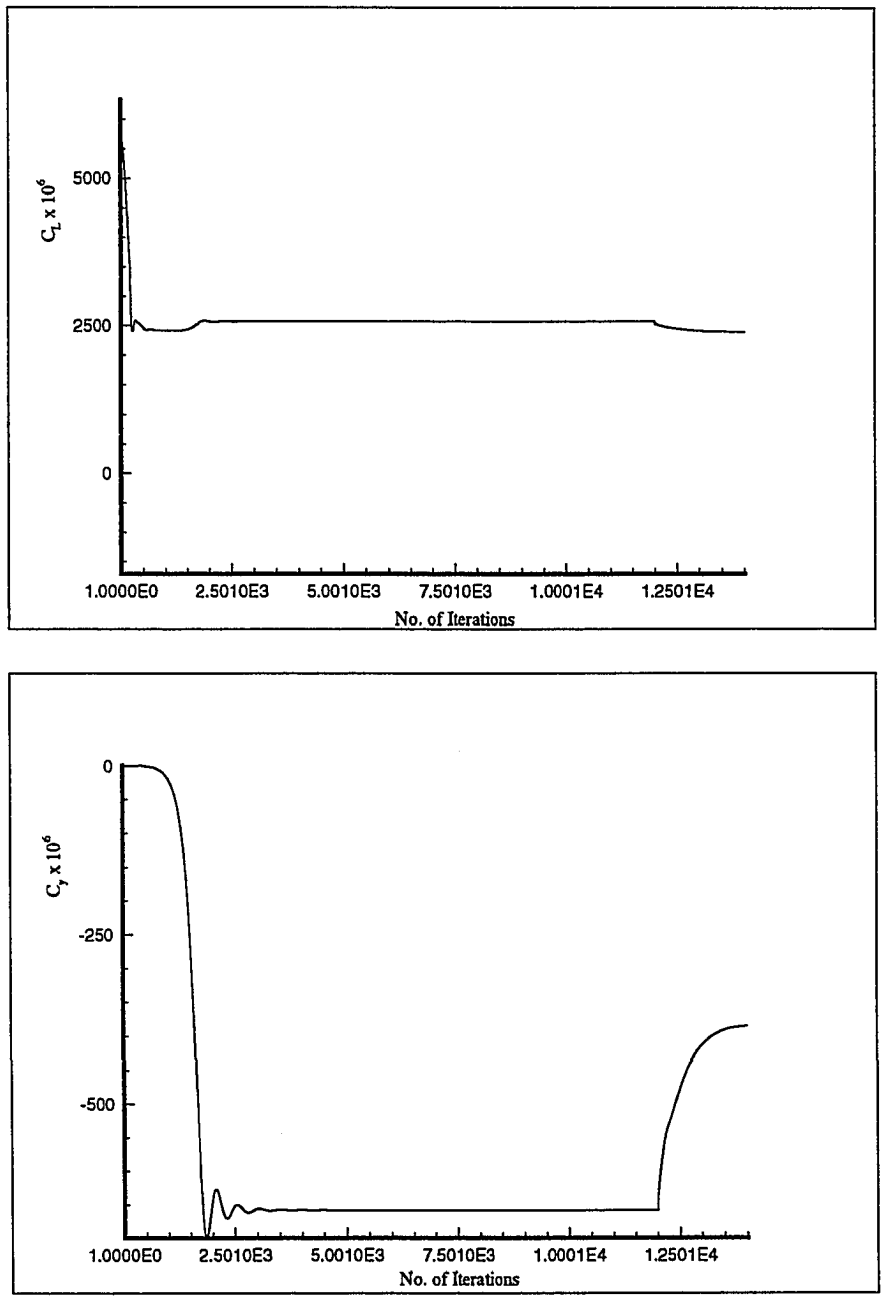

Figure 6.2: Lift coefficient and side-force coefficient history for a circular cone with normal injection control at $\alpha = 20°$, $M_\infty = 1.8$, $R_e = 10^5$, $\dot{m} = 0.01$, $\theta_i = -67.5° \rightarrow 0°$.

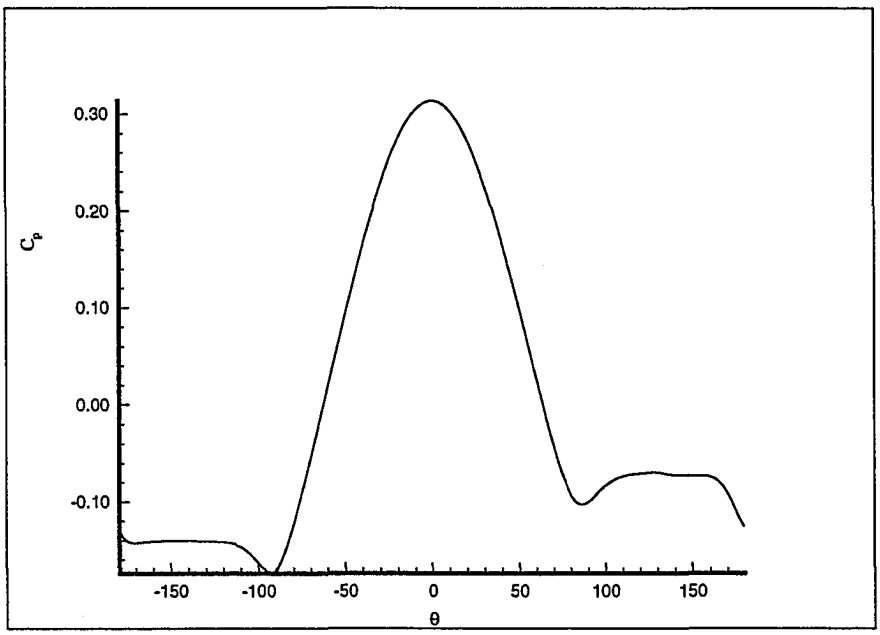

Figure 6.3: Surface pressure coefficient for flow around a circular cone with normal injection control at $\alpha = 20°$, $M_\infty = 1.8$, $R_e = 10^5$, $\dot{m} = 0.01$, $\theta_i = -67.5° \rightarrow 0°$.

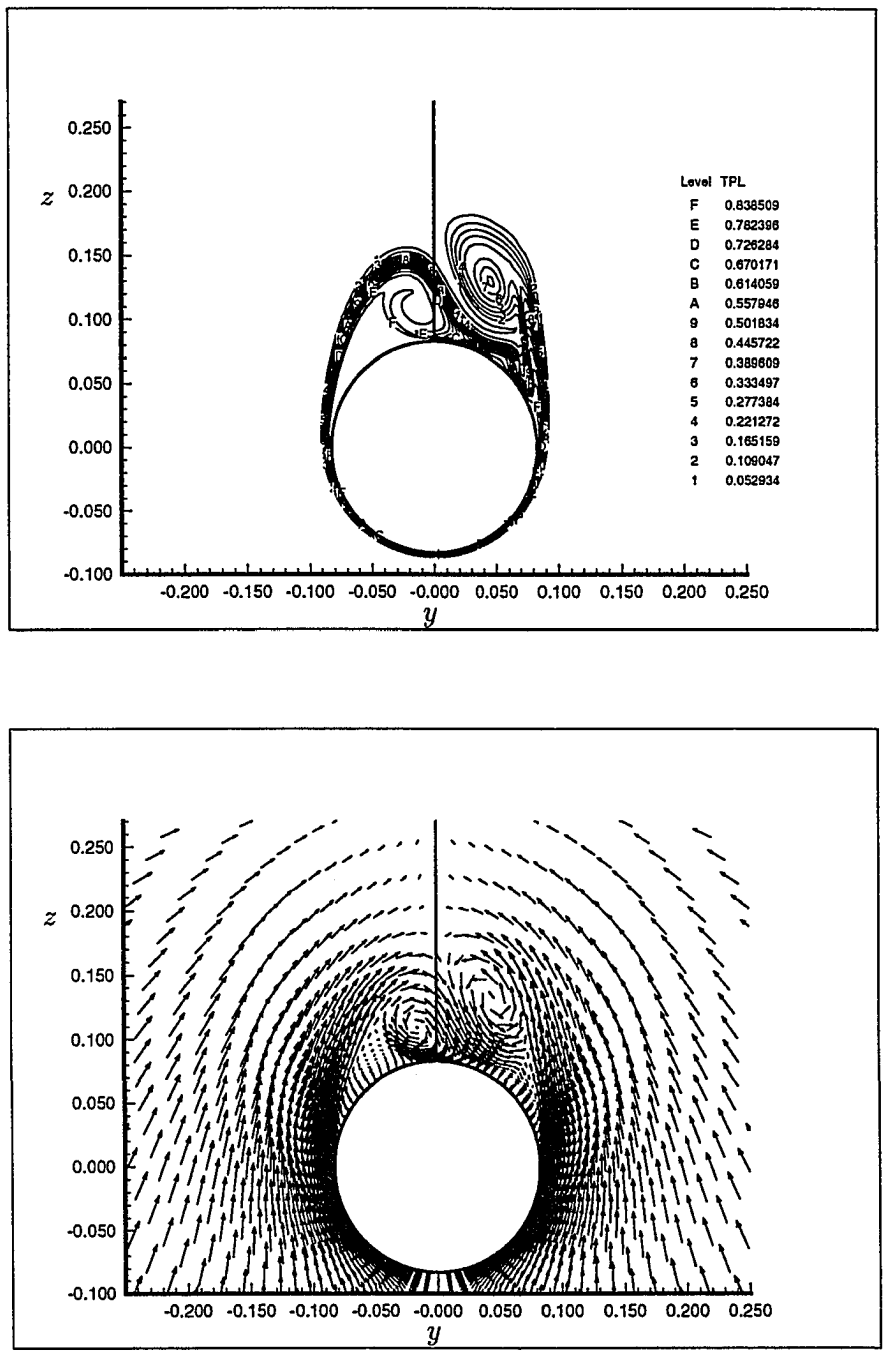

Figure 6.4: Total pressure loss contours, cross-flow velocity vectors, and cross-flow streamlines for a circular cone with normal injection control at $\alpha = 20°$, $M_\infty = 1.8$, $R_e = 10^5$ $\dot{m} = 0.01$, $\theta_i = -67.5° \rightarrow 0°$.

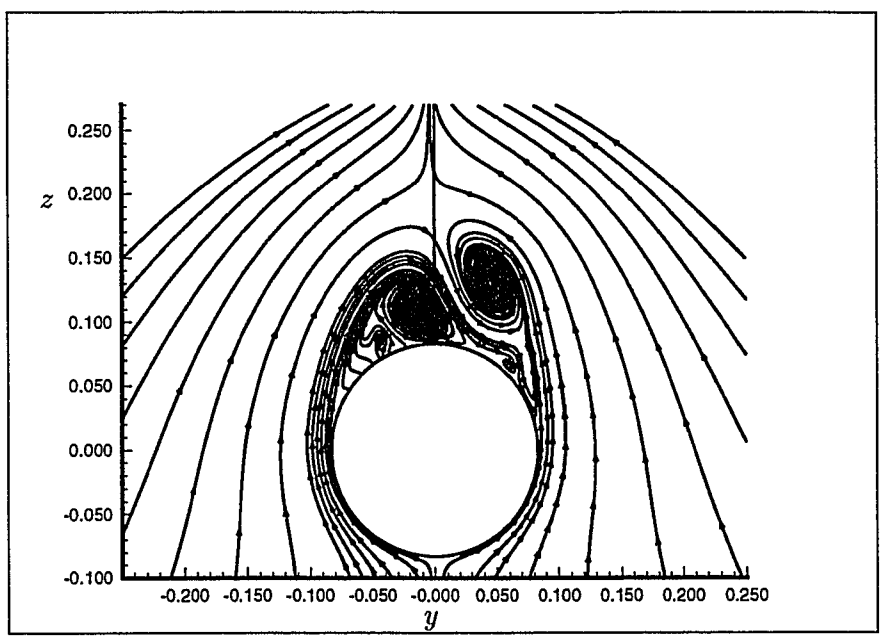

Figure 6.4: Continued

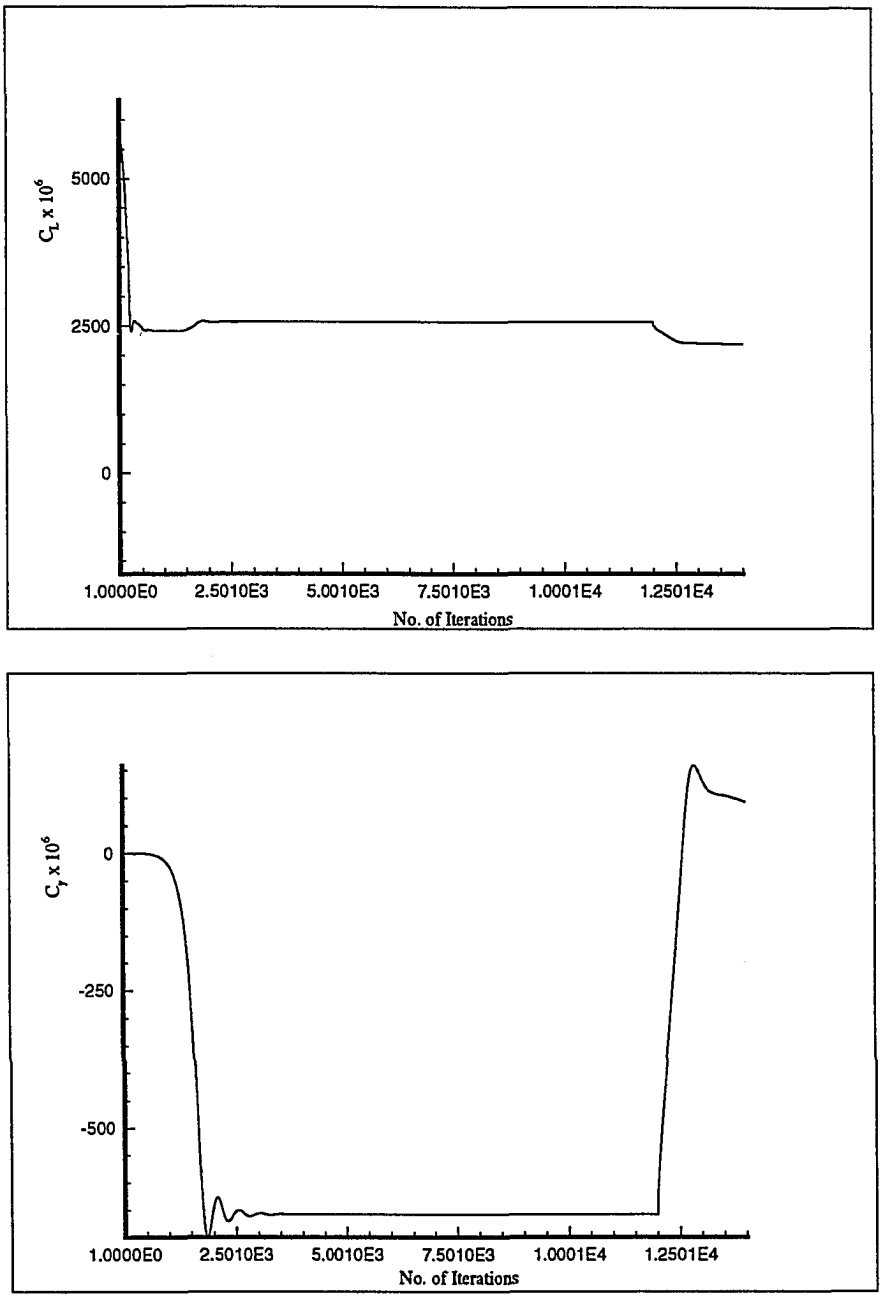

Figure 6.5: Lift coefficient and side-force coefficient history for a circular cone with normal injection control at $\alpha = 20°$, $M_\infty = 1.8$, $R_e = 10^5$, $\dot{m} = 0.02$, $\theta_i = -67.5° \rightarrow 0°$.

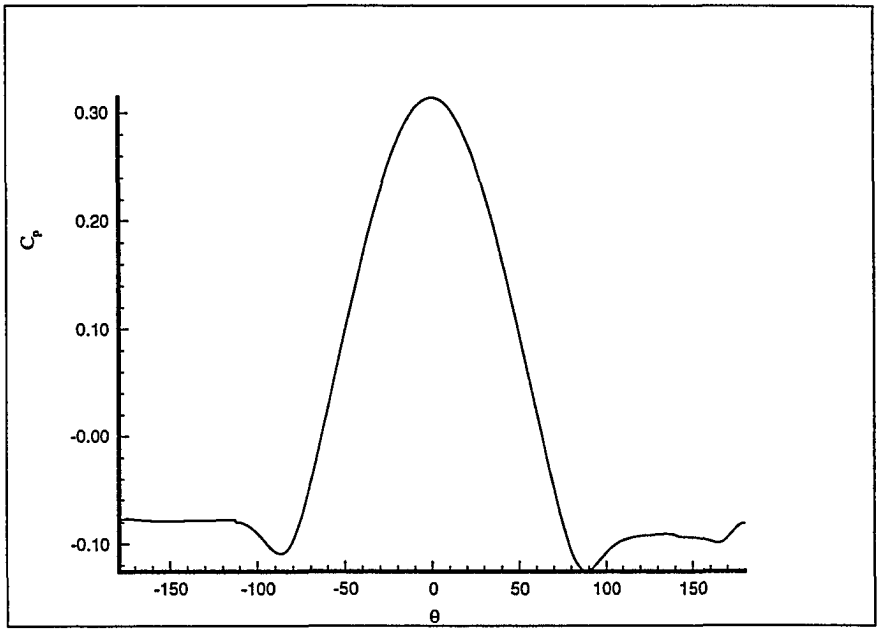

Figure 6.6: Surface pressure coefficient for flow around a circular cone with normal injection control at $\alpha = 20°$, $M_\infty = 1.8$, $R_e = 10^5$, $\dot{m} = 0.02$, $\theta_i = -67.5° \rightarrow 0°$.

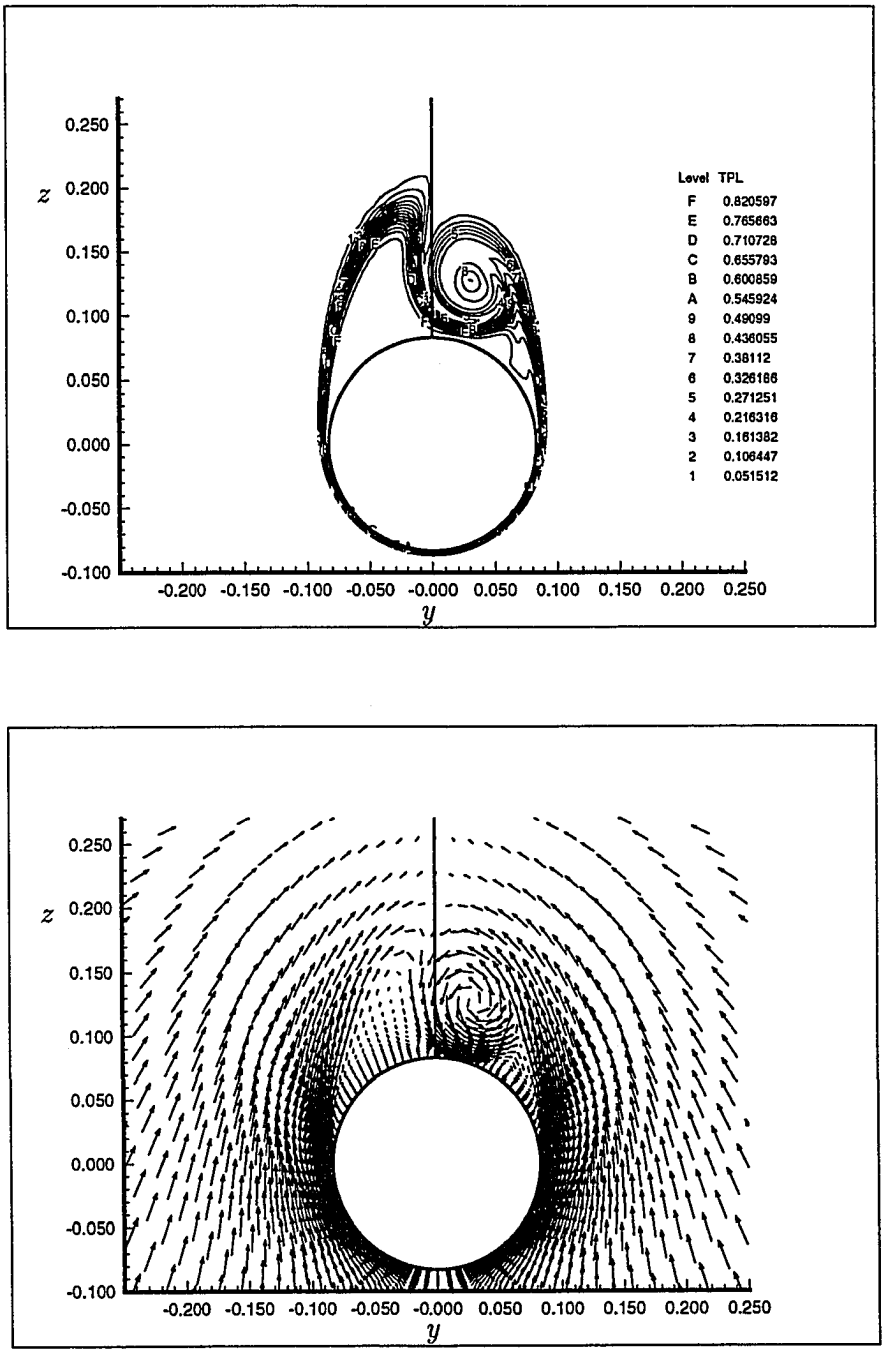

Figure 6.7: Total pressure loss contours, cross-flow velocity vectors, and cross-flow streamlines for a circular cone with normal injection control at $\alpha = 20°$, $M_\infty = 1.8$, $R_e = 10^5$ $\dot{m} = 0.02$, $\theta_i = -67.5° \rightarrow 0°$.

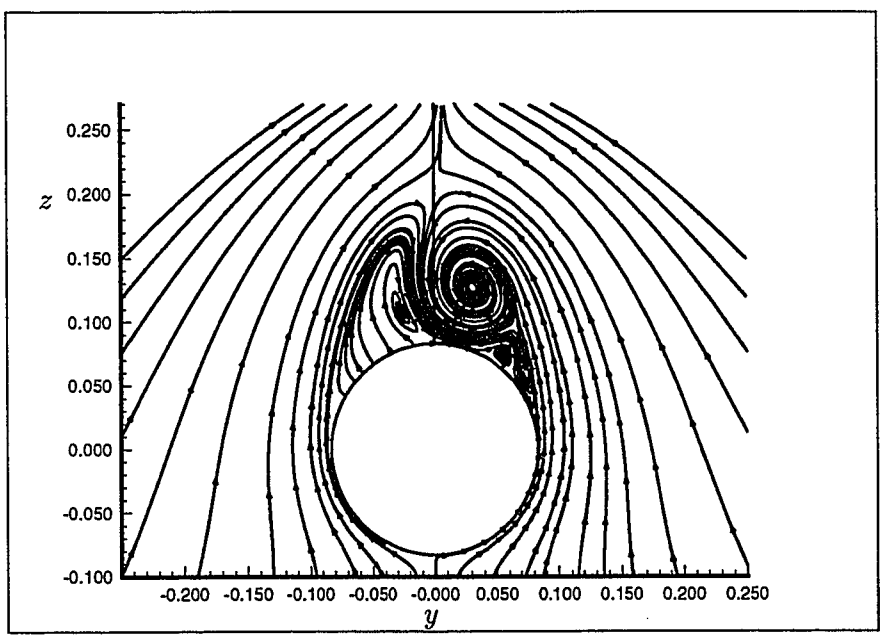

Figure 6.7: Continued

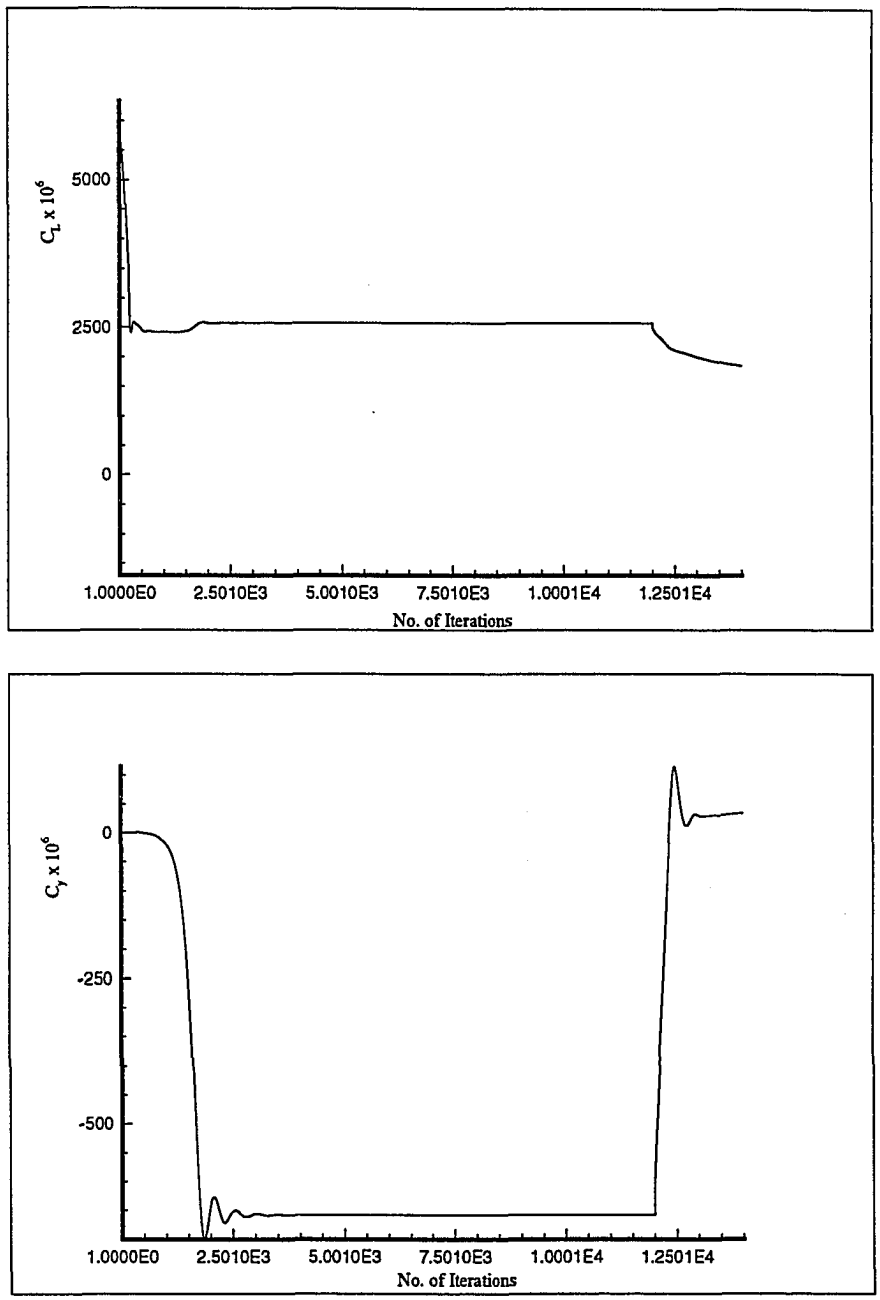

Figure 6.8: Lift coefficient and side-force coefficient history for a circular cone with normal injection control at $\alpha = 20°$, $M_\infty = 1.8$, $R_e = 10^5$, $\dot{m} = 0.03$, $\theta_i = -67.5° \rightarrow 0°$.

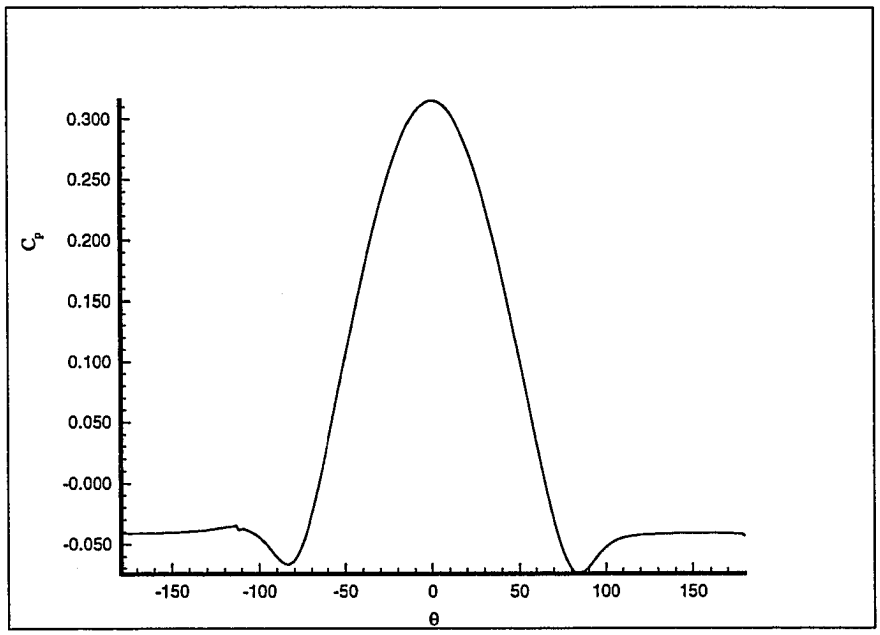

Figure 6.9: Surface pressure coefficient for flow around a circular cone with normal injection control at $\alpha = 20°$, $M_\infty = 1.8$, $R_e = 10^5$, $\dot{m} = 0.03$, $\theta_i = -67.5° \rightarrow 0°$.

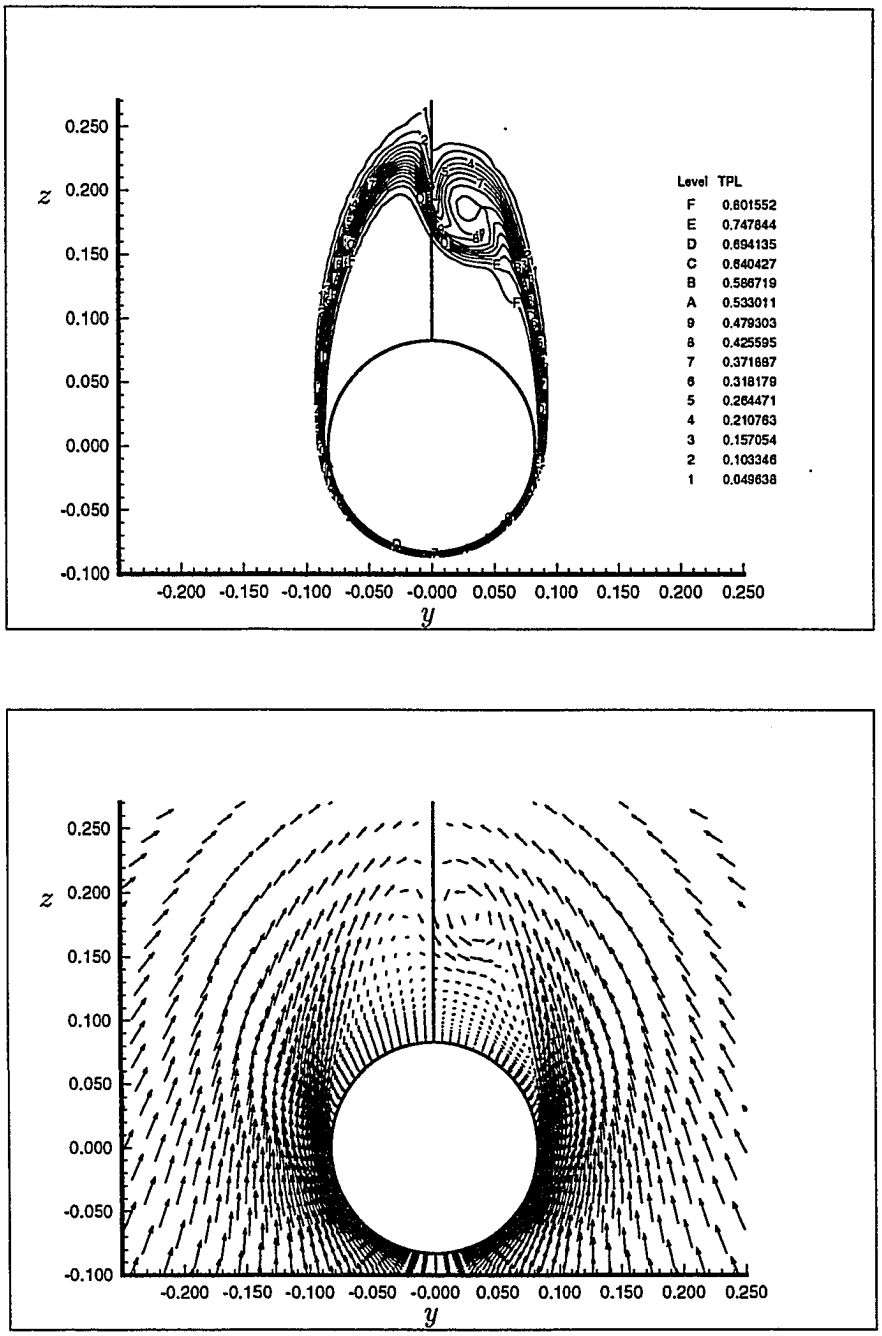

Figure 6.10: Total pressure loss contours, cross-flow velocity vectors, and cross-flow streamlines for a circular cone with normal injection control at $\alpha = 20°$, $M_\infty = 1.8$, $R_e = 10^5$ $\dot{m} = 0.03$, $\theta_i = -67.5° \rightarrow 0°$.

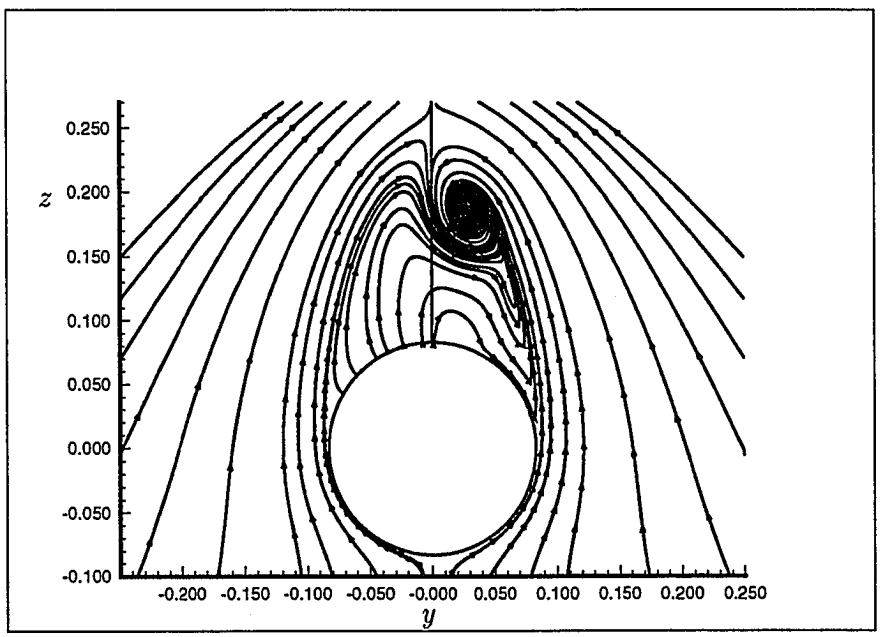

Figure 6.10: Continued

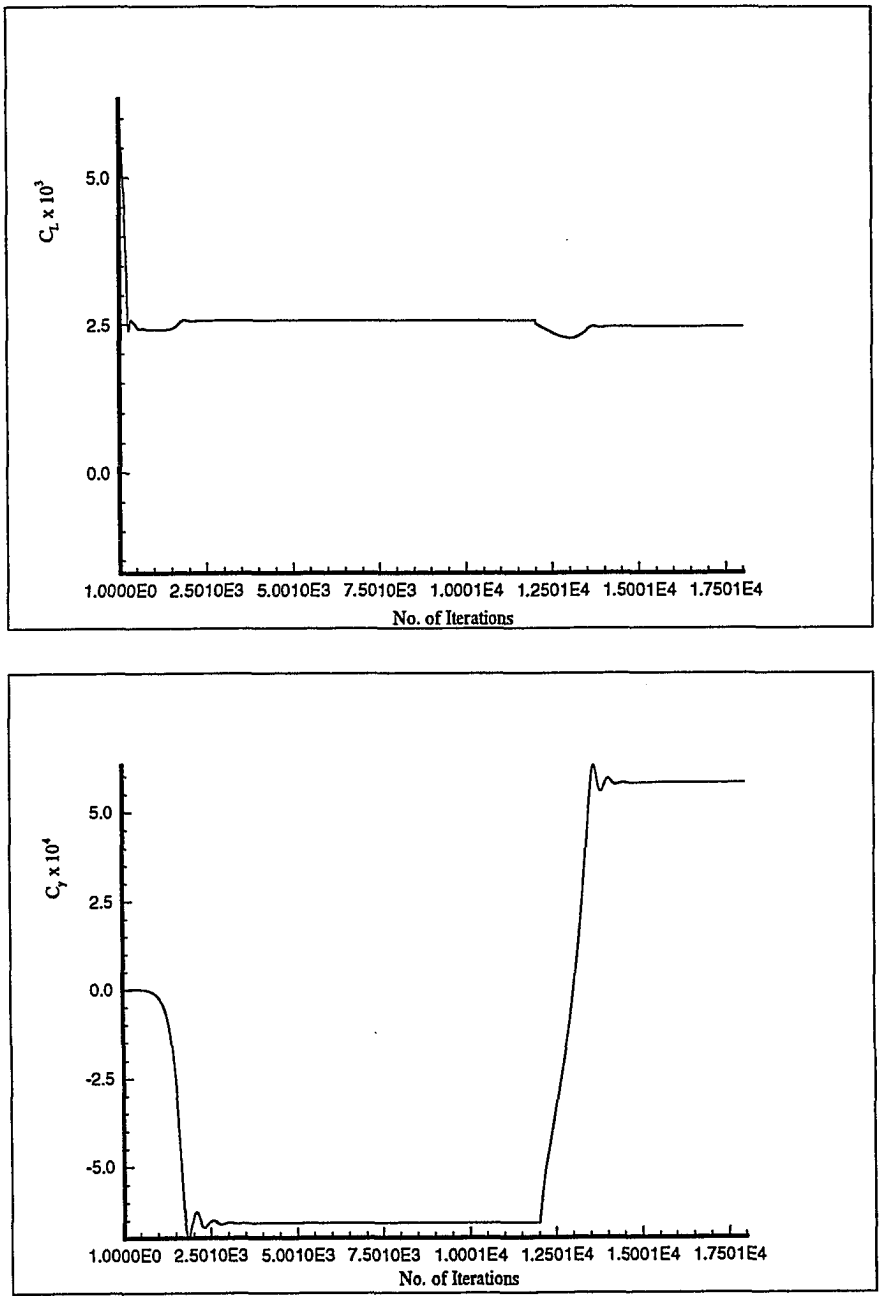

Figure 6.11: Lift coefficient and side-force coefficient history for a circular cone with normal injection control at $\alpha = 20°$, $M_\infty = 1.8$, $R_e = 10^5$, $\dot{m} = 0.03$, $\theta_i = -45° \rightarrow 0°$.

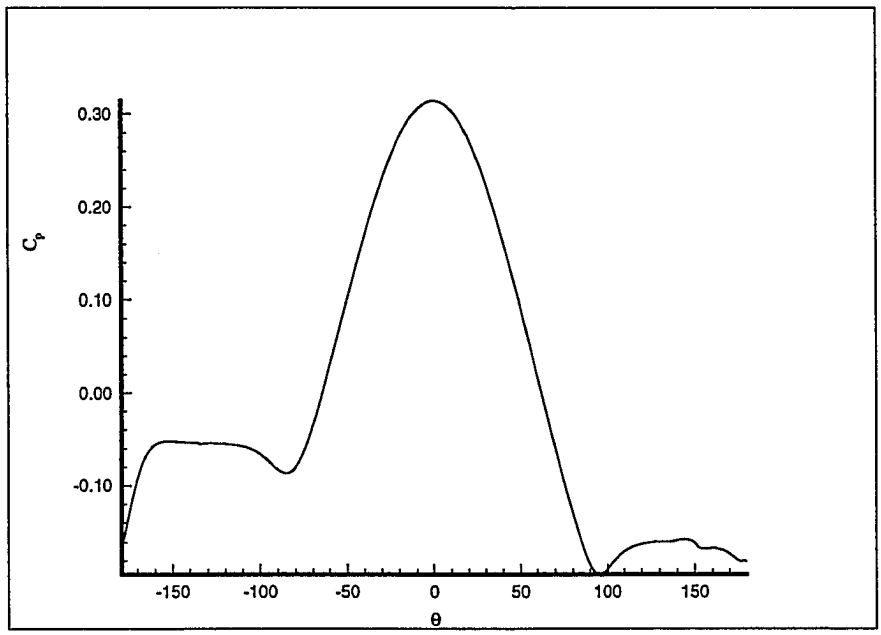

Figure 6.12: Surface pressure coefficient for flow around a circular cone with normal injection control at $\alpha = 20°$, $M_\infty = 1.8$, $R_e = 10^5$, $\dot{m} = 0.03$, $\theta_i = -45° \rightarrow 0°$.

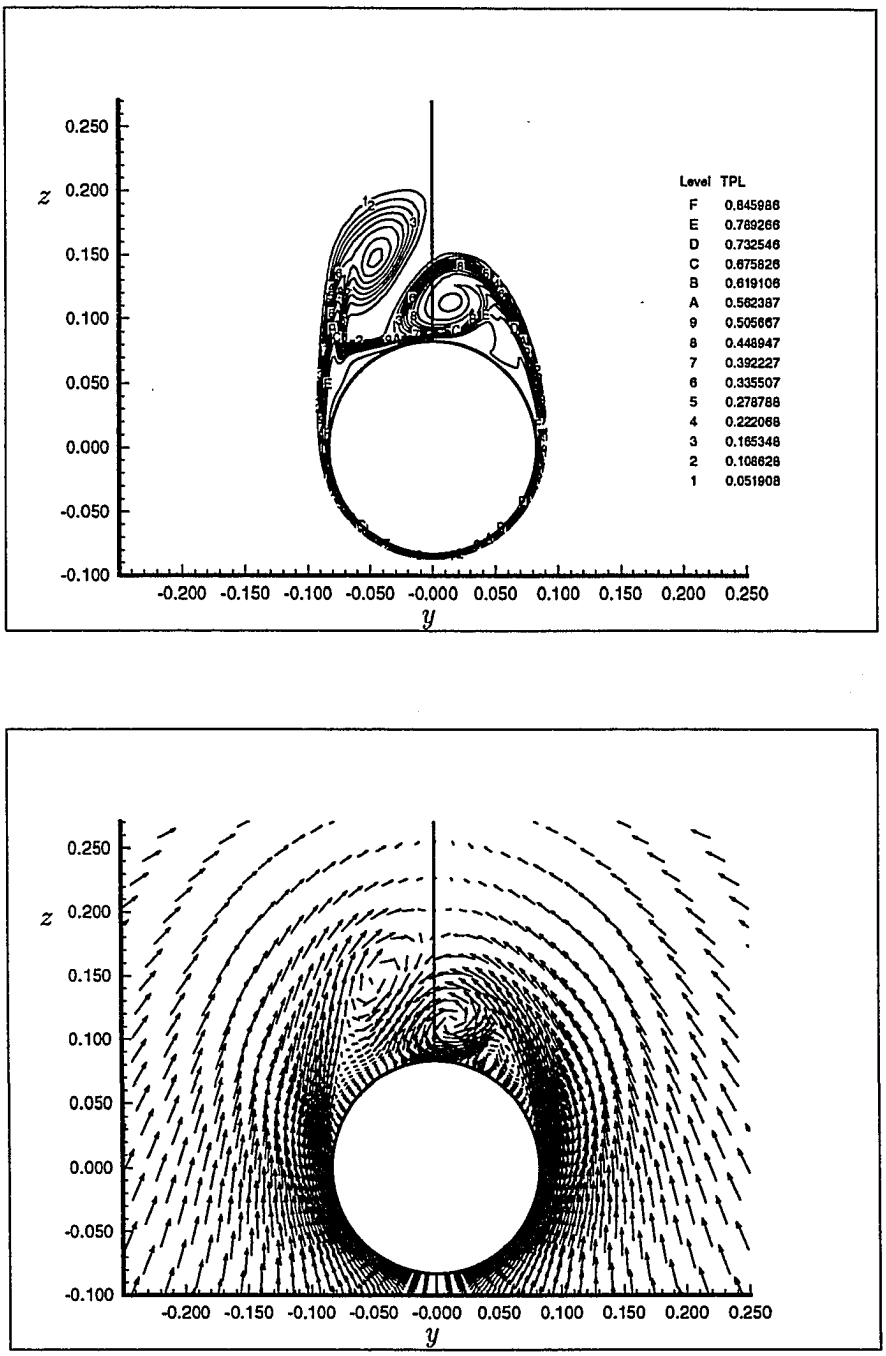

Figure 6.13: Total pressure loss contours, cross-flow velocity vectors, and cross-flow streamlines for a circular cone with normal injection control at $\alpha = 20°$, $M_\infty = 1.8$, $R_e = 10^5$ $\dot{m} = 0.03$, $\theta_i = -45° \rightarrow 0°$.

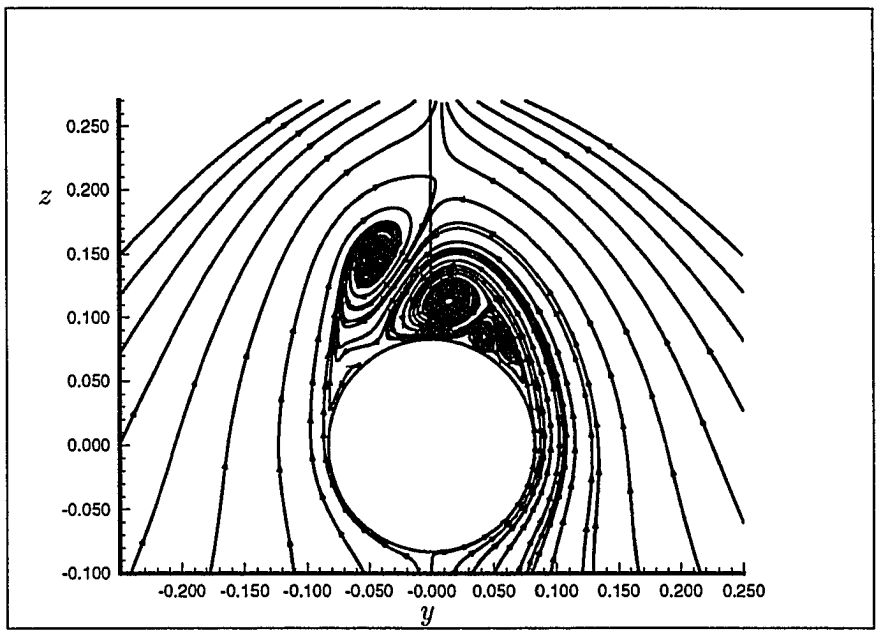

Figure 6.13: Continued

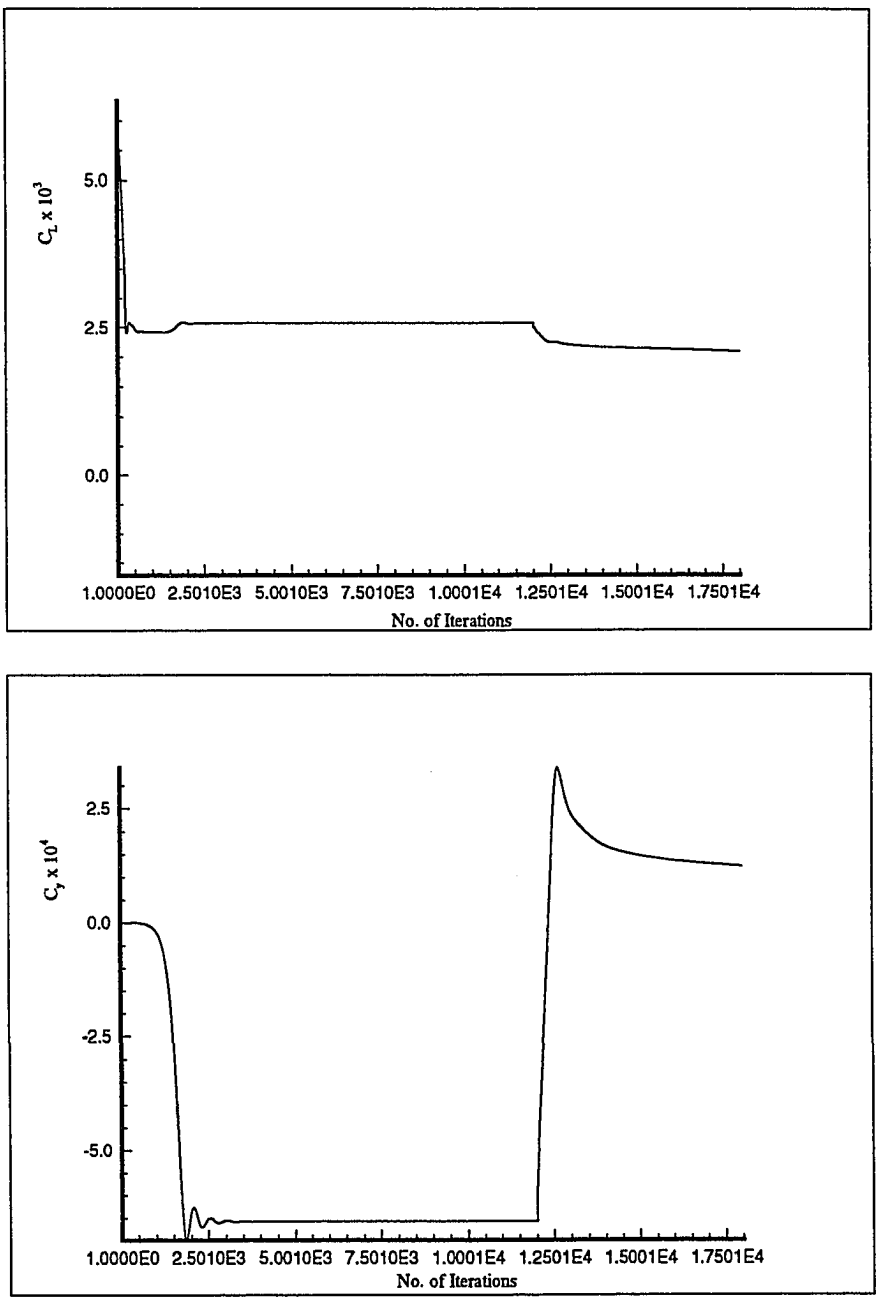

Figure 6.14: Lift coefficient and side-force coefficient history for a circular cone with normal injection control at $\alpha = 20°$, $M_\infty = 1.8$, $R_e = 10^5$, $\dot{m} = 0.02$, $\theta_i = -90° \rightarrow 0°$.

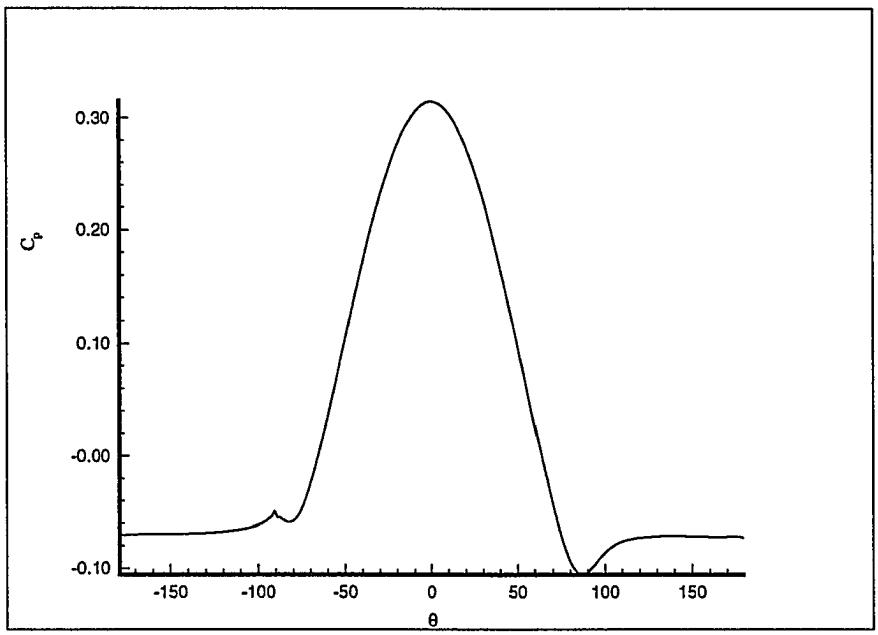

Figure 6.15: Surface pressure coefficient for flow around a circular cone with normal injection control at $\alpha = 20°$, $M_\infty = 1.8$, $R_e = 10^5$, $\dot{m} = 0.02$, $\theta_i = -90° \rightarrow 0°$.

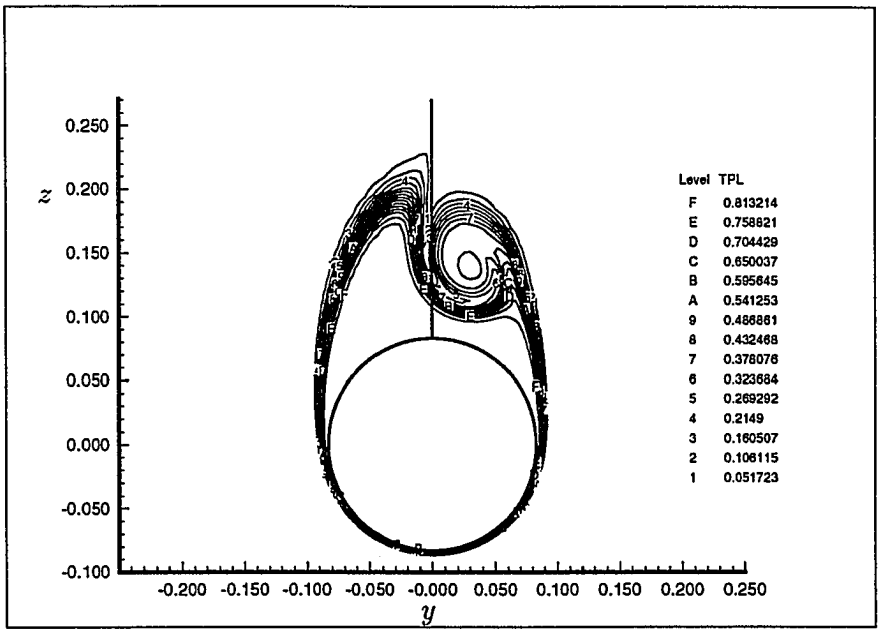

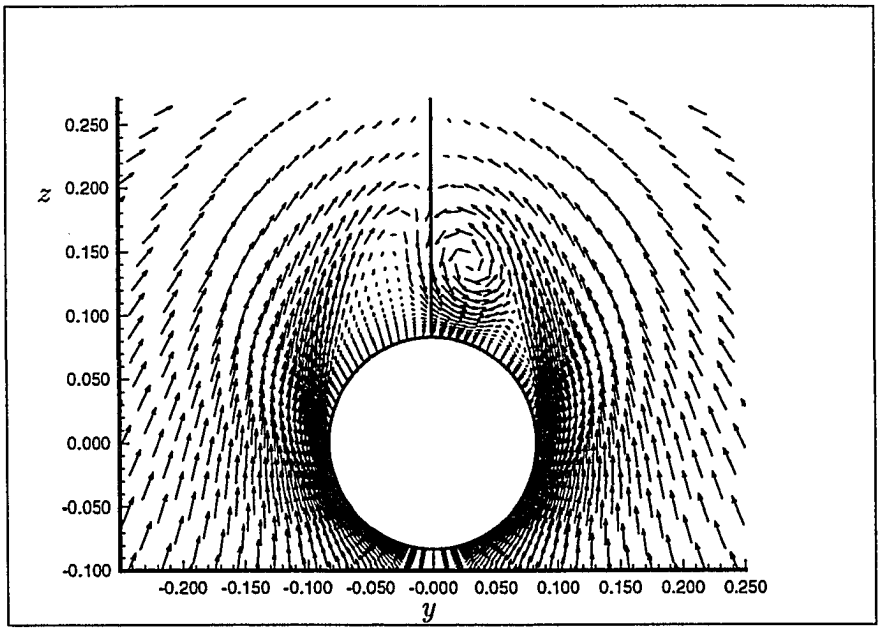

Figure 6.16: Total pressure loss contours, cross-flow velocity vectors, and cross-flow streamlines for a circular cone with normal injection control at $\alpha = 20°$, $M_\infty = 1.8$, $R_e = 10^5$ $\dot{m} = 0.02$, $\theta_i = -90° \rightarrow 0°$.

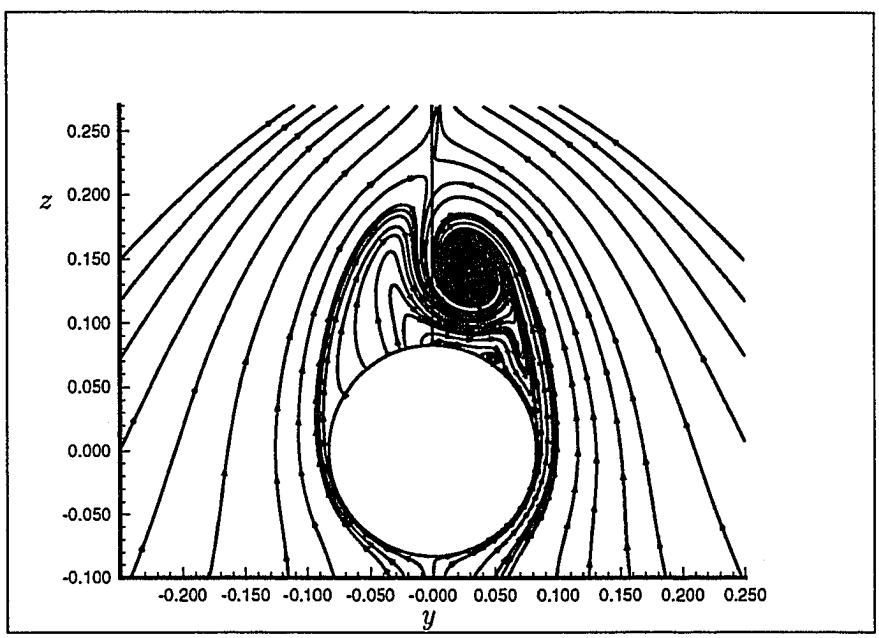

Figure 6.16: Continued

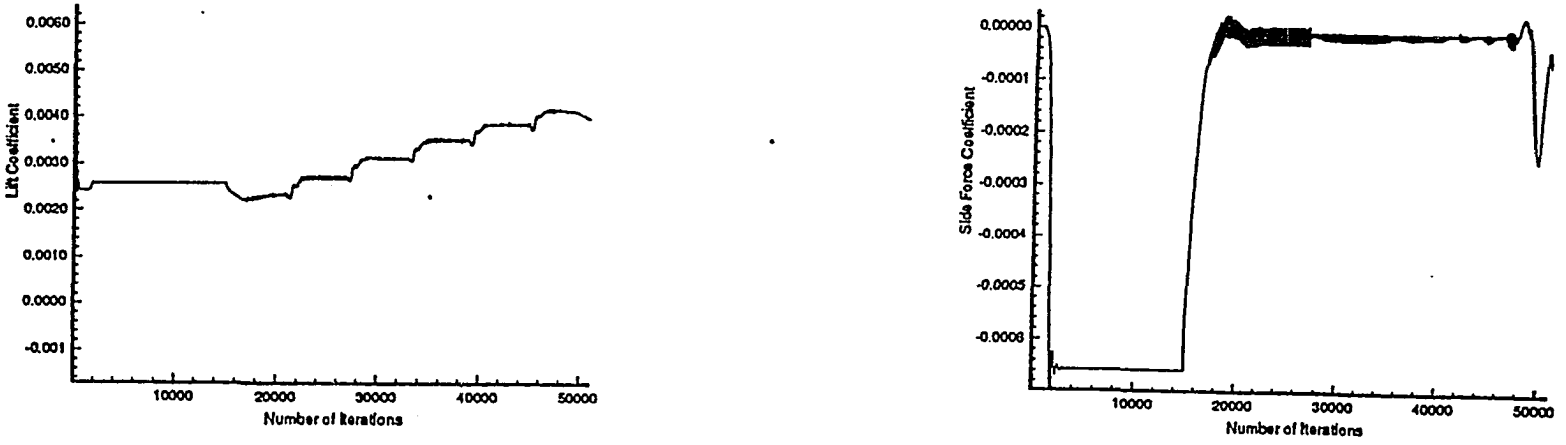

Figure 6.17: Lift and side-force coefficient versus number of time steps for a circular cone with normal injection control at $\alpha = 20° \rightarrow 30°$, $M_\infty = 1.8$, $R_e = 10^5$, $\dot{m}_{max} = 0.03$, $\theta_i = -67.5° \rightarrow 67.5°$.

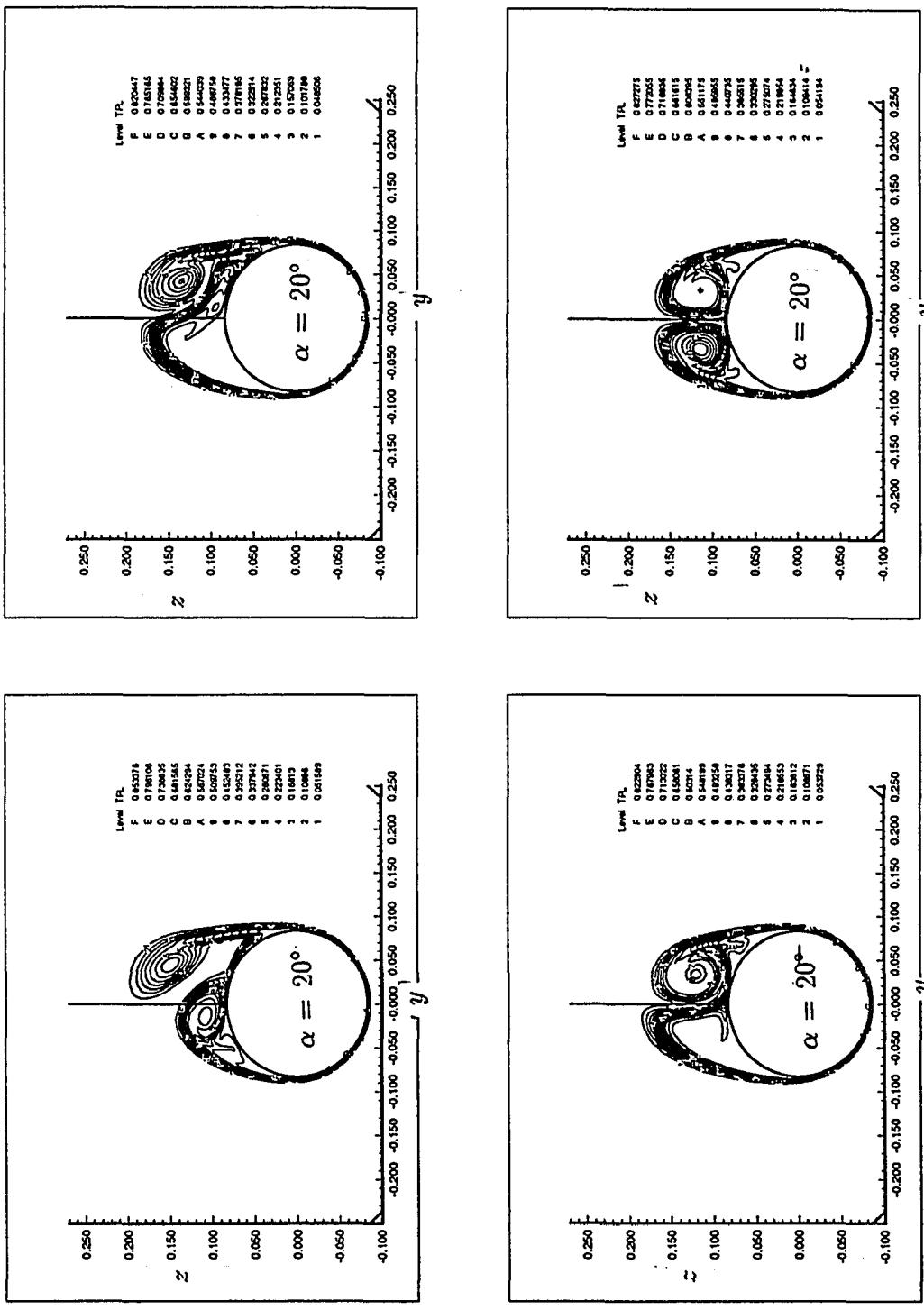

Figure 6.18: Total pressure loss contours for a circular cone with normal injection control at $\alpha = 20°$, $M_\infty = 1.8$, $R_e = 10^5$, $\dot{m}_{max} = 0.03$, $\theta_i = -67.5° \rightarrow 67.5°$.

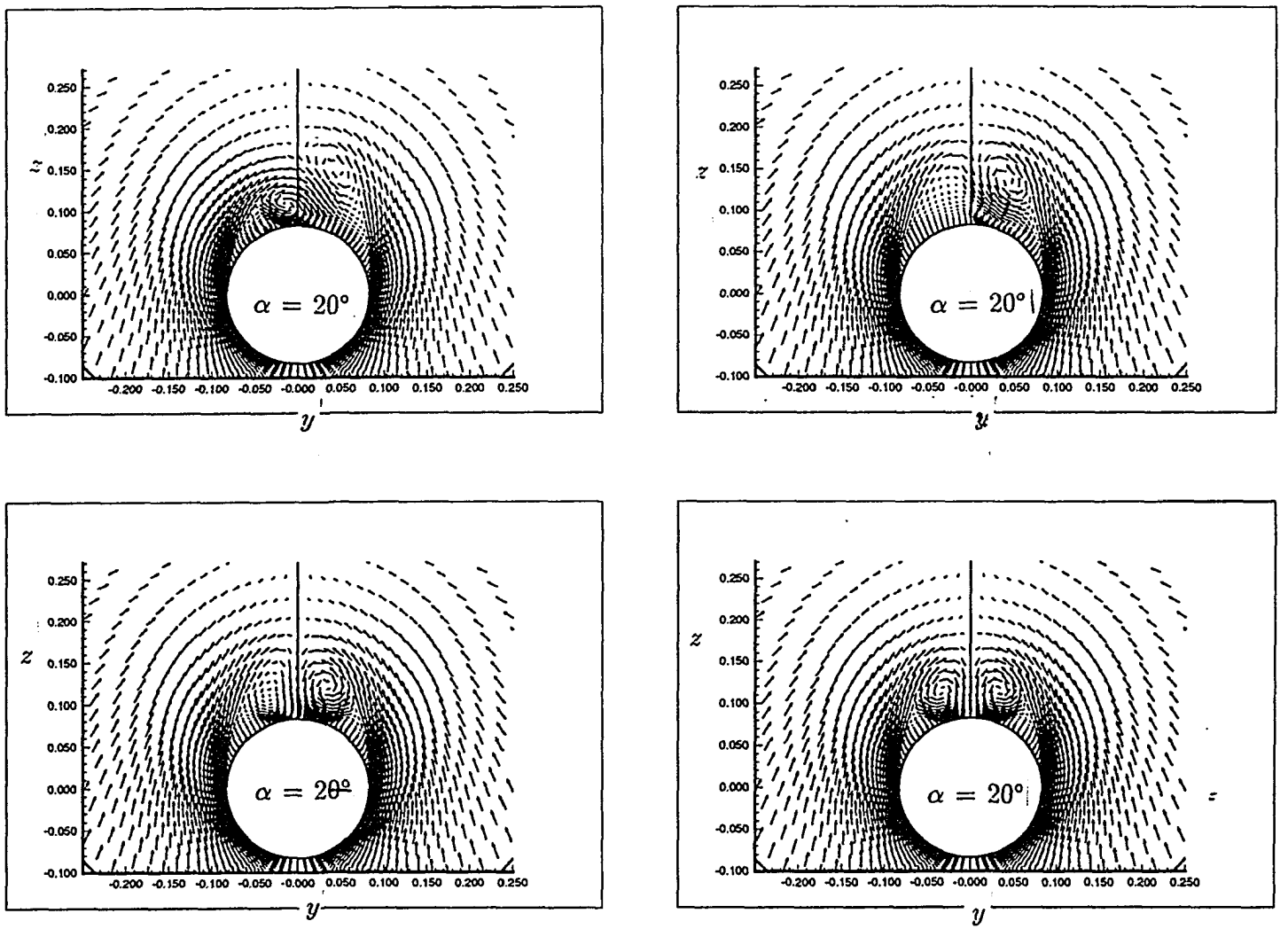

Figure 6.19: cross-flow Velocity vectors for a circular cone with normal injection control at $\alpha = 20°$, $M_\infty = 1.8$, $R_e = 10^5$, $\dot{m}_{max} = 0.03$, $\theta_i = -67.5° \rightarrow 67.5°$.

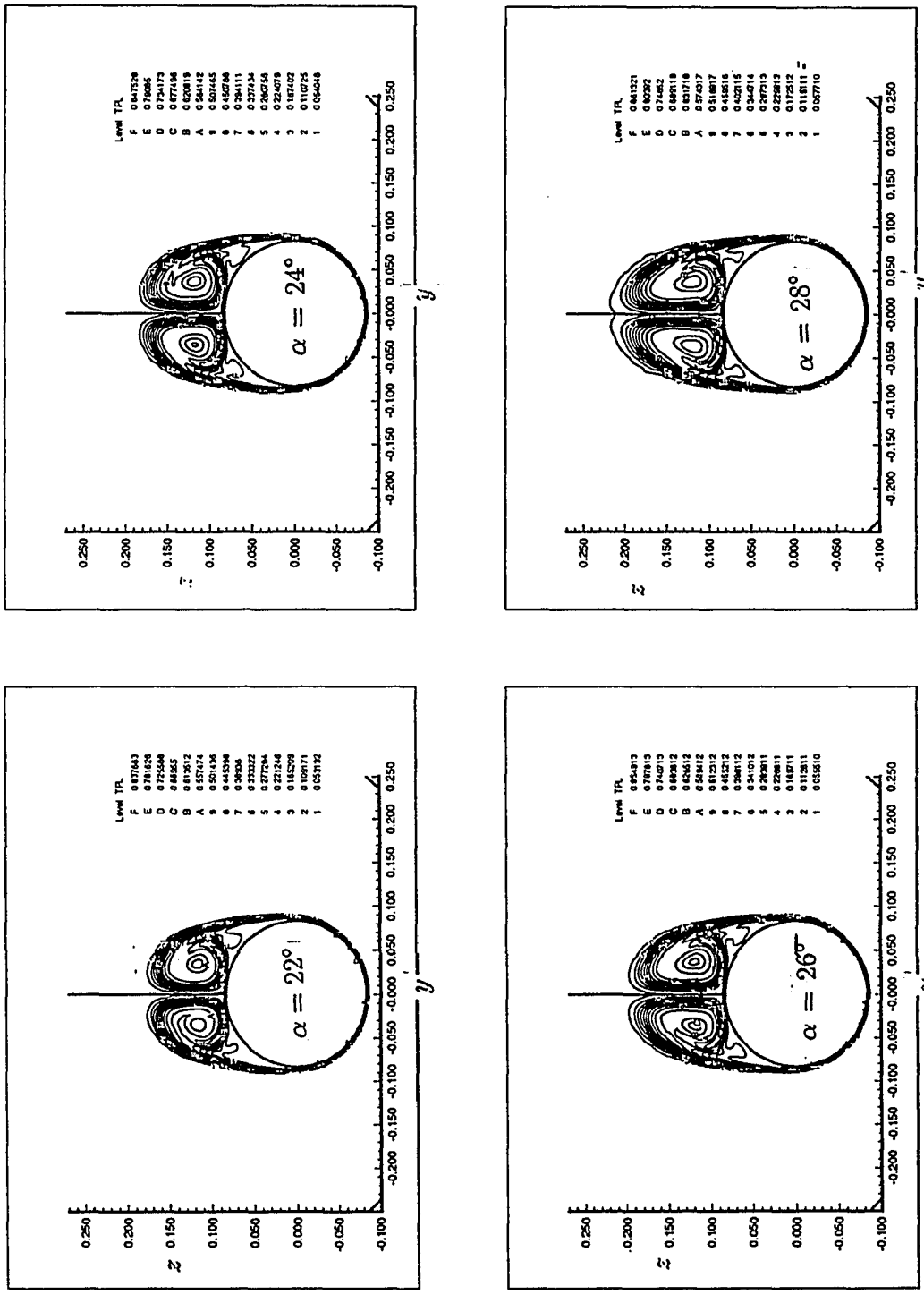

Figure 6.20: Total pressure loss contours for a circular cone with normal injection control at $\alpha = 22°, 24°, 26°, 28°$, $M_\infty = 1.8$, $R_e = 10^5$, $\dot{m}_{max} = 0.03$, $\theta_i = -67.5° \rightarrow 67.5°$.

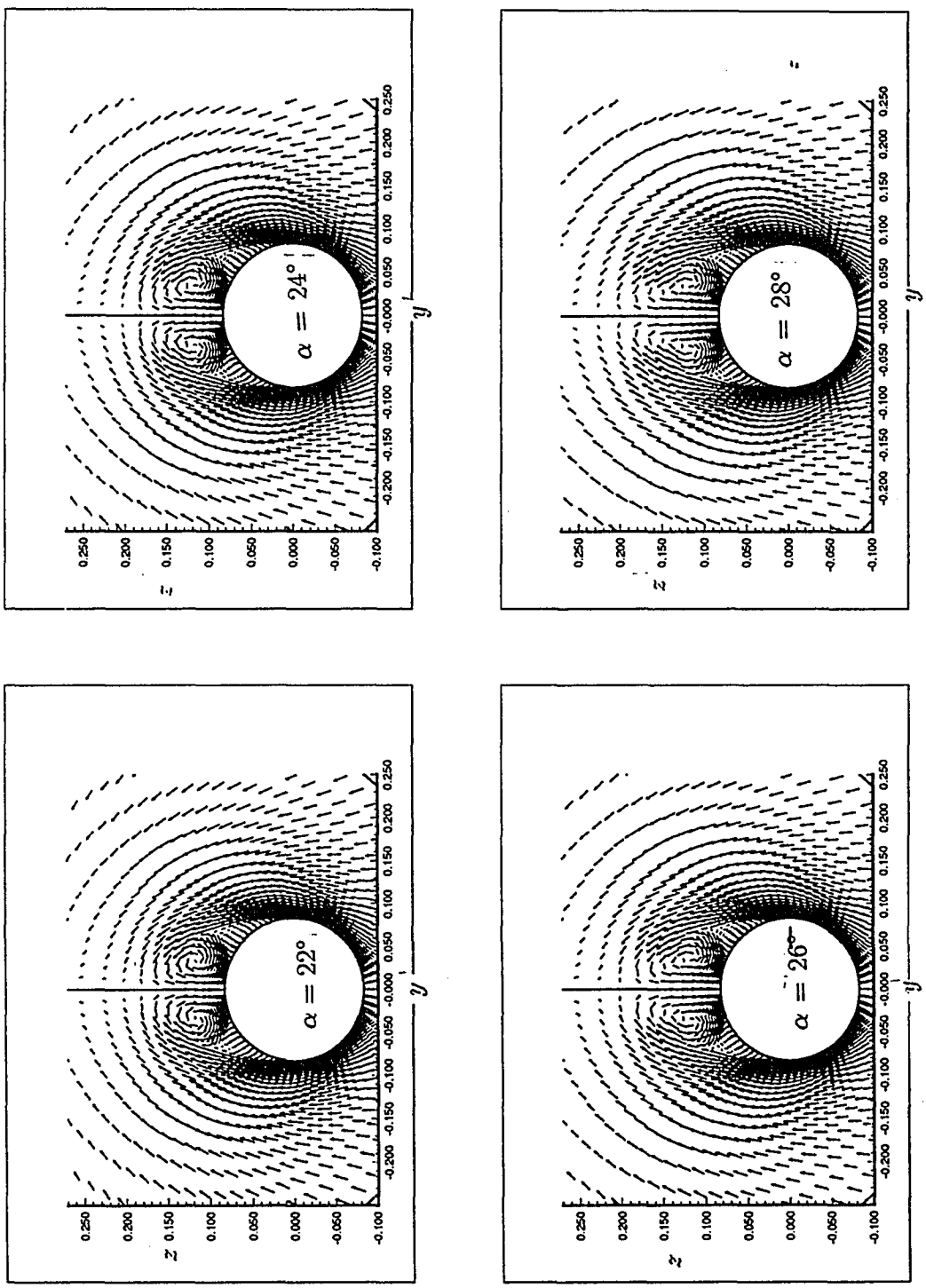

Figure 6.21: Cross-flow velocity vectors for a circular cone with normal injection control at $\alpha = 22°, 24°, 26°, 28°$, $M_\infty = 1.8$, $R_e = 10^5$, $\dot{m}_{max} = 0.03$, $\theta_i = -67.5° \rightarrow 67.5°$.

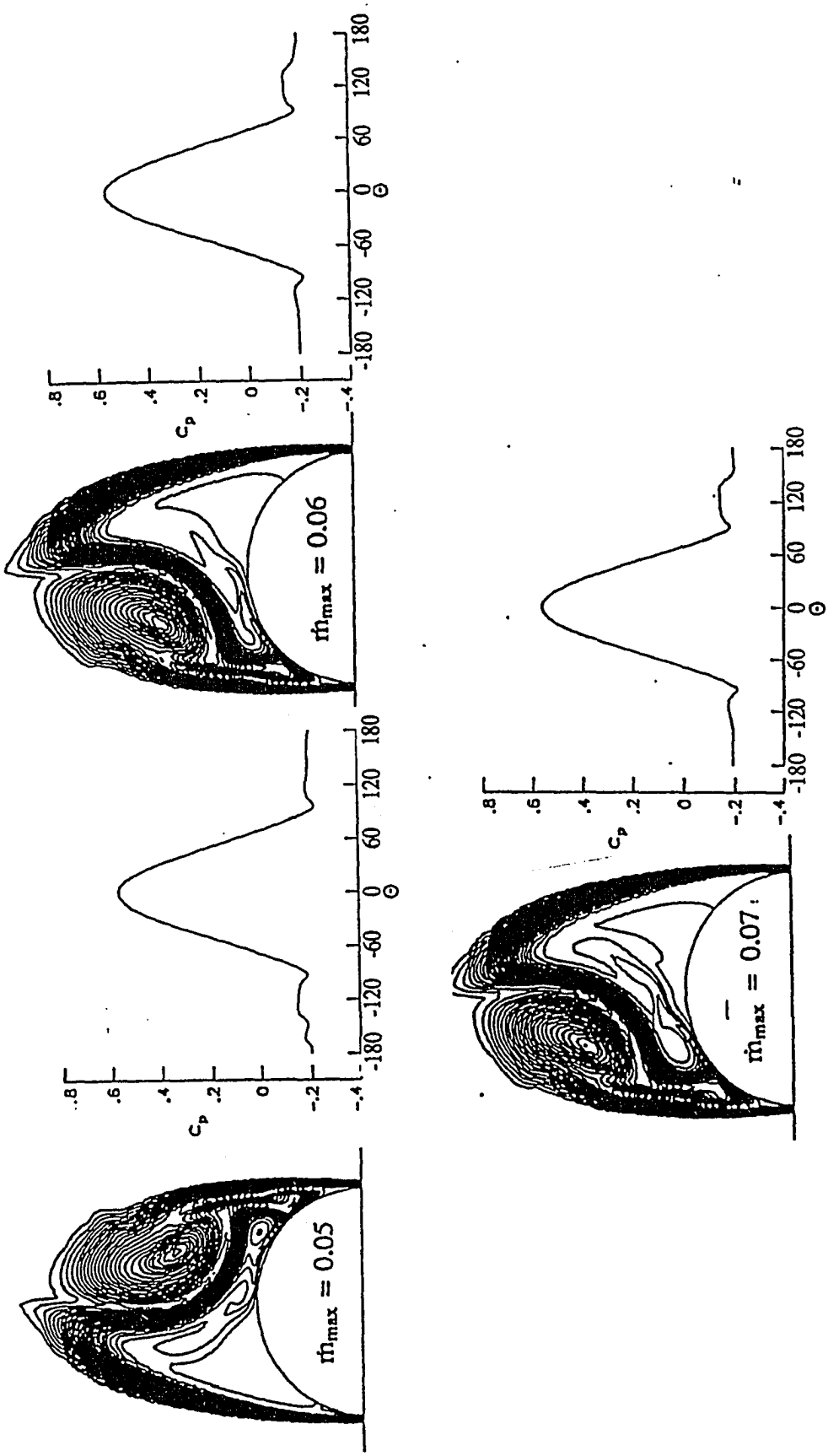

Figure 6.22: Total pressure loss contours and surface pressure coefficient for a circular cone with normal injection control at $\alpha = 30°$, $M_\infty = 1.8$, $R_e = 10^5$, $\dot{m}_{max} = 0.05, 0.06, 0.07$, $\theta_i = -67.5° \rightarrow 67.5°$.

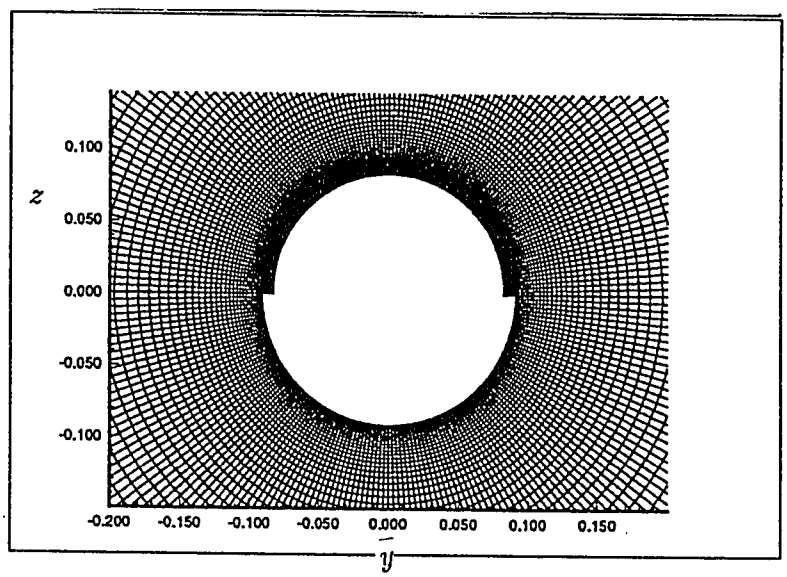

Figure 6.23: Three-block grid over circular cross section of the cone with lip of $0.05r$.

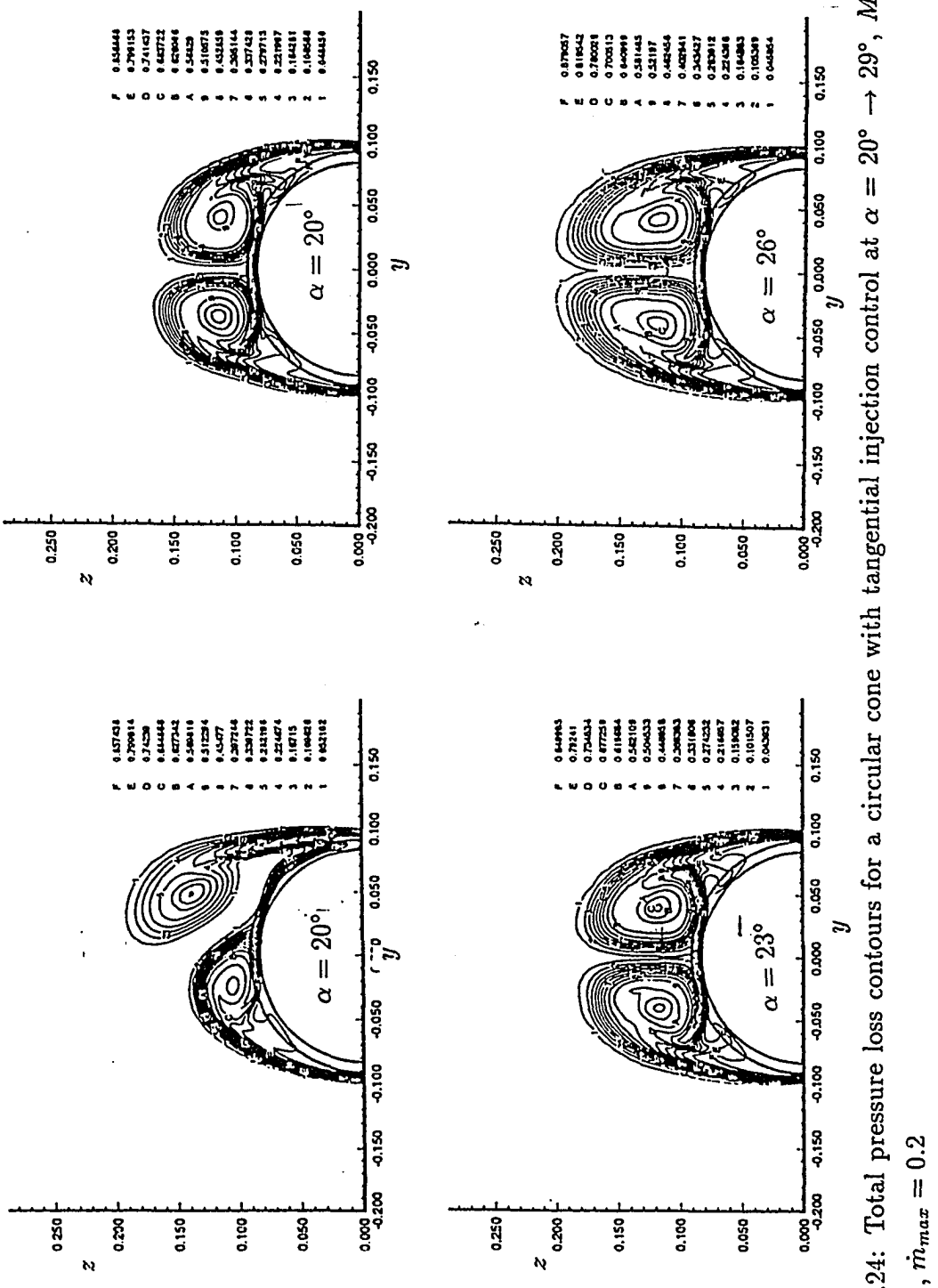

Figure 6.24: Total pressure loss contours for a circular cone with tangential injection control at $\alpha = 20° \rightarrow 29°$, $M_\infty = 1.8$, $R_e = 10^5$, $\dot{m}_{max} = 0.2$

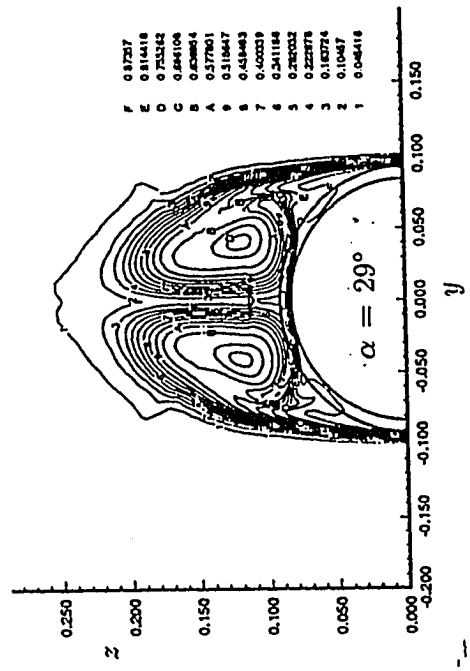

Figure 6.24: Continued

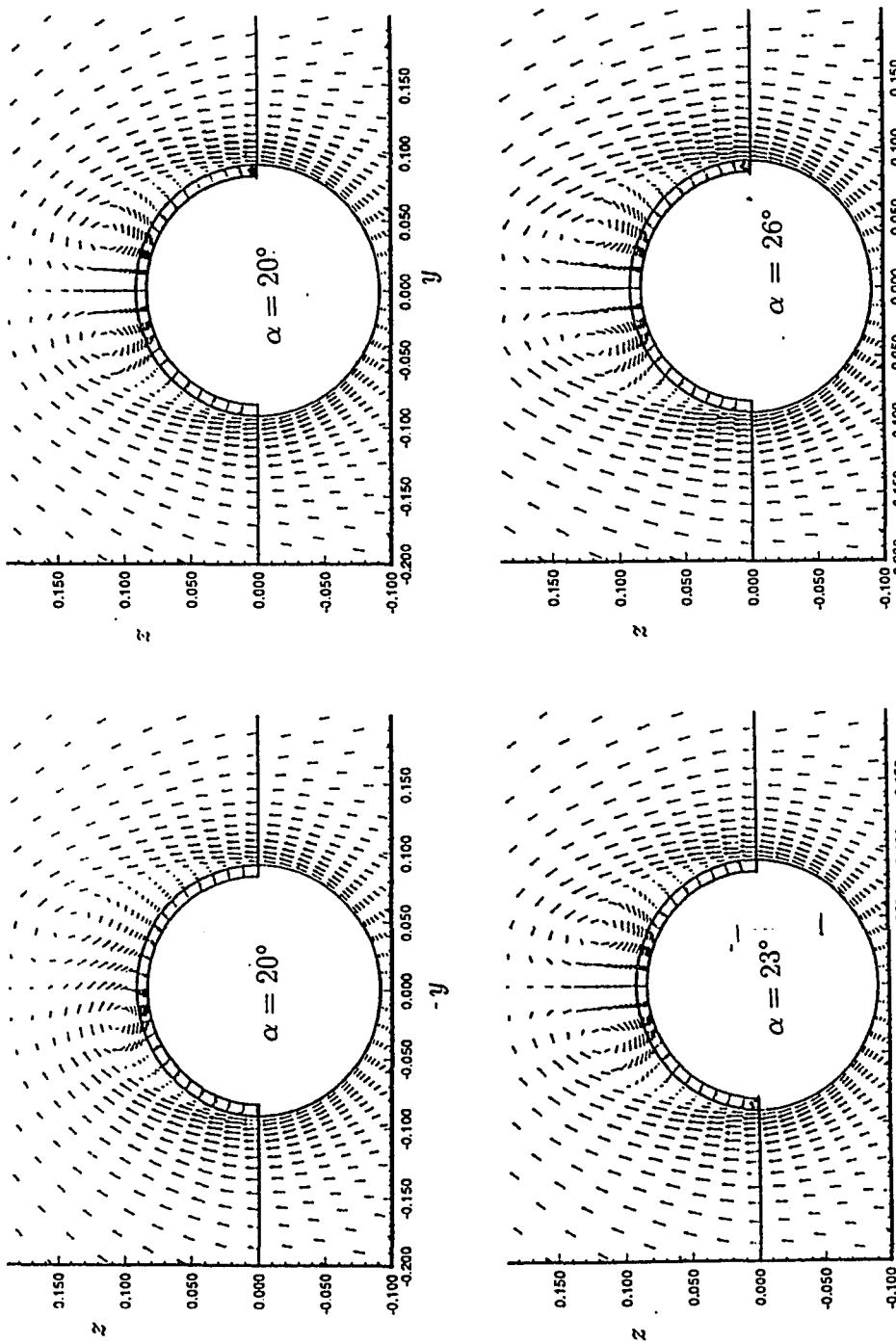

Figure 6.25: Cross-flow velocity vectors for a circular cone with tangential injection control at $\alpha = 20° \rightarrow 29°$, $M_\infty = 1.8$, $R_e = 10^5$, $\dot{m}_{max} = 0.2$

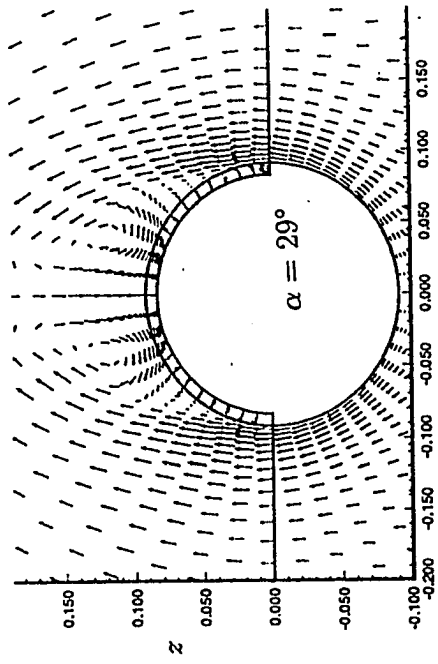

Figure 6.25: Continued

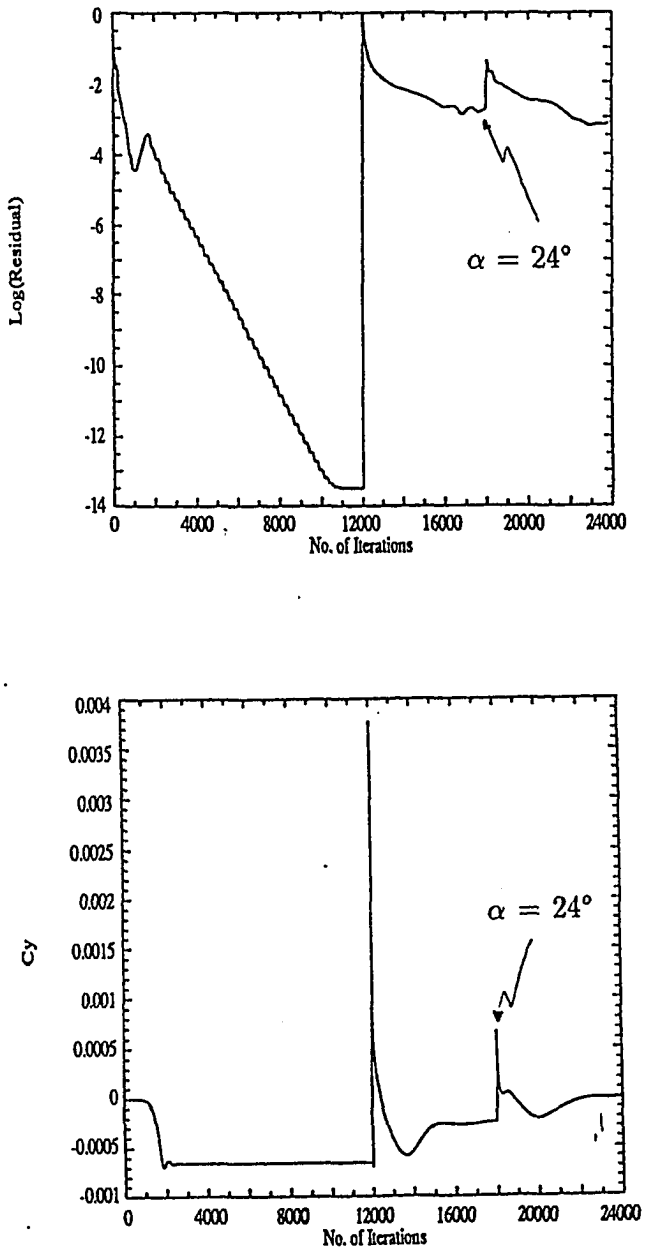

Figure 6.26: Lift and side force coefficients for a circular cone with surface heating control at $\alpha = 20° \rightarrow 24°$, $M_\infty = 1.8$, $R_e = 10^5$

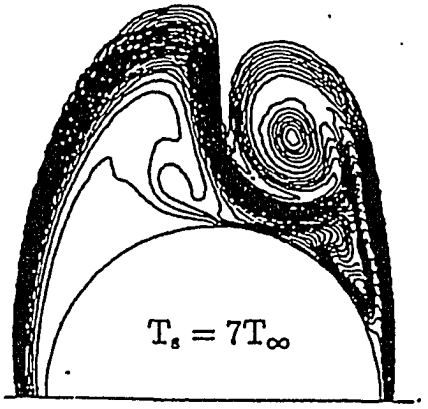

Figure 6.27: Total pressure loss contours for a circular cone with surface heating control at $\alpha = 24°$, $M_\infty = 1.8$, $R_e = 10^5$

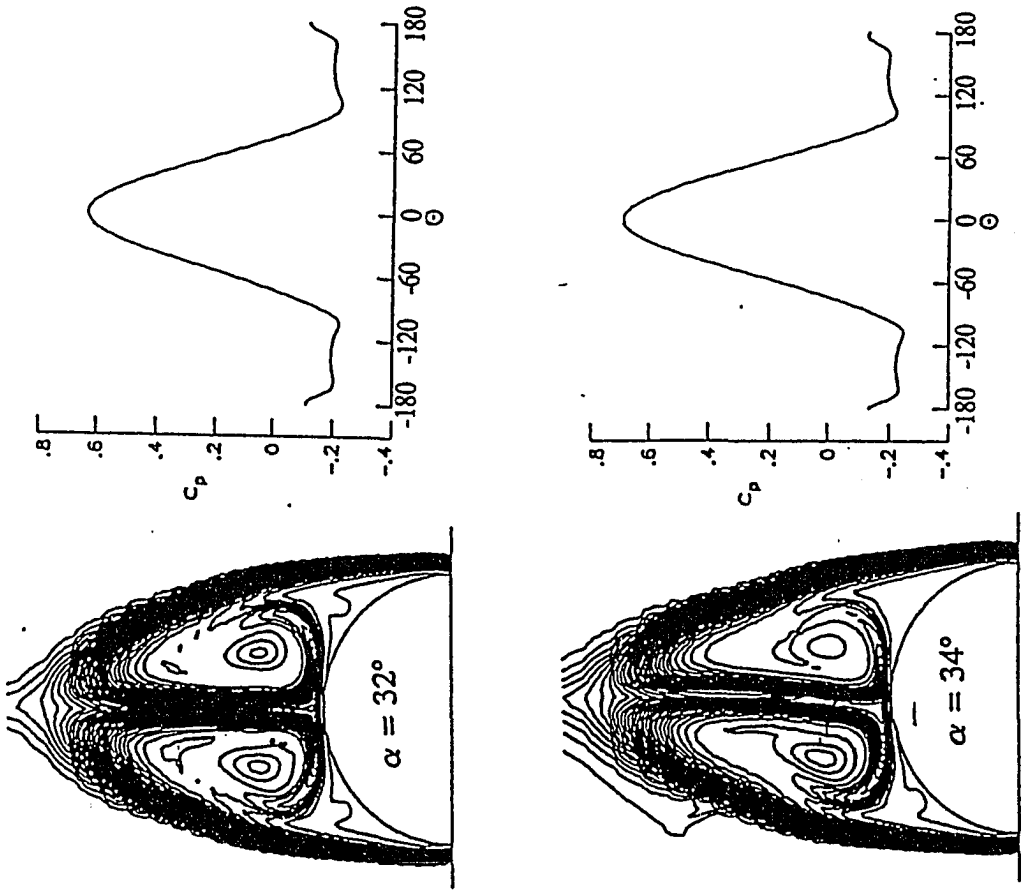

Figure 6.28: Total pressure loss contours and surface pressure coefficient for a circular cone with hybrid heating-injection control at α up to 38°, $M_\infty = 1.8$, $R_e = 10^5$

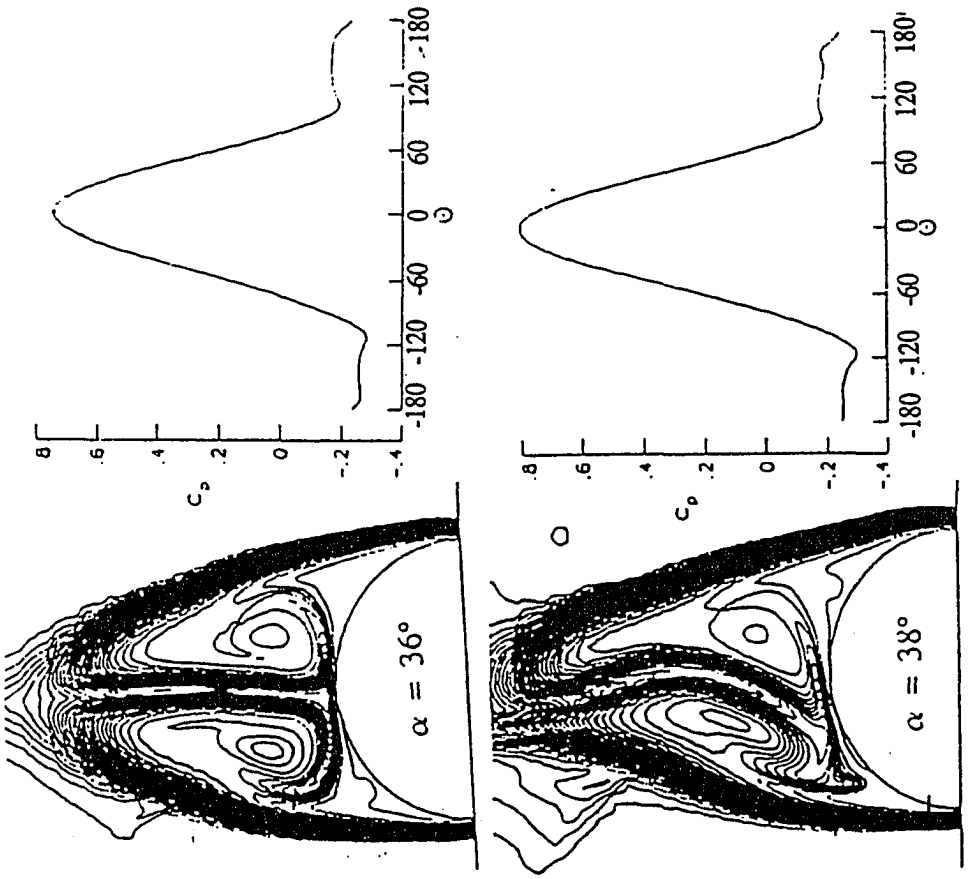

Figure 6.28: Continued

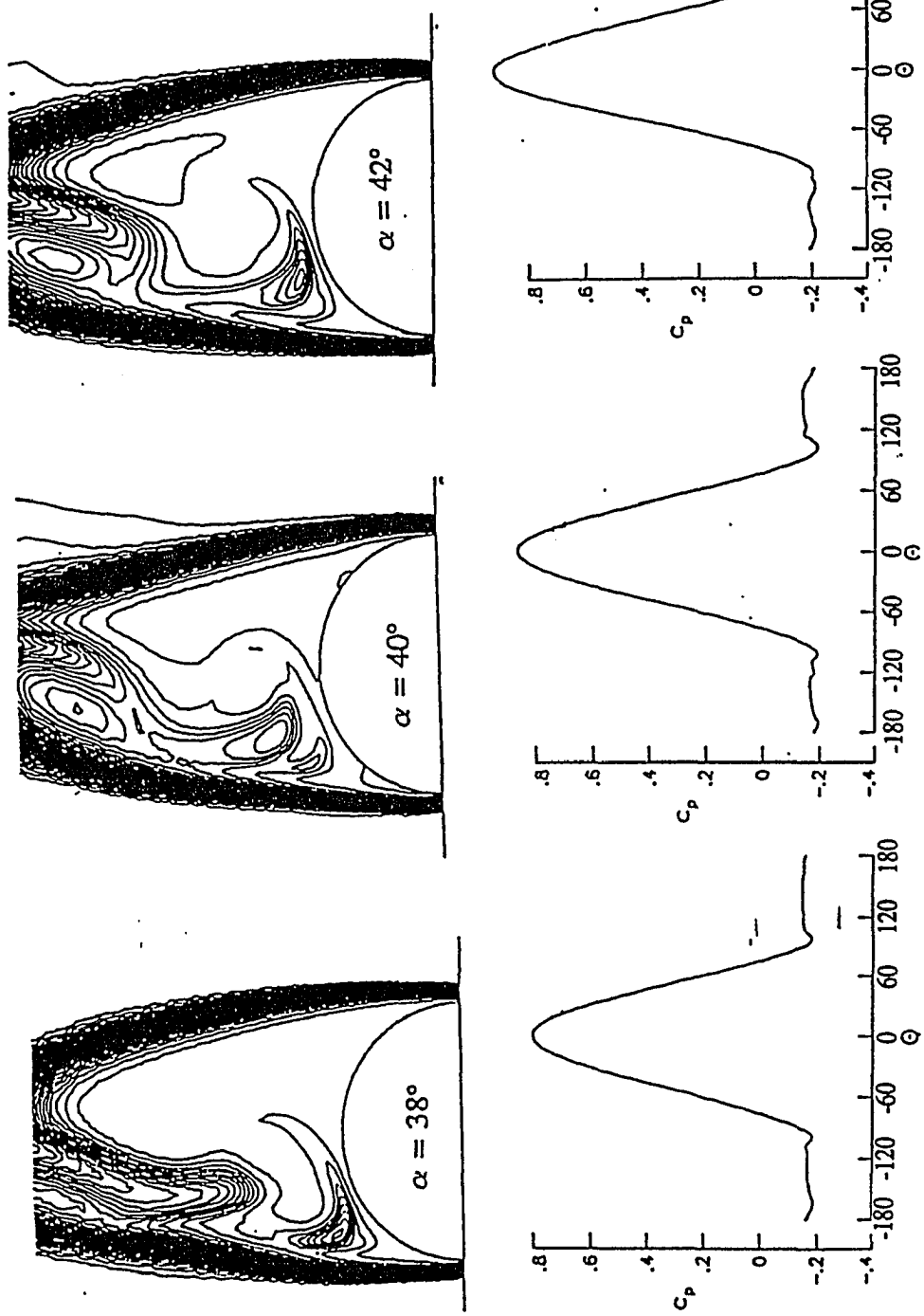

Figure 6.29: Total pressure loss contours and surface pressure coefficient for a circular cone with hybrid heating-injection control at $\alpha = 38° \rightarrow 42°$, $M_\infty = 1.8$, $R_e = 10^5$

CHAPTER 7

ACTIVE CONTROL USING SPINNING AND ROTARY OSCILLATIONS

7.1 Introduction

In this chapter, the effectiveness of spinning and rotary oscillations as active control methods to eliminate or alleviate the side forces for a 5° semi-apex angle circular cone is investigated. The grid is spinning or oscillating rigidly with the cone, according to its motion, and the kinematical and dynamical boundary conditions are modified accordingly. For uniform spinning, the surface speed is constant and assumed to have values of ± 0.06, ± 0.2 and 0.6, while for rotary oscillation, the surface speed is sinusoidal with amplitudes of 0.06, 0.2 and 0.5, which cover a circumferential angle of 45°, 90° and 375°. Similar to Chap. 6, the reference case presented in Sec. 5.2 and its solution, Figs. 5.2, 5.3 and 5.4, will be used throughout this chapter. Starting from that solution which is pseudo time, a time accurate solution for the steady case of the flow over a 5° semi-apex angle cone was obtained by running the code in a time accurate fashion for 1,000 iterations with $\Delta t = 0.001$.

7.2 Spinning Motion

The asymmetric solution which is shown in the Figs. 5.3 and 5.4, was used as the initial solution for the spinning cases. By spinning the cone in the counter-clockwise direction, the velocity of the boundary-layer flow on the right-hand side of the cone was enhanced in terms of resisting flow separation; Conversely the speed of the boundary-layer flow on the left-hand side of the cone was retarded, producing early flow separation 7.1. Moreover, the spinning motion adds either positive or negative vorticity to the flowfield. Hence, by selecting the appropriate spinning rate, the asymmetric vortices can be rendered symmetric. The second effect of spinning is to increase the pressure gradient normal to the body $\left(\frac{\partial p}{\partial n}|_{cone} = \rho\omega^2 r_{cone}\right)$. For small values of ω, the effect on the pressure gradient will not be pronounced. However, for large values of ω, the effect on the pressure will be significant. Also, for nonzero AOA, the magnus effect will contribute to the side force -either positive or negative depending on the spinning direction. In addition, experimental data [62, 111, 112] has shown that spinning produces an oscillatory side-force response. If the mean side force is zero, then the average side force will be zero. In this section, we present the effect of uniform spinning at surface velocities of ± 0.06 and ± 0.2, which correspond to $\pm 2,292$ rpm and $\pm 7,639$ rpm, respectively, for a cone of unit length.

7.2.1 Uniform spinning at ± 0.06

Figures 7.2 and 7.3 show the results for uniform counter-clockwise (CCW) spinning at $V_s = 0.06$, where V_s is the surface velocity, and Figs. 7.4 and 7.5 show the results for uniform clockwise (CW) spinning at $V_s = -0.06$. All spinning cases were started at time step 13,001 and the solutions were obtained using $\Delta t = 0.001$. With the present surface speed of 0.06, the cone rotated one revolution in 9.163 dimensionless time units, which corresponded to 9,163 time steps. Figure 7.2 shows the side force and lift coefficients versus the number of time steps. It is observed that the force

coefficients reach a periodic response very quickly and the period of oscillation is 9.163 dimensionless time, which is of course equal to the time required to rotate the cone one revolution. The side-force curve oscillates between -6.9×10^{-4} and -5.3×10^{-4} with a mean value of -6.1×10^{-4}. The magnitude of the mean side-force coefficient is less than the magnitude of the side-force coefficient without spinning, which was equal to -6.5×10^{-4}. Thus, the CCW spinning reduces the magnitude of the side force on the average. The lift coefficient curve shows a small-amplitude periodic response. In Fig. 7.3, snapshots of the total pressure loss contours, surface pressure coefficient and streamlines are shown at five instants, covering one cycle of periodic side-force response. They are marked by the numbers 1,2,3,4 and 5 on Figs. 7.2 and 7.3. The snapshots show that the right and left vortex heights, lateral positions, strengthens and separation points oscillate slightly. Consequently, the corresponding surface pressures oscillate slightly too. CCW spinning delays flow separation on the right side and expedites flow separation on the left side.

With the CW spinning of -0.06, the side-force and lift coefficient curves of Fig. 7.4 show that their periodic response is also reached very quickly. The side-force coefficient curve oscillates between -7.7×10^{-4} and -5.5×10^{-4} with a mean value of -6.6×10^{-4}. The magnitude of the mean value is slightly higher than the magnitude of the side-force coefficient without spinning. Thus, the CW spinning does not reduce the mean value of the side force. Figure 7.5 shows snapshots of the total pressure loss contours, surface pressure coefficient and streamlines at four instants during one cycle of periodic response. The CW spinning increases flow separation on the right side and delays flow separation on the left side. Comparisons of the snapshots of Fig. 7.5 with the corresponding snapshots of Fig. 7.3, show that the vortex on the right-hand side of Fig. 7.5 (snapshot 1) moves more to the right, while the vortex on the right-hand side of Fig. 7.3 (snapshot 1) moves more to the left. Similar motions are observed for the vortex on the left side of Figs. 7.5 and 7.3 (snapshots 1). Hence, the side force at point 1 of the CW spinning is higher in magnitude than the side force at point 1 of the CCW spinning.

7.2.2 Uniform spinning at ±0.2

Next, uniform spinning was increased to 0.2. The results of CCW spinning are shown in Figs. 7.6 and 7.7, and the results of the CW spinning are shown in Figs. 7.8 and 7.9. With the surface speed of 0.2, the cone rotates one revolution in 2.749 dimensionless time, which corresponds to 2,749 time steps. Figure 7.6 shows that the side-force and lift coefficients curves reach a periodic response very quickly and the period of oscillation is 2.749 dimensionless time. The side-force coefficient curve oscillates between -8.9×10^{-4} and -0.5×10^{-4} with a mean value of -4.7×10^{-4}. The magnitude of the mean side-force coefficient is substantially lower than the magnitude of the side-force coefficient without spinning. Thus, high CCW spinning reduced the mean value of the side force. It should be noticed that the amplitude and frequency of oscillation of the lift coefficient curve were higher than those of Fig. 7.2. Four snapshots of the total pressure loss contours, surface pressure coefficient, and streamlines, during one cycle of the periodic side force coefficient are shown in Fig. 7.7. It is noted that the CCW spinning increases the flow separation substantially on the left side, and delays flow separation on the right side. Also, the right-hand vortex moves further downward and leftward, compared to similar motions in Fig. 7.3.

Figure 7.8 shows the periodic responses of the side force and lift coefficients for the CW spinning with surface velocity of -0.2. The side force coefficient curve oscillates between -10.2×10^{-4} and -2.1×10^{-4} with a mean value of 6.15×10^{-4}. The magnitude of the mean side force coefficient is lower than the magnitude of side force coefficient without spinning, but it is substantially higher than the mean value of the CCW spinning of Fig. 7.6. Snapshots of the total pressure loss contours, surface pressure coefficient, and streamlines at point 1 during one cycle of the periodic side force coefficient, are shown in Fig. 7.9. The CW spinning is observed to increase the flow separation on the right side and the left-hand vortex moves more to the right.

7.2.3 *Uniform spinning at 0.6*

In this case, uniform spinning was increased to 0.6 and the results are shown in Figs. 7.10 and 7.11. With a surface speed of 0.6, the cone rotates one revolution in 0.916 dimensionless time. The side-force coefficient curve shows the periodic response which oscillates between -50×10^{-4} and $+38 \times 10^{-4}$ with a mean value of 6×10^{-4}. With this high value of CCW spinning, the side-force coefficient is oscillating between positive and negative values and the vortices on the left and right sides are changing heights periodically. It is noticed that the boundary layer at certain instances detaches to form a free-shear-layer band around the body, as shown in Fig. 7.11. Although the mean value of the side force is not zero, this test indicated the existence of a certain CCW spinning value at which the mean side force will be zero.

7.3 *Rotary Oscillating Motion*

In this section, the effect of periodic rotary oscillation of the cone on the flow asymmetry and the side force is investigated. The form of the surface speed is given by

$$V_s = \bar{V}_s \cos\left(\frac{2\pi}{\tau}t\right) \tag{7.1}$$

where $\bar{V}_s$ is the surface-speed amplitude and τ is the period of oscillation. Substituting 7.1 into the relation

$$\frac{d\theta}{dt} = \frac{V_s}{r_c} \tag{7.2}$$

and integrating the result with respect to time, the angular motion θ is obtained in the form

$$\theta = \theta_a \sin\left(\frac{2\pi}{\tau}t\right) \tag{7.3}$$

where

$$\theta_a = \frac{\bar{V}_s \tau}{2\pi r_c} \tag{7.4}$$

By specifying $\bar{V}_s$ and τ, one can obtain the amplitude of the angular motion, θ_a, for a particular value of cone radius, r_c. In the next subsections, present the results for different values of $\bar{V}_s$ and τ of the periodic rotary oscillation are presented.

7.3.1 Rotary oscillation $\bar{V}_s = 0.06$, $\tau = 7.2$, $\theta_a = 45°$

The corresponding frequency of this motion is 0.873. The results of this case are given in Figs. 7.12 and 7.13. The period of the side-force coefficient response is observed to be 7.2 which is the same as that of the motion. The side-force coefficient curve oscillates between -7.7×10^{-4} and -5.4×10^{-4}, with a mean value of -6.55×10^{-4}, which is between the mean values of CCW and CW uniform spinning cases of Figs. 7.3 and 7.5. Hence, these values of $\bar{V}_s$, τ and θ_a do not reduce the mean value of side forces.

7.3.2 Rotary oscillation $\bar{V}_s = 0.2$, $\tau = 4.3$, $\theta_a = 90°$

The corresponding frequency of this motion is 1.461. The results of this case are given in Figs. 7.14 and 7.15. The period of the side-force coefficient response is 4.3 which is the same frequency as that of the motion. The side-force coefficient oscillates between -10.5×10^{-4} and -2×10^{-4} with a mean value of -6.25×10^{-4}. This mean value of the side-force coefficient is higher than that obtained in the case of CCW uniform spinning of Fig. 7.6 7.7. Hence, these values of $\bar{V}_s$, τ and θ_a do not reduce the mean value of side force.

7.3.3 Rotary oscillation $\bar{V}_s = 0.5$, $\tau = 7.2$, $\theta_a = 375°$

The corresponding frequency of this motion is 0.873 which is the same as that of the case of Fig. 7.12 and 7.13. However, the amplitudes of the surface velocity and

angular motion are one order of magnitude higher than those of the case of Fig. 7.12. The results of this case are given in Figs. 7.16 and 7.17. Although the side force coefficient response is periodic with the same period as that of the motion, there are several peaks within each period. The side-force coefficient changes sign from positive to negative, and the mean value of the side-force coefficient is zero. This shows that $\bar{V}_s$, τ and θ_a for the rotary oscillation produce a zero value for the side-force coefficient on the average. It should be emphasized here that both the amplitude of the surface velocity and angular motion are one order of magnitude higher than that of the case of Fig. 7.12.

7.3.4 Rotary oscillation $\bar{V}_s = 0.5$, $\tau = 4.3$, $\theta_a = 225°$

The corresponding frequency of this motion is 1.461 which is the same as that of the case of Figs. 7.14 and 7.15. However, the amplitudes of the surface velocity and angular motions are 2.5 times those for the case shown in Figs. 7.14 and 7.15. The results of this case are given in Figs. 7.18 and 7.19. The same features for the side force coefficient that were observed in Figs. 7.16 and 7.17 are shown. The mean value of side-force coefficient is -1.5×10^{-4} which is better than that of any of the uniform spinning cases. However it is higher than that of the previous case. The only difference between this case and the previous case is the period of oscillation and the amplitude of angular motion. Although the magnitude of the side-force coefficient is higher than that of the case of Fig. 7.16, the peak values of side-force coefficient for the present case are substantially lower than those of the previous case. It seems that the best side-force coefficient response (zero mean and small amplitude) can be achieved by using the higher θ_a and the lower τ of the present case and the previous case.

7.4 Summary

In this chapter, the effectiveness of uniform spinning and rotary oscillations as active control methods for alleviating the flow asymmetry and the associated side forces were investigated. It was shown that a large counterclockwise spinning rate was effective in substantially reducing the side force on the average for the given initial case of asymmetric flow. The CCW spinning increased flow separation on the left side and delayed it on the right side, which produced equal positive and negative side forces within each cycle of the side-force response. The rotary oscillation with large surface-velocity amplitude, large angular-motion amplitude and a small period of oscillation was much more effective than uniform spinning for the same surface velocity, since it eliminated the mean side force. Moreover, the effectiveness of the rotary oscillation control did not require a particular initial shape for the vortex asymmetry.

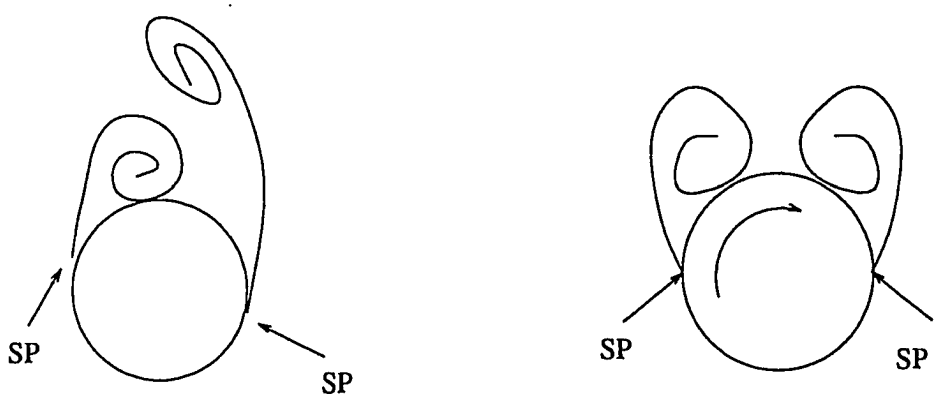

Without Spinning

With Spinning

Figure 7.1: Spinning effect on flow asymmetry

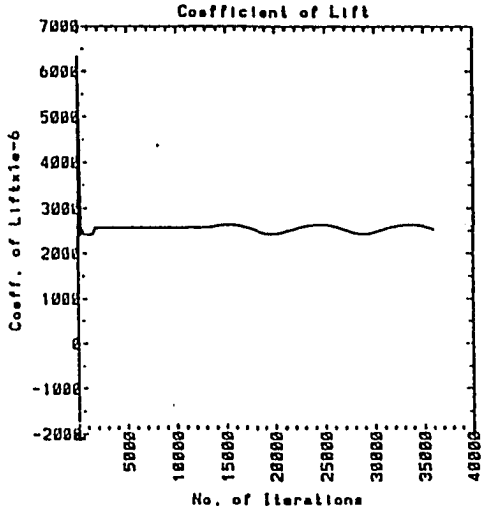

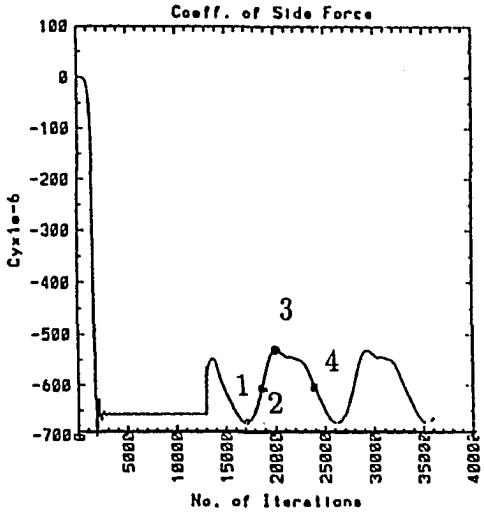

Figure 7.2: Lift coefficient and side-force coefficient history, $V_s = 0.06$ CCW spinning, $\tau = 9.163$, $\alpha = 20°$, $M_\infty = 1.8$, $R_e = 10^5$.

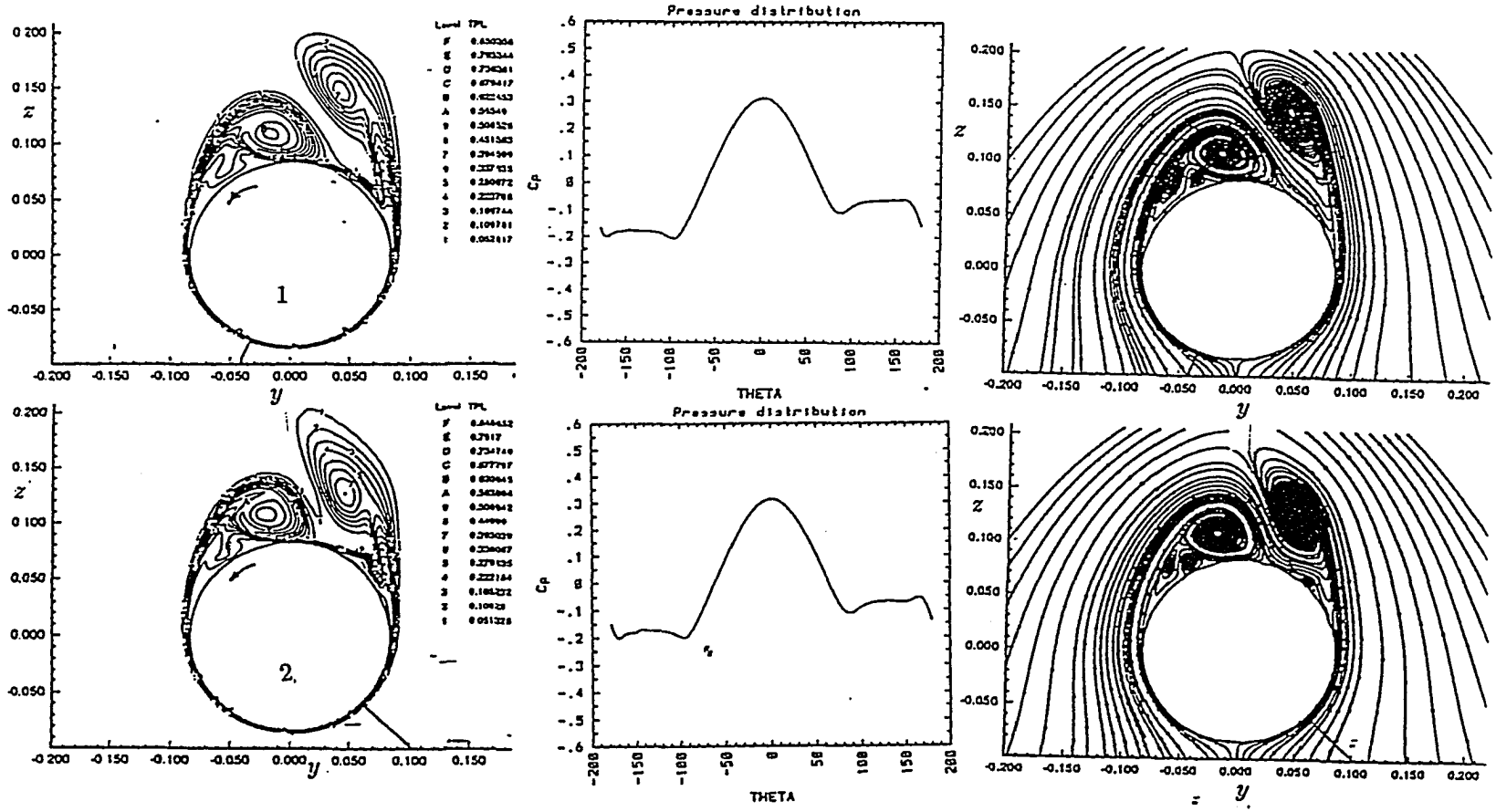

Figure 7.3: Snapshots of total pressure loss contours, surface pressure coefficient and cross-flow streamlines covering one cycle, $V_s = 0.06$ CCW spinning, $\tau = 9.163$, $\alpha = 20°$, $M_\infty = 1.8$, $R_e = 10^5$.

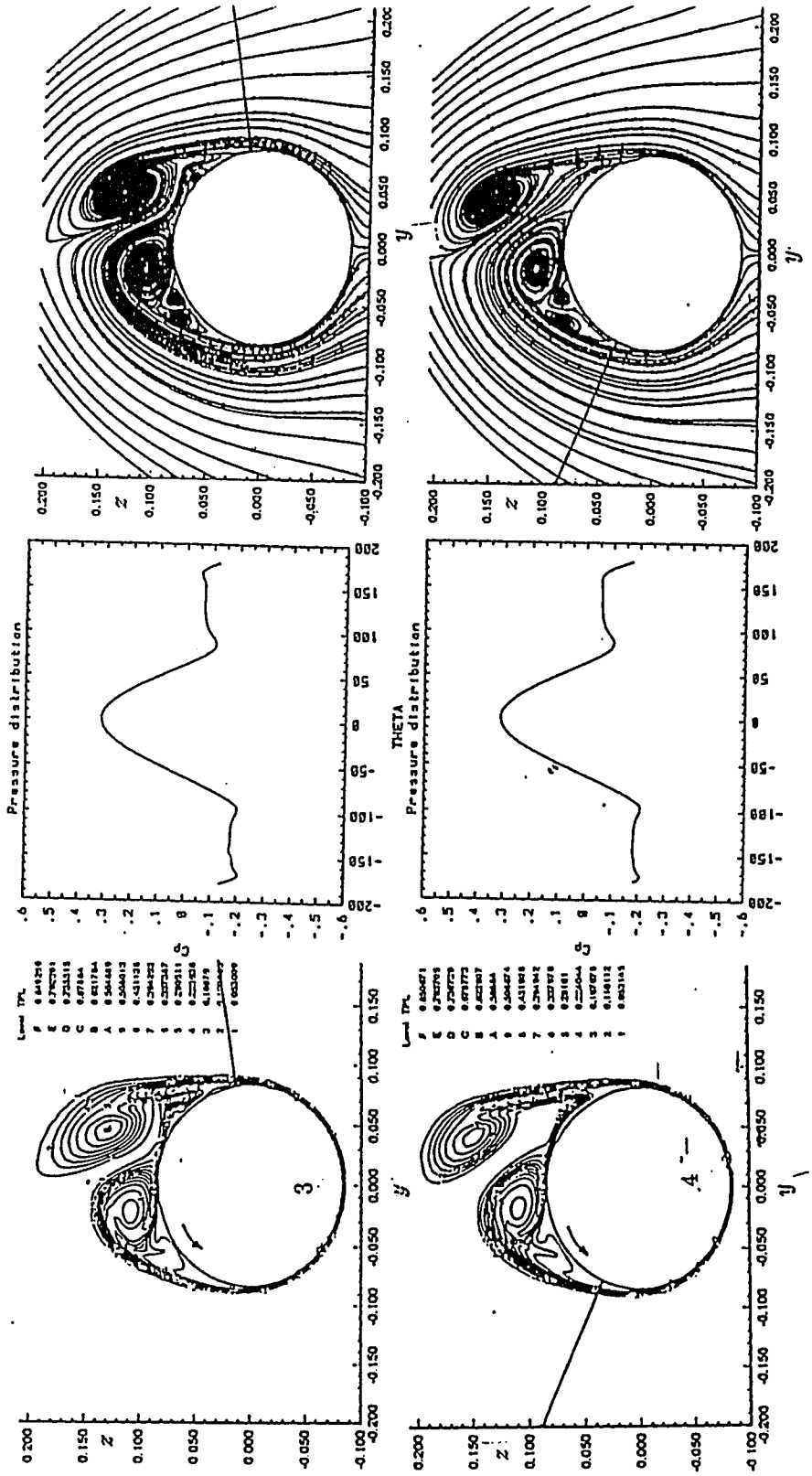

Figure 7.3: Continued

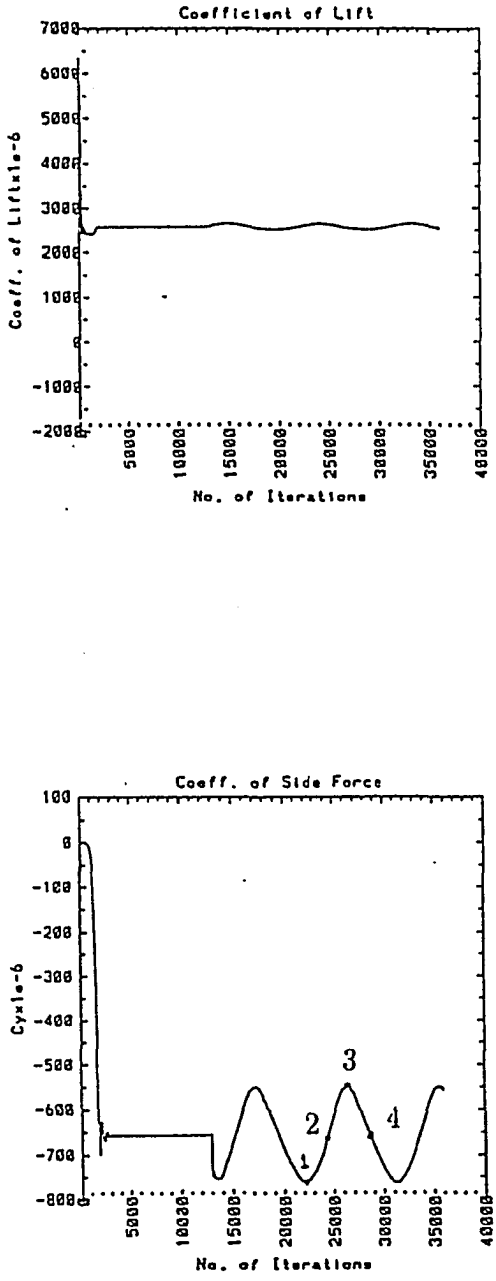

Figure 7.4: Lift coefficient and side-force coefficient history, $V_s = -0.06$ CW spinning, $\tau = 9.163$, $\alpha = 20°$, $M_\infty = 1.8$, $R_e = 10^5$.

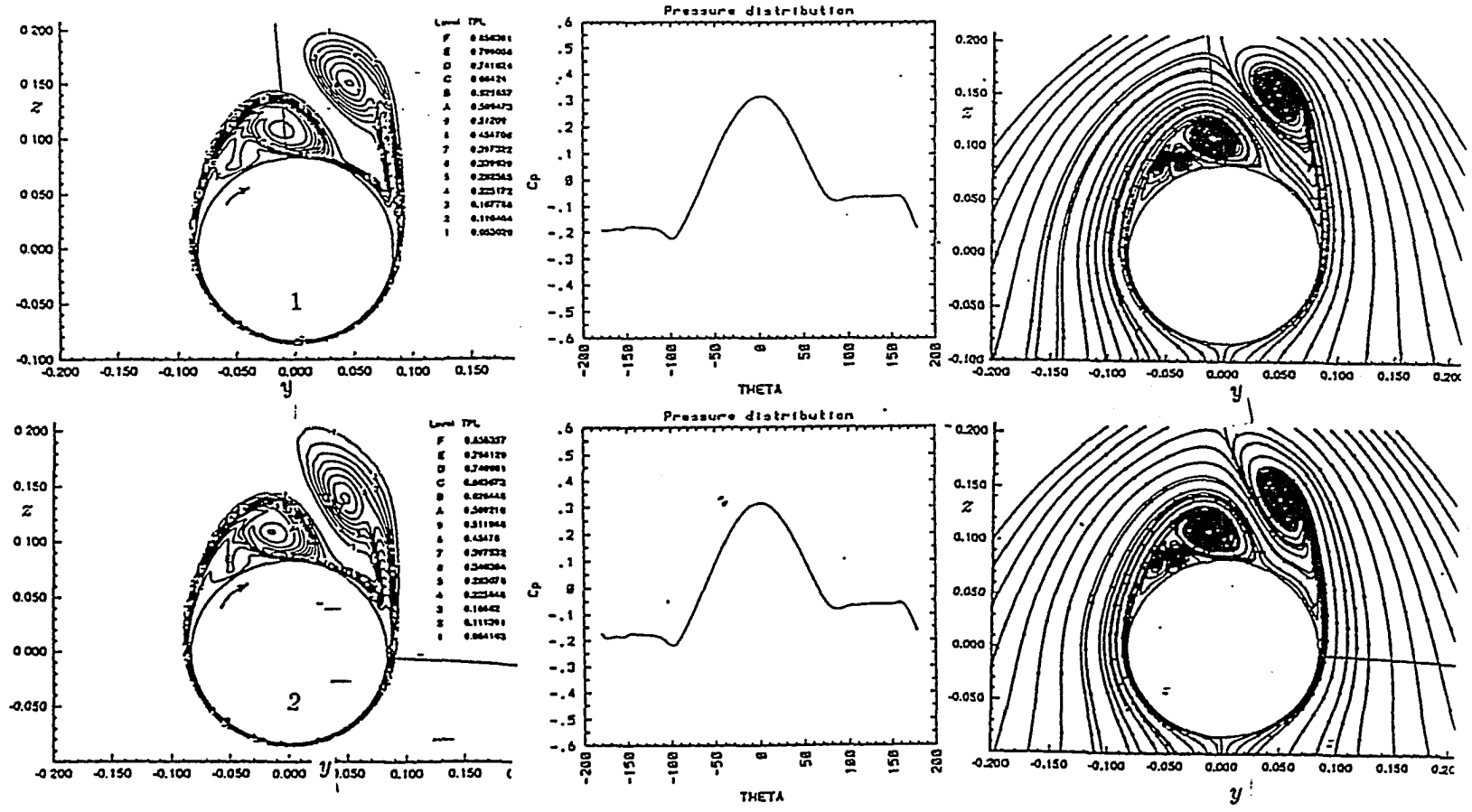

Figure 7.5: Snapshots of total pressure loss contours, surface pressure coefficient and cross-flow streamlines covering one cycle, $V_s = -0.06$ CW spinning, $\tau = 9.163$, $\alpha = 20°$, $M_\infty = 1.8$, $R_e = 10^5$.

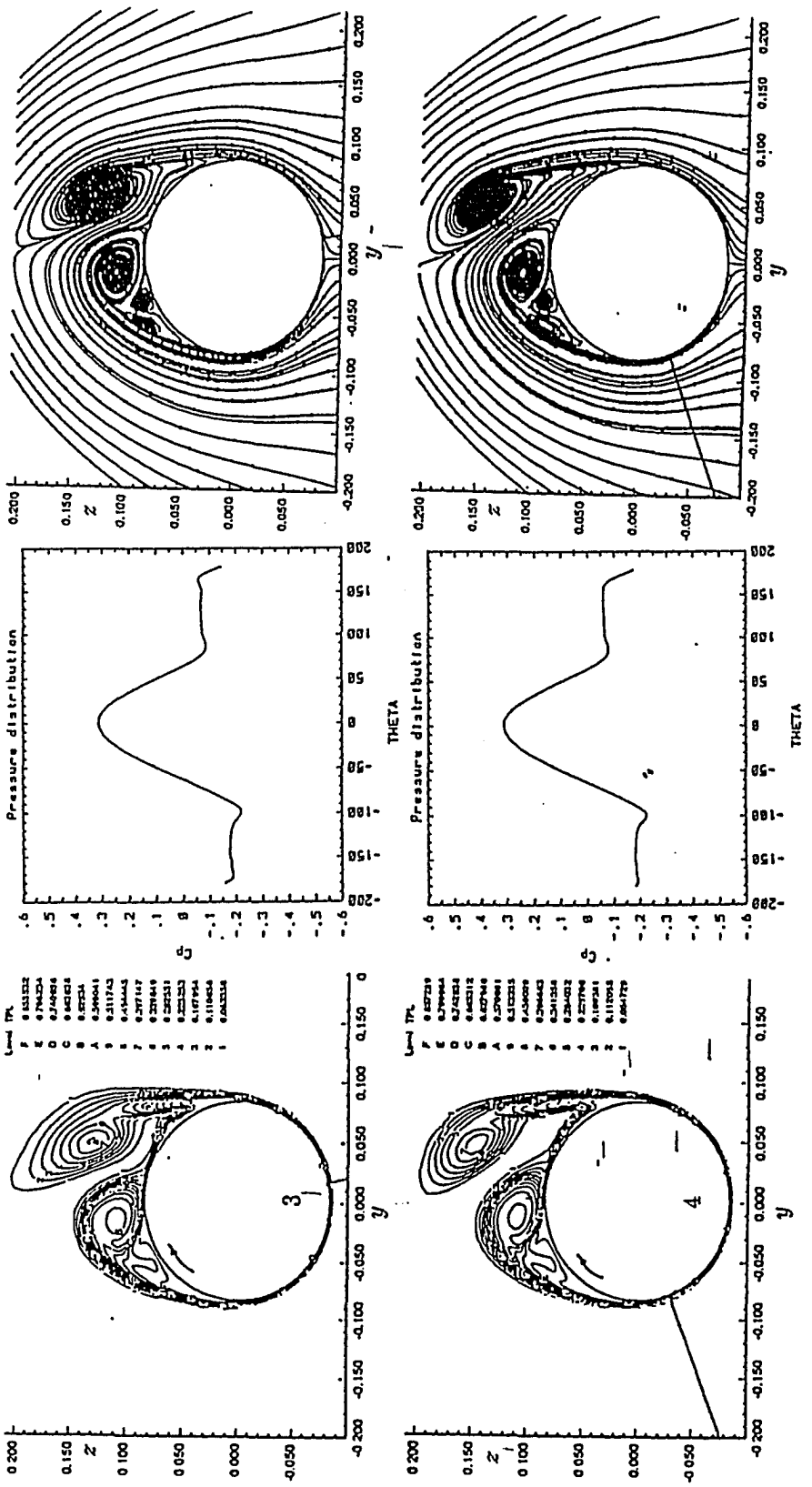

Figure 7.5: Continued

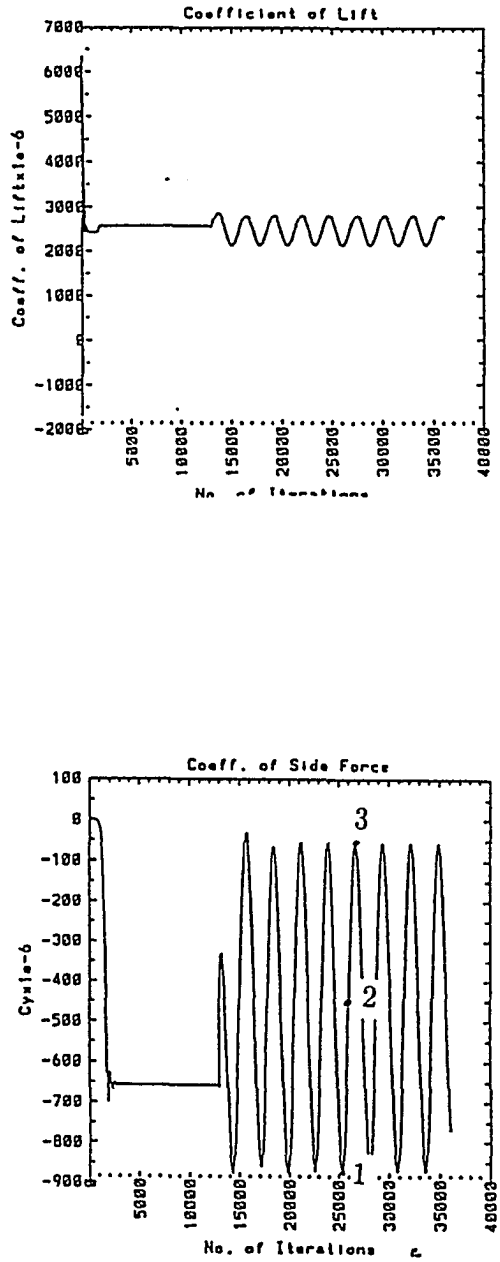

Figure 7.6: Lift coefficient and side-force coefficient history, $V_s = 0.2$ CCW spinning, $\tau = 2.749$, $\alpha = 20°$, $M_\infty = 1.8$, $R_e = 10^5$.

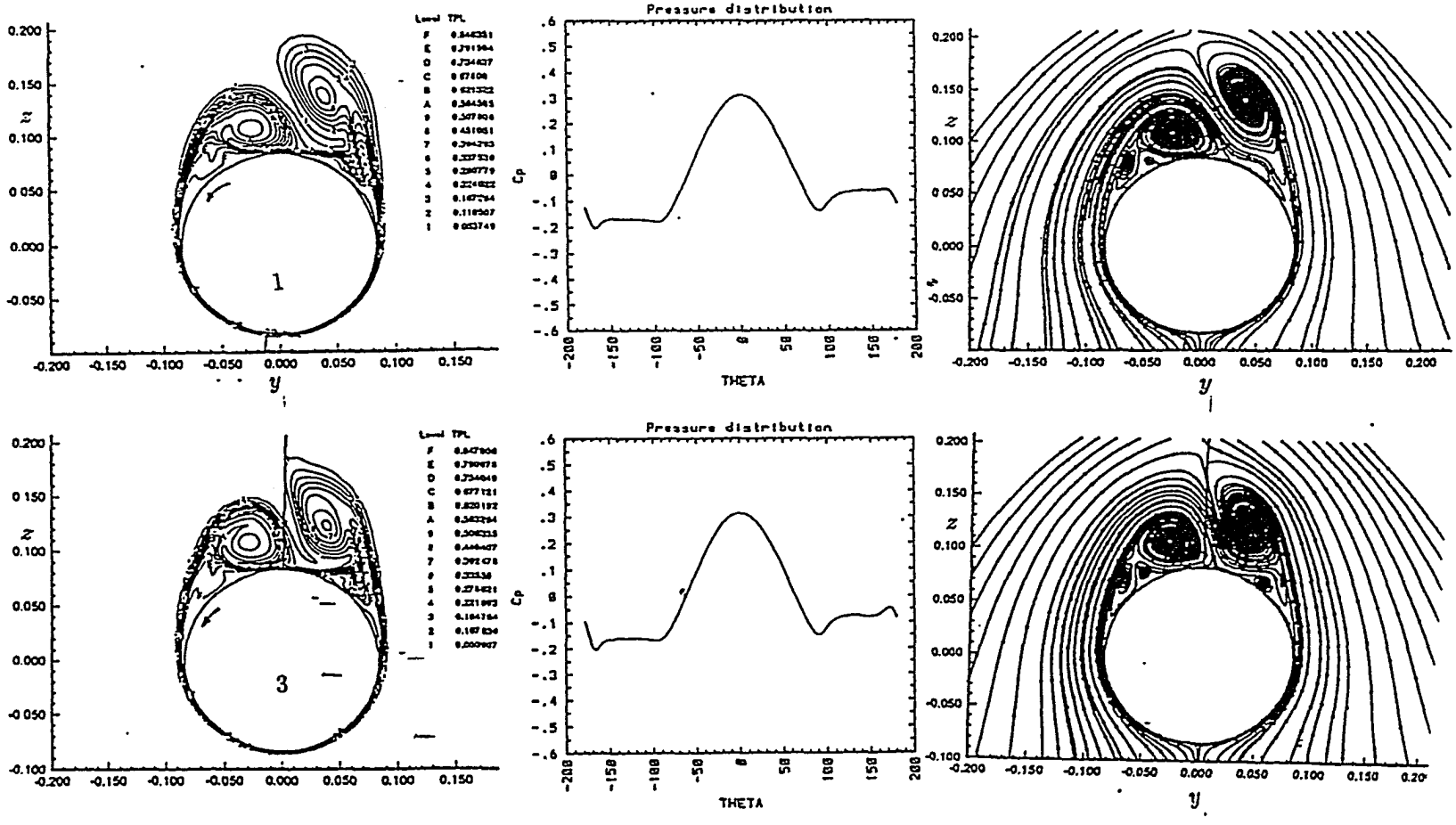

Figure 7.7: Snapshots of total pressure loss contours, surface pressure coefficient and cross-flow streamlines covering one cycle, $V_s = 0.2$ CCW spinning, $\tau = 2.749$, $\alpha = 20°$, $M_\infty = 1.8$, $R_e = 10^5$.

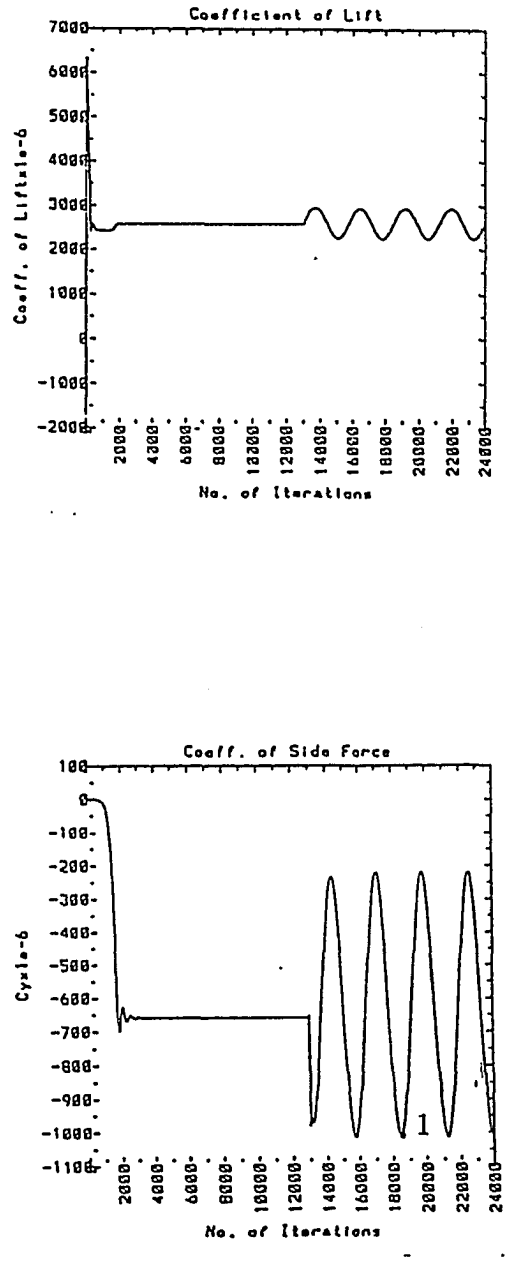

Figure 7.8: Lift coefficient and side-force coefficient history, $V_s = -0.2$ CW spinning, $\tau = 2.749$, $\alpha = 20°$, $M_\infty = 1.8$, $R_e = 10^5$.

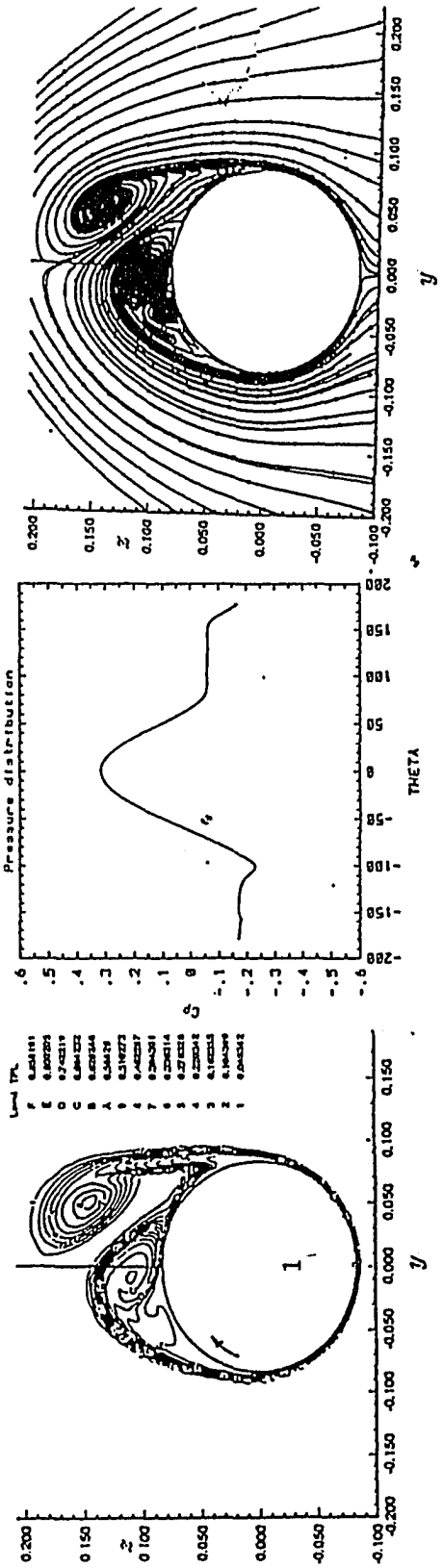

Figure 7.9: Snapshots of total pressure loss contours, surface pressure coefficient and cross-flow streamlines covering one cycle, $V_s = -0.2$ CW spinning, $\tau = 2.749$, $\alpha = 20°$, $M_\infty = 1.8$, $R_e = 10^5$.

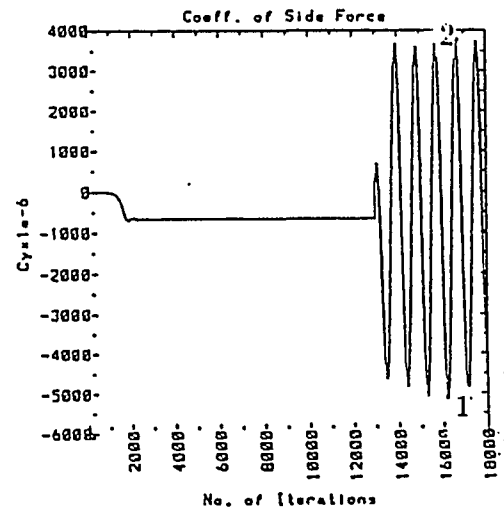

Figure 7.10: Side-force coefficient history, $V_s = 0.6$ CCW spinning, $\tau = 0.916$, $\alpha = 20°$, $M_\infty = 1.8$, $R_e = 10^5$.

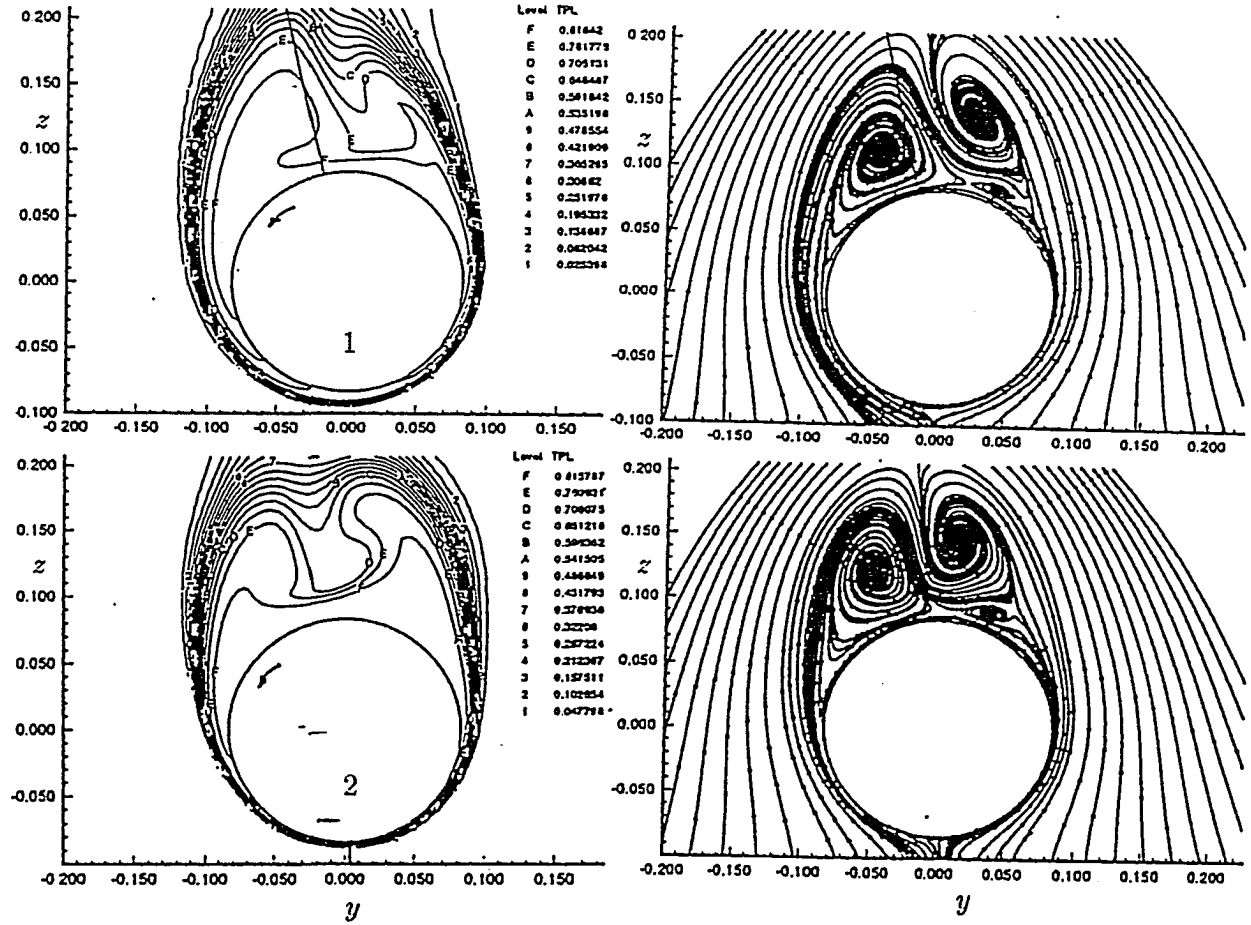

Figure 7.11: Snapshots of total pressure loss contours and cross-flow streamlines covering one cycle, $V_s = 0.6$ CCW spinning, $\tau = 0.916$, $\alpha = 20°$, $M_\infty = 1.8$, $R_e = 10^5$.

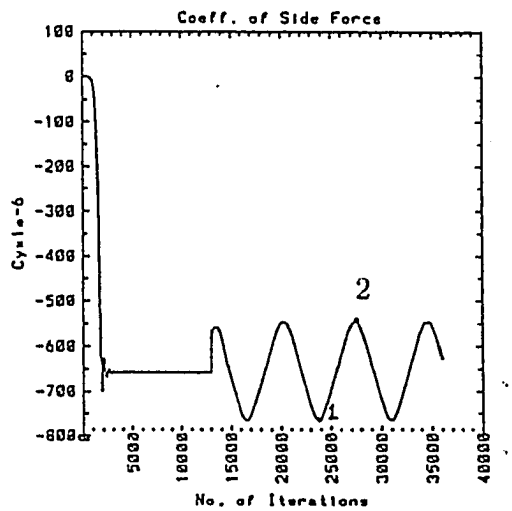

Figure 7.12: Side-force coefficient history, $V_s = 0.06\cos\left(\frac{2\pi}{\tau}t\right)$, rotary oscillation, $\tau = 7.2$, $\theta_a = 45°$, $\alpha = 20°$, $M_\infty = 1.8$, $R_e = 10^5$.

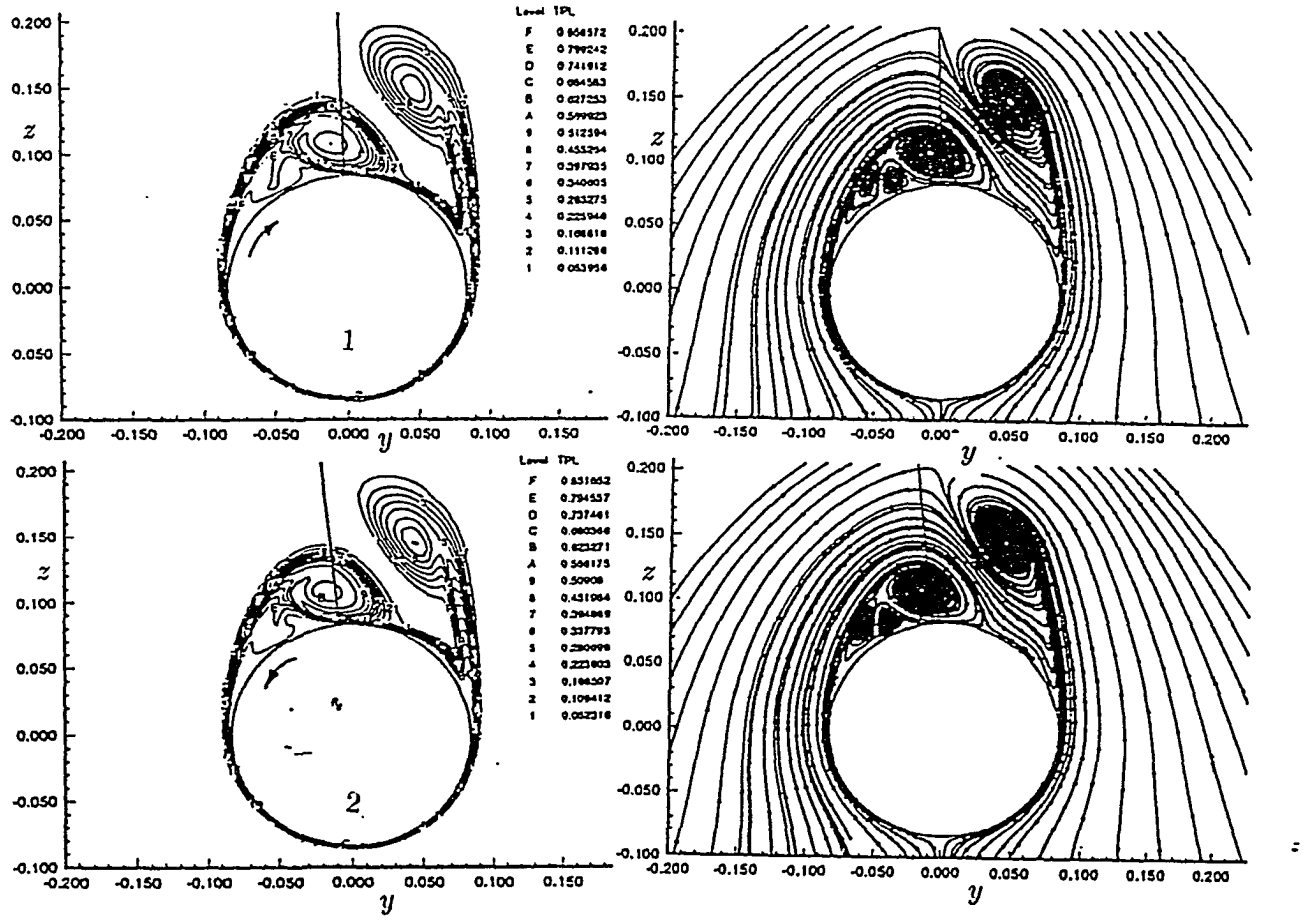

Figure 7.13: Snapshots of total pressure loss contours and cross-flow streamlines covering one cycle, $V_s = 0.06\cos\left(\frac{2\pi}{\tau}t\right)$, rotary oscillation, $\tau = 7.2$, $\theta_a = 45°$, $\alpha = 20°$, $M_\infty = 1.8$, $R_e = 10^5$.

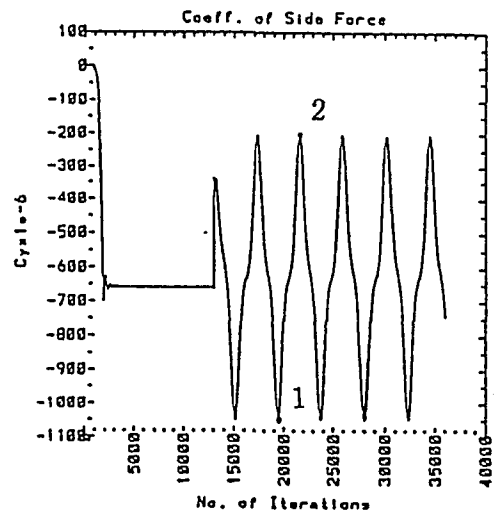

Figure 7.14: Side-force coefficient history, $V_s = 0.2\cos\left(\frac{2\pi}{\tau}t\right)$, rotary oscillation, $\tau = 4.3$, $\theta_a = 90°$, $\alpha = 20°$, $M_\infty = 1.8$, $R_e = 10^5$.

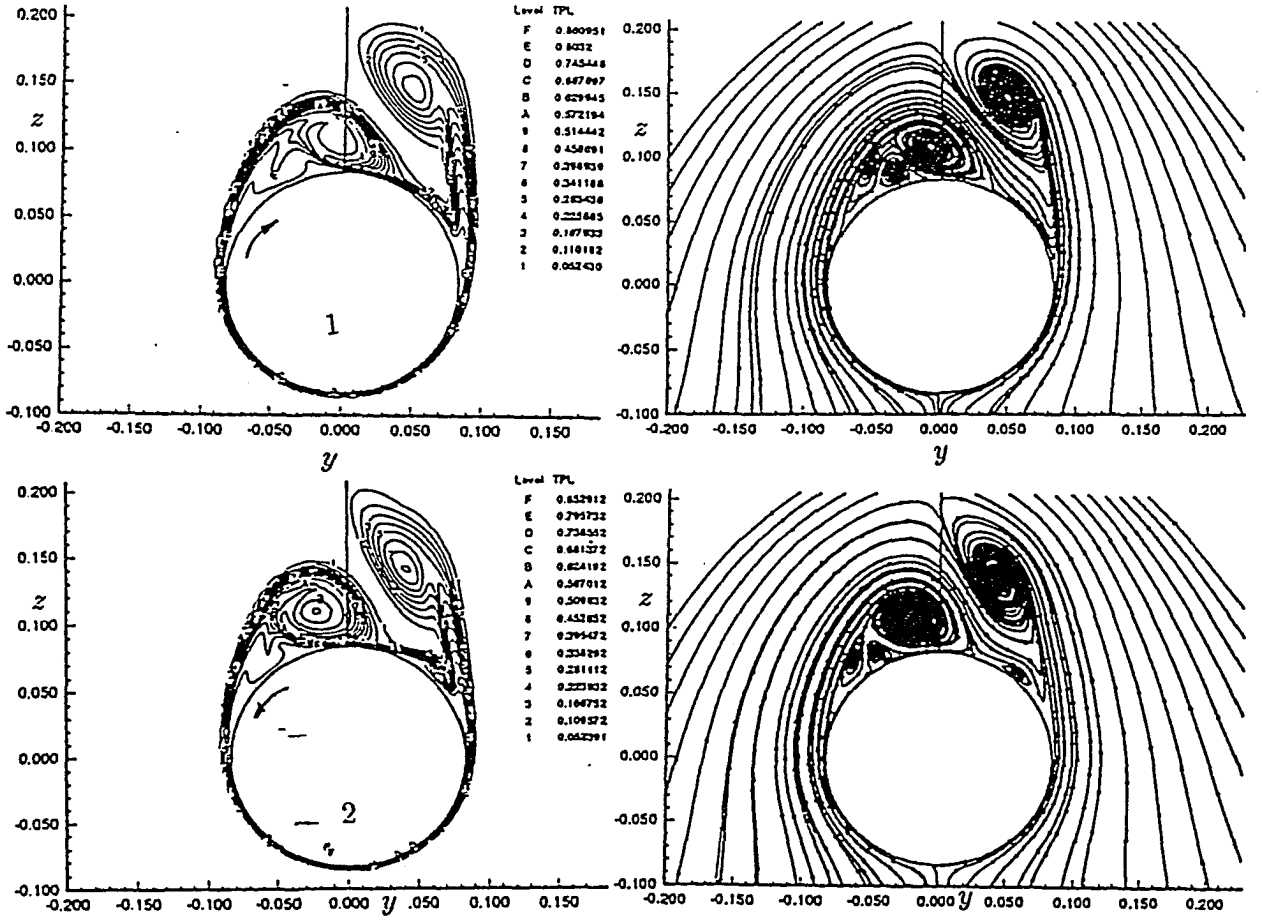

Figure 7.15: Snapshots of total pressure loss contours and cross-flow streamlines covering one cycle, $V_s = 0.2\cos\left(\frac{2\pi}{\tau}t\right)$, rotary oscillation, $\tau = 4.3$, $\theta_a = 90°$, $\alpha = 20°$, $M_\infty = 1.8$, $R_e = 10^5$.

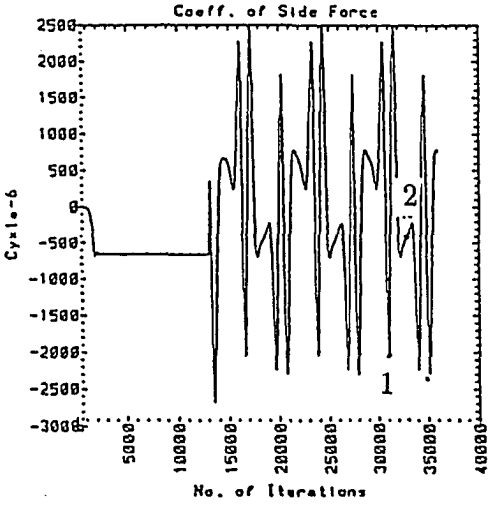

Figure 7.16: Side-force coefficient history, $V_s = 0.5\cos\left(\frac{2\pi}{\tau}t\right)$, rotary oscillation, $\tau = 7.2$, $0_a = 375°$, $\alpha = 20°$, $M_\infty = 1.8$, $R_e = 10^5$.

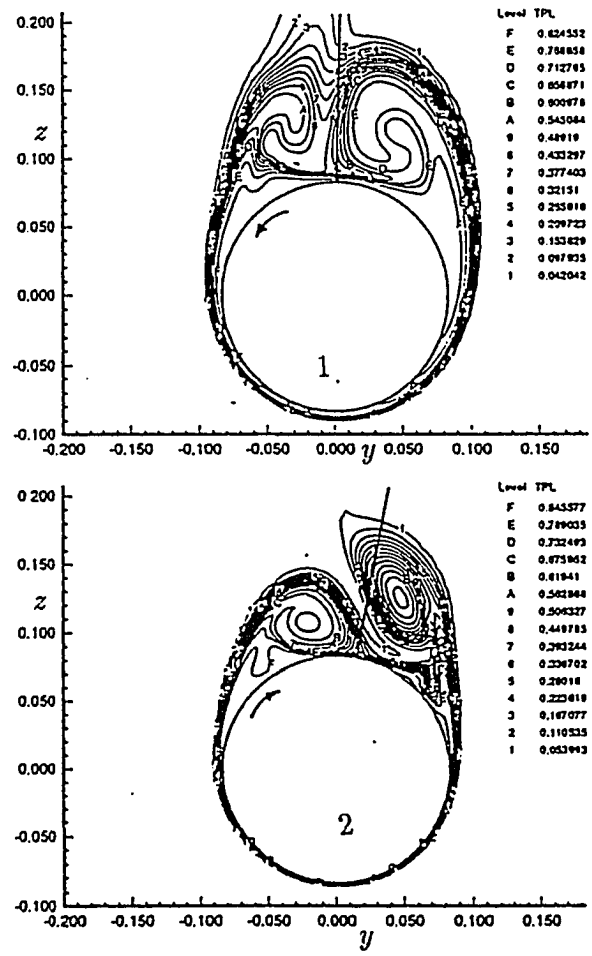

Figure 7.17: Snapshots of total pressure loss contours covering one cycle, $V_s = 0.5\cos\left(\frac{2\pi}{\tau}t\right)$, rotary oscillation, $\tau = 7.2$, $\theta_a = 375°$, $\alpha = 20°$, $M_\infty = 1.8$, $R_e = 10^5$.

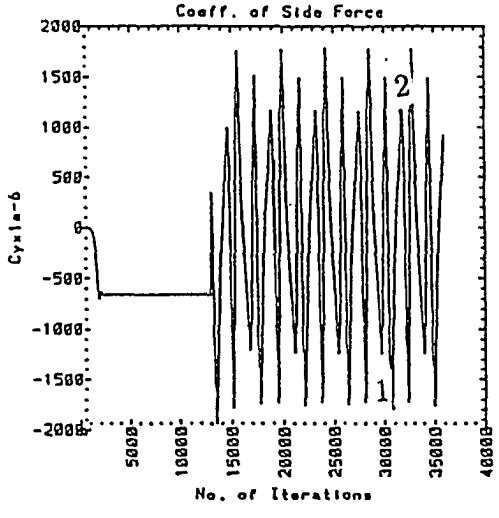

Figure 7.18: Side-force coefficient history, $V_s = 0.5\cos\left(\frac{2\pi}{\tau}t\right)$, rotary oscillation, $\tau = 4.3$, $\theta_a = 225°$, $\alpha = 20°$, $M_\infty = 1.8$, $R_e = 10^5$.

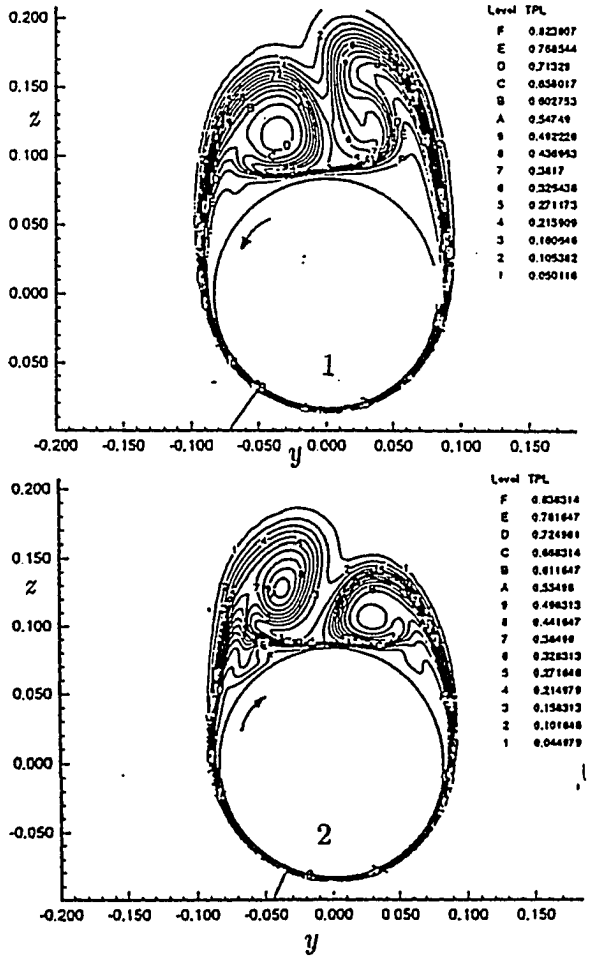

Figure 7.19: Snapshots of total pressure loss contours covering one cycle, $V_s = 0.5\cos\left(\frac{2\pi}{\tau}t\right)$, rotary oscillation, $\tau = 4.3$, $\theta_a = 225°$, $\alpha = 20°$, $M_\infty = 1.8$, $R_e = 10^5$.

CHAPTER 8

THREE DIMENSIONAL ACTIVE CONTROL USING INJECTION

8.1 Introduction

While solving the conical form of Navier-Stokes equations can be used to investigate the effectiveness of the various control methods qualitatively and in an efficient manner, the solution of the three-dimensional Navier-Stokes equations is required to obtain more accurate quantitative results concerning the performance of the different control methods. In this chapter, the solution of the thin-layer Navier-Stokes equations for controlling the flow asymmetry over a 5° semi-apex angle cone, using injection from the cone surface is presented.

8.2 Reference Case

Similar to the procedure used to study the different control methods in the previous chapters for the conical flow approach, a reference case for the three-dimensional asymmetry is presented in this section for the flow over a 5° semi-apex angle cone of unit length. The grid in the cross-flow planes has been generated using a modified Joukowski transformation with a geometric series for grid clustering in the normal direction. Also, a geometric series is used to cluster the grid in the axial direction

close to the nose. The grid used was $161 \times 55 \times 65$ in the wrap-around, normal and axial directions respectively and it is shown in Fig. 8.1.

For the present grid system, the applied boundary conditions were:

1. no slip and no penetration boundary conditions at the wall,

2. freestream boundary conditions at the far-field boundary. This is justified since the computational domain is extended to $21r_c$, where r_c is the local cone radius. Hence, the domain is large enough to capture the conical shock and the flow is entirely supersonic at the far-field boundary, and

3. extrapolation boundary conditions at the inflow and outflow boundaries of the computational domain.

While numerical disturbances are sufficient to simulate the wind tunnel and real flight disturbances in producing asymmetries in the flowfield for conical flow cases, such disturbances are insufficient for the three-dimensional solutions of the thin-layer Navier-Stokes equation due to the three-dimensional relieving effect. The disturbances in such cases must be applied physically, such as a transient short-time side-slip disturbance. For the cases under consideration, a side-slip disturbance of 10° for 300 iteration steps was applied. Next, the disturbance is removed and the asymmetry persisted.

In Fig. 8.2, the surface pressure coefficient is shown at ten different axial locations along the cone length, while Fig. 8.3 shows the total pressure loss contours at the same axial locations. From these figures, as well as Fig. 8.4, which is a three-dimensional view of stagnation pressure contours at different axial stations, one can see that the flowfield is highly asymmetric. Also, It is observed that the vortex structure is changing in the axial direction and hence the side forces is changing from positive to negative along the cone length. Examining the figures at different axial locations,

one can conclude that the asymmetry grows spatially in the axial direction. This is in agreement with both experimental and computational results relating onset of asymmetry with small disturbances starting at the slender body nose and growing in the aft direction. Since the current solution is steady, the vortex shedding is a spatial one.

The fact that the flow asymmetry is not one-side biased constrains the choice of the applicable control method. Uniform injection would be of limited effectiveness, since either it will be applied in a symmetric or antisymmetric way and the two methods will not be effective along the cone length. Hence, a variable injection mass flow rate per unit area approach, similar to that used in the conical flow solution in Chap. 6, was considered.

8.3 Normal Injection

In this section, several cases are presented to investigate the effect of normal injection on the flow asymmetry over a sharp cone, which was presented in the last section. The cases were chosen to investigate the effect of mass flow rate per unit area, and the effective length l_i at which the injection was applied, measured from the cone apex. The effective length, l_i, was chosen to start at the nose because that was where the disturbance producing asymmetry was initiated.

8.3.1 Normal injection, $l_i = 0.1$, $\dot{m}_{max} = 0.05$

The reference case solution was used as the initial condition for the case under consideration, in which l_i was chosen to be 0.1. The effective angle of the injection, θ_i extends from $-67.5°$ to $67.5°$, where θ_i is measured from the leeward side of the geometric plane of symmetry.

Figures 8.5, 8.6 and 8.7 show the surface pressure coefficient at different axial stations, the total pressure loss contours at different axial stations and the stagnation pressure contours over cone, respectively. Comparing these figures with the corresponding figures of the reference case, the following can be observed:

- The asymmetry has been eliminated over about 70% of the cone length, and has been reduced significantly over the remaining 30% of the cone length.
- Both the surface pressure coefficient and the total pressure loss contours show small regions of asymmetry that grow along the cone length.

These observations show that the level or area of injection used is insufficient to eliminate the asymmetry over the entire cone length.

8.3.2 Normal injection, $l_i = 0.15$, $\dot{m}_{max} = 0.05$

The results of this case in which the l_i is increased to 0.15, are shown in Figs. 8.8, 8.9 and 8.10. Comparing these results with the results of the previous case in which $l_i = 0.1$, one can see that the flowfield was symmetric up to about 80% of the cone length. However, asymmetry is observed in the region near the trailing edge.

8.3.3 Normal injection, $l_i = 0.26$, $\dot{m}_{max} = 0.05$

Increasing the effective length of the injection to 0.26 eliminated the flow asymmetry over the entire cone length. The results of this case are shown in Figs. 8.11, 8.12 and 8.13. No asymmetry in the flowfield or the surface pressure can be observed.

8.3.4 *Normal injection,* $l_i = 0.26$, $\dot{m}_{max} = 0.03$

To study the effect of the injection mass flow rate, the previous case with $l_i = 0.26$ and $\dot{m}_{max} = 0.05$ was repeated with $\dot{m}_{max} = 0.03$. The results of this case are shown in Figs. 8.14, 8.15 and 8.16. Not much difference can be observed between the two cases. This is in agreement with the experimental results of Ref. 67. It is concluded that the injection area is an important parameter in the injection control method.

8.4 *Tangential Injection,* $l_i = 0.1$, $\dot{m}_{max} = 0.05$

This case is similar to the normal injection case, the direction of the injection is tangent to the body surface, towards the leeward plane of geometric symmetry. The initial condition for this case was the solution of the reference case obtained in Sec. 8.2. The effective angle of injection is chosen to extend from $-67.5°$ to $67.5°$, and the maximum mass flow rate per unit area was taken to be 0.05, while the effective length of injection was 0.1. The results of this case are shown in Figs. 8.17, 8.18 and 8.19. The figures show that the flow has recovered its symmetry and there is no sign of any significant asymmetry.

Comparing these figures with the equivalent figures for the normal injection case (Figs. 8.5, 8.6) and 8.7, we can conclude that tangential injection is more effective in eliminating the side force for the same flow conditions.

8.5 *Summary*

In this chapter, the three-dimensional thin-layer Navier-Stokes equations were solved for the flow over a cone. A reference case, asymmetric solution, was obtained using a transient short-time side-slip disturbance. The resulting asymmetry was found to

be persistent upon removing the side-slip disturbance. Both normal and tangential injection were investigated. Prescribed effective injection lengths were required to recover the symmetry of the flowfield. The effect of the injection mass flow rate was also investigated. The tangential injection was found to be more effective, compared to the normal injection, when the effective injection angle, effective injection length, and maximum mass flow rate were kept constants.

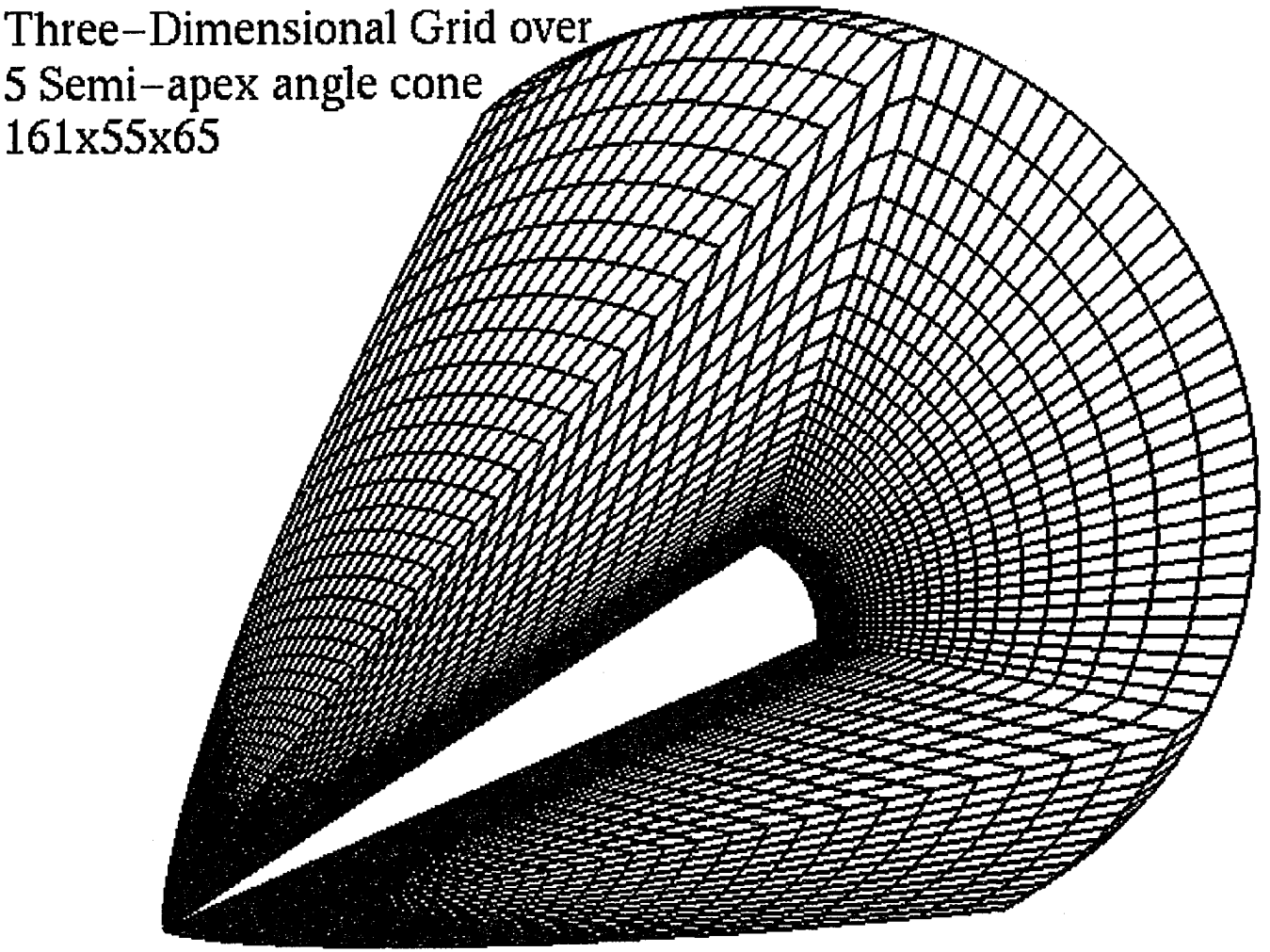

Figure 8.1: Three-dimensional grid over cone, $161 \times 55 \times 65$

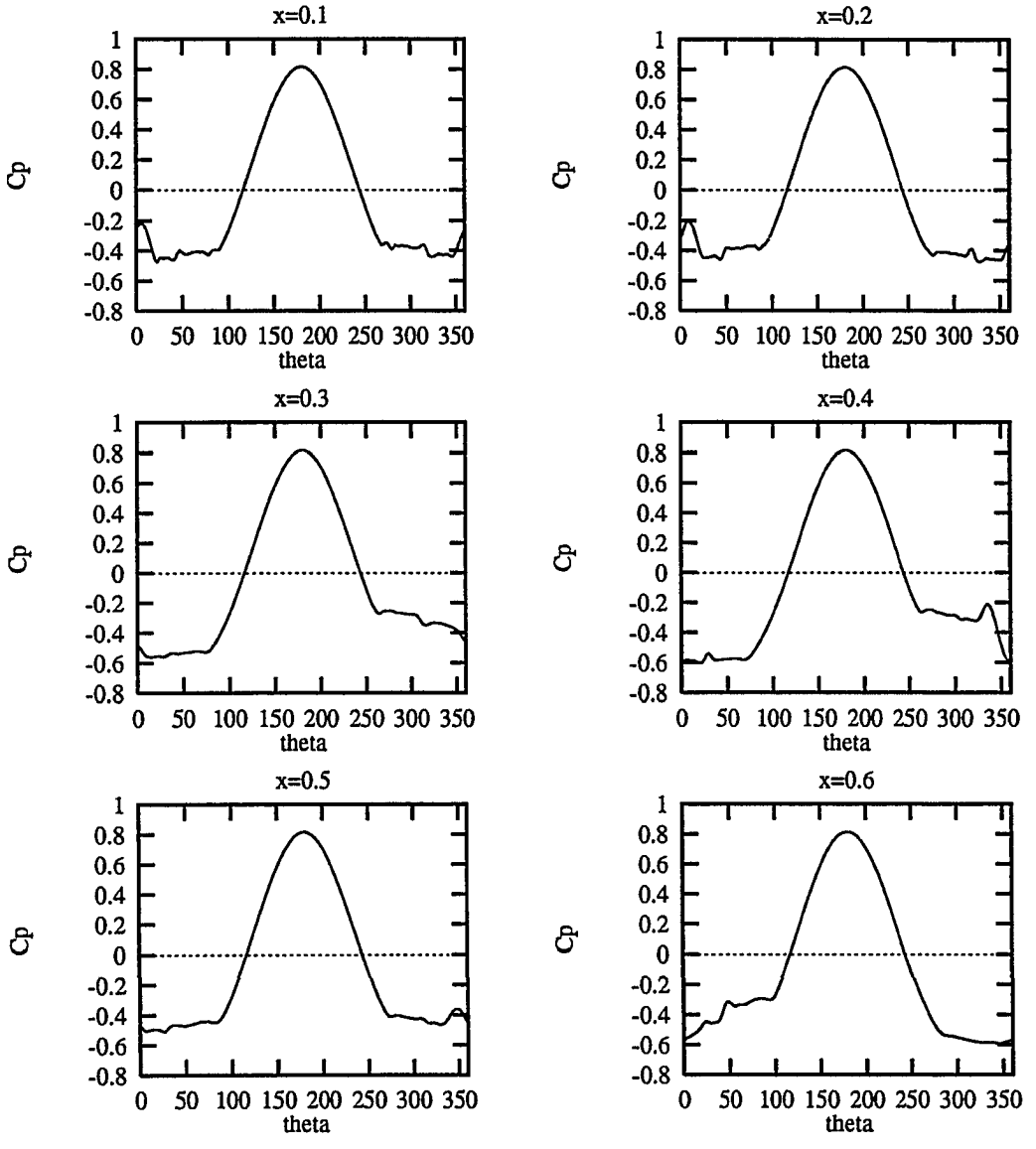

Figure 8.2: Surface pressure coefficient at different axial stations for flow around a circular cone at $\alpha = 40°$, $M_\infty = 1.4$, $R_e = 6 \times 10^6$.

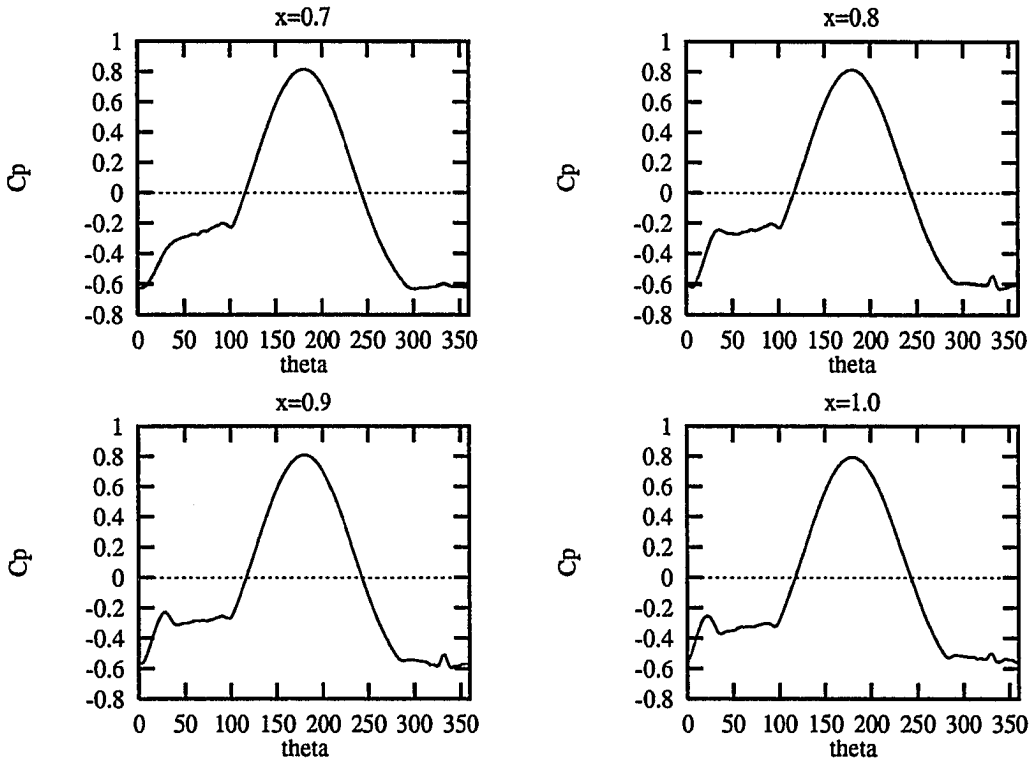

Figure 8.2: Continued

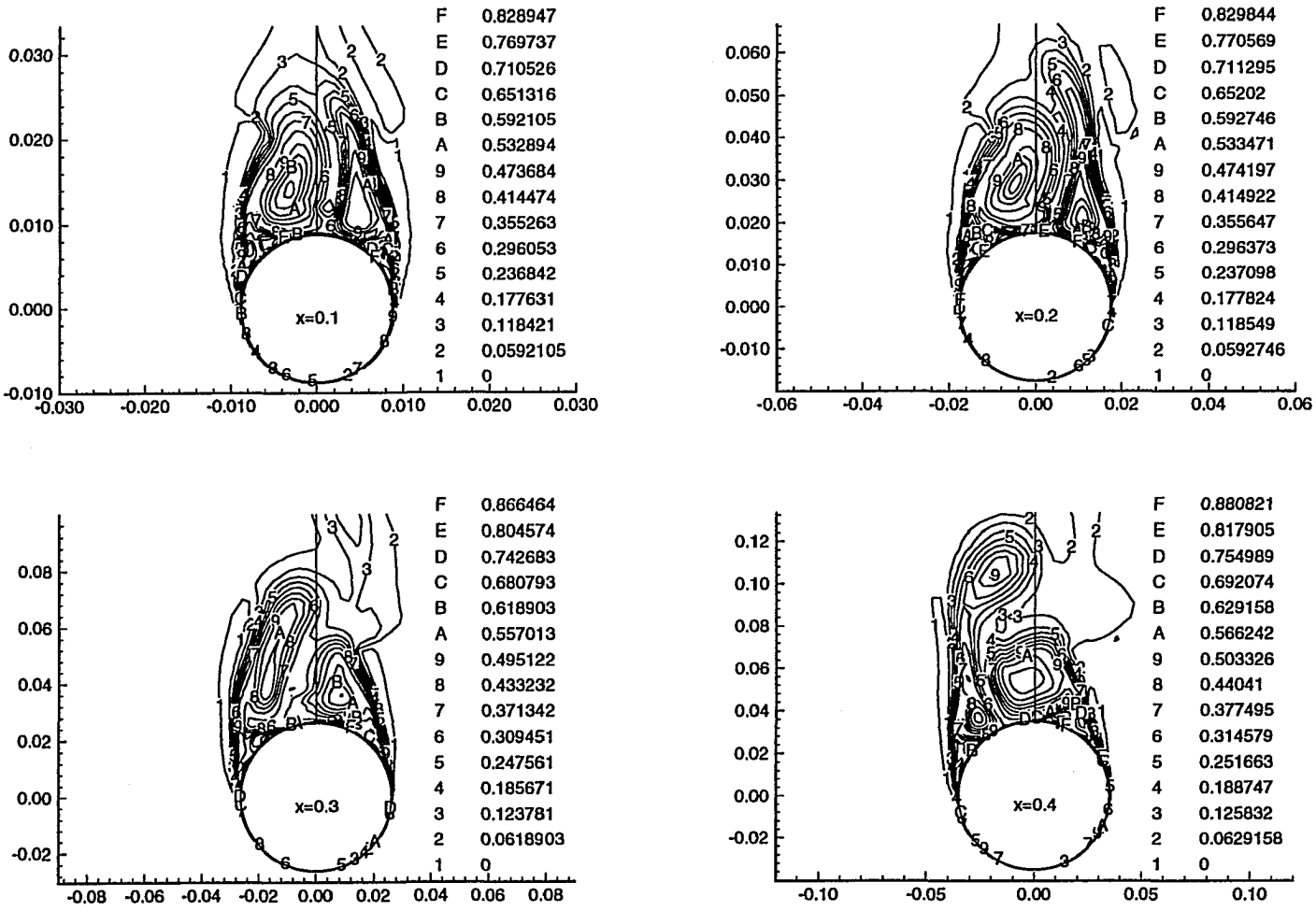

Figure 8.3: Total pressure loss contours at different axial stations for flow around a circular cone at $\alpha = 40°$, $M_\infty = 1.4$, $R_e = 6 \times 10^6$.

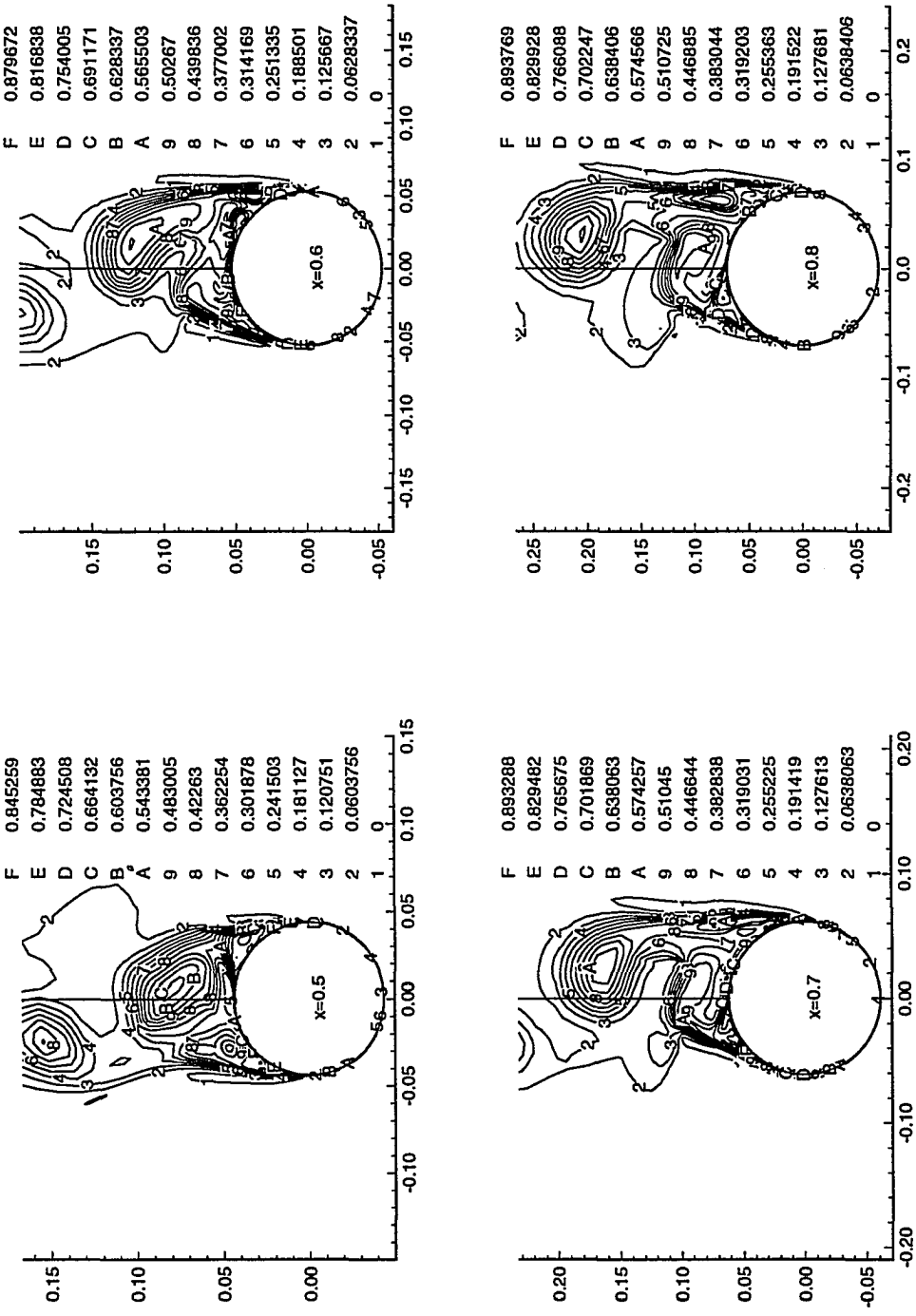

Figure 8.3: Continued

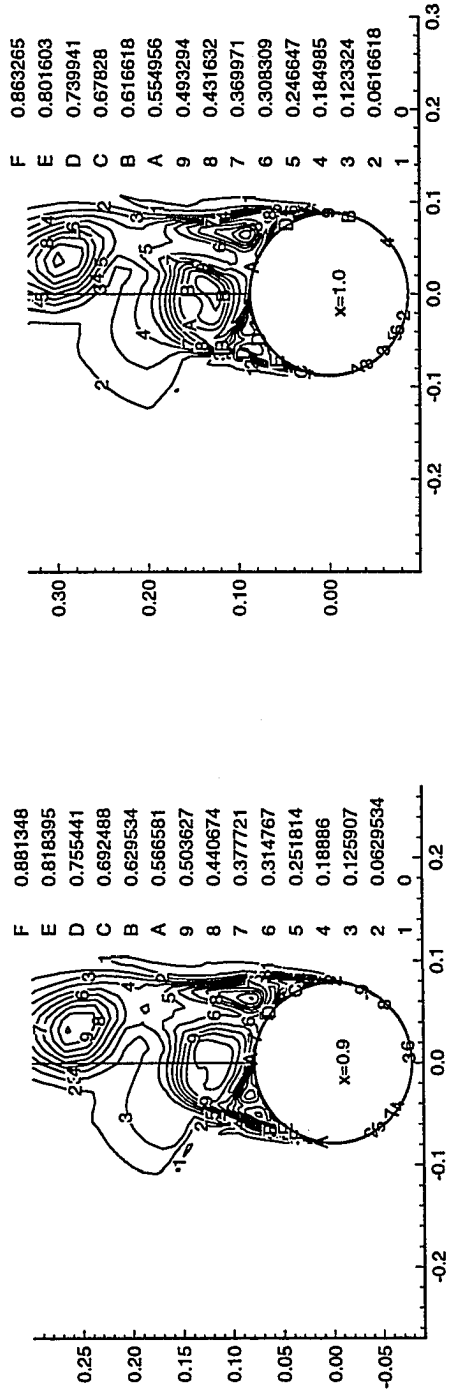

Figure 8.3: Continued

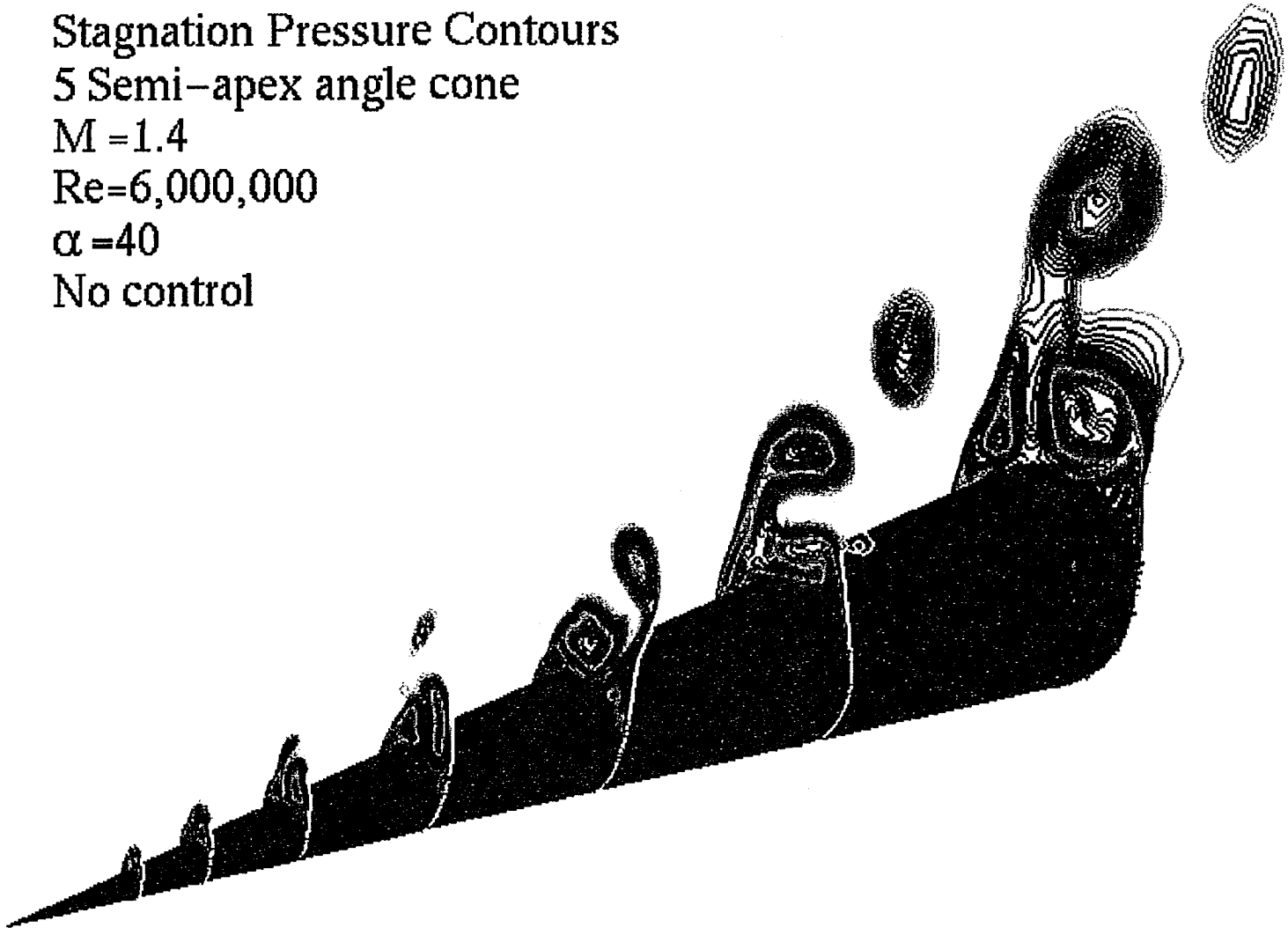

Figure 8.4: Stagnation pressure contours at different axial stations

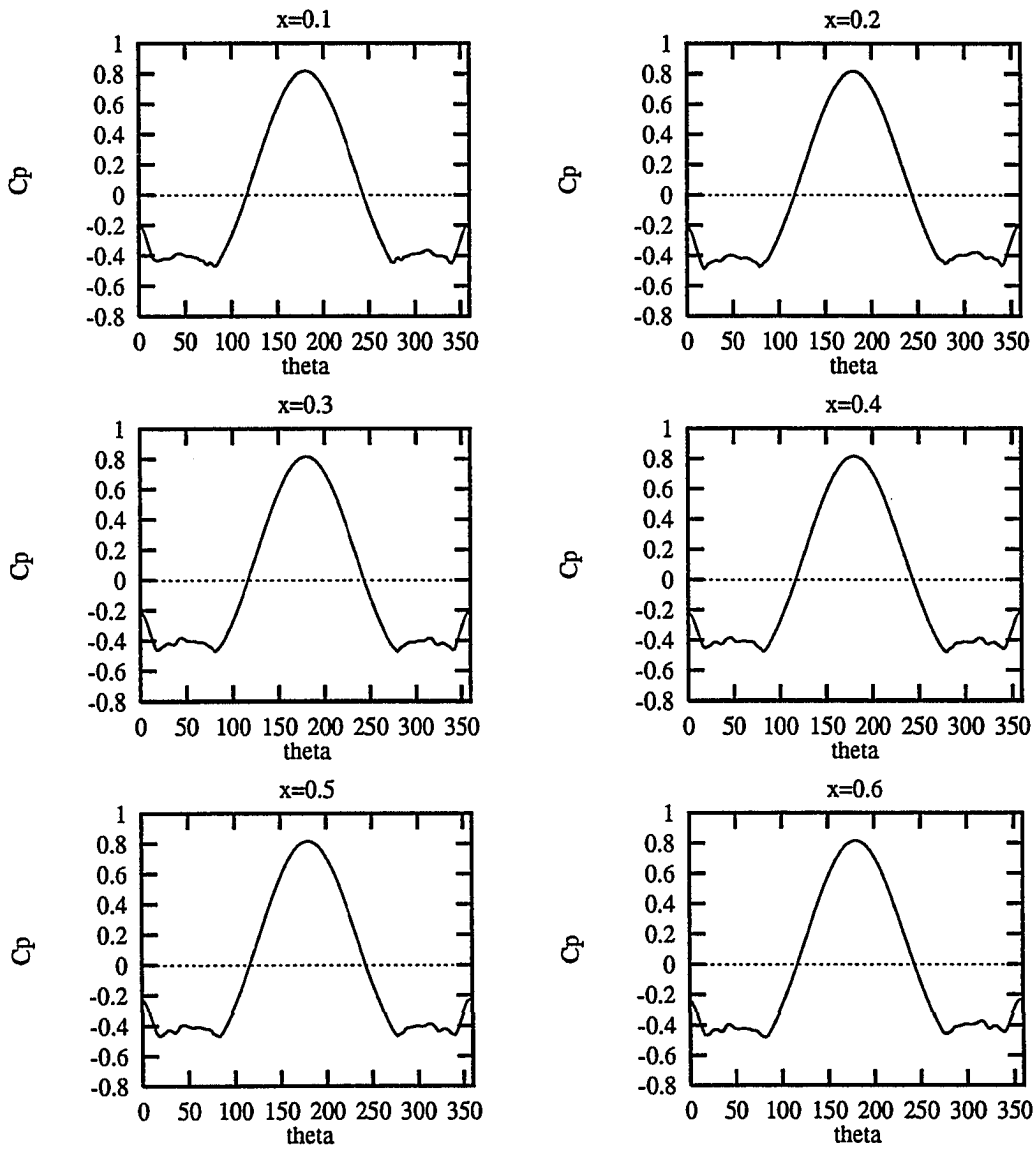

Figure 8.5: Surface pressure coefficient at different axial stations for flow around a circular cone with normal injection at $\alpha = 40°$, $M_\infty = 1.4$, $R_e = 6 \times 10^6$, $l_i = 0.1$, $\theta_i = -67.5 \rightarrow 67.5$, $\dot{m}_{max} = 0.05$.

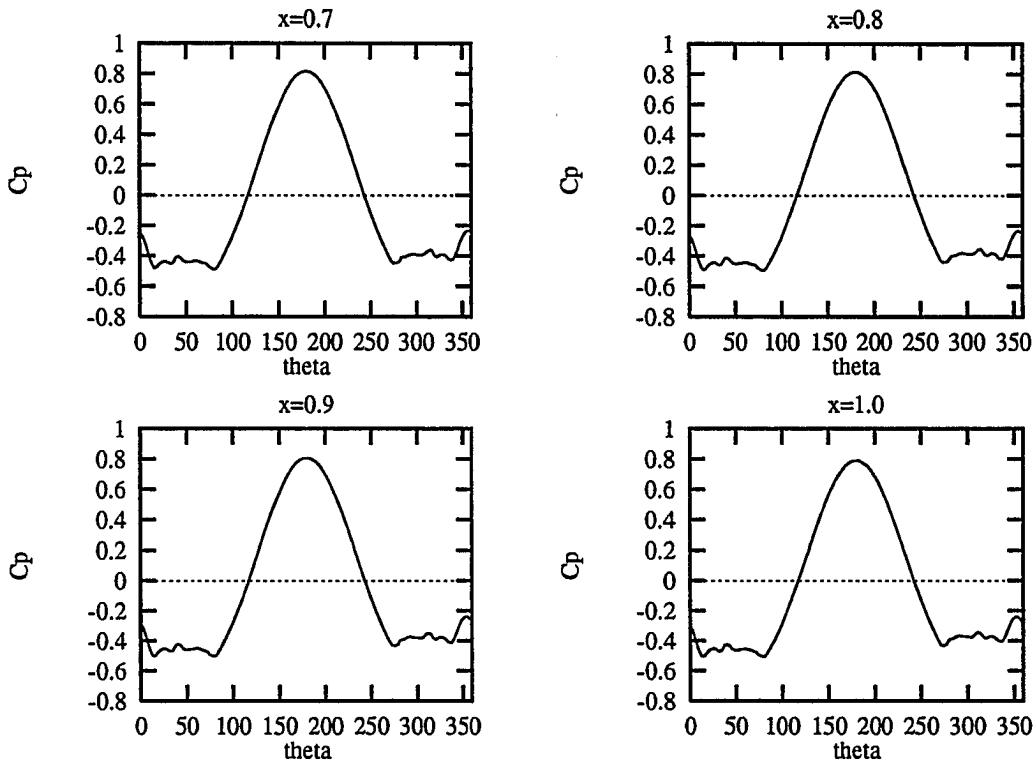

Figure 8.5: Continued

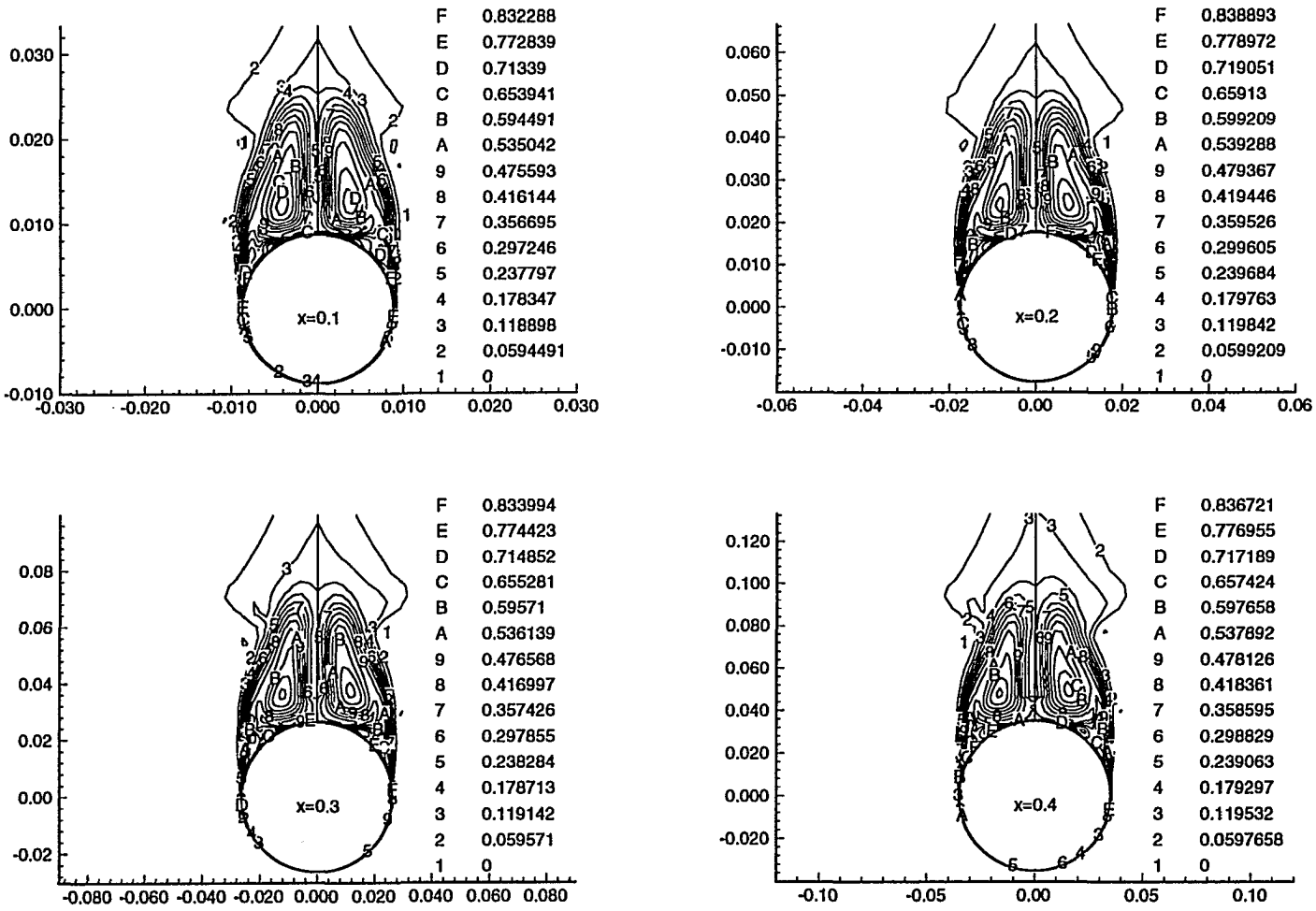

Figure 8.6: Total pressure loss contours at different axial stations for flow around flow around a circular cone with normal injection at $\alpha = 40°$, $M_\infty = 1.4$, $R_e = 6 \times 10^6$, $l_i = 0.1$, $\theta_i = -67.5 \rightarrow 67.5$, $\dot{m}_{max} = 0.05$.

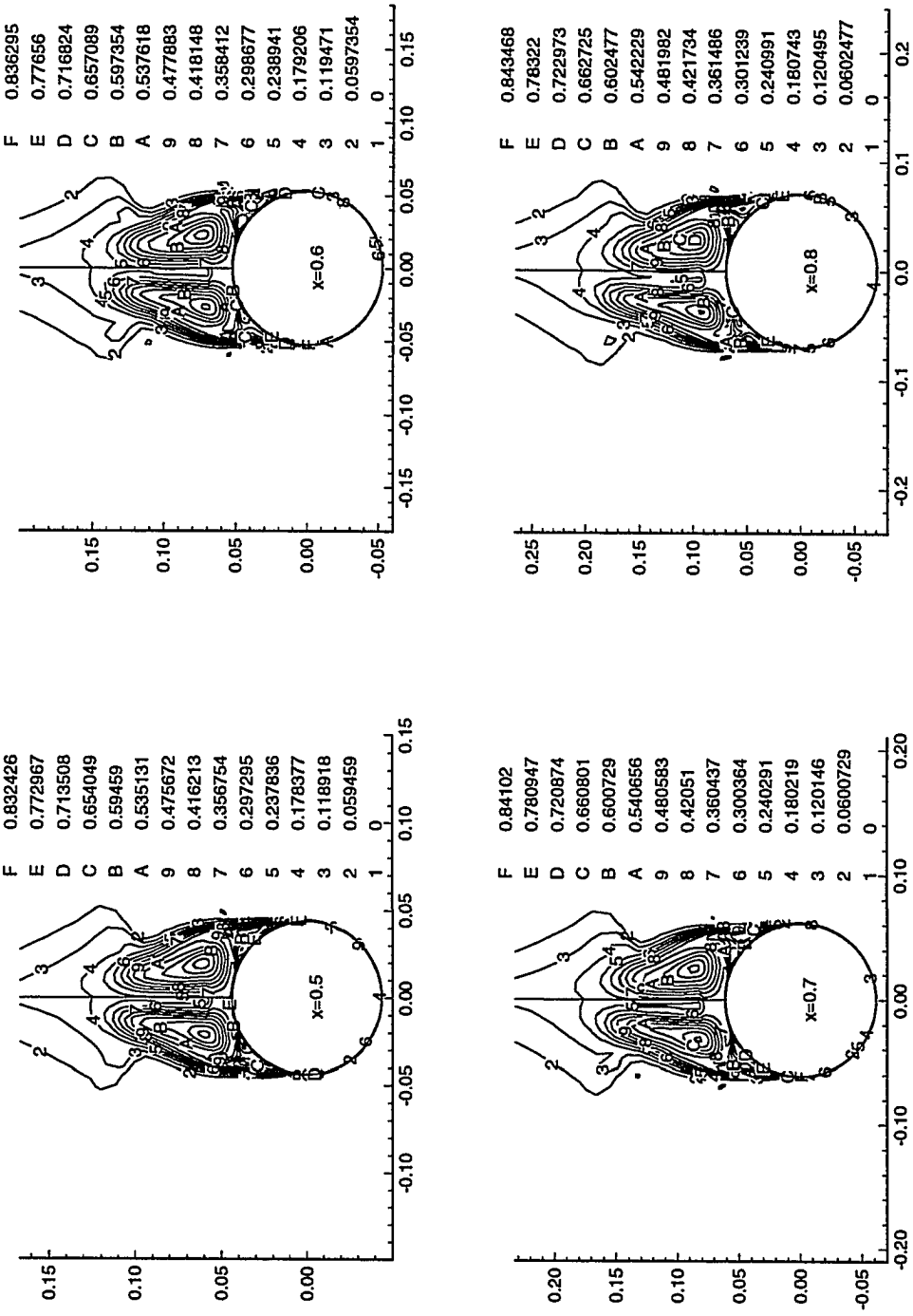

Figure 8.6: Continued

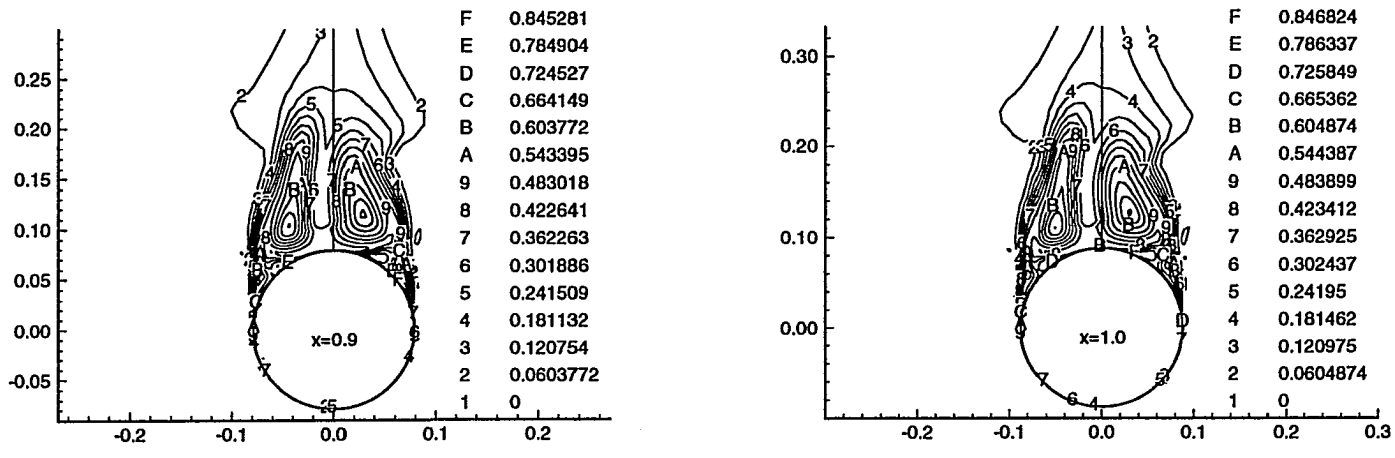

Figure 8.6: Continued

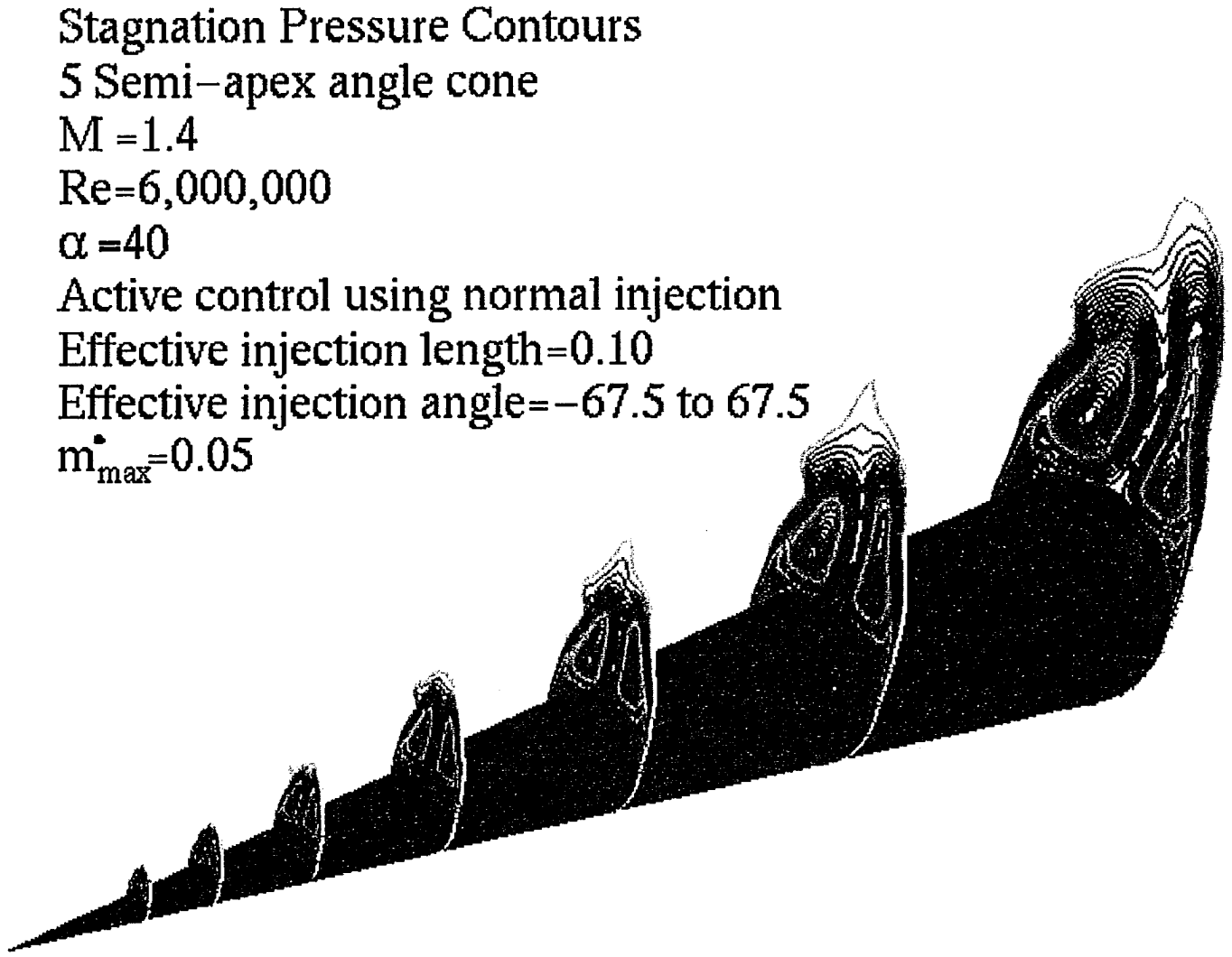

Figure 8.7: Stagnation pressure at different axial stations

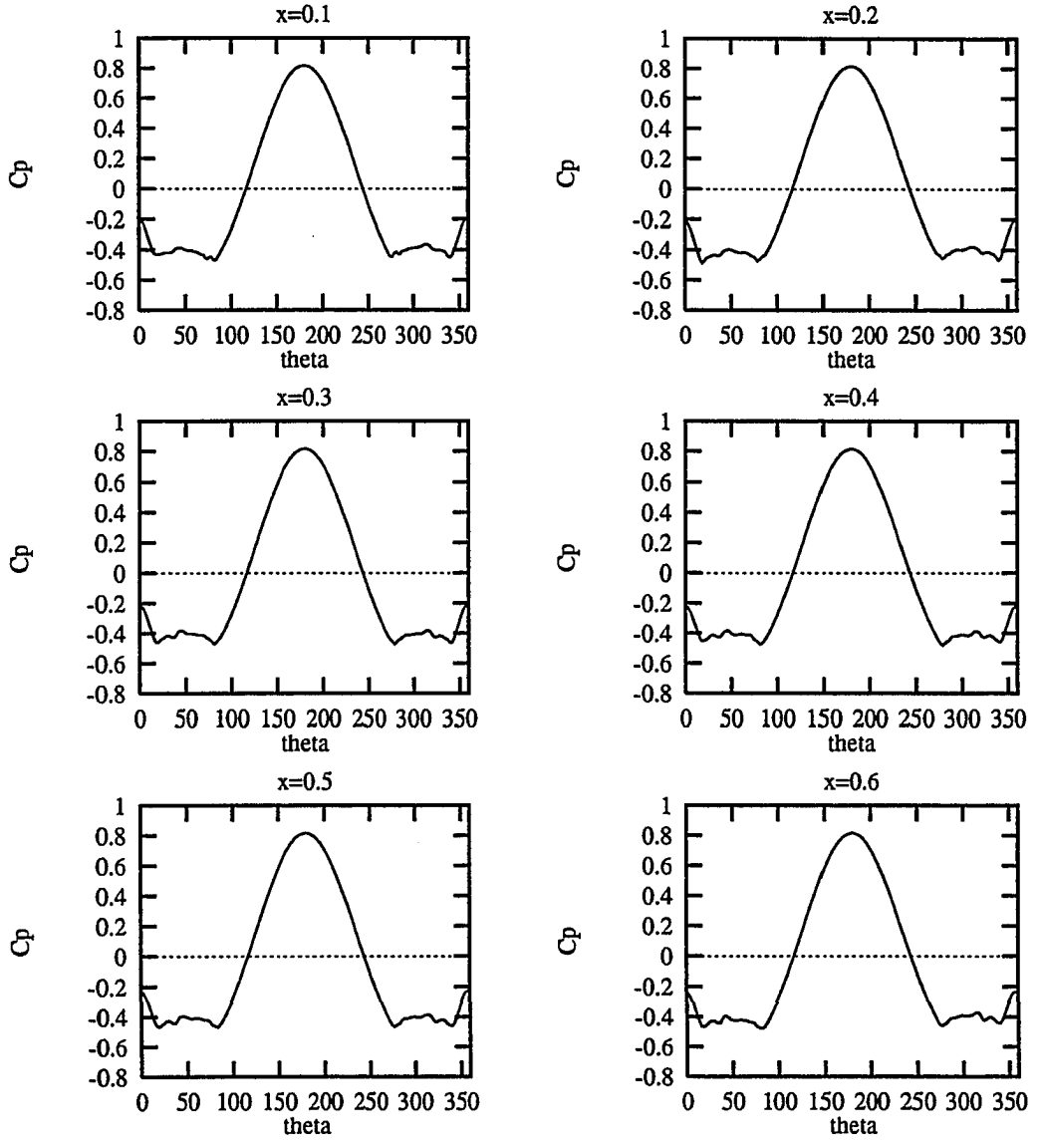

Figure 8.8: Surface pressure coefficient at different axial stations for flow around a circular cone with normal injection at $\alpha = 40°$, $M_\infty = 1.4$, $R_e = 6 \times 10^6$, $l_i = 0.15$, $\theta_i = -67.5 \rightarrow 67.5$, $\dot{m}_{max} = 0.05$.

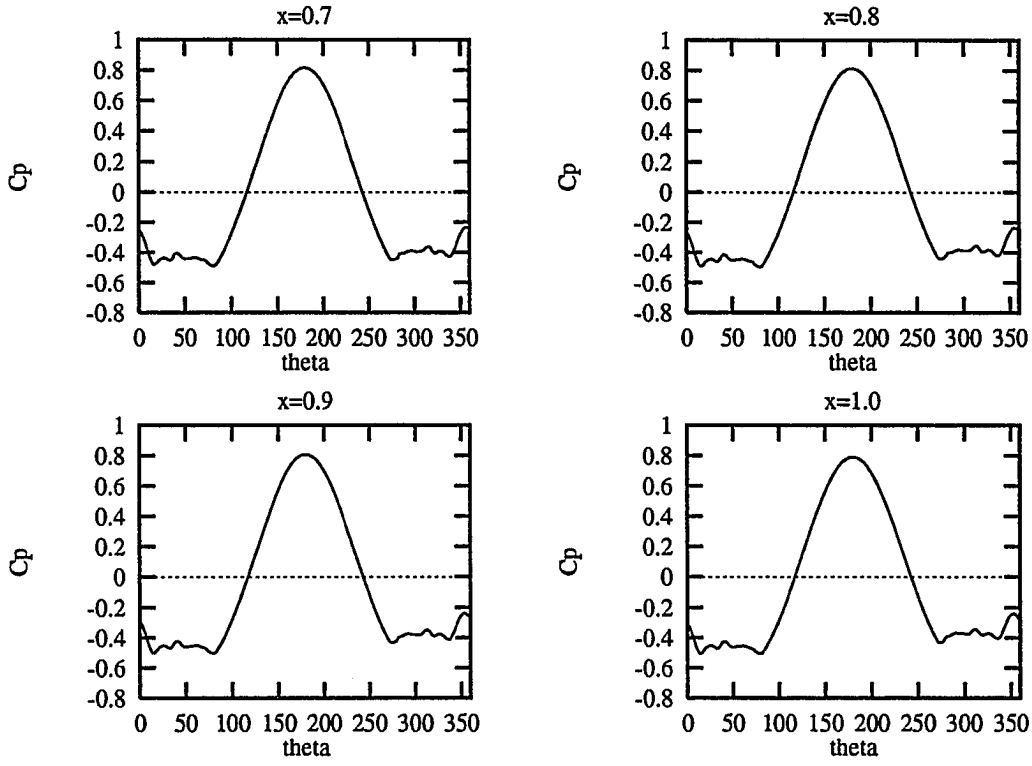

Figure 8.8: Continued

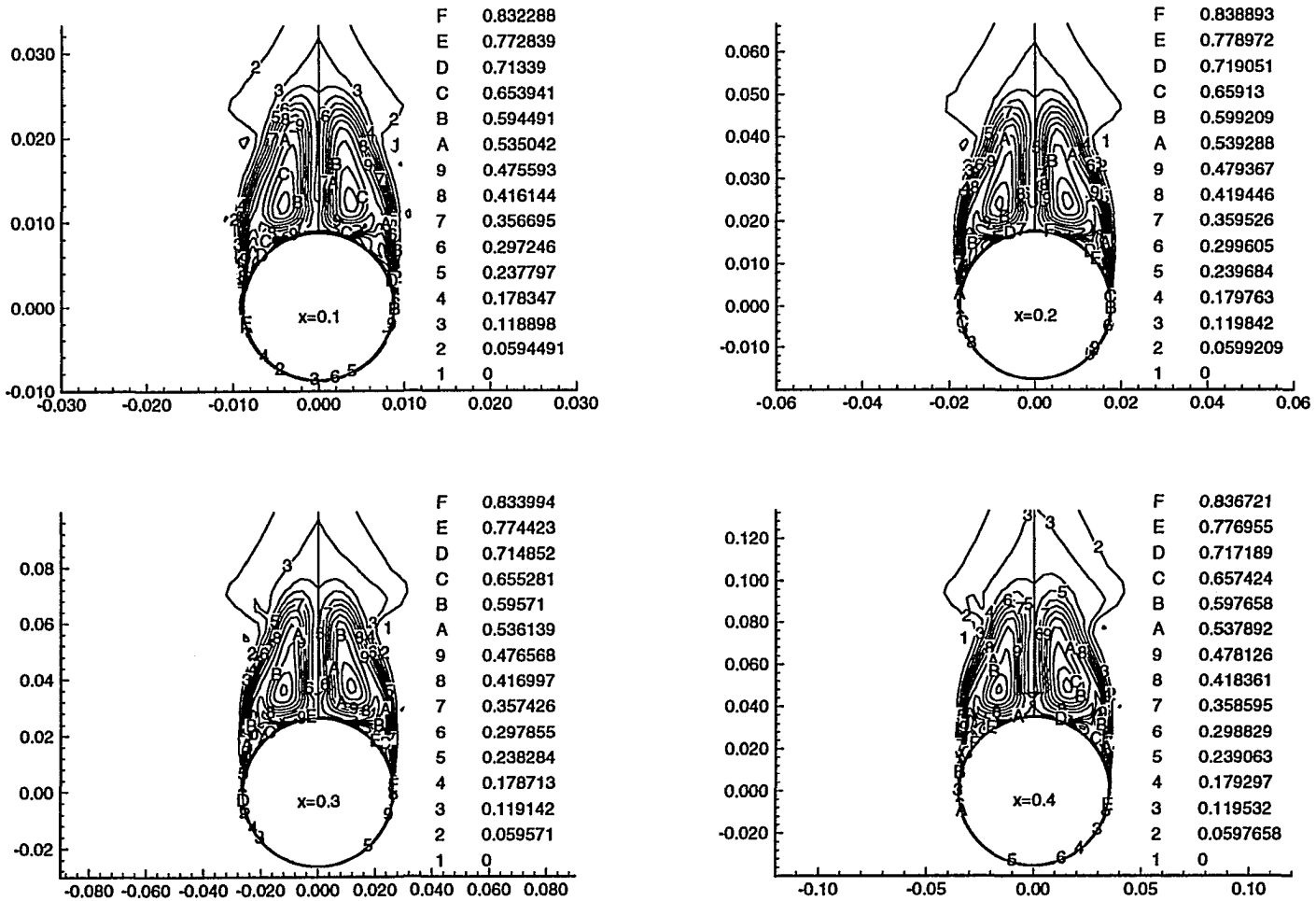

Figure 8.9: Total pressure loss contours at different axial stations for flow around a circular cone with normal injection at $\alpha = 40°$, $M_\infty = 1.4$, $R_e = 6 \times 10^6$, $l_i = 0.15$, $\theta_i = -67.5 \rightarrow 67.5$, $\dot{m}_{max} = 0.05$.

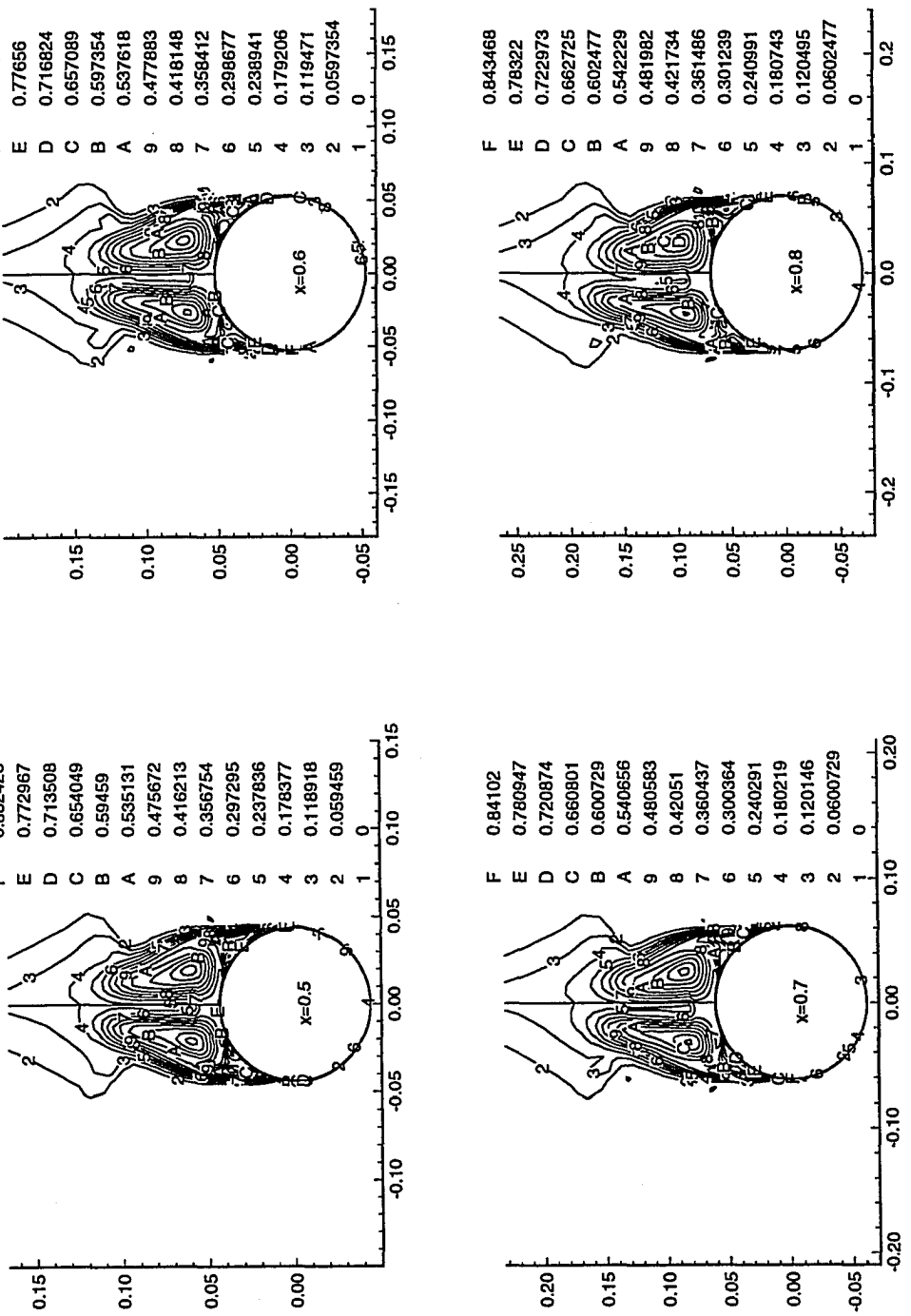

Figure 8.9: Continued

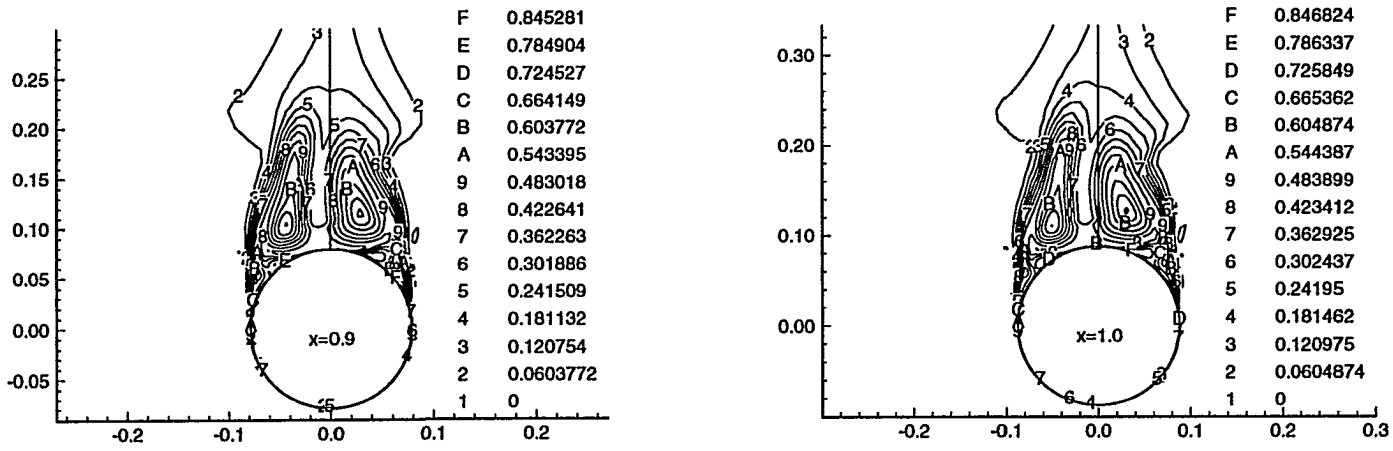

Figure 8.9: Continued

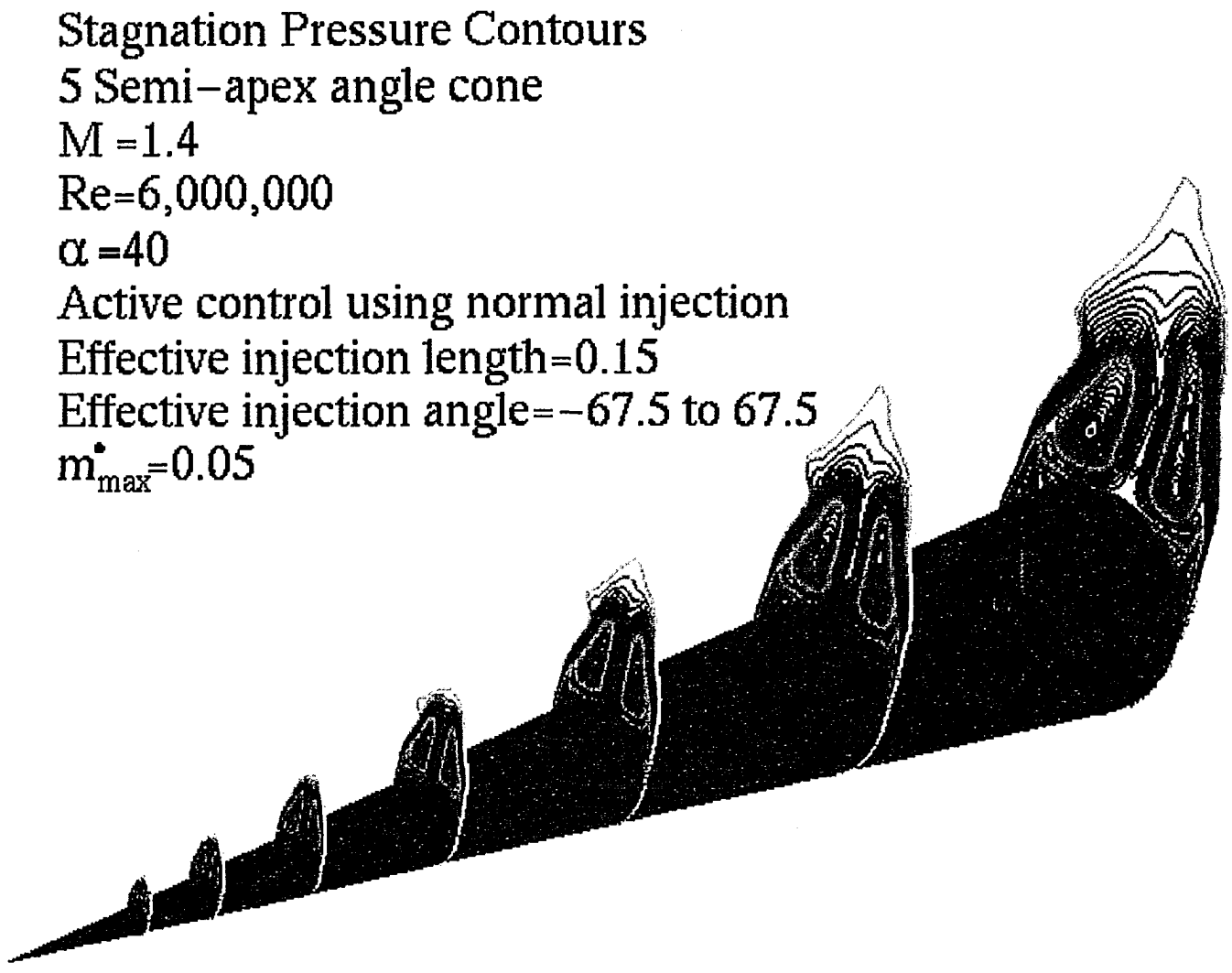

Figure 8.10: Stagnation pressure contours at different axial stations

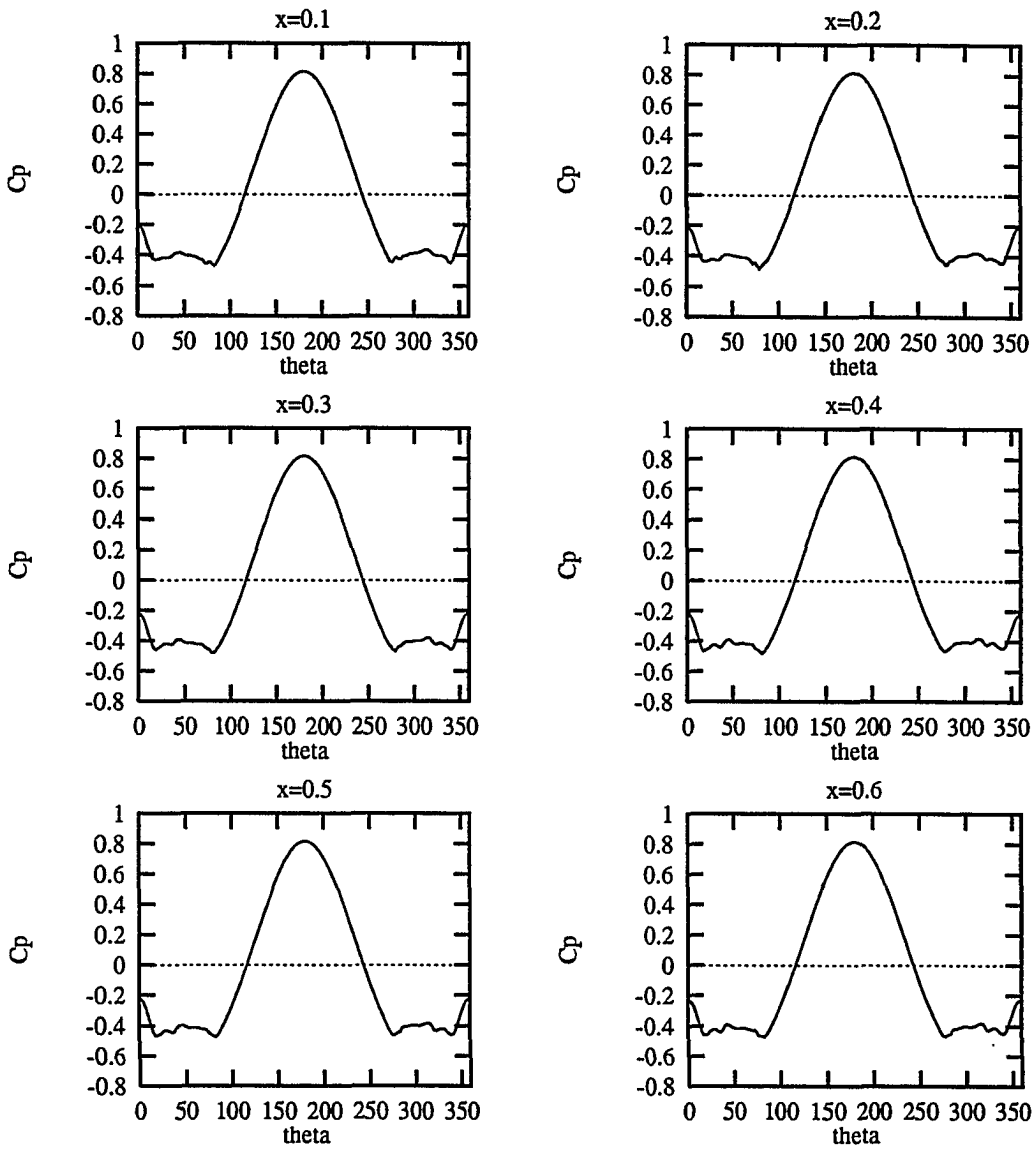

Figure 8.11: Surface pressure coefficient at different axial stations for flow around a circular cone at $\alpha = 40°$, $M_\infty = 1.4$, $R_e = 6 \times 10^6$, $l_i = 0.26$, $\theta_i = -67.5 \rightarrow 67.5$, $\dot{m}_{max} = 0.05$.

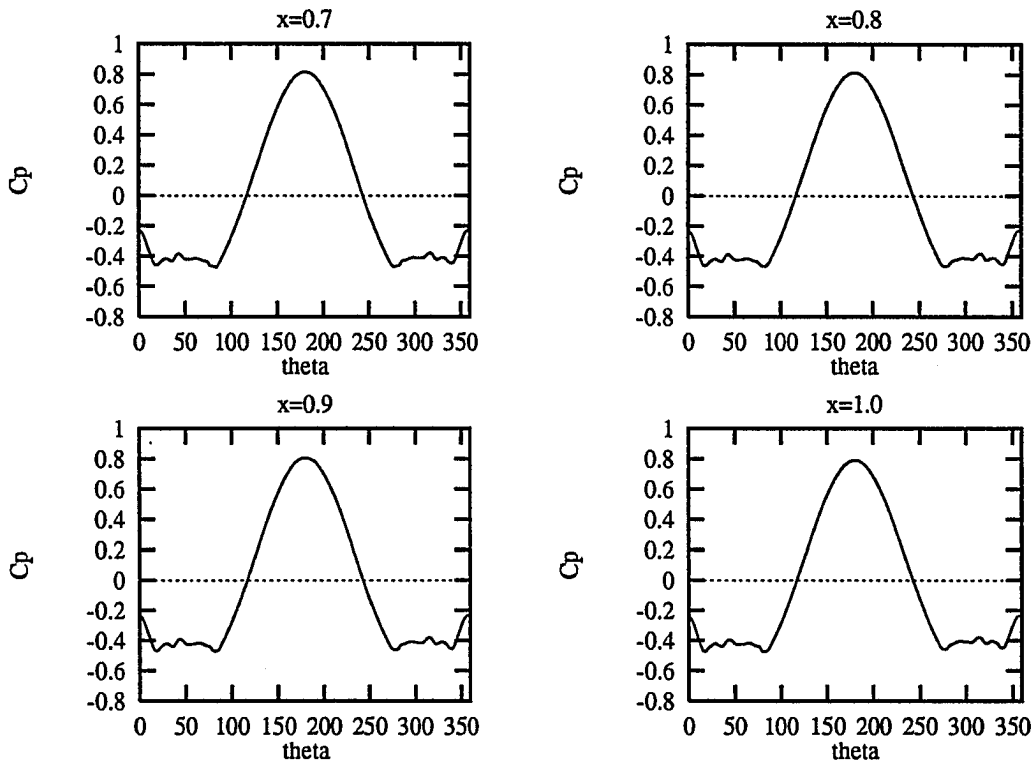

Figure 8.11: Continued

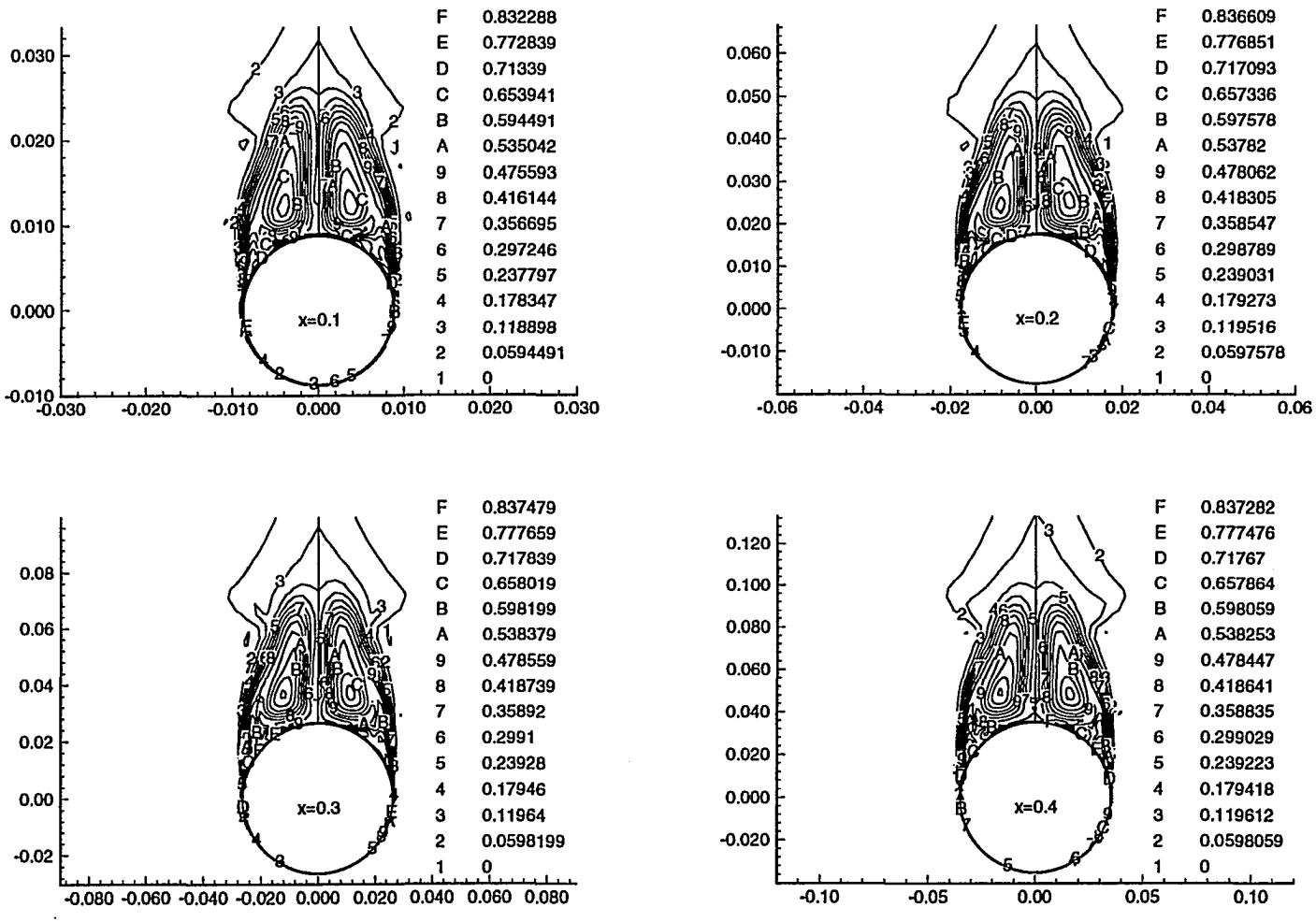

Figure 8.12: Total pressure loss contours at different axial stations for flow around a circular cone at $\alpha = 40°$, $M_\infty = 1.4$, $R_e = 6 \times 10^6$, $l_i = 0.26$, $\theta_i = -67.5 \rightarrow 67.5$, $\dot{m}_{max} = 0.05$.

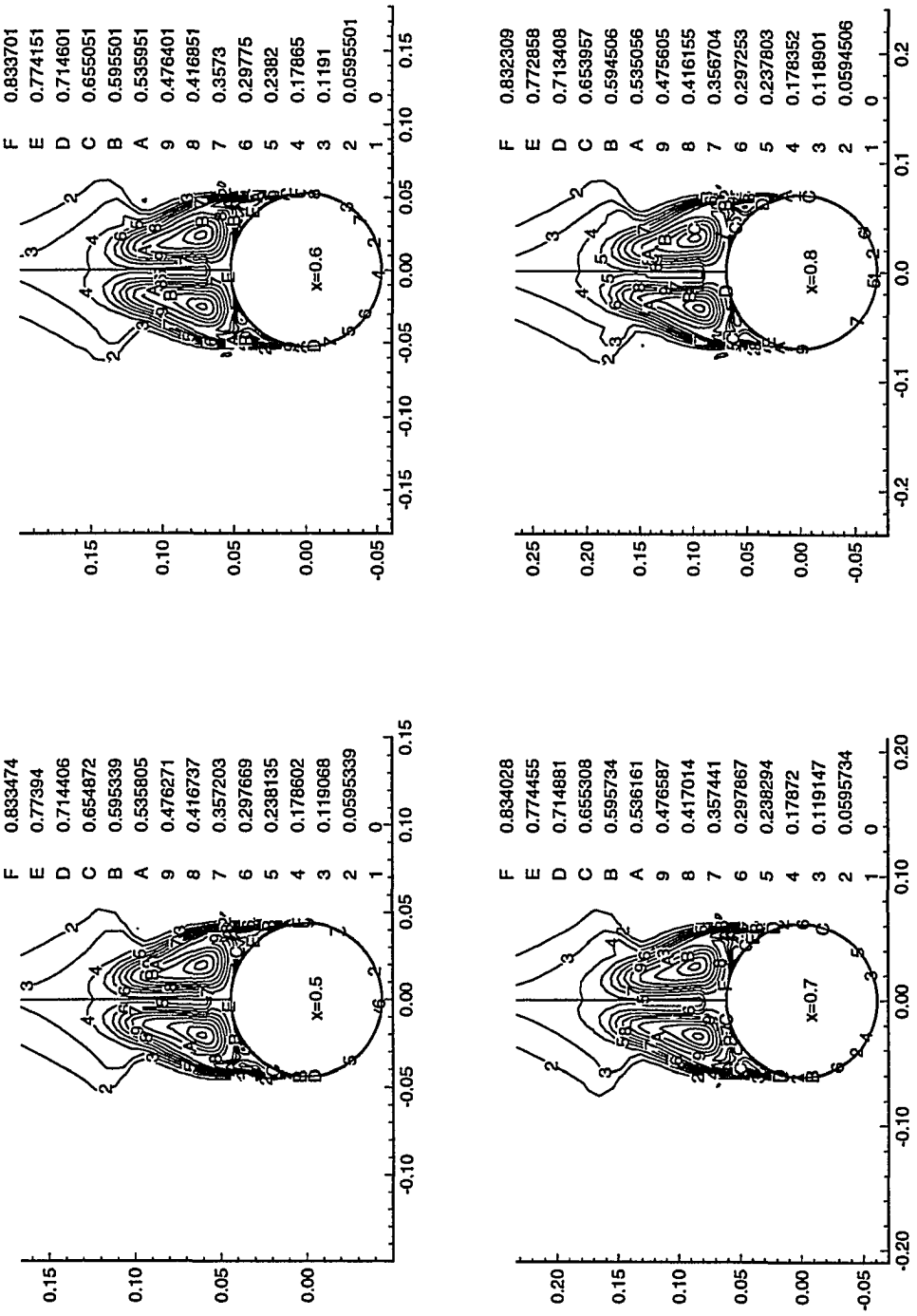

Figure 8.12: Continued

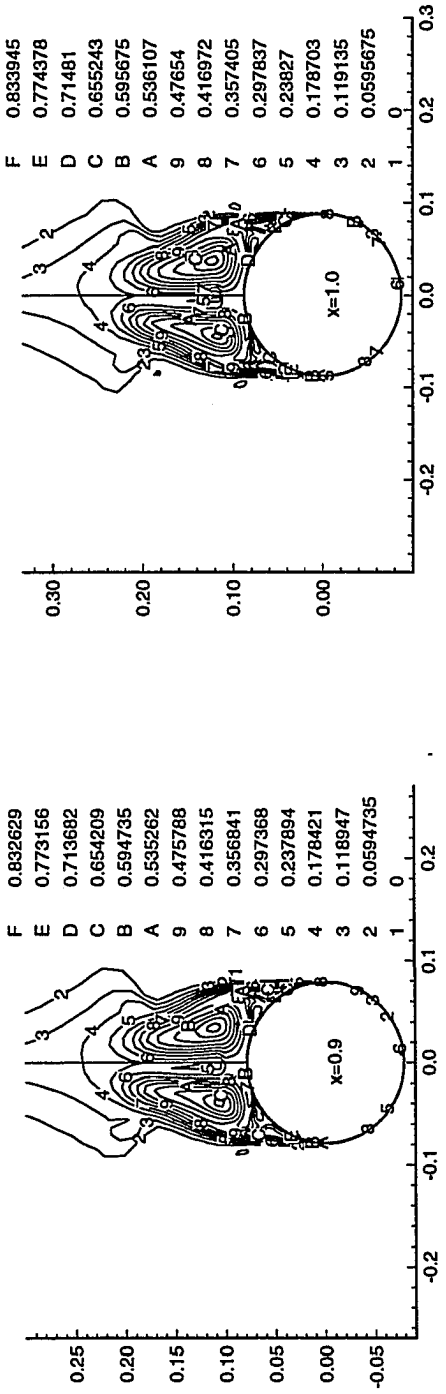

Figure 8.12: Continued

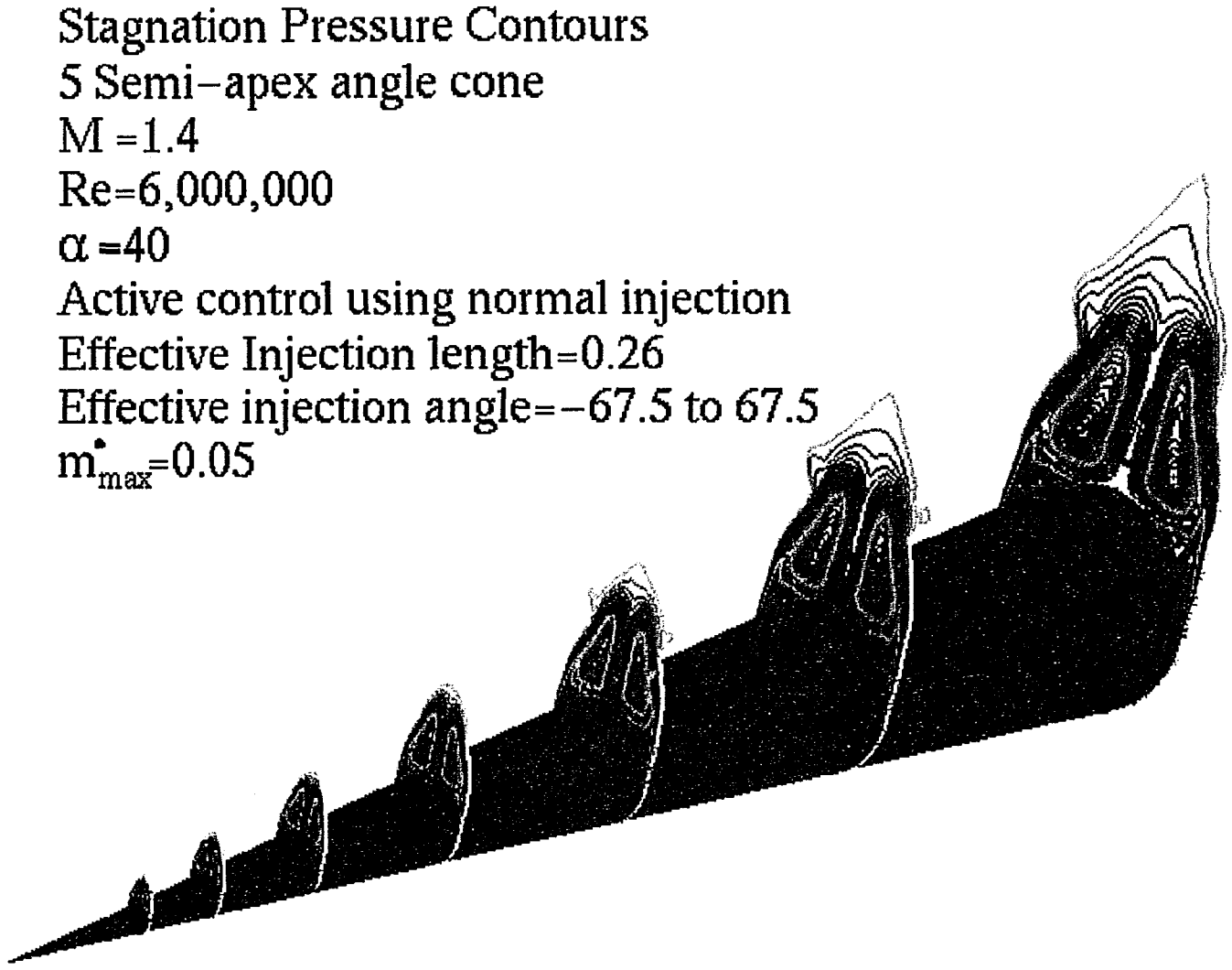

Figure 8.13: Stagnation pressure at different axial stations

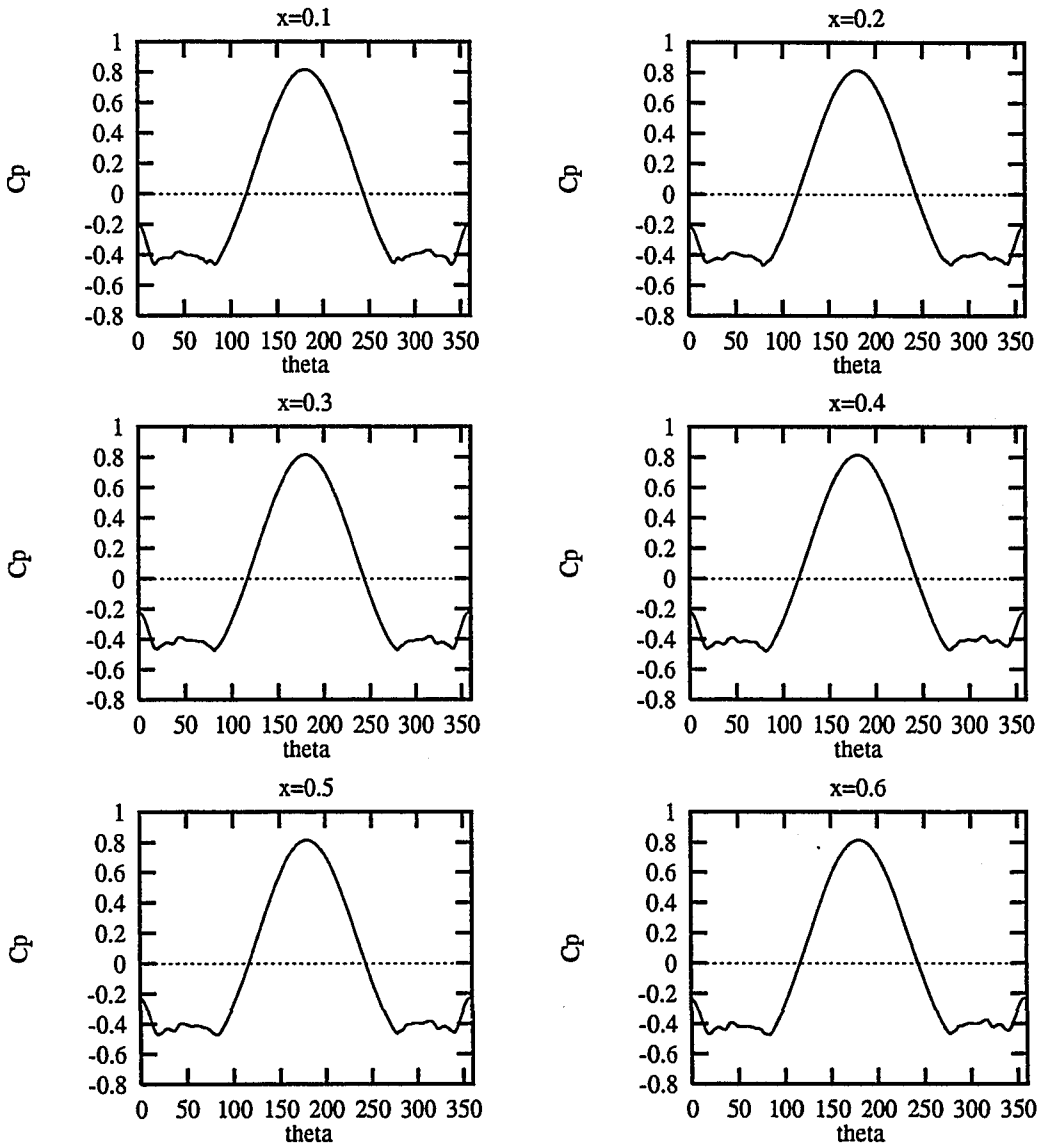

Figure 8.14: Surface pressure coefficient at different axial stations for flow around a circular cone with normal injection at $\alpha = 40°$, $M_\infty = 1.4$, $R_e = 6 \times 10^6$, $l_i = 0.26$, $\theta_i = -67.5 \rightarrow 67.5$, $\dot{m}_{max} = 0.03$.

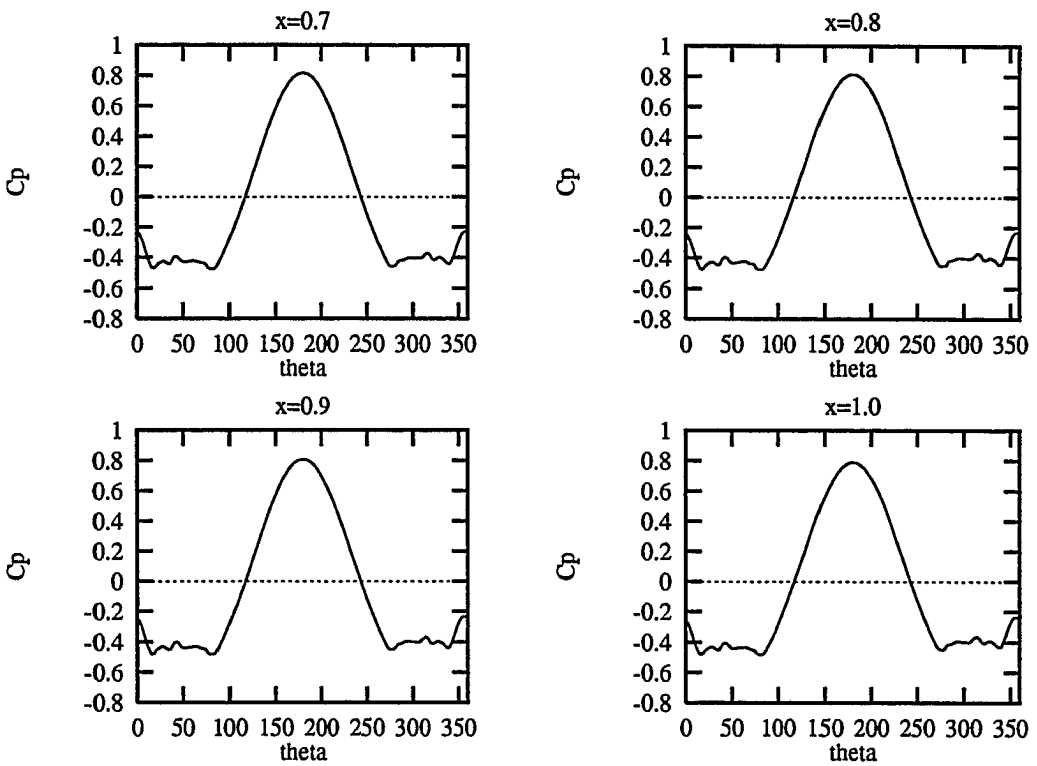

Figure 8.14: Continued

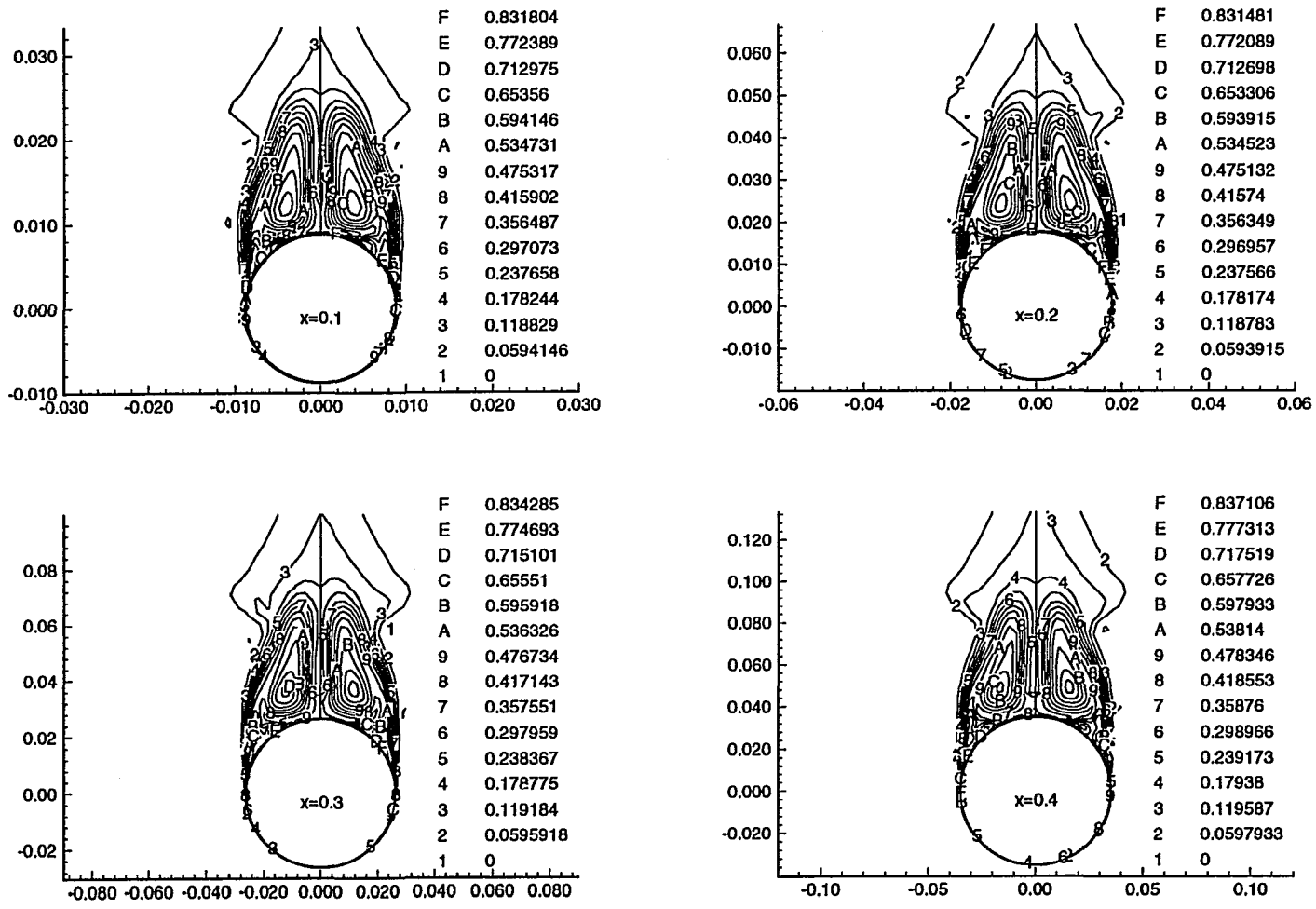

Figure 8.15: Total pressure loss contours at different axial stations for flow around a circular cone at $\alpha = 40°$, $M_\infty = 1.4$, $R_e = 6 \times 10^6$, $l_i = 0.26$, $\theta_i = -67.5 \rightarrow 67.5$, $\dot{m}_{max} = 0.03$.

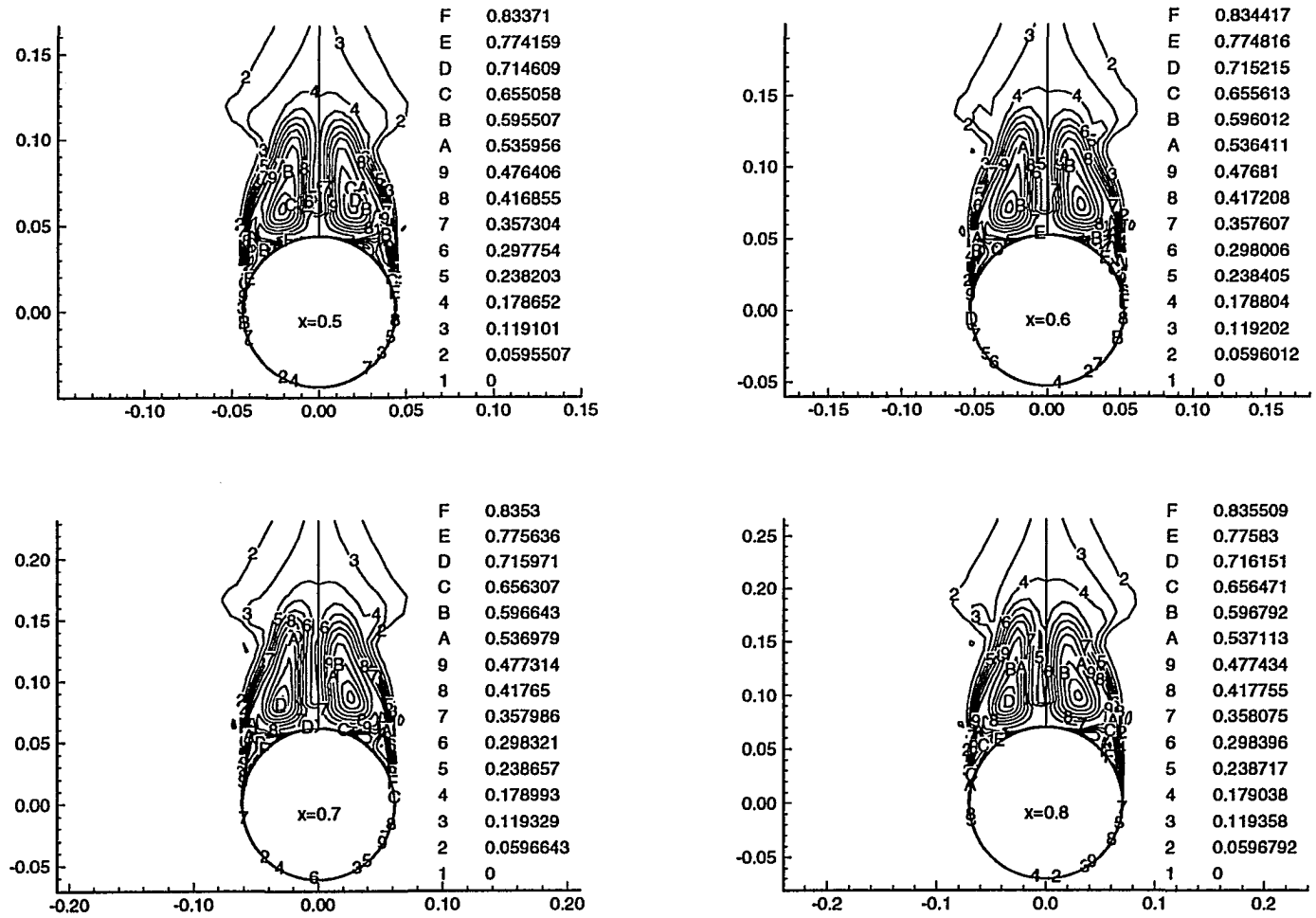

Figure 8.15: Continued

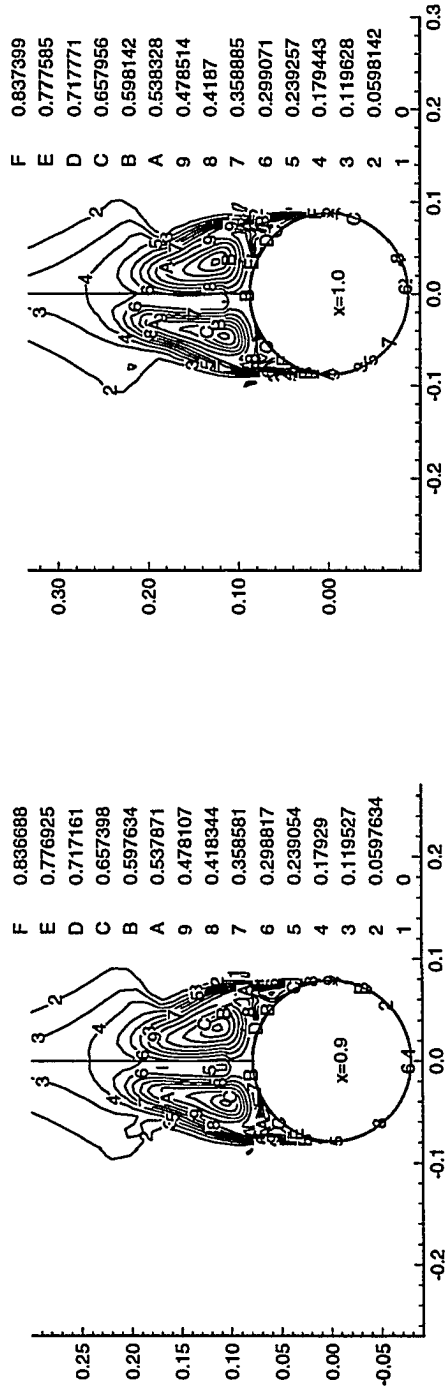

Figure 8.15: Continued

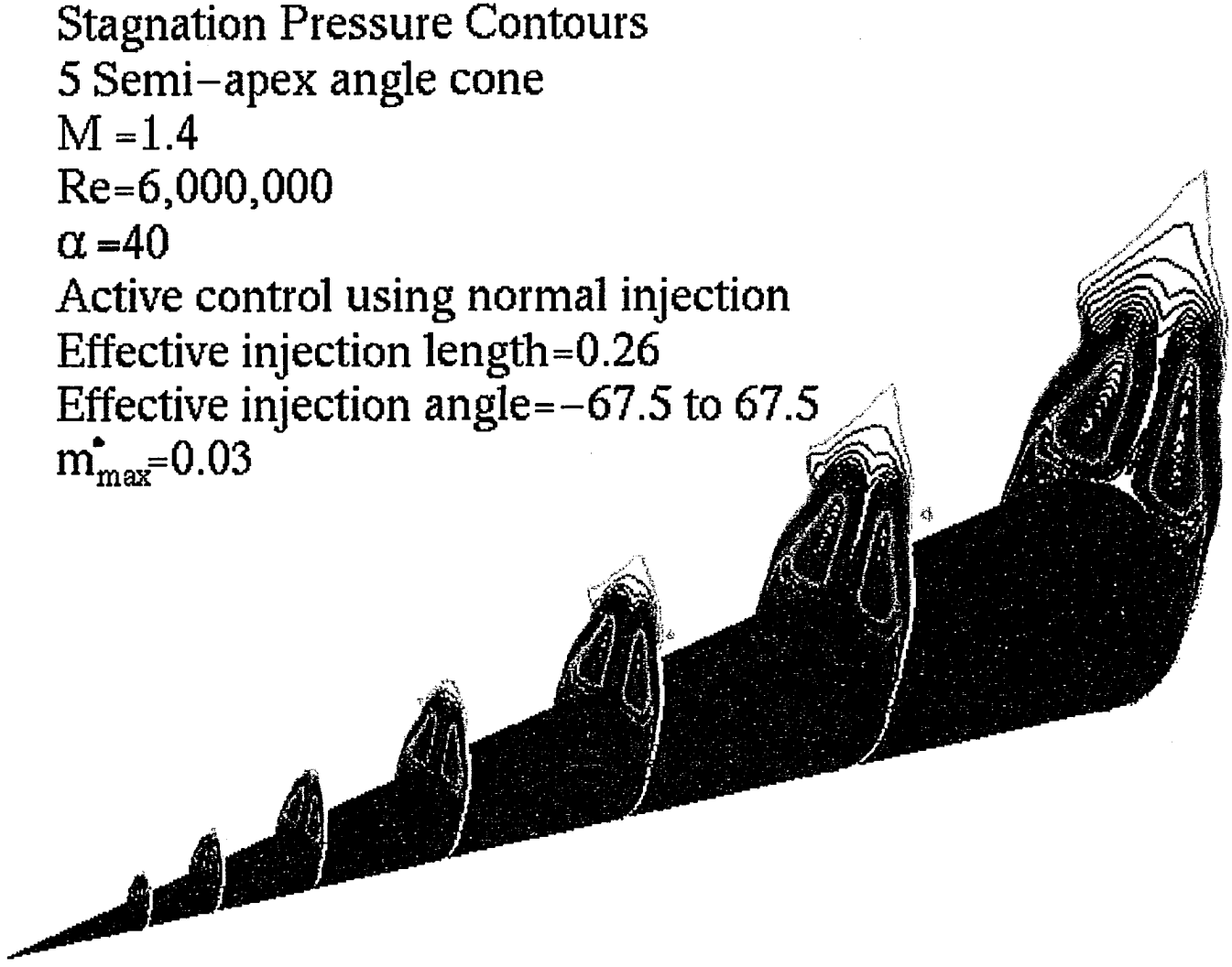

Figure 8.16: Stagnation pressure contours at different axial stations

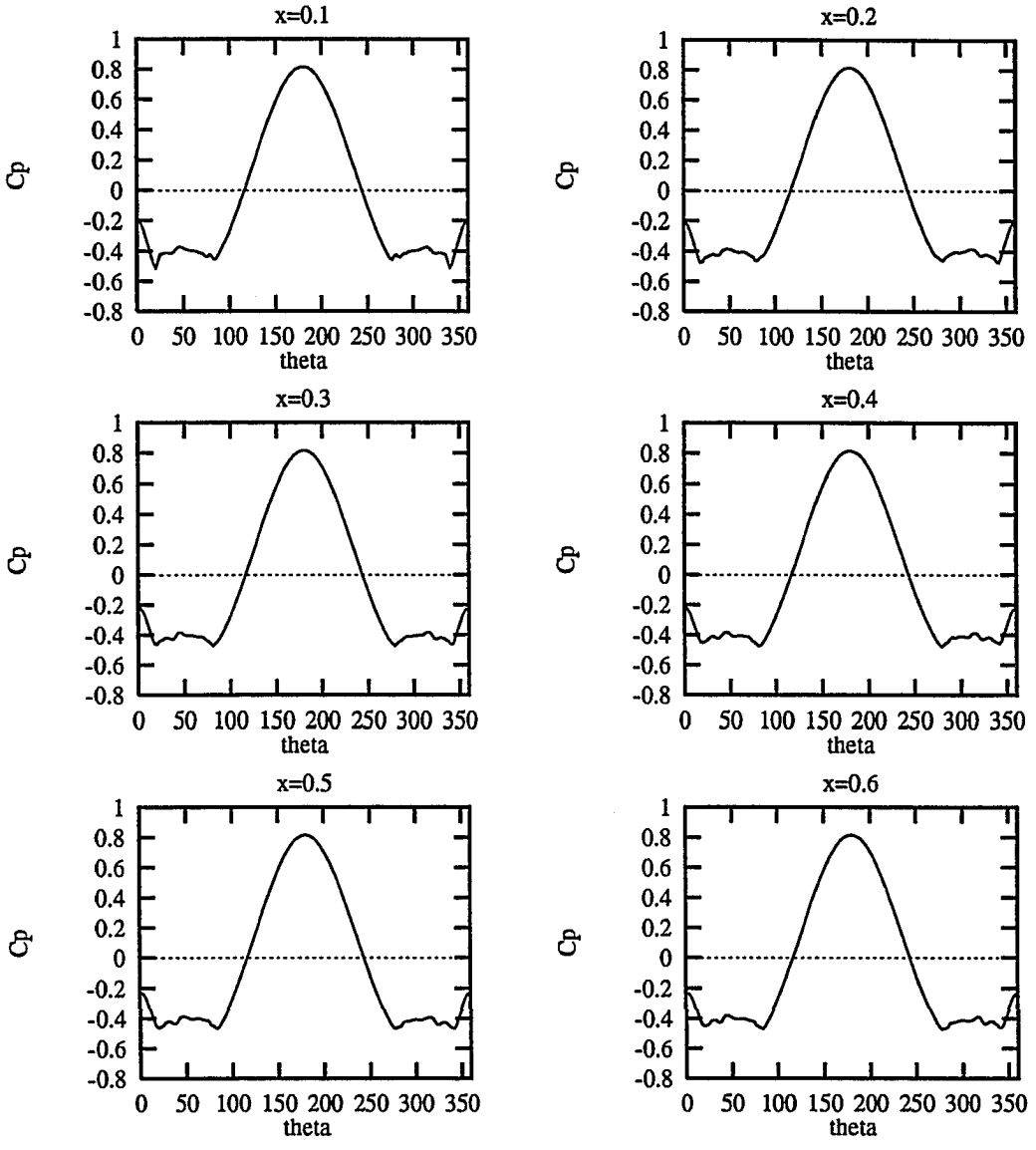

Figure 8.17: Surface pressure coefficient at different axial stations for flow around a circular cone with normal injection at $\alpha = 40°$, $M_\infty = 1.4$, $R_e = 6 \times 10^6$, $l_i = 0.1$, $\theta_i = -67.5 \rightarrow 67.5$, $\dot{m}_{max} = 0.05$.

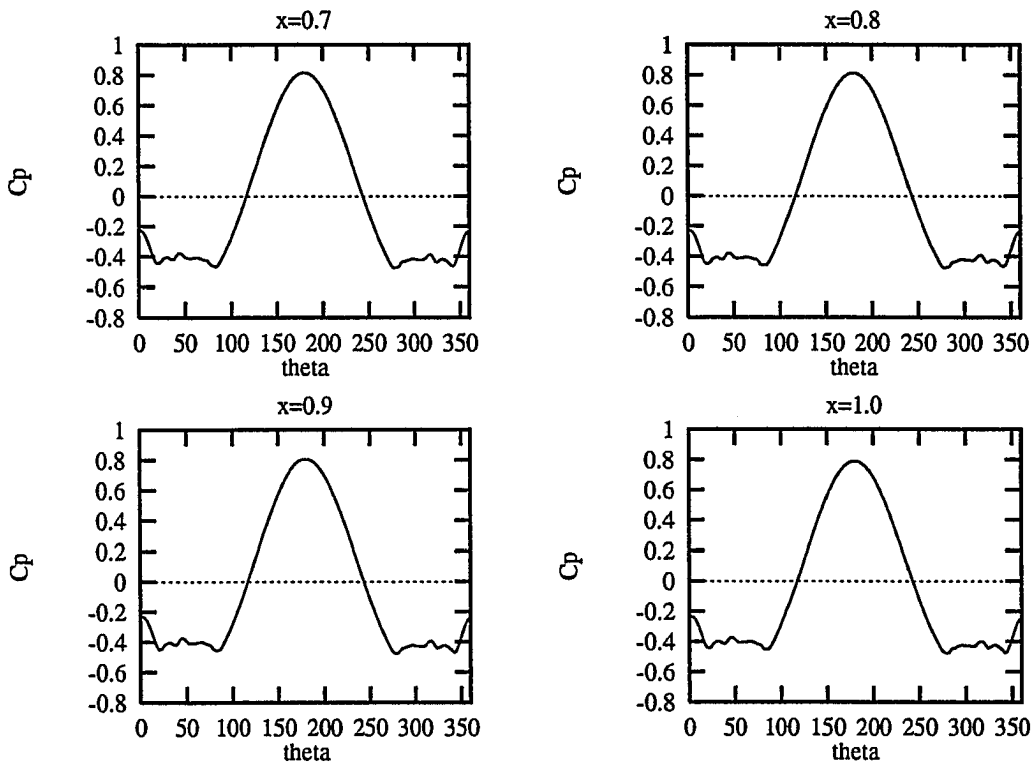

Figure 8.17: Continued

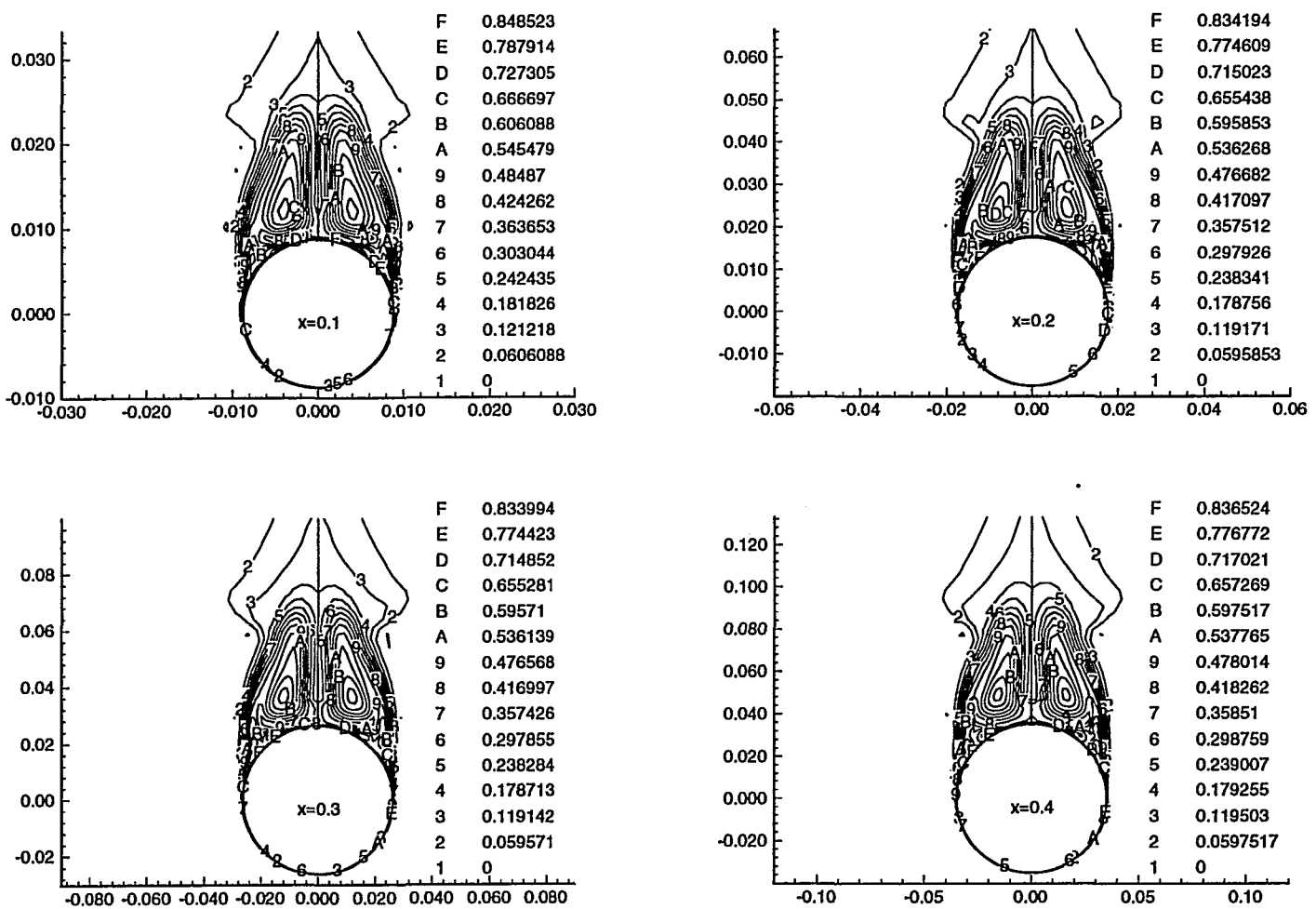

Figure 8.18: Total pressure loss contours at different axial stations for flow around a circular cone with normal injection at $\alpha = 40°$, $M_\infty = 1.4$, $R_e = 6 \times 10^6$, $l_i = 0.1$, $\theta_i = -67.5 \rightarrow 67.5$, $\dot{m}_{max} = 0.05$.

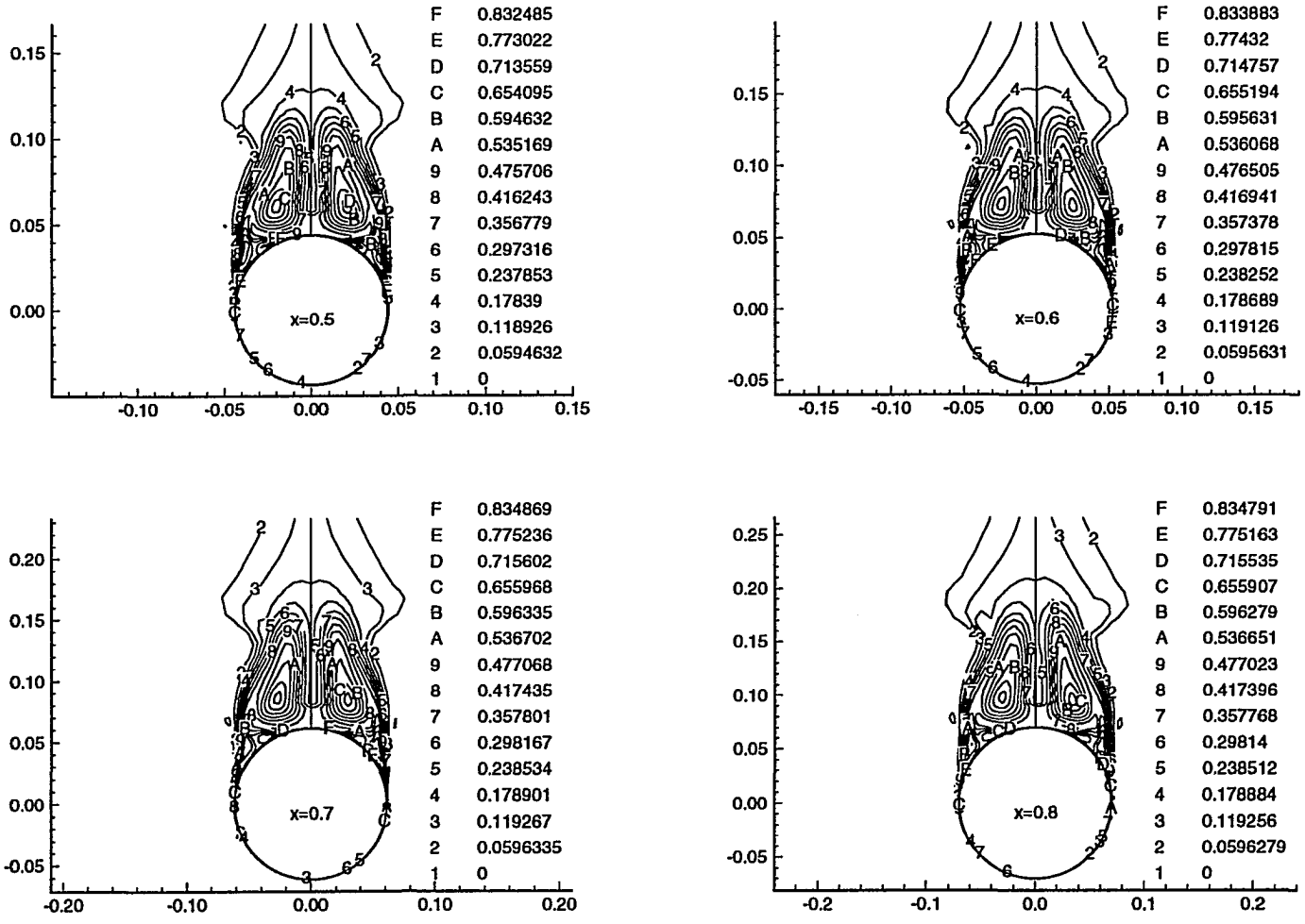

Figure 8.18: Continued

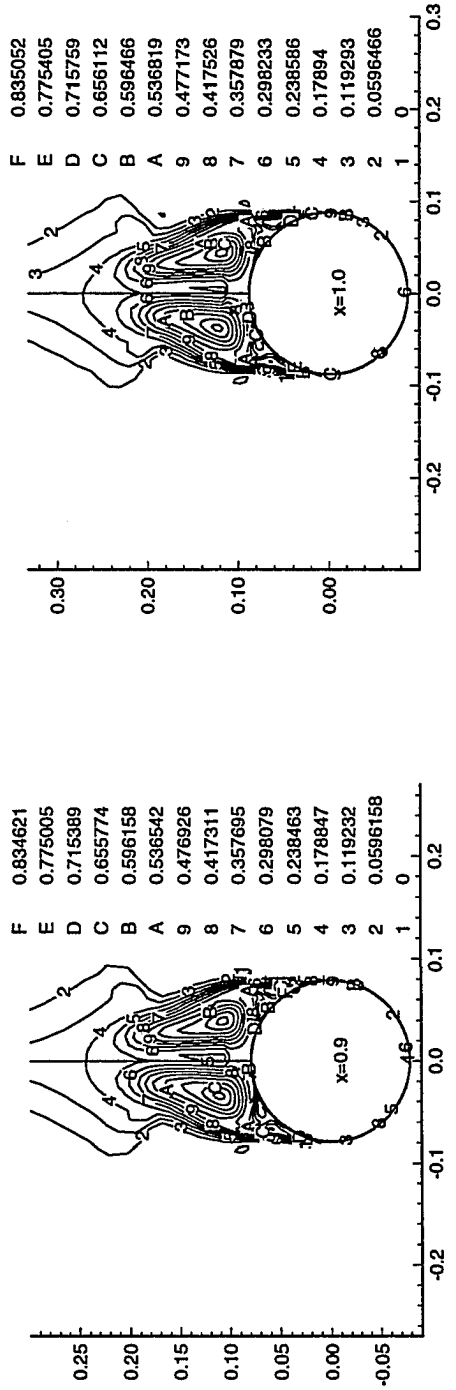

Figure 8.18: Continued

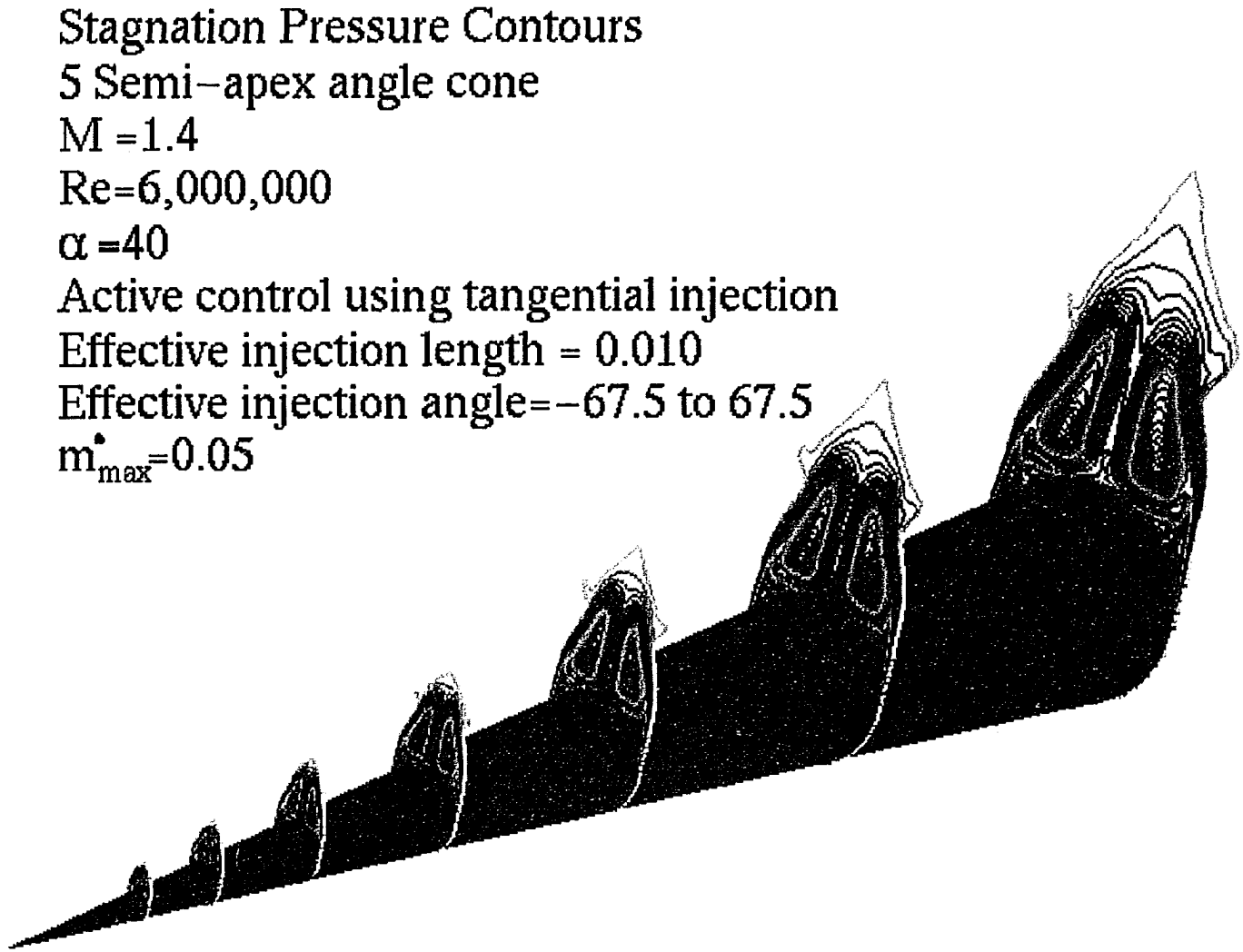

Figure 8.19: Stagnation pressure at different axial stations

CHAPTER 9

CONCLUSIONS AND RECOMMENDATIONS

The main objective of the present research work was to investigate the effectiveness of several control methods, with emphasis on active control methods, to alleviate and possibly eliminate the side force and the flow asymmetry that arise with increased AOA on symmetric bodies. In order to achieve comparisons among the different control methods, the physical flow conditions were confined to the specific conditions: $M_\infty = 1.8$ and $R_e = 10^5$ for the conical flow problems, and $M_\infty = 1.4$ and $R_e = 6 \times 10^6$ for the three-dimensional flow problems. In this chapter, the main findings of the present research are presented followed by recommendations for future computational and experimental work.

9.1 Conclusions

Throughout the present research work, several control methods—both passive and active—were investigated in order to evaluate their effectiveness in alleviating asymmetric side forces and recovering the flow symmetry. The asymmetry of the flowfield was found to be unique and independent of the type or the level of the disturbance which is in agreement with Ref. 22. All the control methods were applied for the

steady flow asymmetry that occurs on the leeward side of the cone at $\alpha = 20°$ for the conical cases and $\alpha = 40°$ for the three-dimensional cases.

The control methods included: finite length side-strakes, normal and tangential injection, surface heating, spinning and rotary oscillations. The effects of side-strakes and their span lengths in reducing the side forces was investigated. The cases considered, covered an AOA range from 30° to 50° and the side-strake span length range from $0.35r$ to $0.5r$. The side-strakes were found to be effective in eliminating the side force and the flow asymmetry up to high AOA. Also, the side-strakes acted as small wings on the body and hence, an increase in lift was observed. The effect of increasing the span length of the side-strake was to enhance flow stability by increasing the lateral distance between the right and left vortices, and hence, they prevented the interaction of the vortices. Also, it can be concluded from the results, presented in this chapter, that the symmetry in the locations of the separation points is another effect of the side-strakes.

Uniform normal injection is an effective tool for eliminating the side force only when a proper choice of location and injection level is made. It should also be mentioned that while the side force was eliminated using this approach, the flowfield was asymmetric due to the antisymmetric injection. On the other hand, the pressure-sensitive mass injection technique that was suggested and applied in Chap. 6, has proved to be effective, not only in eliminating the side force but also in recovering the flowfield symmetry. This technique is effective for AOA up to 30°. The three-dimensional results of the normal and tangential injection for the flow over a cone qualitatively verified the results of the conical flow solutions. Injection was applied close to the nose and the influence of the effective injection length was investigated. A minimum length was required to eliminate flow asymmetry over the entire cone length. The mass flow rate was not a prime factor as long as it exceeded a certain minimum value.

Surface heating proved to be effective in AOA range larger than that of injection. Surface heating followed by normal injection was found to be the most effective method with AOA range up to 40°. It should be mentioned here that the body surface temperature values required to control the flow asymmetry were higher than what can be applied practically.

The effect of spinning and rotary oscillation was different from the other control methods. The resulting side force oscillated and when the average of these oscillations approached zero (or at least was less than the original side force), then the level of asymmetry was reduced on the average. Large uniform spinning rates were effective in reducing the average side force substantially for the given initial case of asymmetric flow. Rotary oscillations with large surface-velocity amplitudes, large angular-motion amplitudes and small periods of oscillation were much more effective than uniform spinning for the same surface velocity, because it eliminated the mean side force. Moreover, the effectiveness of rotary oscillation control did not require a prescribed initial shape for the vortex asymmetry.

9.2 Recommendations for Future Work

9.2.1 Computational methods and grid refinement

In the present study, a scheme which was first order in time and second order in space was used. While this is acceptable when the time step is small enough, some applications require that relatively long time intervals be resolved completely and hence, schemes which are second order accurate in time are needed to study more efficiently and accurately the onset of asymmetry, as well as the effect of the different control methods.

To capture the asymmetric flow, a very fine grid should be used. Adaptive grids represent a step that will make it possible, within the present computational resources, to get a better understanding of the flow asymmetry and better grounds to attack this problem. With advances in computational resources and programming languages, better use and implementation of computational algorithms as well as the use of finer grids required to obtain better resolution of the problem will be feasible. Another method which can be used to avoid the use of very fine grids is the "vorticity refinement" [148–150] in which a term is added to the momentum conservation equations. This term depends only on local variables and is zero outside vortical regions.

9.2.2 Passive control methods

While many research studies have been conducted in recent years to investigate the effect of fins and side strakes, very little work has been done to investigate their problems accurately—directional instability and interference with radar operations. The next step in passive control investigations should be concerned with their applications in real configurations. The effects of strake length, width and shape need to be investigated computationally. Grid clustering in more than one direction is needed for the study of the finite-length strakes and their effect on flow asymmetry, hence, multi-block grids are recommended. Using multi-block grids increases the time requirement, especially where one-to-one patching along interfaces is not feasible.

Helical trips, while being tested and experimentally proven to be an effective asymmetry-suppression method, were not investigated numerically. Several parameters should be considered in such a study including trip shapes, width and location.

9.2.3 Active control methods

The application of different active control methods, presented in this research work, on real aircraft and missiles configurations should be considered. Energy assessment for the active methods should be evaluated and practical methods of implementation should be considered. Spinning and rotary oscillations need to be investigated further using three-dimensional configurations. This requires the use of time accurate marching with reasonable time steps in order to resolve the problem accurately and also the use of fine grids are required to capture the asymmetry. That was beyond the available computational resources. Local surface heating should be considered within practical limitations. Other active control methods such as suction and coning motion that are not included in the present research should also be considered.

Not much work has been done in the hybrid control methods because of the complexity of the problem. Hybrid passive-active control methods are promising but have not been investigated. Such methods include side-strakes or fins with normal or tangential blowing. Spinning and rotary oscillations for configurations with side strakes and fins need to be investigated.

No detailed experimental measurements for the different control methods were available during the course of this study. Detailed experimental investigations are needed to validate the numerical methods. In fact, most of the experimental work that has attacked the problem of asymmetric flow deals mainly with the side force response with the changes of the AOA, while surface pressure measurements are needed for quantitative codes validations.

BIBLIOGRAPHY

[1] Keener, E. R., Chapman, G. T., Cohen, L., and Taleghani, J., "Side Forces on a Tangent-Ogive Forebody with a Fineness Ratio of 3.5 at High Angles of Attack and Mach Numbers from 0.1 to 0.7," Technical Memorandum TM X-3437, NASA, February 1977.

[2] Ericsson, L. E. and Reding, J. P., "Asymmetric Flow Separation and Vortex Shedding on Bodies of Revolution," in *Tactical Missile Aerodynamics: General Topics* (Hemsch, M. J., ed.), vol. 141 of *Progress in Astronautics and Aeronautics*, ch. 10, pp. 391–452, AIAA, 1992.

[3] McElory, G. E. and Sharp, P. S., "An Approach to Stall/Spin Development and Test," *AIAA Paper No. 71-772*, July 1971.

[4] Ericsson, L. E. and Reding, J. P., "Review of Vortex-Induced Asymmetric Loads - Part I," *Z. Flugwiss. Weltraumforsch.*, vol. 5, no. 3, 1981, pp. 162–174.

[5] Fiechter, M., "Uber Wirbelsysteme an schlan ken Rotationskorpern und ihren Einfluss auf die aerodynamischen Beiwerte," *Deutsch-Franzosisches Forschungs-Institut Saint-Louis, Report 10/66*, 1966.

[6] Jorgensen, H. L., "Prediction of Static Aerodynamic Characteristics For Slender Bodies Alone and With Lifting Surfaces to Very High Angles of Attack," NASA Technical Report NASA TR R-474, NASA, September 1977.

[7] Letko, W., "A Low Speed Experimental Study of the Directional Characteristics of a Sharp Nosed Fuselage through a Large Angle of Attack Range at Zero Sideslip," Technical Note NACA TN-2911, NACA, 1953.

[8] Dunn, E. L., "A Low Speed Experimental Study of Yaw Forces on Bodies of Revolution at Large Angles of Pitch and Zero Angle of Side Slip," Technical Memorandum TM-1588, U.S. Naval Ordnance Test Station, 1953.

[9] Pick, G. S., "Investigation of Side Forces on Ogive-Cylinder Bodies at High Angles of Attack in the M=0.5 to 1.1 Range," *AIAA Paper No. 71-0570, AIAA 4th Fluid and Plasma Dynamics Conference*, 1971.

[10] Keener, E. R. and Chapman, G. T., "Onset of Aerodynamic Side Forces at Zero Sideslip on Symmetric Forebodies at High Angles of Attack," *AIAA Paper No. 74-0770, AIAA Mechanics and Control of Flight Conference*, August 1974.

[11] Keener, E. R. and Valdez, J., "Side Forces on a Tangent-Ogive Forebody with a Fineness Ratio of 2.5 at High Angles of Attack and Low Speeds," Technical Memorandum TM X-73,176, NASA, December 1976.

[12] Wardlaw, A.Jr. and Morrison, A., "Induced Side Forces at High Angles of Attack," *Journal of Spacecraft and Rockets*, vol. 13, 1976, pp. 589–593.

[13] Keener, E. R. and Taleghani, J., "Wind Tunnel Investigations of Aerodynamic characteristics of five forebody models at High Angles of Attack at Mach Numbers from 0.25 to 2," Technical Memorandum NASA TM X-73,076, NASA, 1975.

[14] Degani, D. and Schiff, L. B., "Numerical simulation of the effect of spatial disturbances on vortex asymmetry," *AIAA Paper No. 89-0340, 27th Aerospace Sciences Meeting*, January 1989.

[15] Degani, D., "Numerical investigation of the origin of vortex Asymmetry of Flow Over Bodies at Large Angle of Attack," *ICAS-90-6.6.1*, 1990, pp. 1162–1172.

[16] Degani, D., "Numerical investigation of the origin of vortex Asymmetry," *AIAA Paper No. 90-0593, 28th Aerospace Sciences Meeting*, January 1990, pp. 1162–1172.

[17] Degani, D., "Effect of Splitter Plate on Unsteady Flows around a Body of Revolution at Incidence," *Physics of Fluids A*, vol. 3, September 1991, pp. 2122–2131.

[18] Degani, D., "Effect of Upstream Disturbance on Flow Asymmetry," *AIAA Paper No. 92-0408, 30th Aerospace Sciences Meeting*, January 1992, pp. 1162–1172.

[19] Kandil, O. A., Wong, T.-C., and Liu, C. H., "Prediction of Steady and Unsteady Asymmetric Flows around Cones," *AIAA Paper No. 90-0598, AIAA 28th Aerospace Sciences Meeting*, January 1990.

[20] Kandil, O. A., Wong, T.-C., Kandil, H. A., and Liu, C. H., "Computation and Control of Asymmetric Vortex Flow Around Circular Cones Using Navier-Stokes Equations," in *ICAS Paper No. 3.5.3*, vol. 2, 1990, pp. 883–893.

[21] Kandil, O. A., Sharaf El-Din, H. H., and Liu, C. H., "Recent Advances in Computational Active Control of Asymmetric Flows around Conical Forebodies," in *Fourth International Conference of Fluid Mechanics, Cairo, Egypt*, April 1992, pp. 237–249.

[22] Wong, T.-C., *Prediction and Control of Asymmetric Vortical Flows around Slender Bodies Using Navier-Stokes Equations.* PhD thesis, Old Dominion University, May 1991.

[23] Liu, C. H., Wong, T.-C., and Kandil, O. A., "Prediction of Asymmetric Vortical Flows around Slender Bodies Using Navier-Stokes Equations," *Fluid Dynamics Research*, vol. 10, 1992, pp. 409–450.

[24] Siclari, M. J. and Marconi, F., "The Computation of Navier-Stokes Solutions Exhibiting Asymmetric Vortices," *AIAA Paper No. 89-1817, AIAA 20th Fluid Dynamics, Plasma and Lasers Conference*, June 1989.

[25] Siclari, M. J., "Asymmetric Separated Flows at Supersonic Speeds," *AIAA Paper No. 90-0595, 28th Aerospace Sciences Meeting*, January 1990.

[26] Rainbird, W. J., Crabbe, R. S., Peake, D. J., and Meyer, R. F., "Some Examples of Separation in Three-Dimensional Flows," *Canadian Aeronautics and Space Journal*, December 1966, pp. 409–423.

[27] Stetson, K., "Boundary-Layer Separation on Slender Cones at Angles of Attack," *AIAA Journal*, May 1972, pp. 642–648.

[28] Lubard, S. C. and Helliwell, W. S., "Calculation of the Flow on a Cone at High Angle of Attack," *AIAA Journal*, July 1974, pp. 965–974.

[29] McRae, D. S. and Hussaini, M. Y., "A Numerical Simulation of Supersonic Cone Flow at High Angle of Attack," *AGARD CP-247, Paper 23*, October 1978.

[30] Cross, E. J.Jr., "Experimental and Analytical Investigation of the Expansion Flow Field over a Delta Wing at Hypersonic Speeds," Technical Note ARL 68-0027, Aerospace Research Laboratories, February 1972.

[31] Kandil, O. A., Wong, T.-C., and Liu, C. H., "Numerical Simulation of Steady and Unsteady Asymmetric Vortical Flow," *Journal of Fluids and Structures*, vol. 6, 1992, pp. 249–265.

[32] Kandil, O. A., Wong, T.-C., and Liu, C. H., "Prediction of Steady and Unsteady Asymmetric Vortical Flow Around Cones," *AIAA Journal*, vol. 29, December 1991, pp. 2169–2178.

[33] Thomas, J. L., "Reynolds Number Effects on Supersonic Asymmetrical Flows over a cone at High Angles of Attack," *AIAA Paper No. 91-3295, AIAA 9th Applied Aerodynamics Conference*, September 1991.

[34] Dusing, D. W. and Orkwis, P. D., "On Computing Vortex Asymmetries about Cones at Angles of Attack Using the Conical Navier-Stokes Equations," *AIAA Paper No.93-3628-CP, AIAA Atmospheric Flight Mechanics Conference*, August 1993, pp. 122–130.

[35] Rom, J., *High Angle of Attack Aerodynamic.* Springer-Verlag, 1992.

[36] NASA Dryden Flight Research Center, *Fourth High Alpha Conference*, NASA Conference Publication 10143, July 1994.

[37] North Atlantic Treaty Organization, *Special Course on Missile Aerodynamics*, AGARD R-754, 1988.

[38] NASA, *Vortex Flow Aerodynamics, Vol. 1*, NASA Conference Publication 2416, October 1985.

[39] North Atlantic Treaty Organization, *High angle of Attack Aerodynamics*, AGARD LS-121, 1982.

[40] North Atlantic Treaty Organization, *Maneuvering Aerodynamics*, AGARD-CP-497, 1991.

[41] North Atlantic Treaty Organization, *Missile Aerodynamics*, AGARD CP-493, 1990.

[42] North Atlantic Treaty Organization, *Vortex Flow Aerodynamics*, AGARD CP-493, 1990.

[43] North Atlantic Treaty Organization, *High Angle of Attack Aerodynamics*, AGARD CP-247, 1979.

[44] Ericsson, L. E. and Reding, J. P., "Asymmetric Flow Shedding From Bodies of Revolution," in *Tactical Missile Aerodynamics* (Hemsch, M. J. and Nielsen, J. N., eds.), vol. 104 of *Progress in Astronautics and Aeronautics*, ch. VII, pp. 243–296, AIAA, 1986.

[45] Ericsson, L. E. and Reding, J. P., "Aerodynamic Effects of Asymmetric Vortex Shedding from Slender Bodies," *AIAA Paper No. 85-1797*, 1985.

[46] Hunt, B. L., "Asymmetric Vortex Forces and Wakes on Slender Bodies (invited Paper)," *AIAA Paper No. 82-1336, AIAA 9th Atmospheric Flight Mechanics Conference*, August 1982.

[47] Ericsson, L. E. and Reding, J. P., "Review of Vortex-Induced Asymmetric Loads - Part II," *Z. Flugwiss. Weltraumforsch.*, vol. 5, no. 6, 1981, pp. 349–366.

[48] Ericsson, L. E. and Reding, J. P., "Steady and Unsteady Vortex-Induced Asymmetric Loads on Slender Vehicles," *Journal of Spacecraft*, vol. 18, March-April 1981, pp. 97–109.

[49] Skow, A. M. and Titiriga, A.Jr., "A Survey of Analytical and Experimental Techniques to Predict Aircraft Dynamic Characteristics at High Angles of Attack," in *AGARD CP 235, Dynamic Stability Parameters, Paper No. 19*, 1979.

[50] Newsome, R. W. and Kandil, O. A., "Vortical Flow Aerodynamics- Physical Aspects and Numerical Simulation," *AIAA Paper No. 87-0205*, January 1987.

[51] Stahl, W., "Suppression of Asymmetry of The Vortex Flow Behind a Circular Cone at High Incidence," *AIAA Paper No. 89-3372-CP, AIAA Atmospheric Flight Mechanics Conference*, 1989, pp. 231–236.

[52] Ng, T. T., "Effect of a Single Strake on the Forebody Vortex Asymmetry," *Journal of Aircraft*, vol. 27, September 1990, pp. 844–846.

[53] Kandil, O. A., Wong, T.-C., and Liu, C. H., "Asymmetric Supersonic Flow Around Cones with Noncircular Sections," in *AGARD CP 493, Missile Aerodynamics, Paper No. 16*, 1990.

[54] Coe, P. L.Jr., Chambers, J. R., and Letko, W., "Asymmetric Lateral-Directional Characteristics of Pointed Bodies of Revolution at High Angles of Attack," Technical Note D-7095, NASA, November 1972.

[55] Modi, V. J. and Stewart, A. C., "Approach to Side Force Alleviation Through Modification of The Pointed Forebody Geometry," *AIAA Paper No. 90-2834-CP, AIAA Atmospheric Flight Mechanics Conference*, 1990, pp. 349–358.

[56] Modi, V. J., Cheng, C. W., and Mak, A., "Reduction of the Side Force on Pointed Forebodies Through Add-on Tip Devices," *AIAA Paper No. 90-3005-CP, AIAA Applied Aerodynamics Conference*, August 1990, pp. 100–108.

[57] Rao, D. M. and Sharma, G., "Side-Force Control on a Forebody of Diamond Cross-Section at High Angles of Attack," *AIAA Paper No. 93-3407-CP, AIAA Applied Aerodynamics Conference*, August 1993, pp. 43–52.

[58] Murri, D. G., Shah, G. H., DiCarlo, D. J., and Trilling, T. W., "Actuated Forebody Strake Controls for the F-18 High Alpha Research Vehicle," *AIAA Paper No. 93-3675-CP, AIAA Atmospheric Flight Mechanics Conference*, August 1993, pp. 507–517.

[59] Rao, D. M., "Side-Force Alleviation on Slender, Pointed Forebodies at High Angles of Attack," *Journal of Aircraft*, vol. 16, November 1979, pp. 763–768.

[60] Naumann, A., Morsback, M., and Kramer, C., "The Conditions of Separation and Vortex Formation Past Cylinders," in *Separated Flows*, AGARD CP 4, 1966, pp. 547–574.

[61] Brown, R. C., "On the Asymmetric Aerodynamic Forces of Slender Bodies of Revolution," in *Proceedings of BOWACA Meeting*, (McDonnell Aircraft Corp., St. Louis, MO), 1965.

[62] Kruse, R. L., Keener, E. R., Chapman, G. T., and Claser, G., "Investigation of the Asymmetric Aerodynamic Characteristics of Cylindrical Bodies of Revolution With Variations in Nose Geometry and Rotational Orientation at Angles of Attack to 58° and Mach number to 2," Technical Memorandum 78533, NASA, September 1979.

[63] Baysal, O., Fouladi, K., and Miller, D. S., "Computations of Supersonic Flows over a Body at High Angles of Attack," *AIAA Journal*, vol. 27, April 1989, pp. 427–437.

[64] Moskovitz, C. A., Hall, R. M., and DeJarnette, F. R., "Effects of Surface Perturbations on the Asymmetric Vortex Flow Over a Slender Body," *AIAA Paper No. 88-0483, AIAA 26th Aerospace Sciences Meeting*, January 1988.

[65] Moskovitz, C. A., Hall, R. M., and DeJarnette, F. R., "Effects of Nose Bluntness, Roughness and Surface Perturbations on the Asymmetric Flow Past Slender Bodies at Large Angles of Attack," *AIAA Paper No. 89-2236, AIAA 7th Applied Aerodynamics Conference*, August 1989.

[66] Moskovitz, C. A., Hall, R. M., and DeJarnette, F. R., "Experimental Investigation of a New Device to Control the Asymmetric Flow field on Forebodies at Large Angles of Attack," *AIAA Paper No. 90-0069, AIAA 28th Aerospace Sciences Meeting*, January 1990.

[67] Sharir, D., Portnoy, H., and Rom, J., "A Study of the Effect of Jets Injected From a Slender Body of Revolution on the Side Forces Acting on it at Large Angles of Attack in Low Speeds," Tech. Rep. TAE No. 337, Israel Institute of Technology, May 1978.

[68] Peake, D. J. and Owen, F. K., "Control of Forebody Three-Dimensional Flow Separation," in *AGARD CP-262, Aerodynamic Characteristics of Controls, Paper No. 15*, AGARD, Paper No. 15, May 1979.

[69] Peake, D. J., Owen, F. K., and Johnson, D. A., "Control of Forebody Vortex Orientation to Alleviate Side Forces," *AIAA Paper No. 80-0183, 18th Aerospace Sciences Meeting*, January 1980.

[70] Almosnino, D. and Rom, J., "Alleviation of the Side Force and the Yawing Moment Acting on a Slender Cone-Cylinder Body at High Angles of Attack, using Small Jet Injection at Subsonic and Transonic Speeds," Second Annual Technical Report Grant No. DAERO-78-G-119, European Research Office, 1979.

[71] Almosnino, D. and Rom, J., "Lateral Forces on a Slender Body and Their Alleviation at High Incidence," *Journal of Spacecraft*, vol. 18, September-October 1981, pp. 393–400.

[72] Wood, N. J. and Roberts, L., "Control of Vortical Lift on Delta Wings by Tangential Leading-Edge Blowing," *Journal of Aircraft*, vol. 25, March 1988, pp. 236–243.

[73] Wood, N. J., Roberts, L., and Celik, Z. Z., "The Control of Asymmetric Vortical Flows Over Delta Wings at High Angles of Attack," *AIAA Paper No 1989-3347-CP*, 1989, pp. 484–491.

[74] Williams, D., El-Khabiry, S., and Papazian, H., "Control of Asymmetric Vortices around a Cone -Cylinder Geometry with Unsteady Base Bleed," *AIAA Paper No. 89-1004, AIAA 2nd Shear Flow Conference*, March 1989.

[75] Ng, T. T. and Malcolm, G. N., "Aerodynamic Control Using Forebody Blowing and Suction," *AIAA Paper No. 91-0619, 29th Aerospace Sciences Meeting*, January 1991.

[76] Guyton, R. W. and Maerki, G., "X-29 Forebody Jet Blowing," *AIAA Paper No. 92-0017, 30th Aerospace Sciences Meeting & Exhibit*, January 1992.

[77] Cornelius, K. C., Pandit, N., Osborne, R. F., and Guyton, R. W., "An experimental Study of Pneumatic Vortex Flow Control on High Angle of Attack Forebody Model," *AIAA Paper No. 92-0018, 30th Aerospace Sciences Meeting & Exhibit*, January 1992.

[78] Celik, Z. Z. and Roberts, L., "Aircraft Control at High-Alpha by Tangential Blowing," *AIAA Paper No. 92-0021, 30th Aerospace Sciences Meeting & Exhibit*, January 1992.

[79] Lanser, W. R. and Meyn, L. A., "Forebody Flow Control on a Full-Scale F/A-18 Aircraft," *AIAA Paper No. 92-2674, AIAA 10th Applied Aerodynamics Conference*, June 1992.

[80] Lanser, W. R., Meyn, L. A., and James, K. D., "Comparison of Full-Scale, Small-Scale, and CFD Results for F/A-18 Forebody Slot Blowing," in *Fourth High Alpha Conference*, NASA Dryden Flight Research Center, July 1994.

[81] Cornelius, K. C. and Lucius, G. A., "Side Force Augmentation at High Angle of Attack from Pneumatic Vortex Flow Control," *AIAA Paper No. 93-2959, AIAA 24th Fluid Dynamics Conference*, July 1993.

[82] Cornelius, K. C., Pandit, N., Osborn, R. F., and Guyton, R. W., "Experimental Study of Pneumatic Control of Forebody Vortices at High Alpha," *Journal of Aircraft*, vol. 31, January-February 1994, pp. 49–56.

[83] Crowther, W. J. and Wood, N. J., "Tangential Forebody Blowing-Yaw Control at High Alpha," *AIAA Paper No. 93-3406-CP, AIAA Applied Aerodynamics Conference*, August 1993, pp. 34–42.

[84] Kramer, B. R., Suarez, C. J., Malcolm, G., and James, K. D., "Forebody Vortex Control with Jet and Slot Blowing on an F/A-18," *AIAA Paper No. 93-3449-CP, AIAA Applied Aerodynamics Conference*, August 1993, pp. 387–397.

[85] Arena, A. S.Jr., Nelson, R. C., and Schiff, L. B., "Lateral Control at High Angles of Attack Using Pneumatic Blowing through a Chined Forebody," *AIAA Paper No. 93-3624-CP, AIAA Atmospheric Flight Mechanics Conference*, August 1993, pp. 76–85.

[86] Celik, Z. Z., "Dynamic Roll and Yaw Control by Tangential Forebody Blowing," *AIAA Paper No. 94-1853, 12th AIAA Applied Aerodynamics Conference*, June 1994.

[87] Kramer, B. and Smith, B., "F/A-18 and F-16 Forebody Vortex Control, Static and Rotary-Balance Results," in *Fourth High Alpha Conference*, NASA Dryden Flight Research Center, July 1994.

[88] Ross, F. W., "Low-Energy Pneumatic Control of Forebody Vortices," in *Fourth High Alpha Conference*, NASA Dryden Flight Research Center, July 1994.

[89] Tavella, D. A., Schiff, L. B., and Cummings, R. M., "Pneumatic Vortical Flow Control at High Angles of Attack," *AIAA Paper No. 90-0098, 28th Aerospace Sciences Meeting*, January 1990.

[90] Murman, S. M., Rizk, Y. M., Cummings, R. M., and Schiff, L. B., "Computational Investigation of Slot Blowing for Fuselage Forebody Flow Control," *AIAA Paper No. 92-0020, 30th Aerospace Sciences Meeting and Exhibit*, January 1992.

[91] Rosen, B. S. and Davis, W. H., "Numerical Study of Asymmetric Air Injection to Control High Angle-of-Attack Forebody Vortices on The X-29 Aircraft," *AIAA Paper No. 90-3004-CP, AIAA Atmospheric Flight Mechanics Conference*, 1990, pp. 89–99.

[92] Celik, Z. Z. and Roberts, L., "Vortical Flow Control on a Slender Body at High Angles of Attack," *AIAA Paper No. 91-2868l-CP, Fluid Mechanics Conference*, August 1991, pp. 199–211.

[93] Font, G. I., "Force Production Mechanisms of a Tangential Jet on Bodies at High Alpha," *AIAA Paper No. 92-4648-CP, AIAA Atmospheric Flight Mechanics Conference*, August 1992.

[94] Kandil, O. A., Sharaf El-Din, H. H., and Liu, C. H., "Active Control of Asymmetric Vortical Flows Around Cones Using Injection and Heating," *AIAA Paper No. 92-4426, AIAA Atmospheric Flight Mechanics Conference*, vol. 1, August 1992, pp. 244–253.

[95] Kandil, O. A., Sharaf El-Din, H. H., and Liu, C. H., "Injection Active Control of Asymmetric Flows Around Slender Pointed Forebodies," *Paper No. EC406-CP, First Industrial/University Symposium on High Speed Civil Transport Vehicles (HSCTV)*, December 1994.

[96] Kandil, O. A., Sharaf El-Din, H. H., and Liu, C. H., "Three Dimensional Solution of Pneumatic Active Control of Forebody Vortex Asymmetry," *AIAA 95-0101, AIAA 33th Aerospace Sciences Meeting and Exhibit*, January 1995.

[97] Gee, K., Rizk, Y., Murman, S., Lanser, W., and Meyn, L., "Analysis of a Pneumatic Forebody Flow Control Concept About a Full Aircraft Geometry," *AIAA Paper No. 92-2678-CP, 10th AIAA Applied Aerodynamics Conference*, June 1992, pp. 600–613.

[98] Gee, K. and Rizk, Y. M., "Effect of Forebody Tangential Slot Blowing on Flow about a Full Aircraft Geometry," *AIAA Paper No. 93-2962*, July 1993.

[99] Gee, K., Agosta-Greenmuuan, R. M., Rizk, Y. M., Schiff, L. B., and Cummings, R. M., "Computational Analysis of Forebody Tangential Slot Blowing," in *Fourth High Alpha Conference*, NASA Dryden Flight Research Center, July 1994.

[100] Swanson, W. M., "The Magnus Effect: a Summary of Investigations to Date," *Transactions of the ASME, Journal of Basic Engineering*, September 1961, pp. 461–470.

[101] Jacoboson, I. D. and Morton, J. B., "Boundary Layer Stability on a Yawed Spinning Body of Revolution and its Effect on the Magnus Force and moment," NASA Contractor Report NASA CR-2060, NASA, 1972.

[102] Dwyer, H. A., "Three Dimensional Flow Studies over a Spinning Cone at Angle of Attack," Contractor Report 137, USA Ballistic Research Laboratories, 1974.

[103] Jacobson, I. D., "Contribution of a Wall Shear Stress to the Magnus Effect on Nose Shapes," *AIAA Journal*, vol. 12, July 1974, pp. 1003–1005.

[104] Lin, T. C. and Rubin, S. G., "Viscous Flow over Spinning cones at Angle of Attack," *AIAA Journal*, vol. 12, July 1974, pp. 975–985.

[105] Dwyer, H. A. and Sanders, B. R., "Magnus Forces on Spinning Supersonic Cones- Part I: The Boundary Layer," *AIAA Journal*, vol. 14, April 1976, pp. 498–504.

[106] Yoshinaga, T., Tate, A., and Inoue, K., "Coning Motion of Slender Bodies at High Angles of Attack in Low Speed Flow," *AIAA Paper No. 81-1899, AIAA Atmospheric Flight Mechanics Conference*, August 1981.

[107] Miller, M. C., "Wind Tunnel Measurements of the Magnus Induced Surface Pressures on a Spinning Projectile in the Transonic Speed Regime," *AIAA Paper No. 83-1838, AIAA Applied Aerodynamics Conference*, July 1983.

[108] Ericsson, L. E., "Aerodynamic Characteristics of Noncircular Bodies in Flat Spin and Coning Motions," *Journal of Aircraft*, vol. 22, May 1985, pp. 287–392.

[109] Agarwal, R. K., "Computation of Supersonic Turbulent Flow Past a Spinning Cone," *AIAA Paper No. 82-0304, AIAA 20th Aerospace Sciences Meeting*, January 1982.

[110] Netterfield, M. P., "Computation of the Aerodynamics of Spinning Bodies using a Point-Implicit Method," *AIAA Paper No. 91-0339, 29th Aerospace Sciences Meeting*, January 1991.

[111] Kruse, R. L., "Influence of Spin Rate on Side Force of an Axisymmetric Body," *AIAA Journal*, vol. 16, April 1978, pp. 415–416.

[112] Fidler, J. E., "Active Control of Asymmetric Vortex Effects," *Journal of Aircraft*, vol. 18, April 1981, pp. 267–272.

[113] Suarez, C. J., Kramer, B. R., and Malcolm, G. N., "Forebody Vortex Control on an F/A-18 Using Small, Rotatable Tip-Strakes," *AIAA Paper No. 93-3142*, 1993.

[114] Kandil, O. A., Sharaf El-Din, H. H., and Liu, C. H., "Active Control of Asymmetric Conical Flow Using Spinning and Rotatory Oscillation," *AIAA 93-2958, AIAA 24th Fluid Dynamics Conference*, July 1993.

[115] Bushnell, D. M., "Longitudinal Vortex Control- Techniques and Applications," *Aeronautical Journal*, October 1992, pp. 293–311.

[116] Malcolm, G. N., "Forebody Vortex Control," *Progress in Aerospace Sciences*, vol. 28, 1991, pp. 171–234.

[117] Malcolm, G. N., "Forebody Vortex Control," in *AGARD AG 776, Special Course on Dynamics at High Angles of Attack: Experiments and Modeling*, 1991.

[118] Gad-el Hak, M. and Bushnell, D. M., "Separation Control: Review," *Journal of Fluids Engineering*, vol. 113, 1991, pp. 5–30.

[119] Ericsson, L. E., "Control of Forebody Flow Asymmetry: A Critical Review," *AIAA Paper No. 90-2833-CP, AIAA Atmospheric Flight Mechanics Conference*, 1990, pp. 326–348.

[120] Rao, D. M., "Vortex Control- Further Encounters," in *AGARD CP 494, Vortex Control Aerodynamics, Paper No. 25*, 1990.

[121] Ericsson, L. E. and Reding, J. P., "Alleviation of Vortex-Induced Asymmetric Loads," *Journal of spacecraft*, vol. 17, November-December 1979, pp. 546–553.

[122] Chapman, D. R., "Computational Aerodynamics Development and Outlook," *AIAA Journal*, vol. 17, December 1979.

[123] Powell, K. G., *Vortical Solutions of the Conical Euler Equations.* Braunschweig, Germany, 1990.

[124] McRae, D. S., "A Numerical Study of Supersonic Viscous Cone Flow at High Angle of Attack," *AIAA Paper No. 76-97*, January 1976.

[125] Courant, R., Isaacson, E., and Reeves, M., "On the Solution of Nonlinear Hyperbolic Differential Equations by Finite Differences," *Communications of Pure and Applied Mathematics*, vol. 5, 1952, pp. 243–255.

[126] Swanson, R. C. and Turkel, E., "On Central-Difference and Upwind Schemes," *ICASE REPORT NO. 90-44*, 1990.

[127] Hoffman, K. A. and Chiang, S. T., *Computational Fluid Dynamics for Engineers- Volume 2.* Engineering Education Systems, 1993.

[128] Kandil, O. A., Wong, T.-C., Kandil, H. A., and Liu, C. H., "Thin-Layer and Full Navier-Stokes, Locally Conical and Three- Dimensional Asymmetric Solutions," *AIAA Paper No. 91-0547, AIAA 29th Aerospace Sciences Meeting*, January 1991.

[129] Hirsch, C., *Numerical Computation of Internal and External Flows*, vol. 2. John Wiley and Sons, 1990.

[130] Kandil, H. A., *Navier-Stokes Simulation of Quasi-Axisymmetric and Three-Dimensional Supersonic Vortex Breakdown.* PhD thesis, Old Dominion University, May 1993.

[131] Steger, J. L. and Warming, R. F., "Flux Vector Splitting of of the Inviscid Gas-Dynamics Equations with Applications to Finite Difference Methods," *Journal of Computational Physics*, vol. 40, 1981, pp. 263–293.

[132] Hanel, D., Schwane, R., and Seider, G., "On the Accuracy of Upwind Schemes for the Solution of the Navier-Stokes equations," in *Proceedings of AIAA 8th Computational Fluid Dynamics Conference, AIAA Paper No. 87-1105*, 1987, pp. 22–46.

[133] Godunov, S. K., "A Difference Scheme for Numerical Computation of Discontinuous Solution of Hydrodynamic Equations," *Math. Sbornik*, vol. 47, 1959, pp. 271–306.

[134] Roe, P. L., "Approximate Riemann Solvers, Parameter Vectors and Difference Schemes," *Journal of Computational Physics*, vol. 43, 1981, pp. 357–372.

[135] Osher, S., "Riemann Solvers, the Entropy Condition and Difference Approximations," *SIAM Journal of Numerical Analysis*, vol. 21, 1984, pp. 217–235.

[136] Thomas, J. L. and Salas, M. D., "Far-Field Boundary Conditions for Transonic Lifting Solutions to the Euler Equations," *AIAA Journal*, vol. 24, July 1986, pp. 1074–1080.

[137] Thomas, J. L., Walters, R. W., Van Leer, B., and Rumsey, C. L., "An Implicit Flux Vector Split Algorithm for the Compressible Navier-Stokes Equations," *Proceedings of the 1985 Workshop on the Numerical Simulation of Compressible Flows, Vieweg, Braunschweig, Germany*, 1987, pp. 326–341.

[138] Walters, R. W. and Thomas, J. L., *State-of-the-Art Surveys on Computational Mechanics*, ch. 4: Advances in upwind Relaxation Methods. The American Society of Mechanical Engineers, 1989.

[139] Thomas, J. L. and Walters, R. W., "Navier-Stokes Computations for Aerodynamic Configurations at High Angles of Attack," in *Computational Methods in Viscous Aerodynamics* (Murthy, T. K. S. and Brebbia, C. A., eds.), ch. 5, pp. 147–162, Elsevier, 1990.

[140] Thomas, J. L. and Hartwich, P. M., *Tactical Missile Aerodynamics: Prediction Methodology*, vol. 142 of *Progress in Astronautics and Aeronautics*, ch. 12: Navier-Stokes Analyses of Flows over Slender Airframes. AIAA, 1992.

[141] Thomas, J. L. and Walters, R. W., "Upwind Relaxation Algorithms for the Navier-Stokes Equations," *AIAA Journal*, vol. 25, April 1987, pp. 527–534.

[142] Rumsey, C. L. and Thomas, J. L., "Upwind Navier-Stokes Solutions for Separated Periodic Flows," *AIAA Paper No. 86-0247, AIAA 24th Aerospace Sciences Meeting*, January 1986.

[143] Rumsey, C. L., "A Computational Analysis of Flow Separation over Five Different Airfoil Geometries at High Angles-of-Attack," *AIAA Paper No. 87-0188, AIAA 25th Aerospace Sciences Meeting*, January 1987.

[144] Anderson, W. K. and Thomas, J. L., "Extension and Applications of Flux-Vector Splitting to Unsteady Calculations of Dynamic Meshes," *AIAA Paper No. 87-1152-CP, AIAA 8th Computational Fluid Dynamics Conference*, June 1987.

[145] Krist, S. L., Washburn, A. E., and Visser, K. D., "A Computational and Experimental Investigation of a Delta Wing with Vertical Tail," *AIAA Paper No. 93-3009, AIAA 24th Fluid Dynamics Conference*, July 1993.

[146] Skow, A. M. and Erickson, G. E., "Modern Fighter Aircraft Design For High Angle of Attack," in *AGARD Lecture Series, High Angle of Attack Aerodynamics AGARD LS-121, Paper No. 4*, 1982.

[147] Peake, D. J., Fisher, D. F., and McRae, D. S., "Flight Experiments with a Slender Cone at Angle of Attack," *AIAA Paper No. 81-0337*, January 1981.

[148] Steinhoff, J., Yonghu, W., Mersch, T., and Senge, H., "Computational Vorticity Capturing: Application to Helicopter Rotor Flow," *AIAA Paper No. 92-0056, 30th Aerospace Sciences Meeting and Exhibit*, January 1992.

[149] Steinhoff, J. and Underhill, D., "Modification of the Euler Equations for Vorticity Confinement: Application to the Computation on Interacting Vortex Rings," *Physics of Fluids*, vol. 6, August 1994.

[150] Steinhoff, J., Mersch, T., and Decker, F., "Computation of Incompressible Flow over Delta Wings Using Vorticity Confinement," *AIAA Paper No. 94-0646, 32th Aerospace Sciences Meeting and Exhibit*, January 1994.